New Perspectives on Magnetotail Dynamic Processes from Combined Cluster and Double Star Observations

Andrew Paul Walsh

Mullard Space Science Laboratory

Department of Space and Climate Physics

University College London

A thesis submitted to UCL

for the degree of Doctor of Philosophy

June 2009

I, Andrew Paul Walsh, confirm that the work presented in this thesis is my own. Where information has been derived from other sources, I confirm that this has been indicated in the thesis.

Abstract

In this thesis, observations of the Earth's magnetotail from ESA's four Cluster and the two Sino-European Double Star spacecraft are presented. The observations are of intervals where data from the combination of Cluster and Double Star provide insights into the dynamics of the magnetotail that are not possible using data from one mission alone.

In the first study, observations of three magnetic flux ropes are presented, two of which were detected near-simultaneously at Cluster and Double Star TC-1, while the third was detected by Cluster, along with a TCR a few minutes later. The observations represent the first observations of multiple flux ropes existing in the magnetotail simultaneously, providing evidence that flux rope orientation is influenced by neutral sheet tilt and provide further evidence that TCRs in the lobes are caused by the passage of flux ropes in the plasma sheet.

In the second study, a detailed analysis of a plasma bubble is presented, including the first direct observations of the return flows around the flanks of the plasma bubble that are expected from theory and simulation. Furthermore a partially stagnant depleted wake behind the plasma bubble, not predicted by theory or simulation was discovered and the cross-tail extent of the bubble was measured to be $3\,R_E$. The first observations of near-Earth bubble features are also reported.

Finally, in the third study, the substorm onset process itself is investigated using a wide array of space- and ground-based instrumentation. A pseudobreakup and later substorm onset are distinguished using both geomagnetic and auroral data and the establishment of the substorm current wedge is observed in-situ using the TC-2 and GOES12 spacecraft. A link between higher latitude geomagnetic activity and the fast flows and plasma sheet expansion related to the reconnection of lobe field lines is also posited.

Acknowledgements

I should first thank my supervisors, Andrew Fazakerley and Chris Owen, for their guidance and support over the past three and a half years, without which I wouldn't have got very far at all. I'd also like to thank my office-mates past and present: Gethyn Lewis, Paul Henderson, Ilya Alexeev, Kimberley Steed, Colin Forsyth, Yasir Soobiah, Rob Bedington and Segheen Beyene for putting up with my eccentricities and (usually stupid) questions.

I'm indebted to the PEACE operations team, particularly Andrew Lahiff and Rob Wilson, as well as the other Cluster and Double Star instrument teams, without whose efforts this thesis would be a fair bit shorter. I'm also grateful to various other collaborators and co-workers, including but not limited to Martin Volwerk, Matt Taylor, Malcolm Dunlop, Chris Arridge, Sandrine Grimald, Mark Lester, Adrian Grocott and Harald Frey for their help, advice and data.

I'm especially thankful to Ian Mann, Jonny Rae, Kyle Murphy, Dave Miles, Clare Watt *et al.* at the University of Alberta for being gracious hosts and making my stay there a fruitful & enjoyable one, and for continuing to answer my incessant emails long after they could reasonably be expected to ignore me. I suppose I should also thank the waiters and waitresses of Edmonton for ensuring I got my drinks before everyone else, even if it did mean some of them were pink.

I'd also like to thank Jo Bartlett and Glyn Collinson - my house-mates and personal chauffeurs over the past few years, Sam Oates for being a bad influence but a good drinking buddy and Andy Fenney for cheerfully putting up with a lot of the drinking, Sheila Kanani for distracting me and keeping me sane during the last few weeks of writing up, and lastly my parents for not insisting that I got a real job in the first place.

Finally I'd like to acknowledge the Particle Physics and Astronomy Research Council (latterly the Science and Technology Facilities Council) for financial support over the course of my studies, and Vinnie & Hannah at the Kings Head in Holmbury St. Mary for giving me somewhere to spend it.

Contents

List of Figures

List of Tables

Chapter 1

Introduction

> Plasma seems to have the kinds of properties one would like for life. It's somewhat like liquid water – unpredictable and thus able to behave in an enormously complex fashion. It could probably carry as much information as DNA does. It has at least the potential for organizing itself in interesting ways.
>
> *Attributed to Freeman Dyson*

1.1 Plasma Physics Concepts

Plasma is the so-called "fourth state of matter". A plasma is an ionised gas, made up of an ensemble of electrons and ions that exhibits collective behaviour and can interact with and modify electromagnetic fields. Plasmas are made up of equal numbers of positive and negative charges. For each singly charged positive ion there is one electron, for each doubly charged positive ion there are two electrons, and so on. So overall, throughout an entire plasma there is a net charge of zero.

1.1.1 Quasi-neutrality and Debye Shielding

In an ensemble of particles with a net charge of zero, individual particles will still generate and experience electric potentials. Under certain circumstances the interaction between the particles in the ensemble will result in any charge density being shielded so that the ensemble appears to be neutral. This is called quasi-neutrality and a plasma is often a good example of a quasi-neutral fluid.

The electric potential experienced by a test charge due to a single point charge in a vacuum is known as the Coulomb potential and is given by

$$\phi_C = \frac{q}{4\pi\epsilon_0 r} \tag{1.1}$$

where q is the charge, ϵ_0 the permittivity of free space and r the distance from the source of the potential. When sufficient further charged particles are present, as is the case in a plasma, they will move to cancel out, or shield, the potential. In this situation a test charge will not experience a Coulomb potential but rather a Debye potential:

$$\phi_D = \frac{q}{4\pi\epsilon_0 r}\, e^{-\frac{r}{\lambda_D}} \tag{1.2}$$

where λ_D is the Debye length, the distance at which a Coulomb potential is reduced by a factor of e by the presence of shielding particles. The Debye length is controlled by the number density, n, of shielding particles and their temperature, so assuming a proton-electron plasma (i.e. $n_i = n_e$) it is given by

$$\lambda_D = \left(\frac{\epsilon_0 k_B T_e}{n q_e^2}\right)^{\frac{1}{2}} \tag{1.3}$$

where k_B is Boltzmann's constant, T_e is the electron temperature and q_e is the charge on the electron. T_e and q_e are considered rather than the temperature and charge of ions because the electrons have much higher mobility than the ions. Plasmas can only be considered quasi-neutral when their scale size is much larger than the Debye length.

1.1.2 The Plasma Frequency

If a perturbation is applied to a plasma that disturbs its quasi-neutrality, the particles will move to correct any imbalance in the charge density of the plasma. Because of their increased mobility, the electrons will accelerate towards the relatively static ions and, because of their (the electrons') inertia, oscillate about them. The frequency of this oscillation is called the electron plasma frequency, and describes the fundamental mode of oscillation of a plasma. The electron plasma frequency is given by

$$\omega_{pe} = \left(\frac{n_e q_e^2}{m_e \epsilon_0} \right)^{\frac{1}{2}} \tag{1.4}$$

where m_e is the mass of the electron.

1.2 Methods of Describing a Plasma

1.2.1 Single Particle Motion

The simplest method of describing a plasma is to consider each particle individually and solve its equation of motion. Here only the effects on a particle's motion from electric and magnetic fields are considered. Interactions between individual particles are disregarded. The equation of motion of a particle of mass m, charge q and velocity $\boldsymbol{v}$, when exposed to a magnetic field $\boldsymbol{B}$ and electric field $\boldsymbol{E}$ is

$$m\frac{d\boldsymbol{v}}{dt} = q\left(\boldsymbol{E} + \boldsymbol{v} \times \boldsymbol{B}\right) \tag{1.5}$$

where $q\left(\boldsymbol{E} + \boldsymbol{v} \times \boldsymbol{B}\right)$ is the Lorentz force.

1.2.1.1 Particle Motion in a Uniform Magnetic Field

If only a constant magnetic field is considered and the electric field is assumed to be zero, then differentiating Equation 1.5 with respect to time gives

$$\frac{d^2\boldsymbol{v}}{dt^2} = -\left(\frac{qB}{m}\right)^2 \boldsymbol{v} \tag{1.6}$$

which is the equation for a simple harmonic oscillator, $\ddot{\boldsymbol{v}} = -\omega^2\boldsymbol{v}$, with the frequency of oscillation, or gyrofrequency (also called the cyclotron frequency or Larmor frequency) given by

$$\omega_G = \frac{qB}{m} \tag{1.7}$$

The gyroradius (or Larmor radius), R_G is therefore defined by

$$R_G = \frac{v_\perp}{\omega_G} \tag{1.8}$$

where $v_\perp$ is the velocity of the particle perpendicular to the magnetic field.

Thus in the presence of a constant, uniform, magnetic field, charged particles with no component of velocity parallel to the field move in circular orbits in the plane perpendicular to the field. The radius of an orbit is controlled by the strength of the magnetic field and the particle's velocity in the plane of the orbit. The orbit's focus is known as the guiding centre. It should be noted that the component of a particle's velocity parallel to the magnetic field, $\boldsymbol{v}_{//}$, is not modified by the orbital motion and remains at its initial value. The angle between the total velocity vector of the particle (i.e. $\boldsymbol{v}_{//}+\boldsymbol{v}_\perp$) and the magnetic field direction is known as the pitch angle, α, and is given by

$$\alpha = \arctan\left(\frac{|\boldsymbol{v}_\perp|}{|\boldsymbol{v}_{//}|}\right) \tag{1.9}$$

The motion of a particle with a pitch angle of 0° will be entirely along the magnetic field (a field-aligned particle) while a particle with a pitch angle of 90° will move only perpendicular to the magnetic field (a trapped particle). If a particle has a pitch angle between 0° and 90° it will move in a helical manner about its guiding

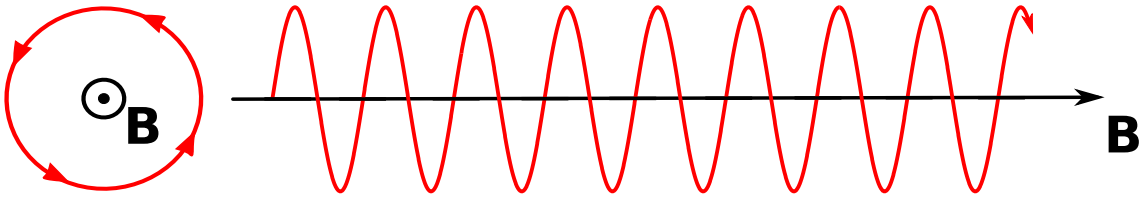

Figure 1.1: The gyromotion of an electron with a component of velocity directed along the magnetic field.

centre, as illustrated for electrons in Figure 1.1

1.2.1.2 Particle Motion in Uniform Electric and Magnetic Fields

If a constant, uniform, electric field is now considered in addition to the uniform magnetic field a particle will no longer describe simple helical motions about a static guiding centre. Differentiating Equation 1.5 with respect to time when $\boldsymbol{E}$ is non-zero but constant leads to

$$\frac{d^2\boldsymbol{v}}{dt^2} = -\omega_G^2 \left(\boldsymbol{v} - \frac{\boldsymbol{E} \times \boldsymbol{B}}{B^2} \right) \tag{1.10}$$

This can be thought of as a further velocity superposed with the particle's gyromotion:

$$\frac{d^2\boldsymbol{v}}{dt^2} = -\omega_G^2 \left(\boldsymbol{v} - \boldsymbol{v}_d \right) \tag{1.11}$$

where

$$\boldsymbol{v}_d = \frac{\boldsymbol{E} \times \boldsymbol{B}}{B^2} \tag{1.12}$$

This additional velocity is in a direction perpendicular to both the electric and magnetic fields and represents a drift of a particle's guiding centre, as illustrated in Figure 1.2.

The component of electric field perpendicular to the magnetic field will accelerate a particle in the plane of its gyromotion, increasing its velocity on one side of a gyration, and decreasing it on the other. This has the effect of increasing the gyroradius for half a gyration and decreasing it for the other half, which imparts a drift velocity to the particle's guiding centre in the $\boldsymbol{E}\times\boldsymbol{B}$ direction, so-called $\boldsymbol{E}\times\boldsymbol{B}$

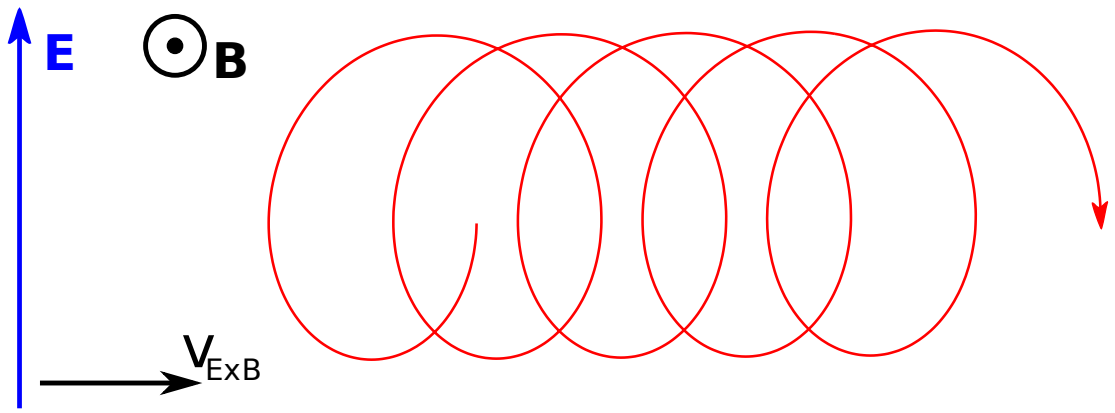

Figure 1.2: The drift motion of an ion exposed to constant, uniform electric and magnetic fields.

drift. Because the drift velocity is independent of particle mass and charge, both ions and electrons have the same $\boldsymbol{E}\times\boldsymbol{B}$ drift velocity.

1.2.1.3 The Effect of Non-Uniform Magnetic Fields

A non-uniform magnetic field, i.e a field with a gradient ($\nabla B \neq 0$) or a curvature ($\nabla \times \boldsymbol{B} \neq 0$), also has a drift motion associated with it. This gradient-curvature drift imparts a velocity to a particle given, for a cylindrically symmetric field, by

$$\boldsymbol{v}_d = \left(v_{//}^2 + \frac{1}{2} v_{\perp}^2 \right) \frac{\boldsymbol{B} \times \nabla B}{\omega_G B^2} \tag{1.13}$$

Because the expression for the gradient-curvature drift velocity involves ω_G, which includes the charge on a particle, the direction of gradient-curvature drift for positively charged and negatively charged particles is different. Gradient-curvature drifts, then, produce a separation of charge and therefore electric currents. For a more complete discussion of gradient-curvature drifts, see Baumjohann and Treumann (1997).

1.2.1.4 Generalised Force Drifts

Equation 1.12 may be generalised to describe the drift experienced by a particle that is exposed to a magnetic field and any force, $\boldsymbol{F}$. Given that $\boldsymbol{F} = q\boldsymbol{E}$, one can substitute for $\boldsymbol{E}$ in Equation 1.12, producing

$$\boldsymbol{v}_d = \frac{\boldsymbol{F} \times \boldsymbol{B}}{qB^2} \tag{1.14}$$

Thus any force that does not depend on charge (for example those exerted by non-uniform magnetic fields or gravity) will impart a charge-dependent drift velocity to particles and any charge-dependent force (such as that exerted by an electrostatic field) will impart a charge-independent drift velocity to particles.

1.2.2 Plasma Kinetic Theory

It is not always feasible to solve the individual equations of motion for large numbers of particles, so instead plasmas are often considered statistically by defining a distribution function of particles. The configuration of a system at a given time can be fully described by six quantities for each particle that makes up the system: three positions (X, Y, Z) and three velocities (v_X, v_Y, v_Z). Each of these quantities is a coordinate in a six-dimensional phase space and by following particle trajectories in phase space one can study the changes of a system with time. In practice, there are usually too many particles in a system to consider their phase space trajectories individually. Instead, the number of particles in a volume element of phase space $(dX, dY, dZ, dv_X, dv_Y, dv_Z)$, the phase space density of particles, or particle distribution function, is used. By integrating the distribution function over the velocity components of phase space (taking moments of the distribution function), the number density of particles and other bulk properties of a plasma can be calculated. The calculation of moments of the distribution function is discussed in more detail in the context of the Cluster PEACE instrument in section 2.2.2.4.

1.2.3 Magnetohydrodynamics

Theories of single particle motion are useful when describing the dynamics of a few particles exposed to an electromagnetic field, however when a large number of particles needs to be considered they are not always appropriate. For some applications the analysis of the evolution of particle distribution functions is also unnecessary. When considering large systems with scale sizes much greater than R_G, that vary over timescales much longer than ω_G^{-1}, the theory of magnetohydrodynamics, or MHD (Alfvén, 1942), can be applied. MHD treats a plasma as an electrically conducting fluid and thus relies only on macroscopic, bulk, quantities (i.e. the moments of the particle distribution functions described above) rather than considering the motions of individual particles, even in a statistical sense.

1.2.3.1 Equations of MHD

MHD is a marriage of the equations of fluid dynamics and Maxwell's equations of electromagnetism and can be derived in terms of one fluid (single-fluid MHD) or one fluid per particle species (multi-fluid MHD). Here quasi-neutrality is assumed, such that $n_i = n_e = n$ and each particle species, s, is represented by its own fluid. If no source or loss processes are operating, the fluid obeys the continuity equation

$$\frac{\partial n_s}{\partial t} + \nabla \cdot (n_s \boldsymbol{v_s}) = 0 \tag{1.15}$$

meaning that particle number density (and thus mass density and charge density) is conserved during the motion of the fluid.

The momentum equation for each species, s, is

$$n_s \left[\frac{\partial \boldsymbol{v_s}}{\partial t} + (\boldsymbol{v_s} \cdot \nabla) \boldsymbol{v_s} \right] + \frac{1}{m_s} \nabla \cdot \mathsf{P}_s - \frac{q_s}{m_s} n_s (\boldsymbol{E} + \boldsymbol{v}_s \times \boldsymbol{B}) = 0 \tag{1.16}$$

where P_s is the pressure tensor for that species. The pressure and density for a

given species are related by an equation of state, which, when isotropic (i.e. scalar) pressure is assumed, can take the well known form

$$p \propto n^{\gamma} \tag{1.17}$$

where γ, the polytropic index can vary from 0 (the isobaric case) to ∞ (the isothermal case). A common assumption regarding the value of γ is that the plasma behaves adiabatically, i.e. $\gamma = \frac{5}{3}$.

In the case of the two fluid (i.e. electron and positive ion) plasma assumed here a further important relation may be derived through subtracting the equation of motion of electrons from the equation of motion of ions. After some manipulation the generalised Ohm's law is obtained:

$$\boldsymbol{E} + \boldsymbol{v} \times \boldsymbol{B} = \eta \boldsymbol{j} + \frac{1}{n q_e} \left(\boldsymbol{j} \times \boldsymbol{B} - \nabla \cdot \mathsf{P}_e \right) + \frac{m_e}{n q_e^2} \frac{\partial \boldsymbol{j}}{\partial t} \tag{1.18}$$

where η is the resistivity of the plasma and $\boldsymbol{j}$ is the current density. For a significant proportion of the magnetosphere, the terms on the right hand side of Equation 1.18 are insignificant compared with those on the left hand side and may be discarded giving

$$\boldsymbol{E} = -\boldsymbol{v} \times \boldsymbol{B} \tag{1.19}$$

Equation 1.19 describes the ideal MHD or frozen-in flow approximation, in which particles and magnetic fields are frozen together. i.e. when the particles move, the magnetic field changes shape such that the particles remain frozen to the same field line, and vice versa.

1.2.3.2 Magnetic Reynolds Number and Frozen-in Flow

If the collisional term on the right hand side of Equation 1.18, $(\eta \boldsymbol{j})$, is retained and the resistivity, η, is replaced with a conductivity, σ (where $\sigma = 1/\eta$), then the

generalised Ohm's law can be written

$$\boldsymbol{j} = \sigma \left(\boldsymbol{E} + \boldsymbol{v} \times \boldsymbol{B} \right) \tag{1.20}$$

substituting for $\boldsymbol{j}$ using Ampère's Law and $\boldsymbol{E}$ using Faraday's Law and applying vector identities leads to

$$\frac{\partial \boldsymbol{B}}{\partial t} = \nabla \times (\boldsymbol{v} \times \boldsymbol{B}) + \frac{1}{\mu_0 \sigma} \nabla^2 \boldsymbol{B} \tag{1.21}$$

where μ_0 is the permeability of free space. The first term on the right hand side of Equation 1.21 describes how the magnetic field changes via convection with the plasma while the second describes the effect of the magnetic field's diffusion through the plasma. The ratio between these terms is known as the magnetic Reynolds number and is a measure of the relative importance of convection and diffusion:

$$R_m = \frac{|\nabla \times (\boldsymbol{v} \times \boldsymbol{B})|}{|\mu_0^{-1} \sigma^{-1} \nabla^2 \boldsymbol{B}|} \tag{1.22}$$

Thus if $R_m \gg 1$ then convection dominates diffusion and the magnetic field is frozen into the plasma, i.e. the plasma can be described by ideal MHD. If Equation 1.21 is rewritten in simple dimensional terms, an alternative expression for R_m can be obtained:

$$R_m = \mu_0 \sigma L V \tag{1.23}$$

Where L represents the spatial scale over which the magnetic field varies and V is the convection velocity of the plasma. The conductivity term is a measure of the frequency of collisions in the plasma so for a collisionless plasma in which the magnetic field varies over a large spatial scale the magnetic Reynolds number is large and ideal MHD is an appropriate assumption.

1.2.3.3 Magnetic Tension, Pressure and the Plasma Beta

Two further consequences of MHD are the concepts of magnetic tension and magnetic pressure. From Ampère's law we know

$$\boldsymbol{j} \times \boldsymbol{B} = \frac{1}{\mu_0} (\nabla \times \boldsymbol{B}) \times \boldsymbol{B} \tag{1.24}$$

which can be rewritten in the form

$$\boldsymbol{j} \times \boldsymbol{B} = -\nabla \left(\frac{B^2}{2\mu_0} \right) + \frac{1}{\mu_0} (\boldsymbol{B} \cdot \nabla) \boldsymbol{B} \tag{1.25}$$

So the $\boldsymbol{j} \times \boldsymbol{B}$ force has two components to it. The first term on the right hand side of Equation 1.25 represents the force exerted by the gradient in magnetic flux density, which is dimensionally a pressure, p_B, and can be defined for the isotropic case as

$$p_B = \frac{B^2}{2\mu_0} \tag{1.26}$$

although more generally is represented by the magnetic pressure tensor. The second term on the right hand side of Equation 1.25 is the magnetic tension force. This represents the force exerted on a plasma by the magnetic field as it changes shape to reach its minimum energy state.

Another quantity, the plasma beta, is defined as the ratio of particle pressure to magnetic pressure:

$$\beta = \frac{2p\mu_0}{B^2} \tag{1.27}$$

When $\beta > 1$ (a high beta plasma) the particle pressure dominates over the magnetic pressure whereas when $\beta < 1$ (a low beta plasma) the magnetic pressure dominates.

1.2.4 Magnetic Reconnection

The magnetic Reynolds number is a measure of how well the particles and magnetic fields are frozen together, i.e. how well the governing assumptions of ideal MHD hold. A consequence of ideal MHD is that magnetic fields with different sources, and the particle populations frozen onto them, cannot readily mix. In low magnetic Reynolds number regimes, for example thin current sheets, the particles are no longer frozen onto magnetic fields and the fields can move through the plasma. In this situation magnetic reconnection can occur. Reconnection is a process by which magnetic field lines can break and reconnect with each other, altering the field topology. A simple, qualitative, picture of reconnection is drawn in Figure 1.3. In Figure 1.3A two magnetic fields (red and blue) are separated by a thin current sheet (grey). If the magnetic fields were to be pushed together, perhaps by a flow of plasma frozen into one of the fields (Figure 1.3B) pairs of magnetic field lines will eventually reconnect, i.e. change their topology such that two new, highly bent field lines are created (Figure 1.3C). Magnetic tension forces then act to straighten these field lines expelling them from the reconnection site and allowing the next pair of field lines to reconnect.

Magnetic reconnection is a method by which magnetic energy can be transferred to the particles. The newly reconnected, bent, field lines, in being pulled from the reconnection site through magnetic tension will accelerate the particles frozen onto the field lines.

1.2.4.1 Quantitative Models of Reconnection

A more quantitative treatment of reconnection, the Sweet-Parker model (Parker, 1957), is illustrated in 1.4. Here the reconnection occurs in a long, narrow diffusion region of length L and thickness 2δ into which the magnetic field is dragged by a plasma with inflow velocity $\boldsymbol{v}_{in}$. After reconnection has occurred the plasma and magnetic field exit the diffusion region with a velocity $\boldsymbol{v}_{out}$.

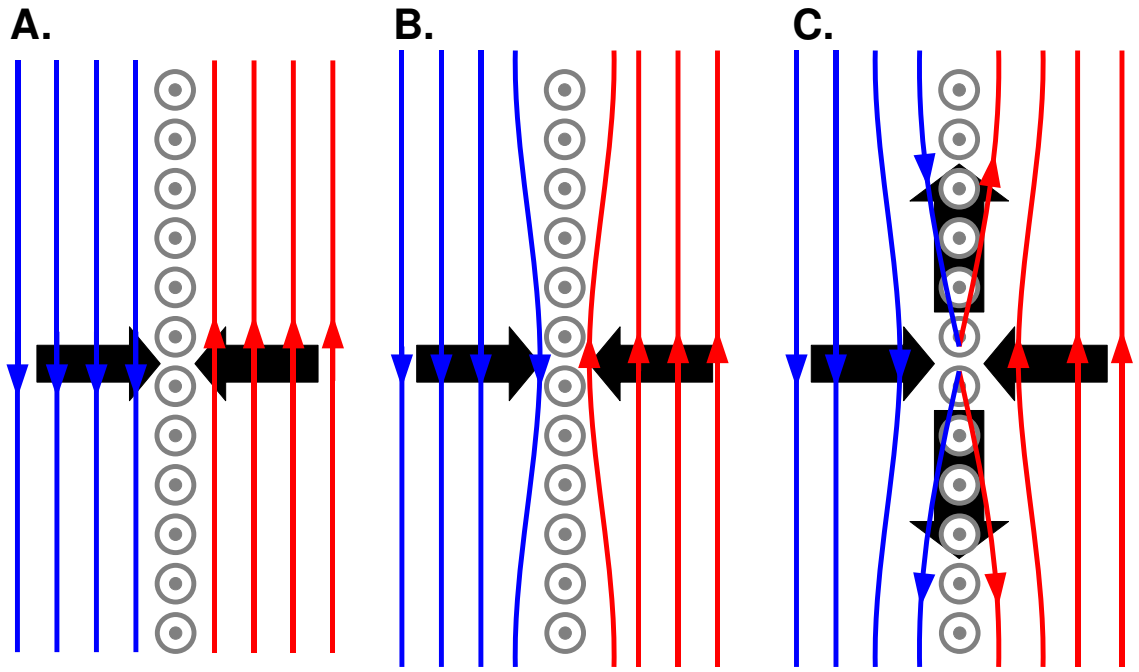

Figure 1.3: A basic reconnection geometry. Two magnetic fields (red and blue) are separated by a thin current sheet (grey). The magnetic fields are pushed together and reconnect, creating two new magnetic field lines that are highly bent. Magnetic tension acts to straighten the bent field lines expelling them from the reconnection site allowing the next pair of field lines to reconnect, and so on.

From conservation of mass we know that

$$L|\boldsymbol{v_{in}}| = \delta|\boldsymbol{v_{out}}| \tag{1.28}$$

and because the inflow is assumed to be steady convection, from Equation 1.12 we know that

$$\boldsymbol{v_{in}} = -\frac{E_Y}{B_X}\hat{\boldsymbol{z}} \tag{1.29}$$

Application of Ohm's Law ($\sigma E_Y = j_Y$) and Ampere's Law leads to the expression

$$v_{in} = -\frac{1}{\mu_0 \sigma \delta} \tag{1.30}$$

the right hand side of which is a measure of the rate of diffusion of magnetic field through the plasma. Thus in the Sweet-Parker model, the rate of diffusion and therefore the rate of reconnection depends on the rate of plasma inflow to the diffusion region. Using the Bernoulli equation and assuming pressure balance either side

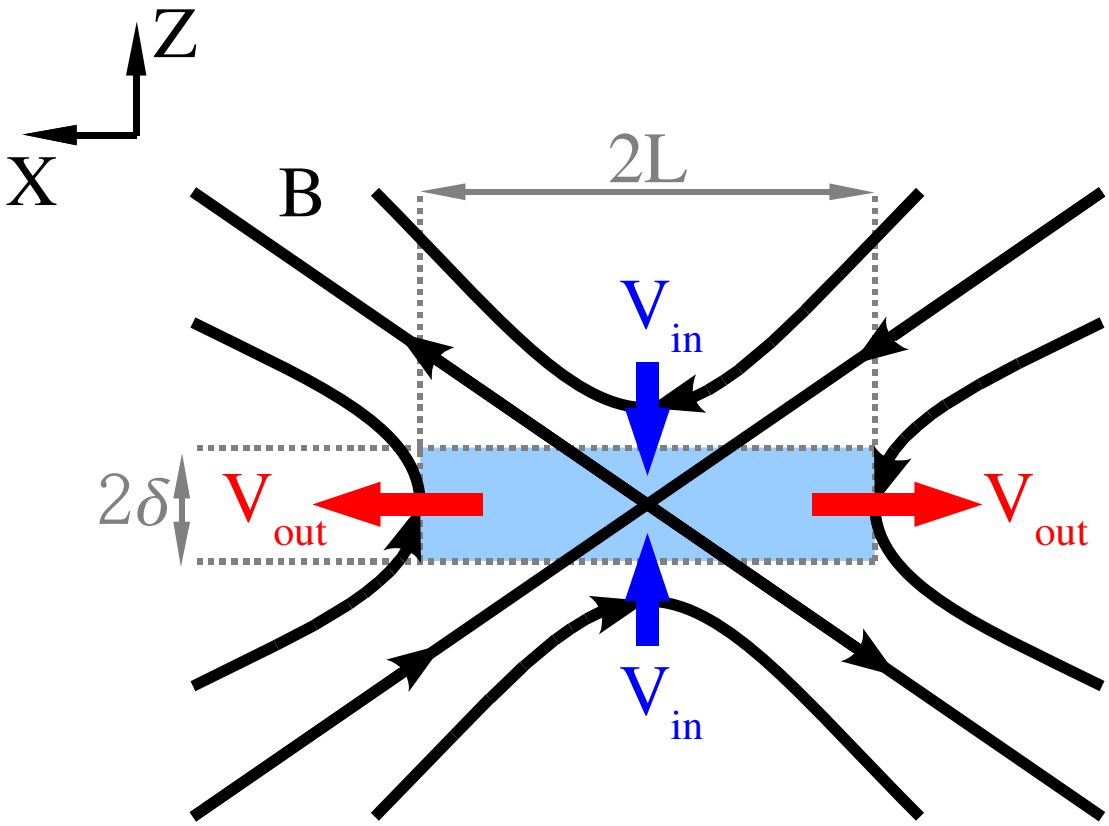

Figure 1.4: The Sweet-Parker reconnection geometry. Plasma inflow ($\boldsymbol{v}_{in}$,dark blue) drags field lines (black) into a diffusion region (light blue) of length L and height δ. After reconnection the field topology is changed and the newly reconnected field lines exit the diffusion region with a velocity $\boldsymbol{v}_{out}$ (red). Note that the convection electric field, E_Y is directed out of the page.
.

of the diffusion region we can write

$$\boldsymbol{v_{out}} = \frac{B_X}{\sqrt{\mu_0 \rho}} \hat{\boldsymbol{x}} \tag{1.31}$$

where ρ is the mass density of the plasma. Now substituting for δ (from Equation 1.28) and $\boldsymbol{v}_{out}$ (from Equation 1.31) in Equation 1.30 giving

$$v_{in}^2 = \frac{B_X}{\sqrt{\mu_0 \rho}} \left(\frac{1}{\mu_0 \sigma L} \right) \tag{1.32}$$

where

$$\frac{B_X}{\sqrt{\mu_0 \rho}} = v_A \tag{1.33}$$

which is the Alfvén velocity, a characteristic velocity in MHD. After some manipu-

lation Equation 1.32 may be written in terms of the Magnetic Reynolds number:

$$v_{in} = \frac{v_A}{\sqrt{R_m}} \tag{1.34}$$

The above has two important consequences: firstly the outflow velocity, $\boldsymbol{v}_{out}$, is equal to the Alfvén velocity in the inflow region, and secondly the inflow velocity, $\boldsymbol{v}_{in}$, and therefore the overall reconnection rate depends on the Alfvén velocity and the magnetic Reynolds number. In most space plasmas the magnetic Reynolds number is large and thus under the Sweet-Parker regime reconnection is a naturally slow process.

The Petsheck Reconnection model (Petschek, 1964) addresses the inherently slow reconnection rate of Sweet-Parker reconnection by not requiring all reconnecting material to pass through an extended diffusion region in order to be accelerated. Instead the majority of the material is accelerated at shocks that lie on the separatrix between unreconnected and newly reconnected flux. This allows the diffusion region to become much smaller (i.e. $L_{Petscheck} << L_{Sweet-Parker}$) and therefore, from Equation 1.32, the reconnection rate can be much larger.

1.3 Plasmas in the Solar-Terrestrial System

The plasma physics described above can be applied to a wide variety of environments found within the the solar system, and indeed the universe at large. The solar corona, interplanetary space, planetary magnetospheres and ionospheres, and the ionospheres and induced magnetospheres of unmagnetised planets, moons and comets are all made up of plasmas threaded by magnetic fields. Here, those solar system plasmas most relevant to this thesis, the solar wind and various regions of the Earth's magnetosphere will be introduced.

1.3.1 The Solar Wind

The solar wind is the name given to the stream of charged particles that is always flowing radially away from the Sun into interplanetary space. It's existence was first mooted by Biermann (1951), who explained the anti-sunward direction of comet plasma tails as a result of their interaction with a flux of protons flowing radially away from the Sun. An early attempt at explaining the existence of the solar wind was made by Chapman and Zirin (1957), who considered a spherically symmetric, steady corona as the source of the solar wind and found, using a hydrostatic argument, that the Sun's gravity was not sufficient to confine coronal plasma, resulting in the flow of plasma away from the Sun. This calculation was expanded upon by (Parker, 1958, 1959), who suggested that the Solar Wind at 1 AU should be supersonic and also considered the effect of the existence of a solar wind on the solar magnetic field. The magnetic Reynolds number in the solar corona is in excess of 10^6 (e.g. Priest, 1995), so the coronal magnetic field can be thought of as frozen in to the plasma. It is thus dragged out into interplanetary space with the solar wind particles, where it is known as the Interplanetary Magnetic Field (IMF). Coronal magnetic field lines, however, have their source deep within the sun and therefore also rotate with it. The consequence of this combined rotational and radial motion of IMF field lines is an archimedian spiral structure. This is known as the Parker Spiral and is illustrated in Figure 1.5.

The solar wind and IMF are highly variable, though the solar wind is often categorised as either slow solar wind when it has a velocity of less than $500\,\mathrm{km\,s^{-1}}$ or fast solar wind when it has a velocity in excess of $600\,\mathrm{km\,s^{-1}}$. The fast solar wind is thought to originate near areas of open coronal magnetic field, while the slow solar wind is thought to originate near areas of closed coronal magnetic field. Typical solar wind and IMF parameters at 1 AU are listed in Table 1.1.

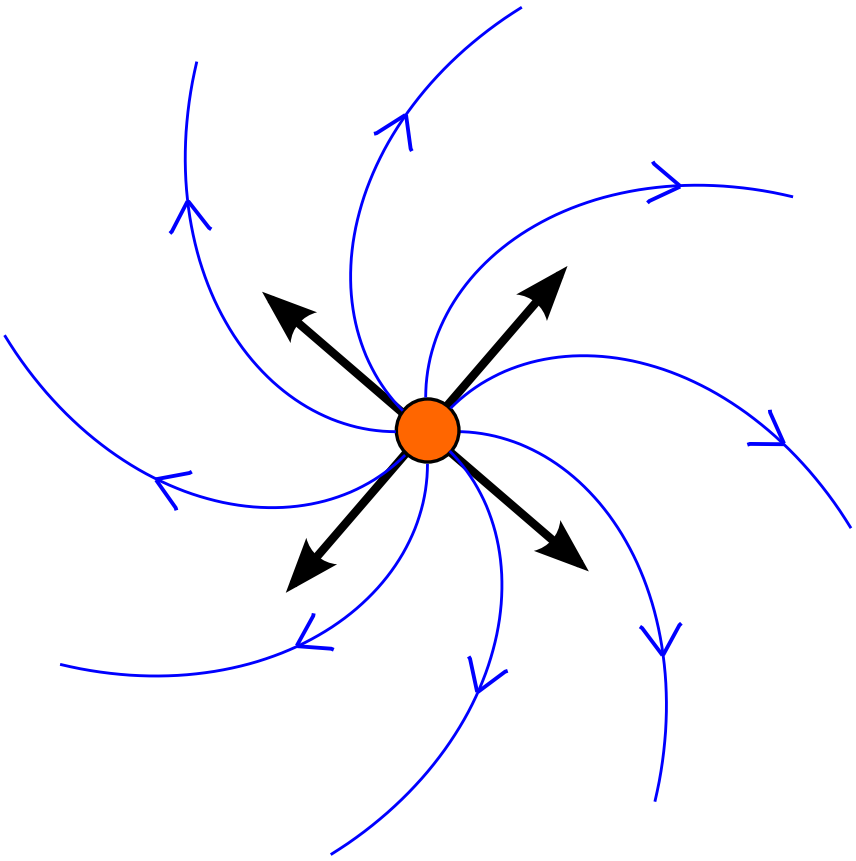

Figure 1.5: The Parker Spiral structure of the IMF. Solar wind streamlines are marked in black, IMF field lines in blue and the solar rotation in red.

n (cm^{-3})	7
T (eV)	4
$\lvert\boldsymbol{B}\rvert$ (nT)	5
$\lvert\boldsymbol{v}\rvert$ ($\mathrm{km\,s}^{-1}$)	400

Table 1.1: Typical solar wind parameters at 1 AU (Parks, 2004)

.

1.3.2 The Earth's Magnetosphere

While the majority of space throughout the solar system is dominated by the IMF and solar wind, the intrinsic magnetic fields of some solar system bodies, like the Earth, Jupiter and Saturn, act to exclude external magnetic fields and the particles that may be frozen on to them. The space close to each of these bodies, then, is instead dominated by the magnetic field of that body and is known as its magnetosphere.

In the absence of the IMF and solar wind, the magnetic field of the Earth would approximate a magnetic dipole, however its interactions with the IMF and solar wind distort this dipole shape, compressing it on the sunward side of the terminator (the dayside) and stretching it into a long tail, the magnetotail, anti-sunward of the terminator (the nightside). This produces a characteristic tear-drop shape. The general morphology of the Earth's magnetosphere is illustrated in Figure 1.6. Several important regions of the magnetosphere are labelled in the figure and will be discussed below in the context of the so-called "closed magnetosphere model", whereby solar wind plasma and the IMF are completely excluded from the magnetosphere because of the frozen-in flux approximation.

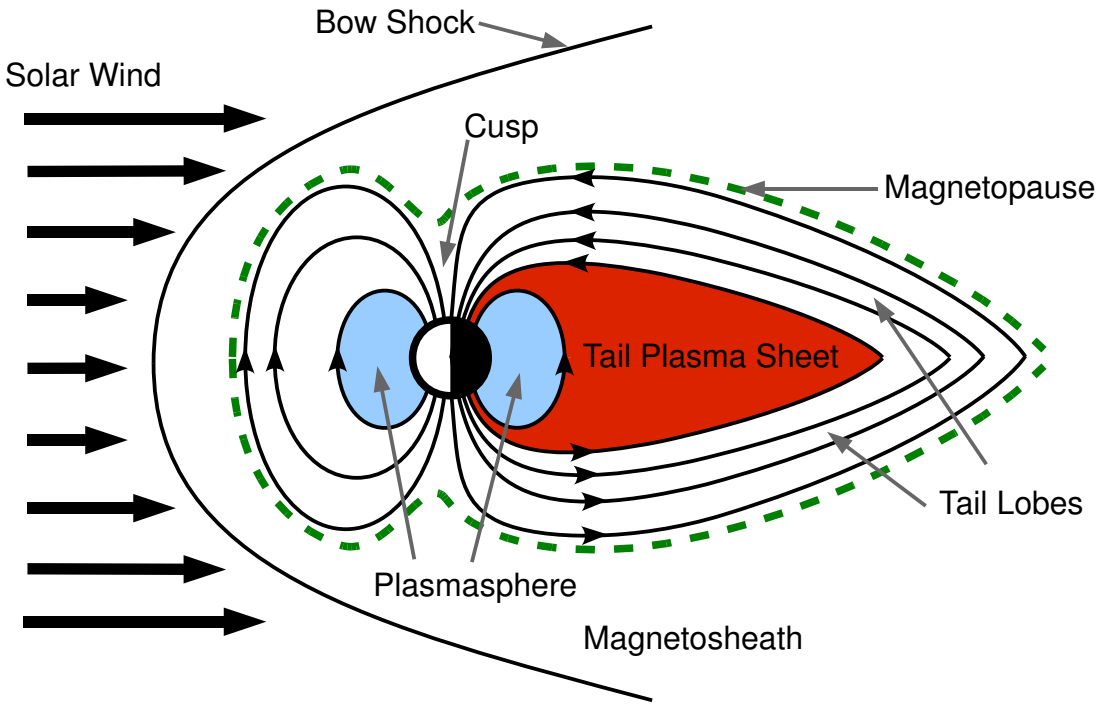

Figure 1.6: A 2-D schematic cut of The Earth's magnetosphere, ignoring the tilts of the Earth's dipole and spin axes, taken in the plane perpendicular to the Earth-Sun line and the plane of the ecliptic (the GSE XZ plane - see Section 1.3.2.1).

1.3.2.1 A Note on Magnetospheric Coordinate Systems

Many different coordinate systems are used in the field of magnetospheric physics, two of the more commonly used systems are the Geocentric Solar Ecliptic (GSE)

coordinate system and the Geocentric Solar Magnetospheric (GSM) coordinate system. In the GSE coordinate system the origin is at the Earth and the X axis points along the Earth-Sun line, positive towards the Sun. The Z axis points perpendicular to the plane of the ecliptic, positive northward, while the Y axis points in the direction opposing the Earth's orbital motion, positive towards dusk. The GSM coordinate system is defined by a rotation about the GSE X axis such that the dipole axis of the Earth's magnetic field lies in the GSM XZ plane. Again the Y axis completes the right handed set. While GSM coordinates are often a more natural coordinate system in studying the magnetosphere, they have the property of changing over a day as the rotation of the Earth moves the position of the magnetic dipole axis with respect to the Earth-Sun line.

1.3.2.2 The Bow Shock and Magnetosheath

Under the frozen-in flux approximation magnetic fields with different sources, and the particle populations that are associated with them, cannot mix. As such the magnetosphere of the Earth presents an obstacle to the flow of the solar wind. The supersonic character of the solar wind means that information about the presence of this obstacle cannot be communicated upstream to incoming particles which therefore cannot divert around the obstacle. Instead, the solar wind particles on encountering the obstacle are abruptly slowed down and heated by a shock wave in the solar wind flow as the particles' kinetic energy is converted to thermal energy. Downstream of the bow shock is the magnetosheath, which comprises a subsonic flow of plasma which can divert around the Earth's magnetosphere. Magnetosheath plasma is denser than unshocked solar wind because mass flux either side of the bow shock must be conserved and hotter since part of the solar wind kinetic energy is converted to thermal energy at the shock. The magnetic field in the magnetosheath is also stronger than the undisturbed IMF because of the frozen-in flux approximation.

1.3.2.3 The Magnetopause and the Cusps

As stated above, under the frozen-in flow approximation there can be no mixing between the Earth's magnetic field and the IMF, so at the boundary between these two regimes a gradient will exist in the magnetic field. By Ampere's Law, a gradient in the magnetic field will result in the presence of a current. This current is the magnetopause - a thin current sheet separating the Earth's magnetic field and the IMF (Chapman and Ferraro, 1931). The stand-off distance of the magnetopause (its distance from the Earth) is governed by the pressure balance between the thermal & magnetic pressure of the Earth's magnetosphere and the thermal, magnetic & dynamic pressure exerted by the solar wind and IMF. Under typical conditions the stand off distance at the sub-solar point, i.e. the position on the Earth-Sun line occupied by the magnetopause, is $\sim 10\,\mathrm{R_E}$ (Earth Radii). The funnel shaped structures above the poles of the Earth are known as the cusps and are an important entry point of solar wind plasma into the magnetosphere (see below).

1.3.2.4 The Inner Magnetosphere and Plasmasphere

The densest region of the magnetosphere, the plasmasphere, is a toroidal region located close to the Earth (usually within $\sim 4\,\mathrm{R_E}$) and is full of cold plasma of ionospheric origin that co-rotates with the Earth. The temperature in the plasmasphere is $\sim 1\,\mathrm{eV}$ and density is $\sim 10^3\,\mathrm{cm^{-3}}$ (Wolf, 1995). The inner magnetosphere is also home to the Van Allen radiation belts, regions of high energy particles that stretch between $\sim 0.1\,\mathrm{R_E}$ and $\sim 6\,\mathrm{R_E}$ of the planet. The electron radiation belt is divided into an inner radiation belt, located between ~ 0.1 & $1.5\,\mathrm{R_E}$ and an outer radiation belt,located between ~ 3 & $6\,\mathrm{R_E}$. The region in between the inner and outer radiation belts is known as the slot region. Conversely, the proton radiation belt is not divided and encompasses the entire radiation belt region.

1.3.2.5 The Magnetotail

While the dayside magnetosphere is compressed through its interaction with the solar wind and IMF, the opposite is true on the nightside. Under the simple closed magnetosphere model viscous interactions between the Earth's magnetic field and the solar wind flow have the effect of stretching the nightside magnetosphere into a long tail-like geometry, the magnetotail. The magnetotail has been calculated to be as long as 600 R_E (Hughes, 1995) and can be broadly split into three different regions: the plasma sheet, the plasma sheet boundary layer. The relative locations of these regions are illustrated in Figure 1.7.

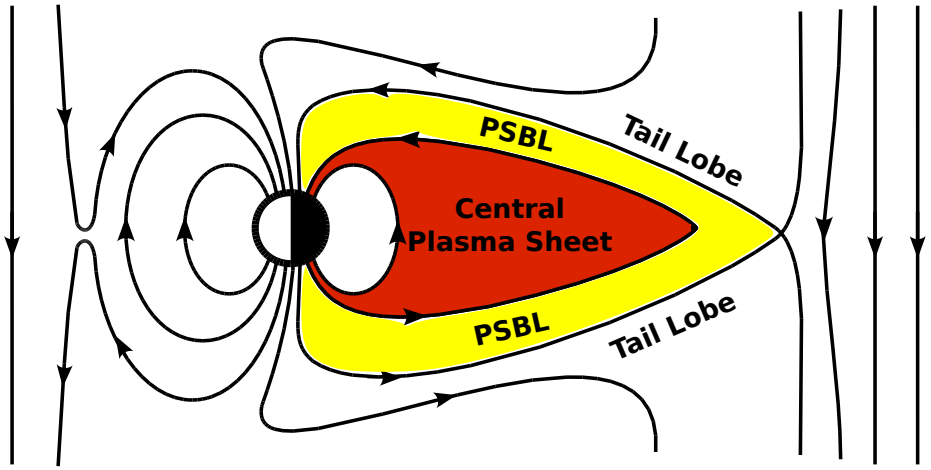

Figure 1.7: The relative locations of the central plasma sheet (red), plasma sheet boundary layer (yellow) and tail lobes.

The tail lobes form the outermost region of the magnetotail and are characterised by a relatively strong magnetic field and a low plasma density. The innermost region of the magnetotail is the central plasma sheet, a region of lower magnetic field and hot, more isotropic, plasma with a high density relative to the tail lobes. At the centre of the plasma sheet is the neutral sheet, a thin layer at which the magnetic field strength drops to near zero as the field changes direction from sunward in the northern hemisphere to anti-sunward in the southern hemisphere. The plasma sheet boundary layer, then, is a transition region between the lower density tail lobes and higher density central plasma sheet and is characterised by a population of field-

	Lobe	PSBL	Plasma Sheet	Neutral Sheet
n (cm^{-3})	0.01	0.1	0.5	1
T (eV)	85	850	4250	4250
$\|\boldsymbol{B}\|$ (nT)	25	20	10	2
β	0.001	0.1	10	40

Table 1.2: Typical plasma and field parameters in the Earth's magnetotail (after Lui, 1987).
.

aligned electrons and ions with densities and temperatures intermediate between those of the tail lobes and the central plasma sheet. Typical magnetic field and plasma parameters for these regions of the magnetotail are summarised in Table 1.2.

1.3.2.6 Current Systems in the Magnetosphere

By Ampere's Law, any deformation of a magnetic field has an electric current associated with it. This is true in the magnetosphere where there are numerous current systems that exist to support the deformation of the Earth's magnetic field from a dipole and exclude the solar wind and IMF. The magnetopause current system separates the solar wind and IMF from the magnetosphere. This current system extends into the nightside magnetotail where it flows around the edges of the tail and closes through the cross-tail current: the current system associated with the change in direction of the magnetotail field from sunward to anti-sunward across the tail neutral sheet. Viewed from the Earth-Sun line, the tail current systems have an approximate Θ shape. Closer to the Earth the ring current plays an important role in inner magnetospheric processes. The ring current is supported by particles that gradient-curvature drift around the Earth, when viewed from the north, the electrons drift in a clockwise direction and the ions in an anticlockwise direction, thus there is a net flow of charge and an electric current. Furthermore, coupling between the magnetosphere and ionosphere is mediated through field-aligned or Birkeland currents which can form at the inner edge of the tail plasma sheet, for example, when a partial ring current is diverted along the magnetic field and closes in the

ionosphere. Other field-aligned currents are discussed in the context of dynamic magnetospheric processes below.

1.4 Magnetospheric Dynamics

The picture of a closed magnetosphere, completely impermeable to solar wind particles and the IMF, depends on the frozen-in flow approximation. A key assumption of ideal MHD is that it is only valid at large scale sizes and for long time scales. When the assumptions of ideal MHD break down, in regimes where the magnetic Reynolds number is low, magnetic fields with different sources can combine and the particle populations associated with them can mix; the process of magnetic reconnection. A thin (i.e. when compared to particle gyroradii) current sheet, such as the magnetopause, is a good example of a regime where ideal MHD does not apply and reconnection can take place; so in reality the closed magnetosphere is an oversimplification and in fact the magnetosphere is open to the solar wind and IMF, and connected to it via magnetic reconnection. This coupling between the IMF and terrestrial magnetic field is a source of energy for the magnetosphere-ionosphere system and drives many dynamic processes within it, some of which will be discussed below.

1.4.1 The Dungey Cycle and Open Magnetosphere

The idea of the open magnetosphere, illustrated in Figure 1.8, was first posited by Dungey (1961) who realised that when the IMF was pointed southward, in opposition to the northward-pointing terrestrial magnetic field (black field lines in Figure 1.8), reconnection might occur at the sub-solar point on the magnetopause. Once this reconnection has taken place the field geometry changes such that two new field lines are present, connected at one end to the IMF and at the other to the one of the magnetic poles of the Earth (red field lines in Figure 1.8). These field lines are

said to be open to the solar wind. These newly-reconnected, highly kinked field lines will straighten through the magnetic tension force. Furthermore, away from the reconnection site the frozen-in approximation still holds, so the end of an open field line in the solar wind will still be dragged anti-sunward by the solar wind flow. Both of these effects stretch the field line and pull it into the magnetotail where it forms part of the magnetotail lobes (yellow field lines in Figure 1.8). Over time more and more newly reconnected magnetic flux is added to the magnetotail, this has the effect of forcing the oppositely directed magnetic fields in the northern and southern hemispheres together resulting in the formation of a further reconnection site in the magnetotail, known as the distant neutral line (green field lines in Figure 1.8). Reconnection at this distant neutral line results in a new closed field line, albeit one that is still stretched and distorted, and another field line connected only to the IMF which travels with the solar wind away from the Earth (blue field lines in Figure 1.8). Magnetic tension forces cause the new closed field line to relax back to a dipole-like configuration by shrinking and convecting, along with the plasma attached to it, earthward (purple field line). It then convects back round to the dayside (grey field line) and is once more connected to the IMF and the cycle begins again. This cycle of magnetospheric convection is known as the Dungey Cycle and represents the framework upon which more complex ideas of magnetospheric dynamics are built.

While the Dungey cycle is only valid under southward IMF, the magnetosphere is not completely closed to the IMF and solar wind under northward IMF either. When the IMF is pointing northward, it and the terrestrial magnetic field can still be pointed in opposite directions tailward of the cusp at the Earthward edge of the tail lobes. Reconnection can occur at these points in one or both hemispheres and is known as single or dual lobe reconnection respectively (Øieroset *et al.*, 1997; Imber *et al.*, 2006).

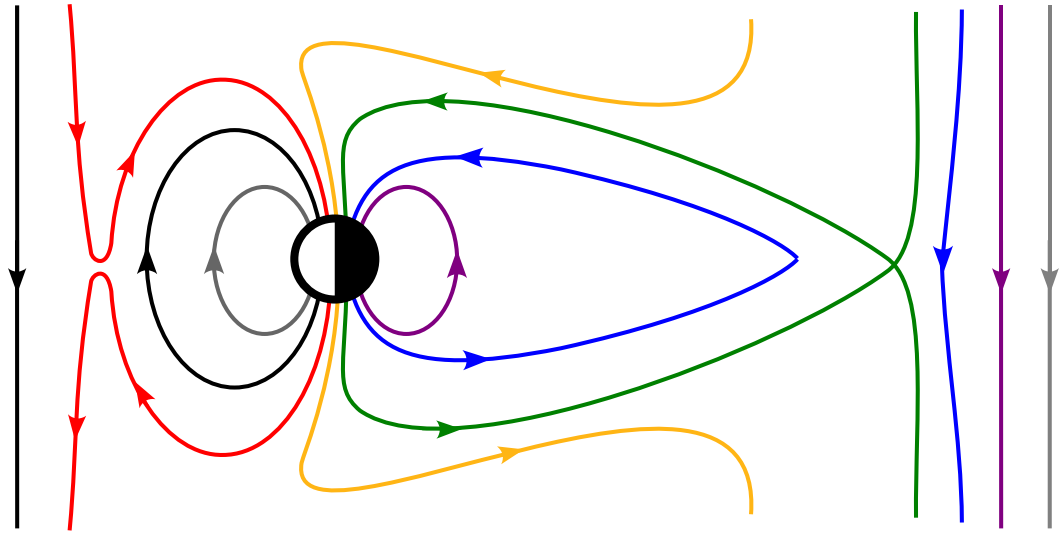

Figure 1.8: The Dungey cycle of magnetospheric convection. Reconnection at the sub solar point opens terrestrial field lines to the IMF and solar wind, resulting them being dragged anti-sunward to form the geomagnetic tail. Eventually further reconnection in the tail closes the field lines again allowing them to return to a dipolar configuration and convect back around to the dayside.

1.4.1.1 The Magnetotail in the Open Magnetosphere model

In section 1.3.2.5 different regions of the magnetotail were described. The different properties of these regions can be explained as a result of the open magnetosphere picture. The tail lobes have a very low plasma density, for example, because they are connected at one end to the IMF and many particles frozen onto them can travel along the field lines into interplanetary space. The PSBL contains those magnetic fields lines that have been recently reconnected in the magnetotail, and their field-aligned particle populations have been accelerated earthward along the field lines by the reconnection at the distant neutral line (Cowley, 1984). The particles mirror at the ionosphere (see Baumjohann and Treumann, 1997, for example) and begin to travel tailwards. It is the interaction between the earthward and tailward particle beams that eventually thermalises the particles, creating the trapped, plasma sheet particle populations (Cowley, 1984).

1.4.1.2 The Ionosphere in the Open Magnetosphere model

Until now, no mention has been made of the ionosphere, the ionised upper atmosphere of the earth through which the terrestrial magnetic field passes. Changes in the configuration of the magnetic field or condition of the plasma in the magnetosphere are reflected in the ionosphere. For example the Dungey Cycle of magnetospheric convection drives an equivalent convection pattern in the ionosphere (e.g. Cowley and Lockwood, 1992). As field lines are dragged from the dayside into the tail their footpoints in the ionosphere are also dragged over the magnetic poles of the earth, taking the ionospheric plasma frozen onto those field lines with them. After reconnection at the distant neutral line, as the field lines convect back around to the dayside around either flank of the magnetosphere their footpoints follow, creating a twin-cell convection pattern.

Looking at the polar ionosphere can also tell us about the connectivity of magnetic field lines. At quiet times, the aurora are confined to an oval with a magnetic latitude of $\sim 70^{\circ}$ (Holzworth and Meng, 1975). Auroral emissions are caused by the collision of incoming ions and electrons with atmospheric neutrals. The probability of a collision, and thus the emission of an auroral photon, depends on the particle flux into the ionosphere, so the region with the most auroral emission, the auroral oval, must map to a region of the magnetosphere on closed field lines where particles cannot be lost to interplanetary space. The region poleward of the auroral oval, the polar cap, where there is usually no auroral emission, therefore maps to the open field lines of the tail lobes.

1.4.2 Substorms

The discussion of the Dungey Cycle above assumes that reconnection at the subsolar point and the distant neutral line in the tail proceeds at the same rate. In the long term, on average, this must be true; in the short term, however, there is no reason why this has to be the case. Indeed numerous observations have shown that

reconnection in the tail and reconnection on the dayside often proceed at different rates as evidenced by the changing open flux content of the tail lobes and therefore the changing size of the ionospheric polar cap (e.g. Lester *et al.*, 2006; Milan *et al.*, 2006). Reconnection is rarely a steady process; instead it can occur in transient bursts called flux transfer events on the dayside (e.g. Fear, 2006, and references therein) and as part of a sequence of events known as a substorm on the nightside. The term substorm was first coined by Akasofu (1964) in the context of the auroral substorm which was described as a brightening of the equatormost auroral arc followed by a poleward and westward expansion of the aurora. Links between visible auroral and geomagnetic activity, and activity in the magnetosphere were soon established and several phenomenological models of substorms have since been developed. There is still no consensus, however, as to the exact sequence of events that occurs in the ionosphere and magnetosphere around the onset of an auroral substorm.

1.4.2.1 General Characteristics of a Substorm

In the simplest case the substorm can be divided into three distinct phases (McPherron, 1970): the growth phase, expansion phase and recovery phase. The growth phase represents the storage of energy and begins with a southward turning of the IMF, which results in the addition of open flux to the magnetotail lobes, increasing the size of the polar cap. There is some controversy over whether (e.g. Russell, 2000) or not (e.g. Morley and Freeman, 2007) transition between the growth and expansion phases requires there to be a northward turning of the IMF, however evidence does suggest there needs to be a critical threshold of magnetic flux present in the tail lobes before expansion phase onset is possible: there is a negligible probability of expansion phase onset when the tail lobes contain a flux of less than 0.3 GWb (Boakes *et al.*, 2009). The expansion phase represents the explosive release of the energy stored in the distended tail lobes resulting in the auroral substorms described by Akasofu (1964) and it is the exact mechanism behind the onset and development

of the expansion phase that is undetermined. The recovery phase represents the aurora and magnetosphere returning to a quiescent state before the growth and onset of the next substorm.

1.4.2.2 The Near-Earth Neutral Line Model of Substorms

A quite widely-accepted model of substorms is the Near-Earth Neutral Line (NENL) model (e.g Baker *et al.*, 1996) which is illustrated in Figure 1.9. In the NENL model onset of the expansion phase begins with reconnection at a Near-Earth neutral line in the magnetotail, thought typically to appear $\sim$25 R_E anti-sunward of the Earth (Nagai *et al.*, 1997). This reconnection generates earthward-propagating fast flows in the plasma sheet known as Bursty Bulk Flows or BBFs (Angelopoulos *et al.*, 1992) and pinches off the closed loop of magnetic flux between the Near-Earth and distant neutral lines (a plasmoid) which is ejected anti-sunward into interplanetary space. The BBFs carry magnetic flux with them as they propagate earthward. These flows brake and the flux they carry piles up in a region 8-10 R_E downtail from the Earth (the Current Disruption region) which has the effect of disrupting the cross-tail current, diverting it into a field-aligned current system that flows into the ionosphere, through the ionosphere then out again, rejoining the cross-tail current. This current system is called the Substorm Current Wedge (SCW, illustrated in figure 1.10) and it is the upward current in the SCW, located at it's western edge, that is responsible for the bright, substorm aurora (McPherron *et al.*, 1973). As the reconnection continues and the substorm proceeds into the recovery phase the NENL retreats downtail forming the new Distant Neutral Line and the process begins again with the continuing addition of open flux to the tail lobes.

1.4.2.3 The Current Disruption Model of Substorms

Another substorm model is the Current Disruption (CD) model (e.g. Lui, 1996). Under the current disruption model, expansion phase onset begins with the disruption

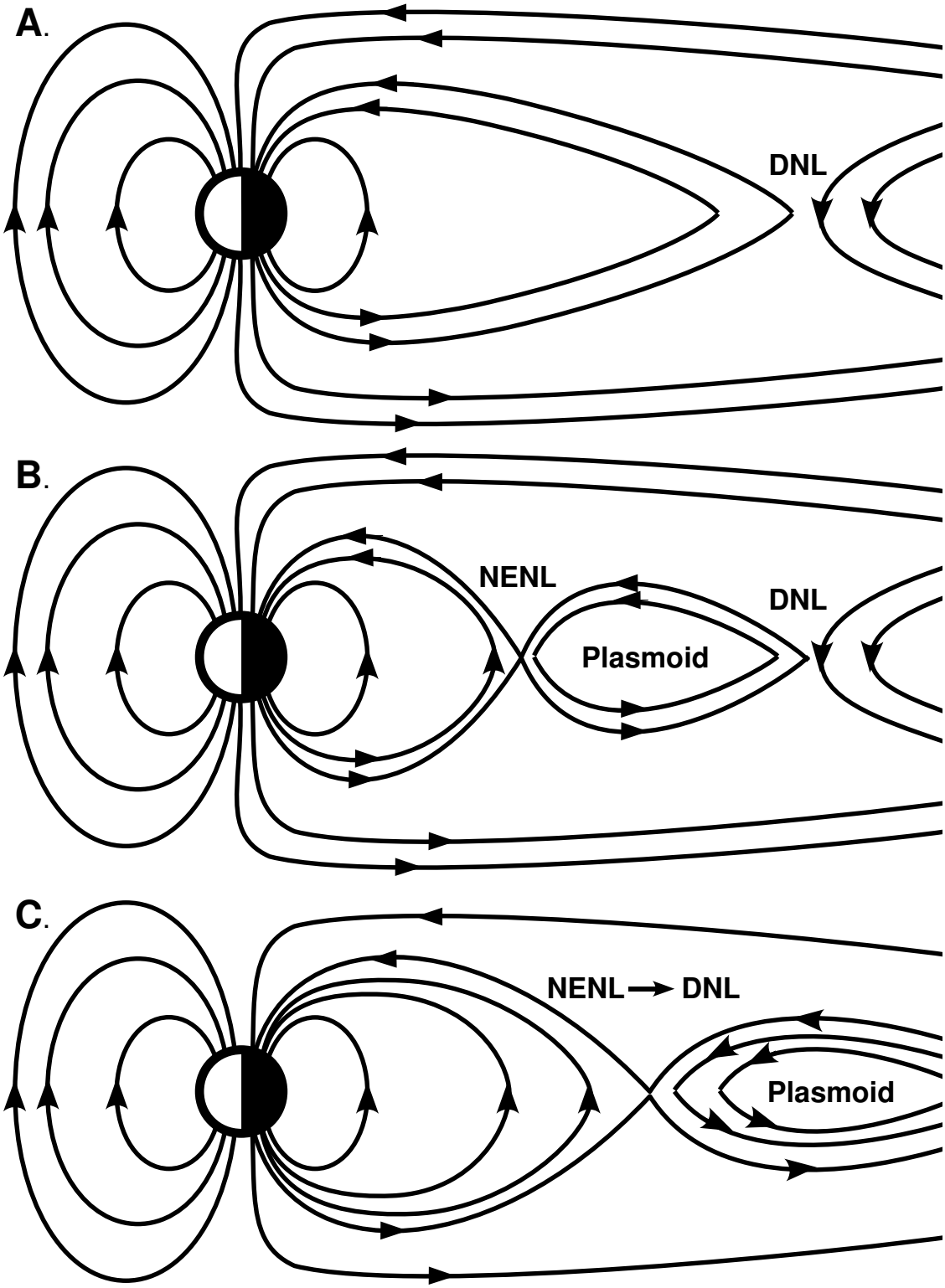

Figure 1.9: The Near-Earth Neutral Line Substorm Model (after Baker *et al.*, 1996). The growth phase is represented in Panel A, the expansion phase in Panel B and the recovery phase in Panel C.

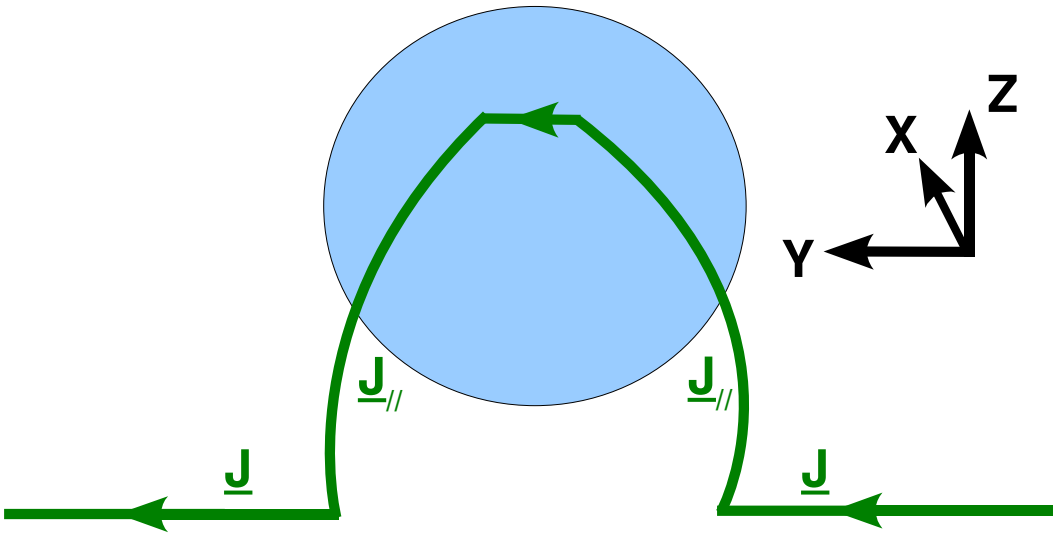

Figure 1.10: The Substorm Current Wedge, the cross-tail current is disrupted and diverted along magnetic field lines into the ionosphere, flows through the ionosphere then back out along the field lines into the magnetosphere.

of the cross tail current, diverting it into the ionosphere via the substorm current wedge and lighting up the aurora. The disruption of the cross tail current also sends a disturbance (a rarefaction wave) propagating tailwards that triggers reconnection at the NENL further downtail generating earthward plasma flows, after which the substorm proceeds into the recovery phase in a similar manner to the NENL model. The actual mechanism behind the disruption of the cross-tail current is still uncertain, however there is evidence that the Kinetic Ballooning instability (Liu *et al.*, 2008) and Alfvén Ion Cyclotron instability (Yoon *et al.*, 2009) are involved.

The differences between the sequence of events surrounding onset in the two models can be summarised as follows:

$$\text{NENL:} \quad \textit{Reconnection} \rightarrow \textit{Current Disruption} \rightarrow \textit{Aurora}$$

$$\text{CD:} \quad \textit{Current Disruption} \rightarrow \textit{Aurora} \rightarrow \textit{Reconnection}$$

The time differences between the start of reconnection and the brightening of the aurora in the NENL model, and the onset of current disruption and triggering of reconnection in the CD model have been calculated to be approximately two

minutes, so distinguishing between the two onset mechanisms in ionospheric and magnetospheric data has become known as the "2 minute problem" (e.g. Ohtani, 2004).

1.5 Summary of Thesis

In reality, the magnetotail, and the magnetosphere in general, are much more complex than the simple two-dimensional picture presented above. In this thesis several examples of departures from that simple picture are discussed. In Chapter 3 the consequences of reconnection occurring at more than one site in the near-earth magnetotail (Multiple X-Point Reconnection), so-called "magnetic flux ropes", are investigated. In Chapter 4 a detailed study of a plasma bubble, a proposed explanation for BBFs, is presented. Finally, in Chapter 5 the circumstances surrounding substorm onset and the disruption of the cross-tail current are studied using a wide array of space- and ground-based instrumentation. In all of these cases the magnetotail exhibits azimuthal structure, highlighting the importance of multipoint space- and ground-based measurements in fully understanding its behaviour.

Chapter 2

Instrumentation

> Obviously I can't be the P.I.; I'm still writing my thesis.
>
> *G. Collinson, 2009*

2.1 Measuring Space Plasmas

Solar System space plasmas are generally too tenuous and too cold to be directly imaged in the traditional manner using telescopes. Instead, if direct measurements of these plasmas are needed the charged particles and electromagnetic fields that make them up must be sampled in-situ by flying spacecraft through them. This also has the advantage of providing measurements of particle distributions functions, impossible using remote sensing techniques. In the context of the Earth's magnetosphere, the coupling between the magnetosphere and the ionosphere via the geomagnetic field can also be exploited because magnetospheric processes can have consequences in the ionosphere, notably the aurora. Thus ground- and space-based remote sensing of the ionosphere and monitoring of the surface magnetic field can be used to provide information about the large-scale behaviour of the magnetosphere, complementing spacecraft measurements.

While in-situ measurements from spacecraft can provide immense detail about the immediate environment of the spacecraft, they are also limited in that they provide a single point measurement within a complex system that may be varying in space and in time. This means it is sometimes difficult to put spacecraft measurements that have been taken in isolation into context. Data from ground-based sources can be used to provide this context to some extent, though this relies on mapping the magnetic field from the ionosphere to the magnetosphere using magnetic field models (e.g. Tsyganenko and Stern, 1996) that are not always reliable. Furthermore the use of more than one spacecraft can not only provide more than one individual dataset, but also by combining data from multiple spacecraft we may obtain insights not possible using single point measurements. Several multi-spacecraft missions to the magnetosphere have been flown, including the Russian-led INTERBALL Project (Galeev *et al.*, 1996) which consisted of two mother-daughter pairs of spacecraft, dedicated to studying the magnetotail and auroral acceleration regions; AMPTE (Bryant *et al.*, 1985) in the 1980s which was made up of three spacecraft; and the ISEE program (Ogilvie *et al.*, 1977) in the 1970s, which included a pair of spacecraft dedicated to magnetospheric studies and an upstream monitor at L1.

More recently, the European Space Agency's (ESA) Cluster mission (Escoubet *et al.*, 2001), the joint Sino-European Double Star Mission (Liu *et al.*, 2005) and NASA's THEMIS (Sibeck and Angelopoulos, 2008) mission have adopted different approaches to multi-spacecraft measurements. Cluster is comprised of four spacecraft whose orbits are designed such that the spacecraft are located at the four vertices of a regular tetrahedron at certain points along their orbital track. This enables them to study small and medium scale (i.e. 10's - 10,000 km) phenomena in three dimensions, while Double Star had two spacecraft, one in a polar orbit and one in an equatorial orbit, and was designed to work closely with Cluster. Conversely, THEMIS has five spacecraft whose orbits are designed to provide radial conjunctions covering large regions of the magnetosphere to investigate larger scale processes, in particular substorms.

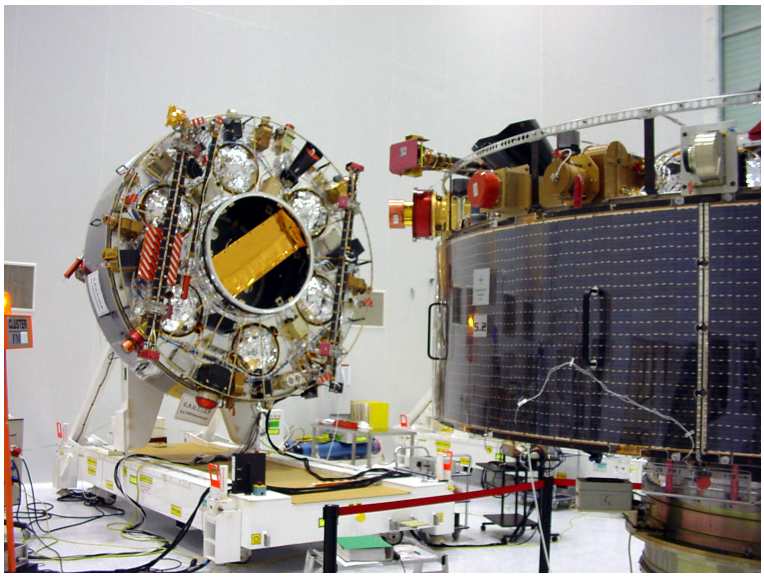

Figure 2.1: Two of the Cluster Spacecraft in the Payload Processing Facility clean room, Baikonour, Kazakhstan (image courtesy ESA).

2.2 Cluster

The ESA's Cluster (Escoubet *et al.*, 2001), or more properly Cluster II, mission was commissioned in 1997 as a replacement for the original Cluster mission, lost during launch with Ariane 501 on 4 June 1996. Cluster consists of four identical spacecraft, two of which are depicted in Figure 2.1. The Cluster spacecraft were launched as two pairs of spacecraft using Soyuz-Fregat launchers on 16 July and 9 August 2000.

Each of the spacecraft was placed in a slightly different elliptical polar orbit, with a perigee of $\sim 4\,R_E$ and apogee of $\sim 19.6\,R_E$. These orbits mean that the Cluster spacecraft fly close together such that they are located at the vertices of a tetrahedron with a desired size, at certain points along the orbit in regions of scientific interest. The planes of the orbits are fixed in inertial space. As the Earth orbits the Sun over the course of a year, the magnetosphere moves with respect to these planes allowing the spacecraft to spend time in different regions of the magnetosphere. The so-called "tail season", which is of most relevance to this thesis, occurs when apogee lies in the magnetotail, roughly between mid-July and mid-October. Conversely, the dayside season when the apogee of Cluster's orbit nominally lies in the solar wind occurs between mid-January and mid-April. The orbit of Cluster over a year,

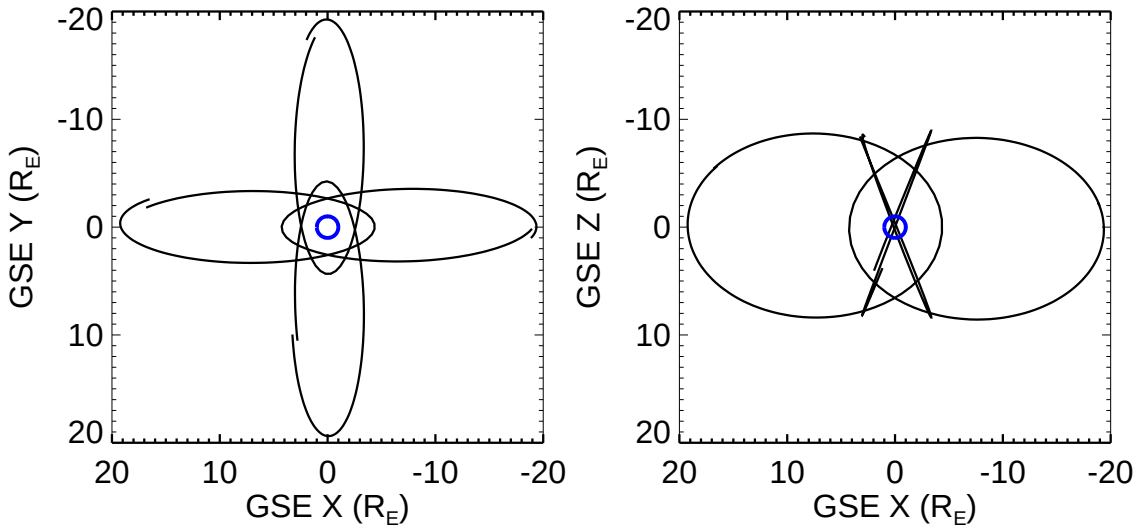

Figure 2.2: The orbit of Cluster over a year, drawn at three month intervals. The left hand panel is the projection of the orbit in the equatorial plane, while the right hand panel is the projection in the noon-midnight meridian (GSE coordinates have been used).

projected into the equatorial and noon-midnight planes in the GSE coordinate system, is drawn at 3 month intervals in Figure 2.2. Note that later in the mission, precession of the orbits has resulted in the apogee dropping south of the equatorial plane, with the effect of moving the orbital track so that the spacecraft pass through different regions of the magnetosphere, for example the sub-solar magnetopause and the current disruption region in the magnetotail

After a period of commissioning, the mission was declared operational in February 2001 and it was originally funded for an operational phase of two years. The mission has since been extended several times and, at the time of writing, is expected to operate until at least December 2009.

Each of the Cluster spacecraft is identically instrumented with a payload of eleven experiments that are capable of measuring AC and DC electromagnetic fields and charged particle velocity distributions from energies of a few eV to 400 KeV for electrons and 1.5 MeV for ions. Table 2.1 lists these instruments.

Data from FGM, CIS and PEACE are employed in this thesis. These instruments will be described in greater detail in the following sections of this chapter.

ASPOC	Active Spacecraft Potential Control
CIS	Thermal & Suprathermal Ions
DWP*	Wave Processor
EDI	Electron Drift Velocity
EFW*	DC Electric Field
FGM	DC Magnetic Field
PEACE	Thermal & Suprathermal Electrons
RAPID	Energetic Ions and Electrons
STAFF*	Magnetic and Electric Fluctuations
WBD*	Electric Field and Waveforms
WHISPER*	Electron Density and Waves

Table 2.1: The eleven instruments carried by each Cluster spacecraft and what they measure. The instruments marked with a * are part of the Wave Experiment Consortium (after Escoubet *et al.*, 2001).

2.2.1 The Cluster Tetrahedron

A unique aspect of the Cluster mission is the tetrahedron which the four spacecraft form in space. The tail season orbits were initially designed such that, close to apogee, the four spacecraft form an almost regular tetrahedron, as illustrated in Figure 2.3. Although orbital mechanics dictate that it is only possible for a perfectly regular tetrahedron to be formed at two points during a year, Cluster makes an almost-regular tetrahedron for a significant proportion of the time it spends near the tail plasma sheet. The size and shape of this tetrahedron has been varied over the Cluster mission in order to address different scientific problems. Table 2.2 summarises the scale sizes of the Cluster tetrahedron for the years 2001-2006.

In the 2004 and 2005 tail seasons, the periods investigated in this thesis, Cluster had substantially different tetrahedron configurations. In 2004, the spacecraft made a regular tetrahedron of side 1,000 km, while in 2005 Cluster was placed in a so-called "Multi-Scale" configuration, with spacecraft 1,2 and 3 making a triangle of side ∼10,000 km in the expected plane of the magnetotail neutral sheet (based on a model) while spacecraft 4 was offset from the triangle by 1,000 km.

Regular tetrahedra allow for the use of powerful multi-spacecraft analysis techniques that give Cluster the ability to measure spatial gradients and therefore cal-

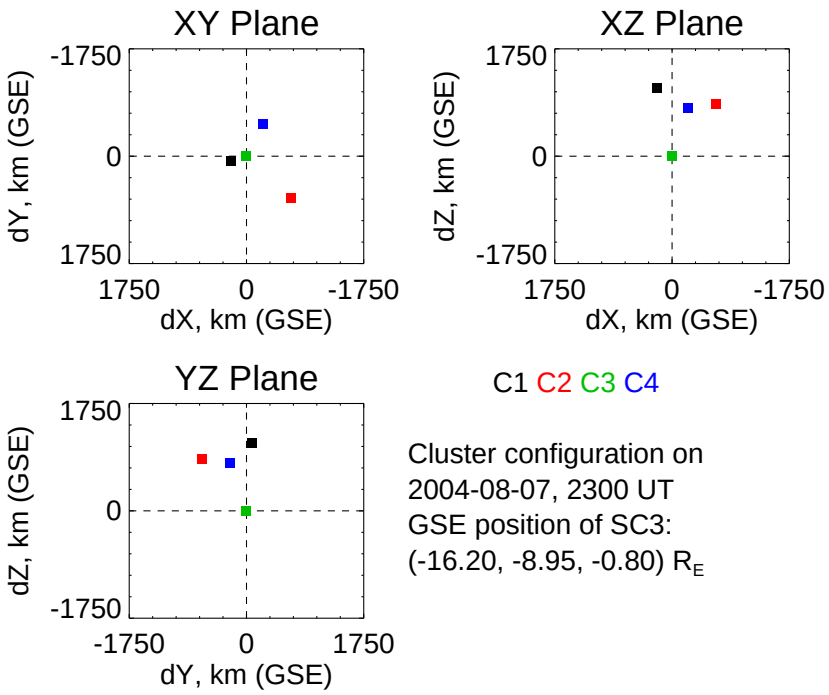

Figure 2.3: An example Cluster configuration near apogee in the 2004 tail season. GSE coordinates have been used.

2001	2,000 km
2002	3,700 km
2003	200 km
2004	1,000 km
2005	10,000/1,000 km
2006	10,000 km

Table 2.2: The Cluster tetrahedron configuration during the 2001-2006 tail seasons.

culate quantities like current density (e.g. Dunlop *et al.*, 2002) or the divergence of pressure tensors (Henderson *et al.*, 2006b, 2008) in three dimensions. Regular tetrahedra can also be used to determine the orientation of structures (for example current sheets) crossed by the spacecraft if the structures can be assumed planar on the scale of the tetrahedron (e.g Dunlop and Woodward, 2000).

2.2.2 Cluster PEACE

The PEACE (Plasma Electron and Current Experiment; Johnstone *et al.*, 1997; Fazakerley *et al.*, 2009) instrument is an electron spectrometer designed to measure

the three-dimensional velocity distribution of electrons in the energy range ∼0.6 eV to ∼26,400 eV at spin-resolution (i.e. every four seconds in the case of Cluster). Each instrument is made up of two sensors, HEEA (High Energy Electron Analyser) and LEEA (Low Energy Electron Analyser) and a DPU (Digital Processing Unit). Both HEEA and LEEA are capable of measuring the full PEACE energy range, though not at any given time, and LEEA has a factor of 5 lower sensitivity than HEEA because it has been optimised for the higher electron fluxes expected at lower energies (for example in the solar wind and magnetosheath). The two sensors are electrostatic analysers of the top hat design and are mounted on opposite sides of each Cluster spacecraft such that their fields of view point radially away from the spin axis. This radial mounting direction was chosen because a look direction tangential to the spacecraft body would enable photoelectrons emitted from the spacecraft body to immediately enter the PEACE sensors. A radial look direction minimises this effect.

2.2.2.1 Top Hat Electrostatic Analysers

A top hat electrostatic analyser (Carlson *et al.*, 1982) is a design of charged-particle spectrometer commonly used in the study of space plasmas (e.g. Rème *et al.*, 2001; McFadden *et al.*, 2008). The basic geometry of a top hat analyser is illustrated in Figure 2.4. It consists of an inner hemisphere, an outer hemisphere and a top cap. For the measurement of electrons, the inner hemisphere is given a positive voltage with respect to the outer hemisphere, which is kept grounded. For a given voltage difference between the inner and outer hemispheres, only the trajectory of a particle with a specific energy will be bent such that it passes through the gap between the hemispheres, impacting on a position-sensitive detector (anode). Particles with higher energies will impact on the outer hemisphere or collimator, and particles with lower energies will impact on the inner hemisphere. Thus by varying the potential difference between the hemispheres, particles with different energies can be selected, allowing the velocity distribution function of particles to be measured.

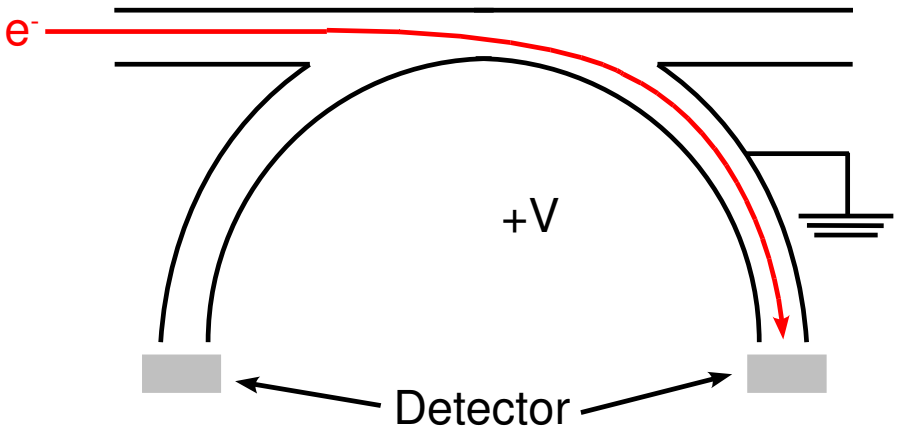

Figure 2.4: The basic geometry of a top hat electrostatic analyser with the hemisphere voltages set for the measurement of electrons.

PEACE is operated in such a way that the voltage on the inner hemisphere is decreased from the voltage required to measure higher energy electrons to the voltage required to measure the lower energy electrons (a sweep), after which it is very swiftly increased again to measure high energy particles at the start of the next sweep. The PEACE energy range is split into 88 different levels, the first 16 levels are linearly spaced in the energy range 0.6eV to 9.5eV while the other 72 are logarithmically spaced over the rest of the energy range. Usually, 60 of the energy levels are covered in a given sweep. Sweeps are synchronised with the spacecraft spin rate such that an integer number of sweeps is completed during a spin, and the sweeps are timed such that higher energy electrons are measured while the instrument aperture is facing the Sun, minimising contamination from photoelectrons produced within the instrument. The actual energy range measured by each PEACE sensor, and the number of energy levels included in a given sweep, can be changed in-flight through the uplinking of commands to the spacecraft from the ground.

Measuring the impact of a single electron (or ion) on a detector can be difficult,

so the Cluster PEACE sensors employ a stack of two micro channel plates (MCPs) mounted between the hemispheres and the anode. MCPs are glass plates containing microscopic pores oriented such that an incoming particle will hit the wall of one of these pores. The impact of a particle on wall of the pore will result in the emission of one or more secondary electrons that are accelerated towards the anode by a voltage applied across the MCP, each secondary will in turn strike the wall of the pore, causing the emission of yet more electrons which are in turn accelerated down the pore until they hit a wall, and so on. A cloud of electrons, much more easily detected than a single particle, will therefore hit the anode after exiting the MCP. Each MCP typically gives a thousandfold increase in the number of electrons, so in the case of PEACE, the total gain from the MCPs is of the order of $1{\times}10^6$.

2.2.2.2 Measuring Direction

In order to construct a full three-dimensional particle distribution it is not only necessary to measure particle flux in terms of energy, but also in terms of direction. The LEEA sensor has a field-of-view of 180° (polar) × 3° (azimuth), while HEEA has a field-of-view of 180° (polar) × 5° (azimuth). Polar angles are measured with respect to the spin axis and azimuth angles are measured in the spin plane. Over the course of a single spacecraft spin each PEACE sensor sweeps out all 360° of azimuth, thus each sensor can observe all 4π sr of sky in four seconds.

The polar resolution of the PEACE sensors is determined by the position sensitive detector. Each detector is divided into 12 zones, or anodes, each corresponding to 15° of the field-of-view in the polar direction, giving each PEACE sensor a 15° polar resolution. The anode that looks along the spin axis is numbered anode 1, while the anode that looks antiparallel to the spin axis is numbered anode 12. The mounting of the sensors on the spacecraft, and the polar fields-of-view and resolution are illustrated in Figure 2.5.

The azimuthal resolution of the PEACE sensors is determined by the number

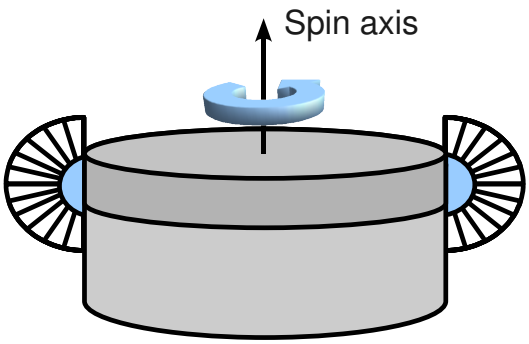

Figure 2.5: The mounting of each PEACE sensor on the Cluster spacecraft. Each sensor is depicted by a blue semicircle and their polar fields of view and resolution (12 bins each covering 15°) are marked with the black fans.

of energy sweeps that can be completed during a spin. The duration of a given sweep is in part determined by the number of energy samples included in the sweep - the more energy samples the longer the sweep, so there is a trade-off between energy resolution and azimuthal resolution. The design of the instrument electronics dictates that there must be 1,024 data accumulation bins in a spin; how these accumulation bins are divided between sweeps is determined by what is known as the sweep mode of the instrument. PEACE has three different sweep modes designed to maximise flexibility. HAR, MAR and LAR (High, Medium and Low Angular Resolution). In HAR mode, each sweep includes 30 energy levels that are accumulated in 15 energy bins, and there are 64 sweeps per spin, giving an azimuthal resolution of 5.625°. In MAR mode a sweep includes 60 energy levels accumulated in 30 energy bins and there are 32 sweeps per spin, giving an azimuthal resolution of 11.25°. In LAR mode a sweep includes 60 energy levels that are accumulated in 60 bins and has 16 sweeps per spin giving an azimuthal resolution of 22.5°. The remaining 64 accumulations per spin make up the so-called "flybacks", during

which the voltage on the inner hemisphere is increased to measure the higher energy electrons at the start of the subsequent sweep. PEACE also has a Fixed Energy mode primarily used for operations/ground test purposes. Although MAR is the most commonly used mode, in some situations HEEA and LEEA operate using different sweep modes. In the magnetotail plasma sheet, for example, HEEA is often operating in MAR mode while LEEA is operating in HAR mode at a subset of HEEA's energies, so the combination of the two sensors provides the best possible energy and angular resolution at energies around the expected peak in the plasma sheet electron distribution.

2.2.2.3 PEACE Data Products

Bandwidth constraints mean that 3D distributions at the full resolution of the instrument are rarely telemetered. Instead, several different data products are sent to the ground depending on the telemetry mode of the spacecraft. The Cluster spacecraft can operate in several telemetry modes, standard telemetry rate "normal" modes and high telemetry rate "burst" modes which are relatively infrequent and scheduled for when the Cluster orbit is expected to pass through regions of particular scientific interest, for example the magnetotail current sheet. Regardless of spacecraft or instrument mode, a certain set of core data products are always telemetered from PEACE. These core products include housekeeping data, two-dimensional pitch angle distributions and on-board calculated moments at spin resolution. These have been designed such that useful scientific data are returned even in the most limited telemetry mode of the spacecraft.

2.2.2.3.1 3D Distributions PEACE rarely has sufficient allocated bandwidth to telemeter a 3D distribution at full resolution (known as 3DF). Even in burst mode, 3DF can only be sent at a rate lower than one distribution per five spins. Instead, one of several reduced resolution 3D products are telemetered depending on spacecraft or instrument mode. In normal mode, 3DR is telemetered from both

the HEEA and LEEA sensors. 3DR is a reduced resolution 3D product. Sets of two adjacent polar zones of each sensor are paired and counts from those zones summed, giving a product with 30° polar resolution. Similarly, adjacent energy bins are also summed, as are adjacent azimuthal bins. In the case of MAR mode, therefore, instead of all 30 measured energy bins and all 32 azimuths (sweeps) being telemetered a product with 15 energy bins and 16 azimuths is transmitted to the ground. Even with this eightfold reduction in resolution there is still not enough bandwidth to send a 3DR distribution every spin on all spacecraft. Cluster 1 and Cluster 3 each send a 3DR distribution every ∼20 spins. Inoperative instruments on Cluster 2 (CIS) and Cluster 4 (EDI) mean that Cluster 2 PEACE and Cluster 4 PEACE have a higher bandwidth allocation than their counterparts on Cluster 1 and Cluster 3, so 3DR can be sent more often. In the case of Cluster 2, 3DR is sent every spin while for Cluster 4, 3DR is sent, on average, for 3 of every 10 spins.

During burst modes one of several higher resolution 3D products, known as 3DX, can be telemetered from one or both of the sensors. The most commonly used 3DX product is 3DXP. In this case, the polar zones paired in the same way as for 3DR, however energy and azimuth resolution are not reduced, with all 30 energy levels and 32 azimuths for a MAR sweep mode, for example, being transmitted to the ground. Conversely in the case of 3DXE, a more rarely used product, the full polar resolution of the instrument is retained while the energy resolution is reduced. The data products that are usually transmitted from each spacecraft during burst modes in the magnetotail are summarised in Table 2.3. In burst mode 3DXP products are usually transmitted every spin, while 3DR products are transmitted as often as available bandwidth allows.

	Cluster 1	Cluster 2	Cluster 3	Cluster 4
HEEA	3DX1P	3DX2P	3DX1P	3DX2P
LEEA	3DR	3DX1P	3DR	3DX1P

Table 2.3: Summary of 3D data products telemetered during magnetotail burst modes. Note that the 1 or 2 designation in the 3DX products determines the commanding order and does not change the details of the data product itself.

In some cases, again because of bandwidth constraints, 3DX1P from Cluster 1 and Cluster 3 is "windowed", i.e. the full energy range and resolution for a given sweep mode are measured but not all of the measured energy bins are transmitted to the ground. This is done to maintain coverage every spin.

2.2.2.3.2 Pitch Angle Distributions Two dimensional pitch angle distributions are returned from each sensor every spin. These pitch angle distributions always have full polar resolution and energy resolution for a given sweep mode, but are constructed such that only two sweeps per spin are returned from each sensor, one when the sensor has the same azimuth as the magnetic field, and one when the sensor azimuth is 180° away from the magnetic field direction, half a spin later. For the first (second) half-spin, anodes from the anode looking parallel (antiparallel) to the field up to anode 12 are used, providing a full pitch-angle distribution over the course of a spin. The acquisition of pitch-angle distributions is illustrated in Figure 2.6. Because the HEEA and LEEA sensors on the spacecraft are mounted on opposite sides of the spacecraft, 180° in azimuth apart, a full pitch angle distribution, collected in only 1/8 of a second can be constructed twice a spin by combining data from both sensors, though these combined pitch-angle distributions are limited to the common energy range of both sensors.

Magnetic field direction is determined onboard using data from the FGM instrument provided via an inter-experiment link. The magnetic field vector measured at the end of the previous spin is selected by PEACE and this vector is then used to select the correct sweeps (i.e. azimuths) and polar zones to return in order to construct a full pitch-angle distribution. This has the disadvantage that if the magnetic field varies significantly over the course of a spin then the information provided to PEACE will be out of date and the instrument will not necessarily select the correct sweep/anode combination for an accurate pitch angle distribution. These errors can be identified and corrected on the ground by comparing the on-board pitch angle distributions to the actual magnetic field direction at the time the sweeps were taken, and reassigning accurate pitch angles to each PEACE anode. It not always

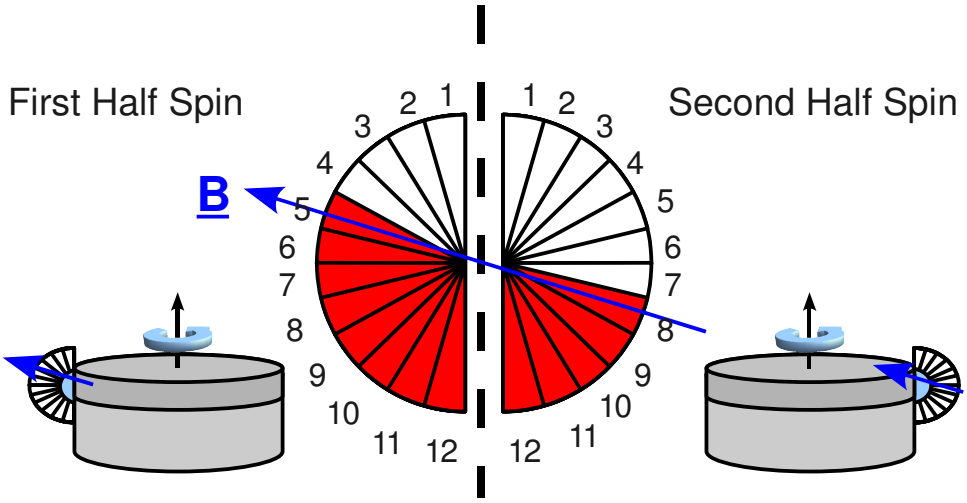

Figure 2.6: Schematic illustrating the acquisition of pitch-angle distributions from a single sensor. During the first half spin Anode 5 is looking along the magnetic field direction so Anodes 5-12 are returned, during the second half-spin Anode 8 is looking antiparallel to the magnetic field so Anodes 8-12 are returned, providing complete pitch angle coverage in four seconds.

the case, however, that full pitch angle coverage will be recovered.

2.2.2.4 Moments

The three-dimensional velocity distribution of particles can be used to calculate the bulk parameters of plasma by taking moments of the distribution function, $f(\boldsymbol{v}, \boldsymbol{r}, t)$ (e.g. Paschmann *et al.*, 2000). In principle there are an infinite number of moments of the distribution function, though only the first few are physically meaningful. The ith moment is given by Equation 2.1.

$$M_i(\boldsymbol{r}, t) = \int_{-\infty}^{\infty} f(\boldsymbol{v}, \boldsymbol{r}, t) \boldsymbol{v^i}\, d^3v \tag{2.1}$$

The zeroth order moment gives the number density of particles (Equation 2.2).

$$n = \int_{-\infty}^{\infty} f(\boldsymbol{v}, \boldsymbol{r}, t)\, d^3v \tag{2.2}$$

The first order moment is related to the bulk velocity of particles, $\boldsymbol{v_b}$, by Equation 2.3.

$$\boldsymbol{v_b} = \frac{1}{n} \int_{-\infty}^{\infty} \boldsymbol{v}\, f(\boldsymbol{v}, \boldsymbol{r}, t)\, d^3v \tag{2.3}$$

It should be noted that $\boldsymbol{v_b}$ is the average bulk velocity of the particle species being measured and does not represent the velocities of individual particles. It is important to bear this in mind when interpreting velocity data because if a distribution contains multiple particle populations that are behaving differently then this will not be obvious when using the bulk velocity moment.

The pressure tensor is calculated from the second order moment using Equation 2.4 and represents any variations in the velocities of individual particles from the bulk velocity.

$$\mathsf{P} = m \int_{-\infty}^{\infty} (\boldsymbol{v} - \boldsymbol{v_b})\, (\boldsymbol{v} - \boldsymbol{v_b})\, f(\boldsymbol{v}, \boldsymbol{r}, t)\, d^3v \tag{2.4}$$

The trace of the third order moment (the heat tensor) gives the heat flux vector, a measure of the transfer of heat through the plasma (Equation 2.5).

$$\boldsymbol{q} = \frac{m}{2} \int_{-\infty}^{\infty} (\boldsymbol{v} - \boldsymbol{v_b}) \cdot (\boldsymbol{v} - \boldsymbol{v_b})\, (\boldsymbol{v} - \boldsymbol{v_b})\, f(\boldsymbol{v}, \boldsymbol{r}, t)\, d^3v \tag{2.5}$$

Equations 2.4 and 2.5 both involve the bulk velocity which is itself the product of a moment calculation; so in the case of PEACE so-called standard moments, involving only $\boldsymbol{v}$, are calculated first and then the above, relative, moments are calculated on the basis of these.

2.2.2.5 Spacecraft Potential and Photoelectron Contamination

In order to calculate accurate plasma moments, the distribution function measured by a particle instrument needs to be free of contamination from particles of spacecraft origin. The most significant source of contaminant electrons are photoelectrons emitted from the spacecraft body. The emission of these photoelectrons has the effect of positively charging the spacecraft and generating a spacecraft electrostatic potential. The magnitude of the spacecraft potential depends on the balance between the flux of photoelectrons and the so-called return current, the flux of ambient plasma electrons accelerated back onto the spacecraft by the positive potential. Thus in regions of higher plasma density, for example the tail plasma sheet, the spacecraft potential is lower than in regions of more rarefied plasma, for example the tail lobes. On Cluster, the level of the spacecraft potential can be further reduced through use of the Active Spacecraft POtential Control (ASPOC) system (Torkar *et al.*, 2001), which emits positive ions at a flux designed to keep the spacecraft potential to a minimum.

The presence of a positive spacecraft potential has the effect of accelerating electrons towards the spacecraft, thus increasing their energy and altering their distribution function from that which would naturally be present. As such it is important to measure the spacecraft potential and correct for this when calculating plasma moments, particularly when measuring lower energy electron populations. The Electric Fields and Waves (EFW) instrument (Gustafsson *et al.*, 2001) has this capability, however spacecraft potential data is not provided to PEACE via the Inter Experiment Link (IEL) on the Cluster spacecraft and as such correction for spacecraft potential cannot be applied to on-board calculated electron moments. Ground-calculated moments, however, can be corrected for spacecraft potential.

The photoelectrons themselves are also detected by PEACE, usually at energies up to the spacecraft potential. Since these photoelectrons change the measured distribution from the natural distribution, and hence will alter the moments, they

should not be included in moments calculations. Photoelectron contamination can often be removed from the moments calculations on the ground. In the case of the onboard moments, however, actual photoelectrons cannot be removed, although the bottom 10 eV of the PEACE energy range is discarded, hopefully removing any photoelectron contamination.

2.2.2.6 The v_Z Problem

The spin plane of the Cluster spacecraft is approximately aligned with the GSE XY plane, so any vector quantities measured by the PEACE instrument in that plane are generally based on electron fluxes recorded by the same anode at different times during a spin. The calculation of v_X, put simply, is based on the electron flux measured by those PEACE anodes with a component of their look direction in the spin plane when the sensor looking earthwards subtracted from the electron flux measured by those anodes when the sensor is looking tailwards. Components of vector quantities out of the spin plane of the spacecraft (notably v_Z), however are calculated based on effectively subtracting the fluxes measured by different anodes and as such can be affected by slight errors in calibration between those anodes - the v_Z problem. The v_Z problem can be seen in uncorrected data as a systematic offset from zero of the GSE Z component of the velocity calculated from the electron distributions. Careful inter-anode calibration can eliminate this problem, however this is an ongoing process as detection efficiencies of the different PEACE anodes change over time, as do the gain levels of the PEACE MCPs

2.2.3 Cluster FGM

Each Cluster spacecraft carries an FGM (FluxGate Magnetometer) instrument (Balogh *et al.*, 2001). Each instrument is made up of two tri-axial fluxgate sensors (for a description of how fluxgate magnetometers work, see Primdahl, 1979). located on one of the two solid booms of the spacecraft. The outermost sensor,

located at the end of the spacecraft boom, 5.2 m away from the spacecraft is designated the primary sensor because it is further away the spacecraft magnetic and its measurements are thus less affected by the spacecraft magnetic field, however either one of the sensors can fill this role, providing redundancy. The FGM sensors are capable of sampling the magnetic field vector at a rate of 201.793 vectors/s, although this is downsampled to lower rates because of telemetry constraints. During normal mode operations, FGM transmits ∼22 vectors per second to the ground, while during burst modes ∼67 vectors per second are transmitted.

The FGM instrument has seven operating ranges and resolutions designed for regions of different magnetic field strengths. Four of these operating ranges are used in-flight and are summarised in Table 2.4

Range no.	Range	Resolution
2	-64 nT to +63.97 nT	7.8×10^{-3} nT
3	-256 nT to +255.87 nT	3.1×10^{-2} nT
4	-1024 nT to +1023.5 nT	0.125 nT
5	-4096 nT to +4094 nT	0.5 nT

Table 2.4: FGM Operating ranges and resolutions as used in flight on Cluster (after Balogh *et al.*, 2001).

FGM has a spin-axis offset problem (a "B_Z" problem) analogous to PEACE's v_Z problem. Measurements taken in the spin plane are much more easily calibrated because a sensor in the spin plane, when exposed to a steady field, will return a sine wave with a DC offset which represents contamination from the spacecraft magnetic field. It is only the offset that needs to be removed. The axial sensor, on the other hand, cannot be calibrated in this way, instead the offset is measured by considering a long term average of data which is taken in regions where that average should be zero (for example the IMF).

2.2.4 Cluster CIS

The Cluster Ion Spectroscopy (CIS) experiment (Rème *et al.*, 2001) consists of two different ion instruments both capable of measuring a 3D ion distribution every spin. The two sensors are named CODIF (COmposition and DIstribution Function analyser) and HIA (Hot Ion Analyser) each of which are of a top hat design and were flown on all four Cluster spacecraft. Unfortunately both CIS sensors on Spacecraft 2 and the HIA sensor on Spacecraft 4 are non-functional. After August 2004 the CODIF sensor on Spacecraft 1 became increasingly unreliable, and the CODIF sensor on Spacecraft 3 has a significant v_z problem analogous to that experienced by PEACE that has worsened due to MCP performance decline, and which has been uncorrectable since February 2003.

2.2.4.1 CODIF

The Composition and DIstribution Function analyser is capable of measuring a full 3D distribution function at spin resolution between the energies of $\sim$15 eV/e and $\sim$38 KeV/e. CODIF is also designed to measure the distribution functions of different ion species, including H^+, He^+, He^{2+} and O^+, using a time-of-flight mechanism (Möbius *et al.*, 1985), although in regions of very high ion flux, the heavier mass channels can be contaminated with protons. Ions are energy per charge selected using the top hat analyser in a similar manner to PEACE. They then pass through a thin carbon foil which creates a cloud of secondary electrons that are then detected at a secondary detector. The detection of these electrons starts a timer which measures the elapsed time between the ions passing through the carbon foil and their subsequent detection at the primary detector. From this elapsed time and the known geometry of the instrument, q/m for the ions can be calculated. CODIF also has an RPA (Retarding Potential Analyser) mode which is used to measure ions of energies lower than 15 eV. When this mode is active, however, ions of higher energies cannot be measured and as such it is rarely used. Also, in the presence of a

positive spacecraft potential, for example when the ASPOC system is switched off, lower energy ions are repelled from the spacecraft and as such cannot reach CODIF.

In order to accurately measure the high dynamic range of ion fluxes that the Cluster spacecraft routinely experience, the CODIF sensor is divided into two sections, a "high G" section and a "low g" section, both of which have fields of view of $180° \times 8°$. CODIF is mounted on the spacecraft such that the field of view of the instrument is tangential to the spacecraft body, whereas for PEACE the field-of-view is perpendicular to the spacecraft body. This is because the high G and low g sides of the sensor make up two 180° sections of the same 360° analyser - one looks spinward, the other antispinward. The sensitivities of the two sections have been designed such that CODIF can measure a statistically significant number of counts in both higher density regions like the solar wind and magnetosheath and lower density regions like the tail plasma sheet. The low g side has a geometric factor approximately 100 times lower than the high G side. Each side of the instrument is divided into 8 polar anodes giving a polar resolution of 22.5°. A CODIF sweep lasts 125 ms, giving an azimuthal resolution of approximately 11.2°. Bandwidth constraints mean that only one of the sides of CODIF is operated at once, so changes between high G and low g modes are scheduled according to estimates of when the Cluster spacecraft will move between plasma regimes better suited to observation by one side of the instrument or the other. Care needs to be taken that the instrument is in the correct mode when analysing data, particularly when the spacecraft is located close to magnetospheric boundaries as mode changes are based on predictions that are not always correct. High G mode is the most appropriate mode for use in the magnetotail.

2.2.4.2 HIA

The Hot Ion Analyser (HIA) is a simpler instrument than CODIF. It is a top hat analyser that has no ion species discrimination and measures ions with an energy/charge ratio in the range 5 ev/e to 32 KeV/e. Like CODIF, HIA has both "low

g" and "high G" sections optimised for different plasma environments each with a field-of-view of $180° \times 8°$. The difference in sensitivity of the two sides of HIA is a factor of $\sim$25 rather than $\sim$100. Also like CODIF, HIA is mounted such that the fields of view of the instrument point tangential to the spacecraft body, with the high G and low g sides looking in opposite directions. The high G side is divided into 16 polar zones giving a polar resolution of 11.25°. The low g side is divided such that it has 8 central polar zones with a resolution of 5.625° and 8 outer zones (4 either side of the central zones) with a resolution of 11.25°, which allows for high resolution measurements of solar wind ion distributions. Two 22.5° low g sections parallel and antiparallel to the spin axis (either side of the spin plane) have been left blank to avoid contamination between the high G and low g sides of the instrument. Like CODIF, the high G mode is most appropriate for use in the magnetotail.

2.2.4.3 CIS Data Products

CIS has a wide variety of modes and data products that are sent from the spacecraft depending on instrument bandwidth. In the magnetotail, during a normal mode 3D distributions cannot be transmitted to the ground every spin, but in a burst mode spin resolution distributions are often available. Like PEACE, both onboard and ground calculated moments are available from both CIS sensors. In the case of HIA, ground-calculated moments are based on lower resolution distributions that are telemetered to the ground. HIA onboard moments are calculated from full resolution distributions and, because the onboard and ground calibrations for the instrument are the same, the higher resolution onboard moments are preferred. Calibration issues, however, mean that CODIF ground calculated moments are usually superior to onboard moments. Plasma sheet ion distributions can sometimes extend in energy beyond the energy range of both the HIA and CODIF sensors so moments will not include the entire ion population, such that densities, temperatures and velocities are underestimates. Because the upper limit of HIA's energy range is lower than that of CODIF, this occurs more often for HIA, and as such moments from CODIF

are better suited for the study of the magnetotail plasma sheet.

In this thesis, then, data from CODIF are used in preference to data from HIA, however during the 2005 tail season only Cluster 4 CODIF was returning reliable data so Cluster 1 and Cluster 3 HIA data have also been used.

2.3 Double Star

The Double Star Project (Liu *et al.*, 2005) is the first cooperative project between ESA and the Chinese National Space Administration (CNSA) and also the first purely scientific Chinese space mission. It consists of two spacecraft that were launched on 29 December 2003 and 25 July 2004 on Chinese Long March 2C Rockets. The first spacecraft, Tan Ce 1 (TC-1), was injected into an equatorial orbit with perigee 570 km and apogee 79,000 km ($\sim$12 R_E), while the second spacecraft (Tan Ce 2) was placed in a polar orbit of perigee 560 km and apogee 38,000 km ($\sim$6 R_E). The Double Star orbits, plotted for August 2004 in Figure 2.7, were designed to maximise conjunctions with Cluster with the aim of increasing the scientific return from both missions. Data from Double Star provides valuable contextual information to complement Cluster's detailed multi-point measurements, for example, and phenomena on larger scales than that of the Cluster tetrahedron, like substorms, can be better studied with six point measurements than four point measurements.

As well as their orbits, the payloads of Cluster and Double Star complement each other well. Each of the Double Star spacecraft carry a combination of Chinese and European instruments. Many of the European instruments are flight spares from the Cluster project (or very similar) allowing for easy comparisons between measurements made by Cluster and Double Star. The instruments flown on TC-1 and TC-2 are listed in Table 2.5.

The Double Star Mission was originally intended to end in July 2005, however TC-1 remained operational until it re-entered on 14 October 2007 while at the

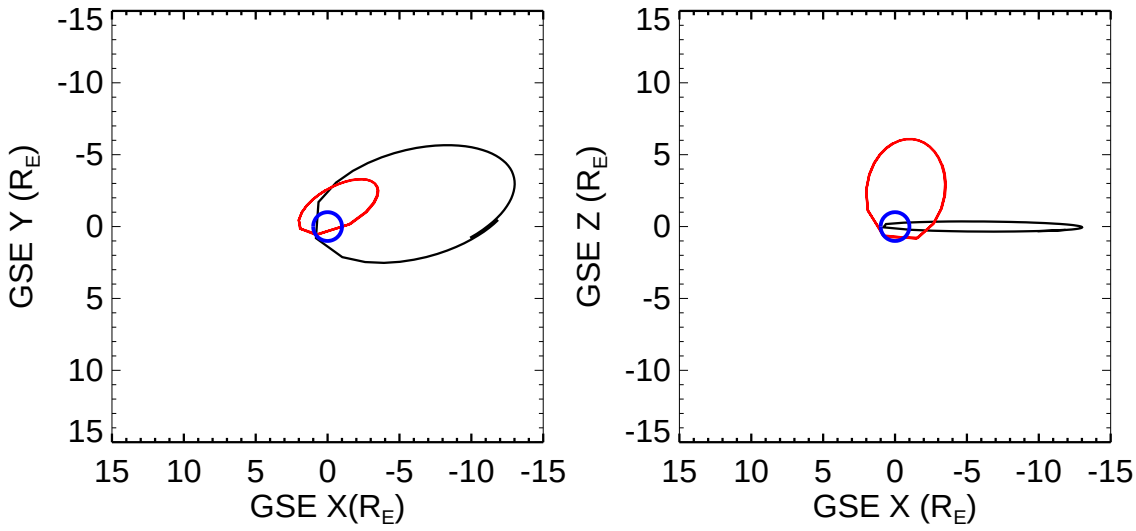

Figure 2.7: The orbits of the two Double Star spacecraft, plotted for 21 August 2004. TC-1's orbit is drawn in black, TC-2's in red. GSE coordinates have been used.

ASPOC*	TC-1	Active Spacecraft Potential Control
FGM*	TC-1/2	DC Magnetic Field
HEED	TC-1/2	High Energy Electrons
HEPD	TC-1/2	High Energy Protons
HIA*	TC-1	Thermal Ions
HID	TC-1/2	Heavy Ions
LEID	TC-2	Thermal Ions
LFEW	TC-2	Low Frequency Electromagnetic Waves
NUADU*	TC-2	Energetic Neutral Atoms
PEACE*	TC-1/2	Thermal Electrons
STAFF/DWP*	TC-1	Magnetic and Electric Fluctuations

Table 2.5: The instruments carried by the Double Star Spacecraft spacecraft and what they measure. The instruments marked with a * are European built (after Liu *et al.*, 2005).

time of writing TC-2 remains in operation, albeit sporadically as the failure of the spacecraft's attitude control system means that its solar panels are not optimally oriented with respect to the Sun for much of the year.

Data from Double Star TC-1 and TC-2 FGM, PEACE and TC-1 HIA have been used in this thesis, and these instruments are described in more detail below.

2.3.1 Double Star PEACE

The Cluster II PEACE flight spare instrument and the Cluster I spare DPU formed the basis of the Double Star PEACE instrument (Fazakerley *et al.*, 2005). The spare HEEA sensor flew on TC-1 while the spare LEEA sensor is flying on TC-2. The sensors were modified slightly from their original configuration, the major modification being the addition of extra shielding to the sensors so that they could better operate in the harsher radiation environments encountered by the Double Star spacecraft. Changes to the DPUs were also necessary because the export of some radiation hardened components to China is not permitted under U.S. Government regulations.

The operation of the Double Star PEACE instruments is also slightly different because of the presence of only one sensor. In order to cover the same energy range as the combination of LEEA and HEEA on Cluster can provide, a Double Star PEACE sensor alternates between covering a LEEA-like, lower, energy range and a HEEA-like, higher, energy range from spin to spin. As such the full PEACE energy range is covered in two spins rather than one. While there is sometimes significant overlap between the LEEA- and HEEA-like energy ranges so electrons at intermediate energies are still measured every spin, the overlap is often not transmitted to the ground because of bandwidth constraints. The lower energy spins are still necessary even in comparatively hot plasma environments such as the tail plasma sheet because there is no means of directly measuring spacecraft potential on either of the Double Star spacecraft and no potential control system analogous to ASPOC

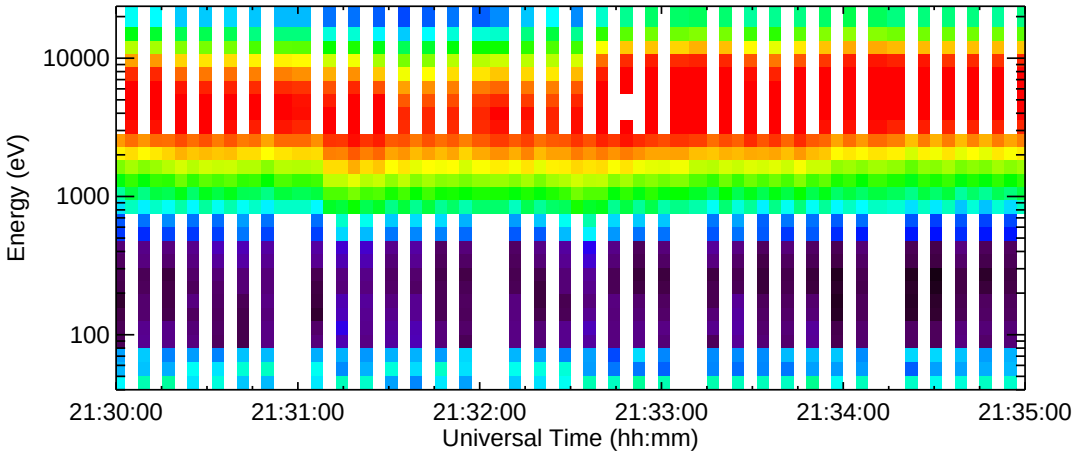

Figure 2.8: An example spectrogram from TC-1 PEACE illustrating the alternating energy ranges on successive spins. Note that the photoelectron population at lower energies is not covered by the high energy sweep.

on TC-2. The low energy sweeps can provide a means of estimating spacecraft potential through the measurement of photoelectrons. An example of data taken using alternating high and low energy spins is given in Figure 2.8.

Double Star PEACE data products are also somewhat different to those from Cluster PEACE. Through the use of JPEG data compression algorithms, and because of a higher telemetry allocation for PEACE, a full-resolution 3DF distribution can be sent from Double Star PEACE almost every spin. Similar housekeeping data to Cluster are also transmitted. Limited memory in the DPU means that no onboard moments or onboard selected pitch-angle distributions are produced; instead these products are generated on the ground.

2.3.2 Double Star FGM

Each of the Double Star Spacecraft also carries an FGM instrument (Carr *et al.*, 2005). Similarly to Cluster, each instrument is made up of two tri-axial fluxgate sensors, one of which is positioned on the end of the spacecraft's boom, which has a length of 3.1 m (the outboard sensor) and the other is positioned 0.5 m closer to the spacecraft body (the inboard sensor). Each instrument also includes a data

processing unit, which, like PEACE, has a different design from its Cluster equivalent because of export controls. Also like PEACE, additional shielding has been included in the design.

While there is no burst mode for the Double Star spacecraft, Double Star FGM can operate in one of two modes. The first mode is analogous to Cluster normal mode operations whereby ∼22 vectors per second are returned from the primary sensor (by default this is the outboard sensor) while ∼3 vectors per second are returned from the secondary sensor. The other operating mode is a so-called "gradiometer" mode in which both sensors are run at the same rate, returning approximately 12.5 vectors per second. This mode makes possible direct comparison of the output of the inboard and outboard sensors which allows for the characterisation of the spacecraft magnetic field. This is important because the TC-1 spacecraft's solar panels are wired in such a way that they generate time-varying, unpredictable magnetic fields. These fields are a serious problem and correction is only possible for spin-resolution data in routine processing, even with the gradiometer mode active by default. On TC-2, where contamination from the spacecraft field is much smaller, the first mode is active by default.

2.3.3 Double Star TC-1 HIA

Thermal ion measurements are provided on TC-1 by an HIA instrument (Rème *et al.*, 2005), the flight spare from Cluster. Similarly to PEACE and FGM, extra shielding has been installed on the instrument box and the instrument electronics have been relocated to within the HIA box (the Cluster CIS DPU electronics are located in the CODIF instrument box). Double Star HIA has solar wind and magnetospheric modes. In the magnetospheric modes data is taken from the high G side of the instrument and the specific data products that are telemetered are generated on board from the 62 energies and 88 solid angles that make up a complete 3D distribution. Typically a reduced resolution 3D distribution, a pitch angle distribution

and on-board calculated moments are returned every spin. Full details of TC-1 HIA modes and data products are listed in Tables 1-6 of Rème *et al.* (2005).

2.4 Supporting Space Missions

2.4.1 IMAGE

The Imager for Magnetopause to Aurora Global Exploration (IMAGE) was a NASA mission dedicated to imaging geospace (Gibson *et al.*, 2000). It was launched on 25 March 2000 from Vandenberg Air Force Base and remained operational until December 18th 2005 when contact with the spacecraft was lost. IMAGE was equipped with a comprehensive payload for imaging in Extreme and Far Ultraviolet wavelengths and the detection of Energetic Neutral Atoms and plasma waves. In this thesis we use auroral images from the WIC (Wideband Imaging Camera) instrument (Mende *et al.*, 2000b), which is part of the FUV suite (Mende *et al.*, 2000a). WIC is a camera sensitive to ultraviolet light in the wavelength range 140 nm to 190 nm. It has a field-of view large enough that the instrument can image the entire polar region of the Earth from the apogee of the IMAGE spacecraft's orbit ($\sim$8 R_E) and resolve auroral features as small as 1-2° in latitude. The camera is capable of taking up to 30 frames per second, which are then corrected for the effects of the satellite's rotation. 300 frames are then summed in memory to create one WIC image. Due to Telemetry constraints, and the small proportion of a spacecraft spin that the WIC camera is looking at the Earth, however, only one image per spacecraft spin ($\sim$2 minutes) is generally available. The time tag of each IMAGE is set to be the end of the two minute period during which it was taken, so any auroral features that develop become evident in a given image could have first appeared up to two minutes beforehand.

2.4.2 ACE

The Advanced Composition Explorer (ACE) spacecraft is a NASA mission dedicated to the study of the solar wind (Stone *et al.*, 1998). It was launched on August 25 1997 and operates at the L1 point. Since then it has become a vital resource for magnetospheric science, providing almost continuous data about the condition of the solar wind and IMF upstream of the Earth. This information is important in understanding how the magnetosphere reacts to changes in solar wind conditions. In this thesis data from the ACE magnetometer experiment (Smith *et al.*, 1998) are used for precisely this reason.

2.4.3 Geotail

The Geotail satellite, a cooperative project between NASA and JAXA, the Japanese space agency, was launched on July 24 1992 and at the time of writing remains operational. Geotail was designed to study the tail of the Earth's magnetosphere using a comprehensive set of in-situ instrumentation. For the first two years of the mission, the orbit was designed so that Geotail could study the distant magnetotail of the Earth, at distances of up to $210\,\mathrm{R_E}$. From 1995, Geotail's near-equatorial orbit has had a perigee of $\sim 10\,\mathrm{R_E}$ and apogee of $\sim 30\,\mathrm{R_E}$. Similarly to Cluster, in the reference frame of the magnetosphere, the apogee of Geotail's orbit moves throughout the year. During Cluster magnetotail seasons Geotail's apogee often lies in the solar wind, so the spacecraft can provide a useful monitor of the IMF close to the Earth, eliminating uncertainties that arise from time-lagging data taken by ACE at the L1 point to the magnetopause. It is in this context that data from Geotail's magnetic field instrument (Kokubun *et al.*, 1994) are used in this thesis.

2.5 Supporting Ground-Based Instruments

2.5.1 CARISMA

CARISMA, The Canadian Array for Realtime InvestigationS of Magnetic Activity (Mann *et al.*, 2008) is a network of 28 fluxgate magnetometer stations deployed throughout Canada and the northern USA. CARISMA is funded under the Canadian Space Agency's Canadian GeoSpace Monitoring (CGSM) program (13 stations) and by the Canadian Foundation for Innovation (15 stations) and is operated by the University of Alberta. CARISMA officially began operating in April 2005, before which the 13 CGSM stations were operated under the auspices of the CANOPUS program (Rostoker *et al.*, 1995). The locations of the CARISMA magnetometer stations, illustrated in Figure 2.9, provide coverage at auroral, sub- and super-auroral latitudes (and therefore at L-Shells from 4 to infinity) and span 3 hours in local time, allowing for the study of the spatial propagation of disturbances in the magnetic field.

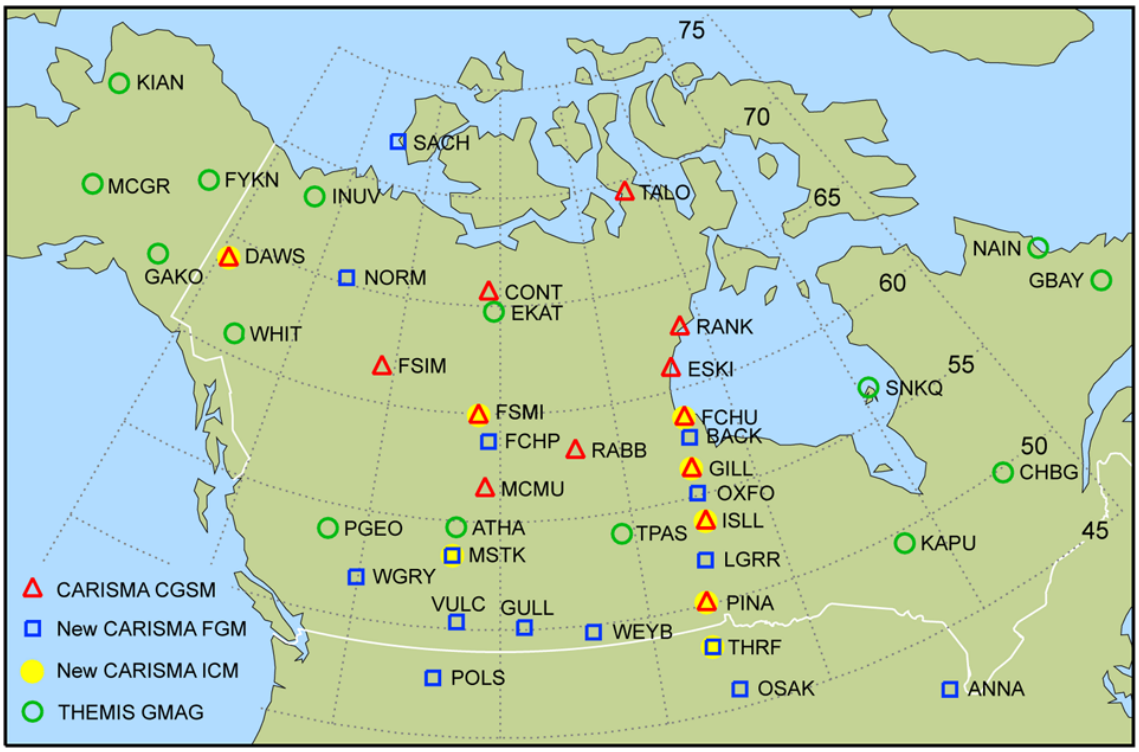

Figure 2.9: The locations of the various CARISMA magnetometer stations (Mann *et al.*, 2008, Figure 1).

In the CARISMA era, data is publicly available at a resolution of 1 vector per second, with up to 8 vectors per second available on request. By the end of 2009, eight of the CARISMA sites will also be equipped with induction coil magnetometers for the study of magnetic pulsations at higher frequencies than possible with the fluxgates. The line of magnetometer stations including PINA, ISLL, GILL, FCHU and RANK is known as the Churchill Line.

Ground-based magnetometers are useful in the study of substorms and the magnetotail because the geomagnetic field responds to currents flowing in the ionosphere, enhancements of which are often related to substorm and magnetotail activity. Pulsations in the magnetic field, like Pi1 and Pi2 pulsations, which are signatures of substorm onset, can also be detected by ground-based magnetometers.

2.5.2 SuperDARN

The Super Dual Auroral Radar Network, or SuperDARN (Greenwald *et al.*, 1995; Chisham *et al.*, 2007), is a network of coherent scatter radars with stations located in both the northern and southern polar regions. SuperDARN radars send radio pulses into the ionosphere which can scatter from ionospheric irregularities and are then subsequently received by the radar. Any motion of the features in the ionosphere from which the radio pulses scatter will alter the frequency of the return signal through the Doppler effect, so the radar measurements can be used to measure flow patterns in the ionosphere. Only motion along the line of sight of a radar, however, is detectable in this manner so radars are often deployed in pairs with overlapping fields of view, providing the true velocity vector when backscattered signals are received by both radars at the same time.

Through the combination of flow velocities from numerous radars over long periods of time, the statistical ionospheric convection pattern for various different IMF directions has been modelled (the map-potential technique) and can be used to provide average convection patterns or ionospheric potentials for given IMF conditions.

However only at positions where, and times when, this model is properly constrained by data from radars can it be considered representative of actual ionospheric conditions.

2.5.3 NORSTAR Riometers

Riometers (Relative Ionospheric Opacity METERS) are passive antennae that measure the absorption of radio waves in the ionosphere, more specifically they measure the opacity of the ionosphere to radio noise from extra-solar sources. The opacity of the ionosphere to radio waves is related to the ionospheric electron density, which increases during more geomagnetically active periods, like substorms, due to increased particle precipitation at these times. Riometers are sensitive to absorption caused by precipitating particles with energies above 30 keV, and as such are often used to study the injections of these particles that occur during substorms (e.g. Spanswick *et al.*, 2007). In this thesis data from the NORSTAR (formerly CANOPUS; Rostoker *et al.*, 1995) riometer network, located in Canada and sharing some observation sites with the CARISMA magnetometers, are used.

2.6 Minimum Variance Analysis

While not an instrument, Minimum Variance Analysis (MVA; Sonnerup and Cahill, 1967; Sonnerup and Scheible, 2000) is a useful analysis technique that will be employed throughout this thesis. MVA is often used with single spacecraft data to find the normal to a current layer or other boundary in space. It works by assuming that, in an ideal one-dimensional case, the component of magnetic field normal to the current layer is independent of distance from that current layer and that the field has no systematic time-variation on the timescale of the current layer crossing by a spacecraft. Under these ideal conditions, where $\boldsymbol{B}\cdot\hat{\boldsymbol{n}}$ is constant across the layer, 3 measured magnetic field vectors are required to determine the normal to the current

layer: one vector measured either side of the layer and one vector measured close to its centre. In real applications, many more vectors are used and the direction in which the magnetic field variance is minimised (the minimum variance direction) approximates the normal to the current layer.

The output of a minimum variance analysis, derived in Sonnerup and Scheible (2000), is a rotation matrix of which the eigenvectors are the unit vectors corresponding to the minimum, intermediate and maximum variance directions in the coordinate system of the original data and the eigenvalues represent the degree of variance in each of those three orthogonal directions. The separation of the eigenvalues is an indicator of how well defined the minimum variance direction is; if any two eigenvalues are close together the variance matrix is said to be degenerate. In the worst case where the eigenvalues are all approximately equal, or when the eigenvalues corresponding to the minimum and intermediate directions are approximately equal, no information about the direction of the normal to the boundary can be obtained, if the eigenvalues corresponding to the intermediate and maximum variance directions are similar, then the normal to the surface can still be determined, however no information regarding the components tangential to the surface can be obtained.

In this thesis MVA is used to determine the orientation of the magnetotail neutral sheet (Chapters 3 and 4) and to identify, and estimate the axis orientation of, magnetic flux ropes (Chapter 3). MVA in the context of magnetic flux ropes is discussed in Section 3.1.4.

Chapter 3

Magnetic Flux Ropes and Multiple X-Point Reconnection

> Give a thief rope enough, and he'll hang himself.
>
> *J. Ray, English Proverbs, 1670*

3.1 Introduction

In this chapter observations of three magnetic flux ropes are presented. The observations were made on 7 August 2004 by the Cluster and Double Star TC-1 spacecraft, at that time located in the tail of the Earth's magnetosphere. The first two flux rope signatures were observed, near-simultaneously, by Cluster and TC-1, which were located at (-16.3, -8.7, 0.10) R_E GSM and (-10.3, -7.11, 0.81) R_E GSM respectively, a separation of $6.3R_E$. A third signature was observed some four minutes later by two of the four Cluster spacecraft, while the other two spacecraft observed a feature resembling a Travelling Compression Region (TCR). These observations are interpreted as three individual flux ropes existing in the magnetotail, the first

Portions of this chapter have been published under the title "Near-Simultaneous Magnetotail Flux Rope Observations with Cluster and Double Star" (Walsh *et al.*, 2007).

two, at least, simultaneously. The formation mechanism of the flux ropes and the consequences of their presence for the structure of the magnetotail during this event are discussed in the context of multiple X-point reconnection.

3.1.1 Multiple X-Point Reconnection

The widely-invoked Near-Earth Neutral Line (NENL) model of substorms (e.g. Baker *et al.*, 1996), involves reconnection at a neutral point in the near-Earth tail. However this model does not emphasise the possibility of reconnection at more than one site in the tail, or so-called multiple X-point reconnection (MXR; Zwingmann, 1983). While there have been no direct observations of multiple X lines existing simultaneously in the Earth's magnetotail, evidence of Near-Earth (in the context of the NENL model) reconnection sites has been seen at locations in the tail between X=-9 R_E and X=-30 R_E (e.g. Sergeev *et al.*, 2008; Borg *et al.*, 2005; Nagai *et al.*, 1997). If multiple reconnection sites in the tail exist their reconnection rates will not necessarily be the same, because different conditions may exist local to each reconnection site (Schindler, 1974). All reconnection sites in the magnetotail must first reconnect closed plasma sheet field lines before reconnecting the open field lines of the tail lobes, so the site with the fastest rate of reconnection of plasma sheet field lines will begin to reconnect lobe flux first. The reconnection of open lobe field lines generates faster outflow jets than the reconnection of closed plasma sheet field lines so the outflow from the fastest, dominant, reconnection site will sweep the entire system of multiple X-lines, and the loops of magnetic flux in between them, earthward or tailward dependent on their location with respect to the dominant X-line because the rest of the system of X-Lines is enclosed within magnetic field lines reconnected by the dominant reconnection site. This idea is illustrated in Figure 3.1; Figure 3.1A shows the situation before any of the reconnection sites begin to dominate and Figure 3.1B the situation once a single X-line dominates and begins reconnecting lobe field lines.

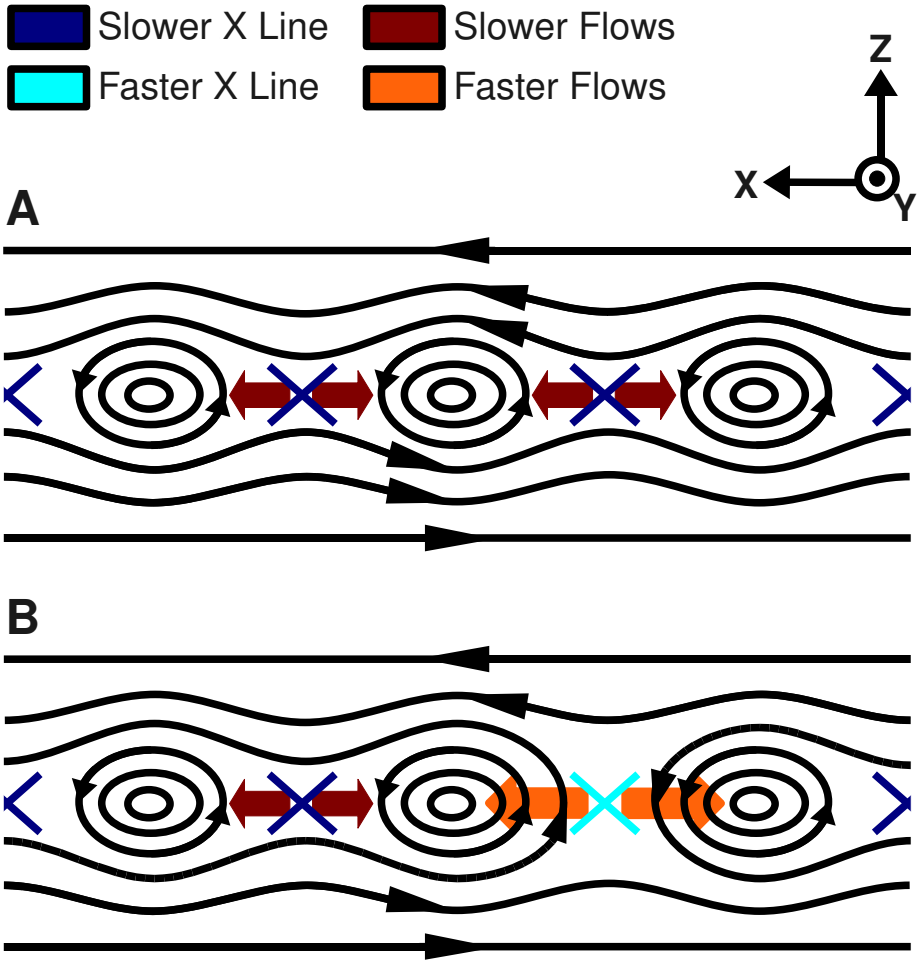

Figure 3.1: An 2-D sketch of a possible Multiple X-Point reconnection geometry in the magnetotail. In Panel A, reconnection sites have developed that are reconnecting closed plasma sheet field lines, forming loops of trapped magnetic flux in between them. In Panel B one of the X lines has begun reconnecting open, lobe field lines, generating fast jets that sweep the remaining X lines and loops of magnetic flux earthward or tailward.

3.1.2 Magnetic Flux Ropes

If there is a cross-tail component of the magnetic field present in the magnetotail, the reconnected flux that lies between the multiple X-lines is expected to form helical structures of magnetic flux, or magnetic flux ropes (Hughes and Sibeck, 1987; Ogino *et al.*, 1990) with their ends connected to either the IMF or the Earth's ionosphere. The simplest model of the flux rope is known as the force-free flux rope (e.g. Lepping *et al.*, 1990), which is the minimum energy configuration for helical magnetic fields. The force-free model is so-called because there is no net force acting on the magnetic structure. Any force arising from the electric currents flowing through the flux rope ($\boldsymbol{j}\times\boldsymbol{B}$) will be balanced by the magnetic pressure exerted by the stronger magnetic field found in the centre of the flux rope. One popular mathematical solution of the force-free flux rope is the so-called "constant alpha" model (e.g. Lepping *et al.*, 1990) where the currents are proportional to the magnetic field, related by a constant of proportionality, α. The structure of the ideal force-free flux rope is cylindrical with an azimuthal magnetic field at the edge of the rope which becomes increasingly directed along the axis of the rope toward its centre. The geometry of a force-free flux rope is illustrated in Figure 3.2 (left hand side), along with the magnetic field variations that a pair of notional spacecraft would observe if they passed through the flux rope on two different trajectories (right hand side). The magnetic fluctuations are presented in a Cartesian coordinate system defined such that the axial field of the flux rope (marked as B_A on Figure 3.2) points along the Y axis. The azimuthal component of the field (marked as B_T on Figure 3.2) therefore lies in the X-Z plane. In the simplest case in the magnetotail this coordinate system is assumed to align with the GSM coordinate system. The field fluctuations will be described in that context below. Departures from the force free state can be caused by a flux rope's interaction with its surroundings (Slavin *et al.*, 2003b,a) or if it had a particularly strong core field (Xiao *et al.*, 2004; Henderson *et al.*, 2006a).

The spacecraft trajectory and associated field signatures marked in red on Figure 3.2 represent a spacecraft passing from the earthward edge of a GSM-aligned force-

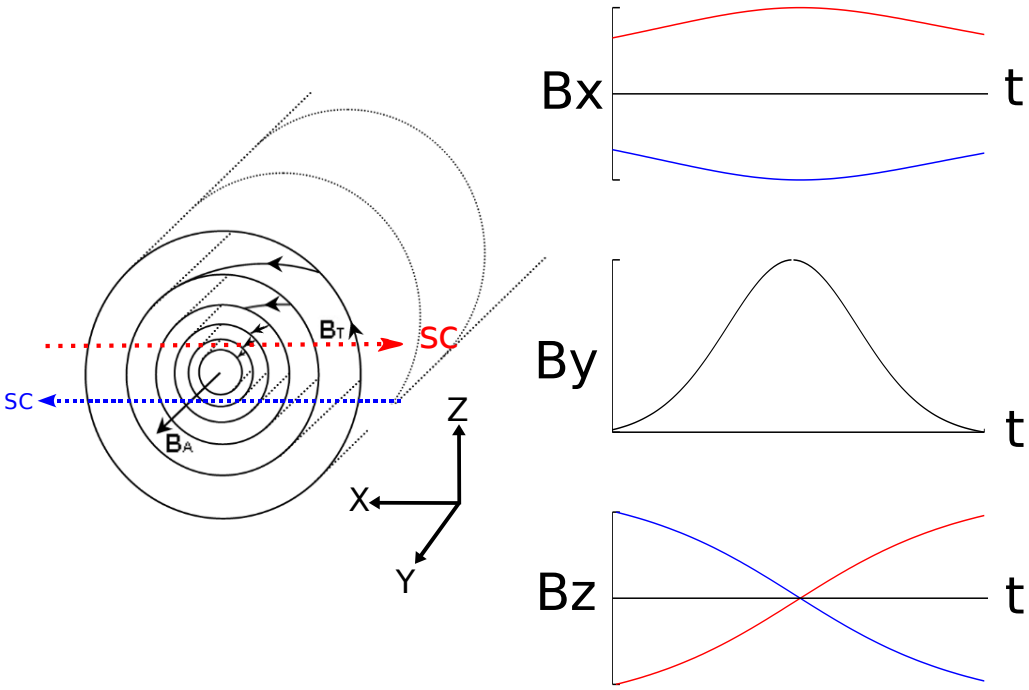

Figure 3.2: Illustration of the geometry of a force-free flux rope and the observational signatures expected when a spacecraft passes through the flux rope on two different trajectories. In the context of the magnetotail, The flux rope is assumed to be aligned with GSM such that its axial field lies along the GSM Y direction. The red dashed line represents a spacecraft passing from the earthward edge of the flux rope to the tailward, north of the rope's centre and the blue dashed line from the tailward to the earthward, south of the rope's centre. Traces of the corresponding colours represent the magnetic signature a spacecraft would see on following that trajectory through the flux rope. The axial field, plotted in black, would look the same for both trajectories (Figure adapted from Henderson *et al.*, 2006a, Figure 1).

free flux rope to the tailward edge (i.e. an earthward moving flux rope) north of the flux rope's centre line. The blue trajectory and field signatures represent a spacecraft passing from the tailward edge to the earthward (i.e. a tailward moving flux rope) south of the flux rope's centre line. In both cases the signature of the axial field (B_Y on Figure 3.2) seen by a spacecraft will be the same - a unipolar increase in the field with a maximum at the point of closest approach to the flux rope centre. The signature of the tangential field will vary depending on the spacecraft trajectory. In the B_X component, a spacecraft will observe a unipolar signature in B_X; positive if the spacecraft passes north of the rope centre (the red trajectory on Figure 3.2), negative if the spacecraft passes south of the rope centre (the blue trajectory on Figure 3.2). In the B_Z component, the spacecraft will observe a bipolar signature, negative-positive (south-north, red) for an earthward moving flux rope and positive-negative (north-south, blue) for a tailward moving flux rope. In both cases the bipolar signature will pass through zero as the spacecraft passes above or below the centre of the flux rope (i.e. where $|B_X|$ maximises). A further signature of force-free flux ropes in the magnetotail is the detection of a transient peak in the magnetic field magnitude as the flux rope passes the spacecraft, largest when the spacecraft is at its point of closest approach to the flux rope axis.

Flux ropes have also been observed in the Venusian ionosphere (e.g. Russell and Elphic, 1979) and in the solar wind, where Interplanetary Coronal Mass Ejections containing flux ropes are known as magnetic clouds (e.g. Bothmer and Schwenn, 1994).

3.1.3 Travelling Compression Regions

The passage of flux ropes and plasmoids through the magnetotail plasma sheet is thought to create a bulge in the plasma sheet, compressing the overlying magnetic field in the PSBL and tail lobes (Slavin *et al.*, 1984; Slavin *et al.*, 2005). This compression of the magnetic field, known as a travelling compression region (TCR)

would move with the flux rope or plasmoid and manifests as a transient increase in $|B|$ accompanied by a bipolar signature in B_Z and a unipolar signature in B_X in spacecraft magnetic field data, again assuming flux rope or plasmoid alignment with GSM. Depending on the position of the spacecraft relative to the lobe/PSBL interface, the passage of a TCR might have the effect of pushing a spacecraft from the lobe into the PSBL, resulting in an increase in the fluxes of particles detected by that spacecraft at the same time as the magnetic signature (Owen and Slavin, 1992; Owen *et al.*, 2005).

3.1.4 Methods of Determining Flux Rope Orientation

We have presented a simple case in which flux ropes in the magnetotail are assumed to be perfectly aligned with a magnetospheric coordinate system such as GSM, in reality this is not always true. In order to study the properties of flux ropes and their effect on the magnetotail as a whole (and indeed to identify them in the first place) it is often helpful to determine the orientation of the flux rope axis with respect to the magnetotail and to derive a natural coordinate system for the flux rope, such as that described in subsection 3.1.2.

There are several methods of determining flux rope axis orientation. A visual inspection of the magnetic field components is sometimes used to estimate the axis orientation of ICME flux ropes in the solar wind (e.g. Klein and Burlaga, 1982), however this method is subjective and is not suitable when comparing flux ropes with similar orientations such as those observed in the magnetotail. Henderson *et al.* (2006a) used Cluster 4-spacecraft timing techniques (a method later formalised by Zhou *et al.*, 2006) to determine the axis orientation of flux ropes in the tail of the Earth's magnetosphere. This method involves determining the normal to the flux rope surface which is assumed planar on the scale of the Cluster tetrahedron both at the tetrahedron's entry to and exit from the flux rope. The cross product of these two vectors, then, gives the flux rope axis orientation. This method, however,

is only applicable when the scale of the Cluster tetrahedron is small relative to the radius of curvature of the flux rope surface. For typical flux rope diameters of $\sim \mathrm{R_E}$, this was generally only true during the 2003 tail season, when the tetrahedron had a separation of 100 km and as such this method cannot be used here. More recently Zhang *et al.* (2007) used Grad-Shafranov techniques to reconstruct the magnetic structure of a magnetotail flux rope using multi-spacecraft Cluster data.

Minimum Variance Analysis (MVA, Sonnerup and Cahill, 1967; Sonnerup and Scheible, 2000) is also widely used in determining flux rope axis orientation (e.g. Xiao *et al.*, 2004; Steed *et al.*, 2008). In the case of a force-free flux rope, the bipolar signature is found in the component of $\boldsymbol{B}$ in the maximum variance direction, B_{MAX} (B_Z on Figure 3.2) and the axial field in the intermediate variance direction, B_{INT} (B_Y on Figure 3.2). The minimum variance direction (B_{MIN}), then, represents the spacecraft trajectory through the flux rope (Xiao *et al.*, 2004). Note that any departure from the force-free state will affect the results of the MVA. So-called "strong core field" flux ropes, for example, will show the bipolar signature in the intermediate variance direction and the axial field in the maximum variance direction (Xiao *et al.*, 2004). Furthermore the accuracy of flux rope MVA is affected by the impact parameter, i.e. how close the spacecraft passes to the axis of the flux rope. At larger distances from the flux rope axis, MVA accuracy decreases (Beyene *et al.,* 2009[1]).

Another useful method of determining the orientation of a flux rope's axis is the fitting of a mathematical flux rope model to the data returned by a spacecraft (e.g. Lepping *et al.*, 1990; Khurana *et al.*, 1995; Mulligan and Russell, 2001). This method, assuming an appropriate model is chosen, can not only provide the orientation of the flux rope axis with respect to the rest of the magnetosphere, but also other parameters such as the diameter of the flux rope and total magnetic flux contained within the structure.

In this chapter, minimum variance analysis is used to confirm the identity of

[1]Manuscript in Preparation

suspected flux ropes in the Cluster and TC-1 FGM data, while the flux rope model of Mulligan and Russell (2001) is used to determine the orientations and other characteristics of the flux ropes.

3.1.5 Previous Magnetotail Flux Rope Observations

Flux ropes, similar to those described by a force-free model, have been observed by Geotail, moving both Earthward, embedded in bursty bulk flows, and tailward, as so-called plasmoid type flux ropes (Slavin *et al.*, 2003a). Earthward moving flux ropes have also been observed by Cluster (e.g. Slavin *et al.*, 2003b; Henderson *et al.*, 2006a), which implies that multiple X-lines may exist in the tail within 20 R_E of the Earth. Observational evidence of flux ropes, however, is often based on measurements taken either by a single spacecraft or at a single location in the tail (e.g. Eastwood *et al.*, 2005; Zhang *et al.*, 2007). Observations of structures related to MXR, for example flux ropes, existing simultaneously at different locations in the tail would provide valuable experimental evidence for the theory. In this chapter we present unusual observations from the Cluster and Double Star TC-1 spacecraft of two flux ropes that we interpret as existing simultaneously in the tail, separated by approximately 6R_E, and a third flux rope observed by Cluster some 4 minutes later. To the best of our knowledge, these are the first such observations.

3.2 Observations

3.2.1 Event Context

Between 7 August 2004, 19:00 UT and midnight UT, the Auroral Electrojet (AE) index (Davis and Sugiura, 1966), plotted in Figure 3.3, shows four small enhancements, each lasting ∼1 hour, indicating increased magnetospheric convection, starting at ∼ 18:50 UT, ∼ 20:05 UT, ∼ 21:20 UT and ∼ 23:00 UT. We will concentrate on the

fourth AE enhancement in this period (marked by the dashed line on Figure 3.3), thought by Nakamura *et al.* (2005b) to be related to a substorm with an onset at 23:00 UT.

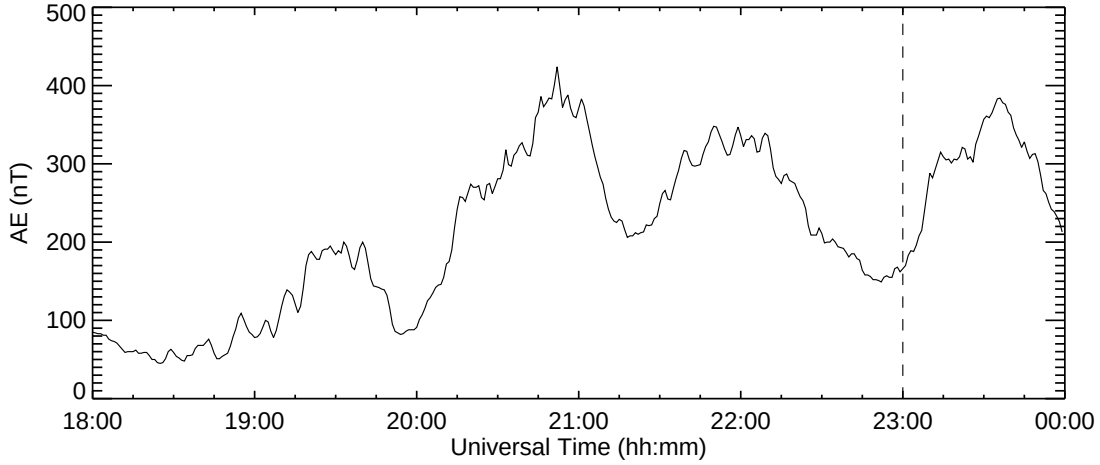

Figure 3.3: The AE index from 18:00-24:00 UT on 7 August 2004. The dashed line at 23:00 UT marks the beginning of the AE enhancement of interest.

Southern hemisphere auroral images that were taken by the FUV-WIC (Mende *et al.*, 2000b) instrument onboard the IMAGE spacecraft are plotted in Figure 3.4. These reveal two bright spots in the aurora at 23:00 UT, separated by $< 5°$ magnetic latitude and 2 hours MLT (Figure 3.4, top right image), while, according to the list of Frey and Mende (2006) onset of an auroral substorm occurred at 23:09 UT (Figure 3.4, middle bottom image). The poleward expansion of the auroral oval and the westward-travelling surge associated with the development of the substorm can be seen in the image taken at 23:17 UT (Figure 3.4, bottom right). It should be noted here that during this interval the attitude of the IMAGE satellite, and therefore the pointing of the WIC instrument is not precisely known. Thus the absolute positions of any auroral features seen on the images are not reliably known.

During this interval the four Cluster spacecraft (henceforth referred to as C1, C2, C3 and C4), were located at GSM (-16.3, -8.7, 0.1) R_E, configured in an approximately equilateral tetrahedron of side ∼1,000 km. Double Star TC-1 was located at GSM (-10.3, -7.1, 0.8) R_E, a separation of 6.3 R_E from Cluster (GSM coordinates will be used throughout this chapter, unless otherwise specified). At this time the Geotail

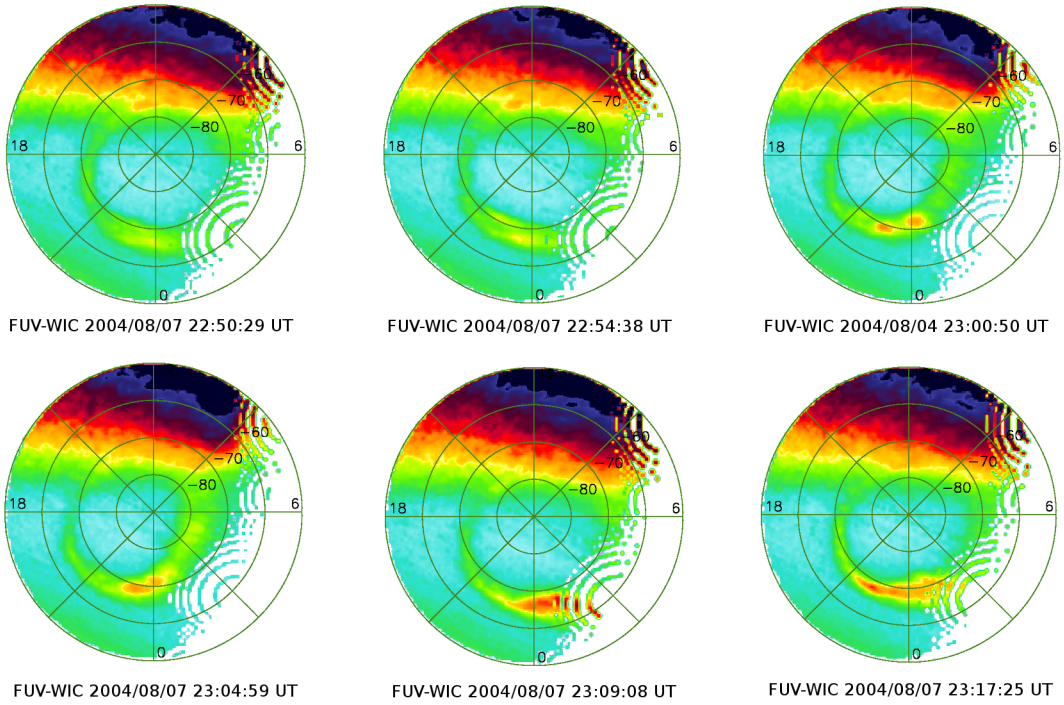

Figure 3.4: Auroral images taken by the FUV-WIC instrument onboard the IMAGE spacecraft. Note the substorm onset that occurred at 23:09 UT (Middle bottom panel)

spacecraft was located at (17.2, 6.0, 3.9) R_E, upstream of the Earth, providing a solar wind monitor. Figure 3.5, Panels A-C and Panels D-F show the spacecraft locations at 23:00 UT and configuration of the Cluster tetrahedron at 23:00 UT respectively. The IMF seen by Geotail (Figure 3.5, Panels G-K) was directed predominantly southward from 21:00-22:00 UT, turning northward at 22:00 UT and remaining that way until the end of the interval. The IMF was, however, dominated by a positive B_Y until 22:45 UT at which point a change in B_Z caused the clock angle to rotate from ∼80°to ∼40°. At 23:20 UT the clock angle returned to ∼80°. The presence of a B_Y-dominated IMF might have caused a twisting of the tail along its axis (e.g. Cowley, 1981).

3.2.2 Event Overview

In Figure 3.6 data from Cluster and TC-1 are presented, providing an overview of the interval of interest (22:50 UT - 23:50 UT). Panel A shows the magnitude of

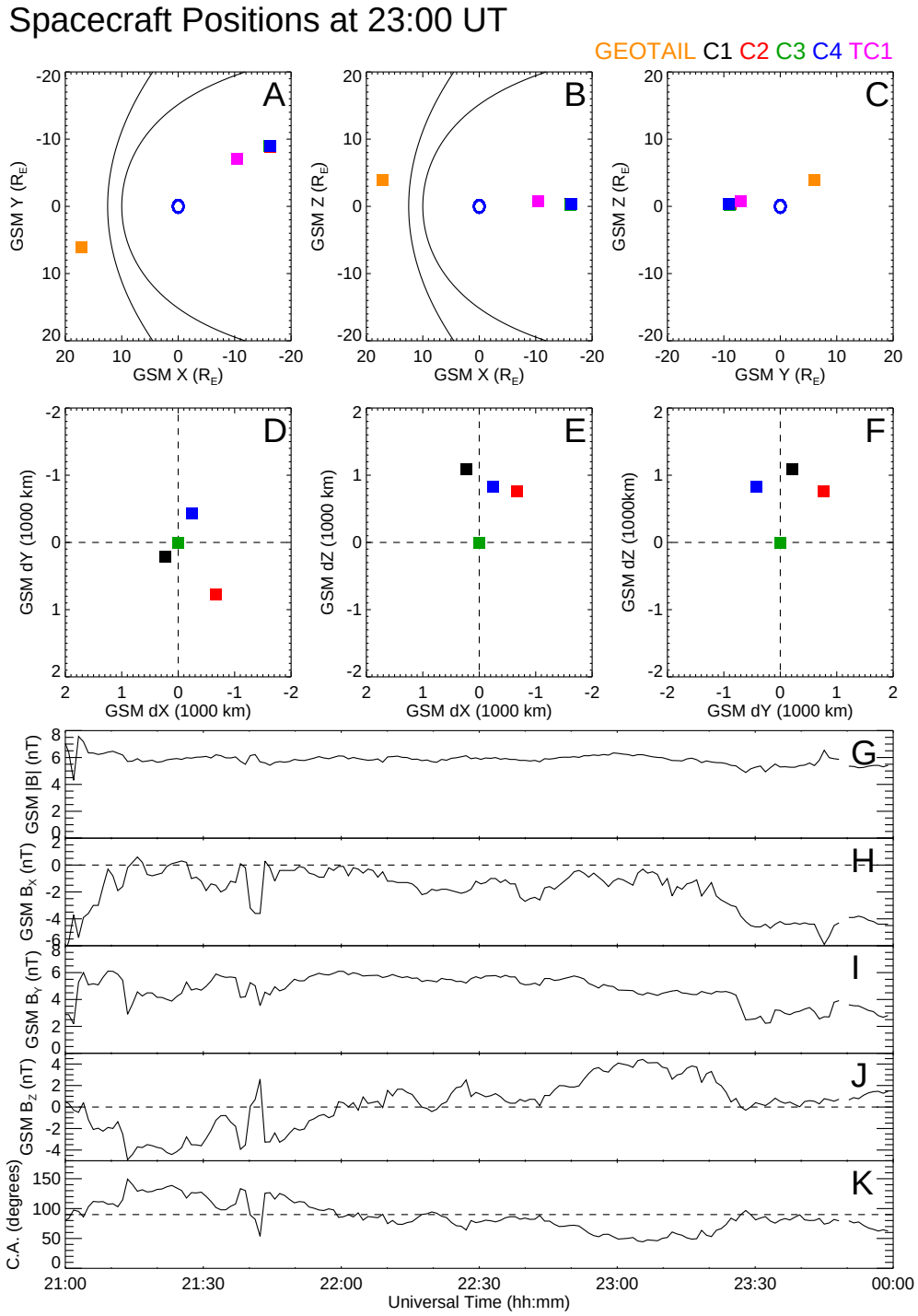

Figure 3.5: GSM spacecraft positions at 23:00 UT (Panels A-C); the configuration of the Cluster tetrahedron in GSM coordinates (Panels D-F) and the condition of the IMF as measured by Geotail (Panels G-K). In the top six panels, black, red, green and blue represent C1, C2, C3 and C4 respectively, magenta represents TC-1 and orange Geotail. A model magnetopause (Shue *et al.*, 1997) and bow shock (Farris and Russell, 1994) are plotted in Panels A and B.

the magnetic field as measured by the FGM instruments onboard the four Cluster spacecraft (Balogh *et al.*, 2001) and TC-1 (Carr *et al.*, 2005). Panels B-D show the three GSM components of magnetic field for the five spacecraft while Panel E shows the partial plasma-β (i.e. the ratio between the plasma pressure from a subset of the particles and the magnetic pressure) from C1 (protons) and TC-1 (ions). Panel F shows the X component of velocity perpendicular to the magnetic field projected onto GSM axes ($v_{\perp X}$) from CIS-CODIF (protons) (Rème *et al.*, 2001) for C1 and C4 and HIA (ions) (Rème *et al.*, 2005) for TC-1 (the TC-1 velocity has been multiplied by 2 for clarity). This quantity is a proxy for magnetic flux transport. Panel G is a PEACE (Johnstone *et al.*, 1997) energy-time spectrogram plotting omnidirectional electron differential energy flux from C1 and Panel H the equivalent PEACE (Fazakerley *et al.*, 2005) spectrogram from TC-1.

At 22:50 UT Cluster observed a plasma sheet-like electron population (Figure 3.6, Panel G) $\beta \sim 5$ (Figure 3.6, Panel E) and a $B_X \sim$ -10 nT (Figure 3.6, Panel B), indicating the tetrahedron was located in the central plasma sheet south of the neutral sheet. A short-lived weakening of B_X to $\sim$ -2 nT at 22:58 UT, accompanied by an increase in the plasma β to ~ 10 indicates that the spacecraft moved closer to the neutral sheet but did not cross it. A neutral sheet crossing occurred at 23:02 UT, indicated by a change of sign in B_X from negative to positive, again accompanied by an increase in β to ~ 10. At 22:50 UT, $\boldsymbol{v}_\perp$was close to zero. Between 22:58 UT and 23:03 UT however, at the time of the neutral sheet encounter and crossing $v_{\perp X}$ strengthened, reaching a value of approximately -300 km s^{-1} (Figure 3.6, Panel F). This tailward-directed fast flow may indicate the presence of an active reconnection X-line Earthward of Cluster.

Shortly after the neutral sheet crossing at 23:02 UT, the Cluster spacecraft encountered the neutral sheet again. In the period 23:04-23:10 UT C1 and C4 remained predominantly north of the neutral sheet, C3 predominantly south of the neutral sheet while C2 crossed it three times. This indicates that the current sheet was thinner than, or as thin as, the greatest separation of the Cluster spacecraft.

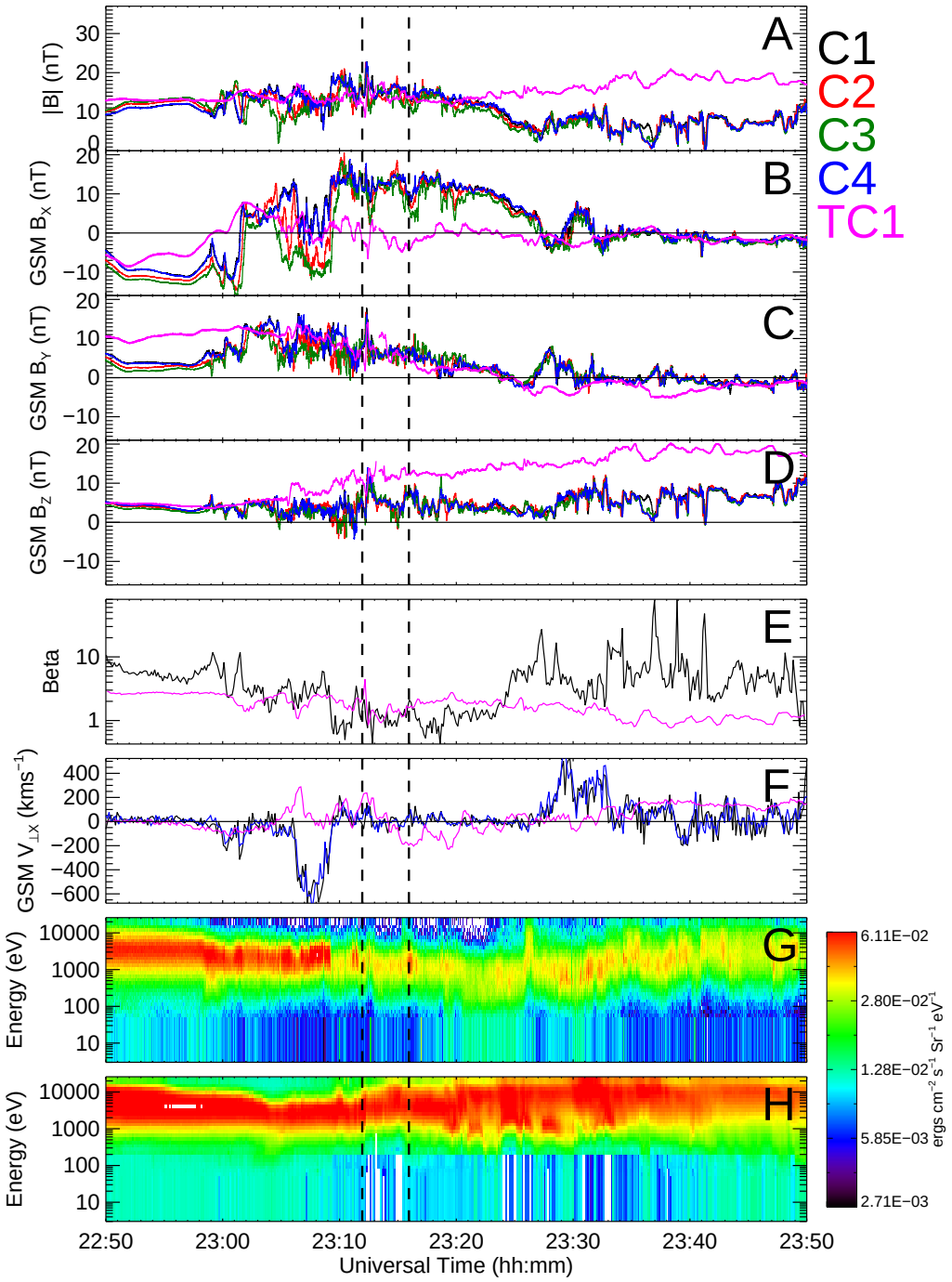

Figure 3.6: Overview of the event. Panels A, B, C and D show the magnitude and GSM X, Y and Z components of the magnetic field respectively for all four Cluster spacecraft (C1 - black, C2 - red, C3 - green, C4 - blue) and TC-1 (magenta), as measured by the FGM instruments. Panel E is the partial plasma beta for C1 (black) and TC-1 (magenta), calculated from CIS-CODIF and HIA respectively, and FGM. Panel F shows GSM $v_{\perp X}$, the velocity of magnetic flux transport, as measured by CIS-CODIF (C1, black and C4, blue) and HIA (TC-1, magenta). The TC-1 velocity is multiplied by 2 for clarity. Panel G is a PEACE electron spectrogram from Cluster 1, Panel H the equivalent spectrogram from Double Star TC-1. The two vertical dashed lines mark the times of spacecraft encounters with Signatures 1 & 2, and Signature 3, respectively.

From 23:06 UT to 23:09 UT a stronger tailward fast flow was also measured ($v_{\perp X}$∼-700 km s^{-1}) and enhanced electron fluxes of energy ∼3 keV were seen. At 23:09 UT all four spacecraft exited the thin current sheet region, moving north of the neutral sheet. The plasma β dropped below 1 at this point, and remained close to 1 until ∼ 23:25 UT, placing the spacecraft closer to the Plasma Sheet Boundary Layer (PSBL) during this period. Between 23:27 UT and 23:33 UT, the tetrahedron crossed the neutral sheet again, measuring a plasma with a high β. An Earthward-directed fast flow of ∼400 km s^{-1} was also detected, now suggesting an active X-line tailward of Cluster.

We will focus on a period beginning at 23:12 UT, when the Cluster spacecraft briefly returned to the central plasma sheet (B_X small) and a short Earthward flow of $v_{\perp X}$∼200 km s^{-1} was detected, together with a south-north bipolar signature in B_Z and a peak in B_Y (Signature 1). A smaller south-north bipolar signature was seen by Cluster at 23:16 UT (Signature 3), accompanied by Earthward flows of ∼ 120 km s^{-1}. At both times enhanced electron fluxes of energy ∼3 keV were seen.

At 22:50 UT TC-1, like Cluster, was located south of the tail neutral sheet in the plasma sheet. At 22:59 UT, the spacecraft crossed the neutral sheet and remained in the northern plasma sheet until 23:05 UT, after which it crossed the neutral sheet several times before 23:21 UT and then remained predominantly south of the neutral sheet until the end of the interval. Given that the plasma β remained ∼ 2 after the initial neutral sheet crossing it can be inferred that TC-1 was located in the central plasma sheet throughout the interval. The presence of plasma sheet-like electrons in the PEACE spectrogram confirms this. HIA observed Earthward-directed flows of $v_{\perp X}$∼150 km s^{-1} from 23:04 UT to 23:08 UT and 23:10 UT to 23:14 UT at which time a flow reversal occurred and $v_{\perp X}$ changed to ∼-120 km s^{-1}. These flows lasted until 23:21 UT. A south-north bipolar signature in B_Z (Signature 2) was observed at ∼ 23:12 UT. Between 23:05 UT and 23:35 UT B_Z increased steadily from 5 nT to 19 nT, the magnetic field near TC-1 becoming increasingly dipolar in character, consistent with reconnection occurring in the tail throughout this interval. However between

23:05 UT and 23:25 UT the B_Y component decreased by a similar amount, although the magnitude of the magnetic field remained approximately the same. This is consistent with a rotation of the magnetotail about its axis, and may be related to the IMF clock angle rotations observed by Geotail. These Cluster and TC-1 data, have been interpreted by Nakamura *et al.* (2005b) in their study of dipolarisations during this event as indicating the presence of a "source of disturbance" (which we have interpreted as at least one reconnection X-line) located between TC-1 and the Cluster tetrahedron.

3.2.3 Flux Rope Observations

The south-north bipolar signatures observed in B_Z by Cluster and TC-1 at 23:12 UT (Signatures 1 and 2, respectively) were accompanied by peaks seen in B_Y and $|\boldsymbol{B}|$. While bipolar signatures in the magnetic field can be caused by numerous phenomena, we argue that the B_Y signature is best explained as the observation of a well-formed flux rope core field in these events, and that these signatures can be interpreted as an Earthward moving flux rope passing over the spacecraft. This is supported by the observed direction of $\boldsymbol{v}_\perp$ at both Cluster and TC-1, and the results of 4-spacecraft timing on the peak in B_Y by Cluster, which determined the propagation velocity of Signature 1 across the tetrahedron to be $146\,\mathrm{km\,s^{-1}}$ in an Earthward direction, comparable to the measured ion flow velocity, $\boldsymbol{v}_\perp$. It should be noted, however, that the earthward direction of motion determined by the 4 spacecraft timing does not rule out explanations other than an Earthward-moving flux rope, for example a possible signature of 3D reconnection (Shirataka *et al.*, 2006).

The flux rope signatures and exact times of the encounters at C1 and TC-1 are shown in Figure 3.7. The time of a flux rope encounter is defined here as the time at which the local maximum in $|\boldsymbol{B}|$ is seen by a spacecraft. The four Cluster spacecraft each encountered the flux rope between 23:12:14 UT (SC3) and 23:12:21 UT (SC4) and TC-1 encountered a flux rope at 23:12:28 UT. The signature seen by Cluster

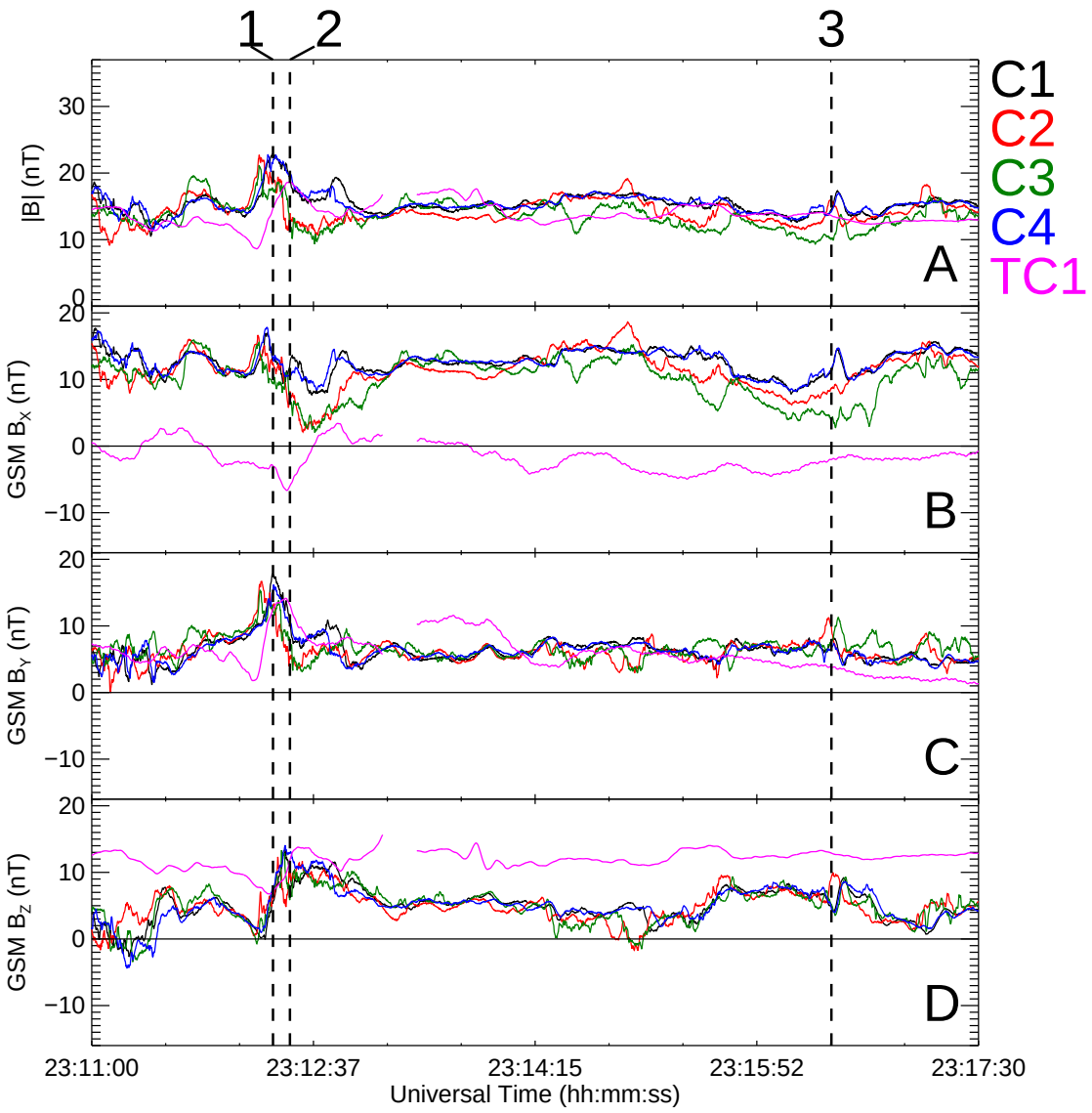

Figure 3.7: Flux rope signatures for all four Cluster spacecraft (Signatures 1 and 3) and TC-1 (Signature 2). Panel A shows the magnitude of the magnetic field and Panels B-D the three GSM components. Dashed lines labelled 1, 2 and 3 mark the flux rope signatures. Trace colours are as for Figure 3.6, Panel A.

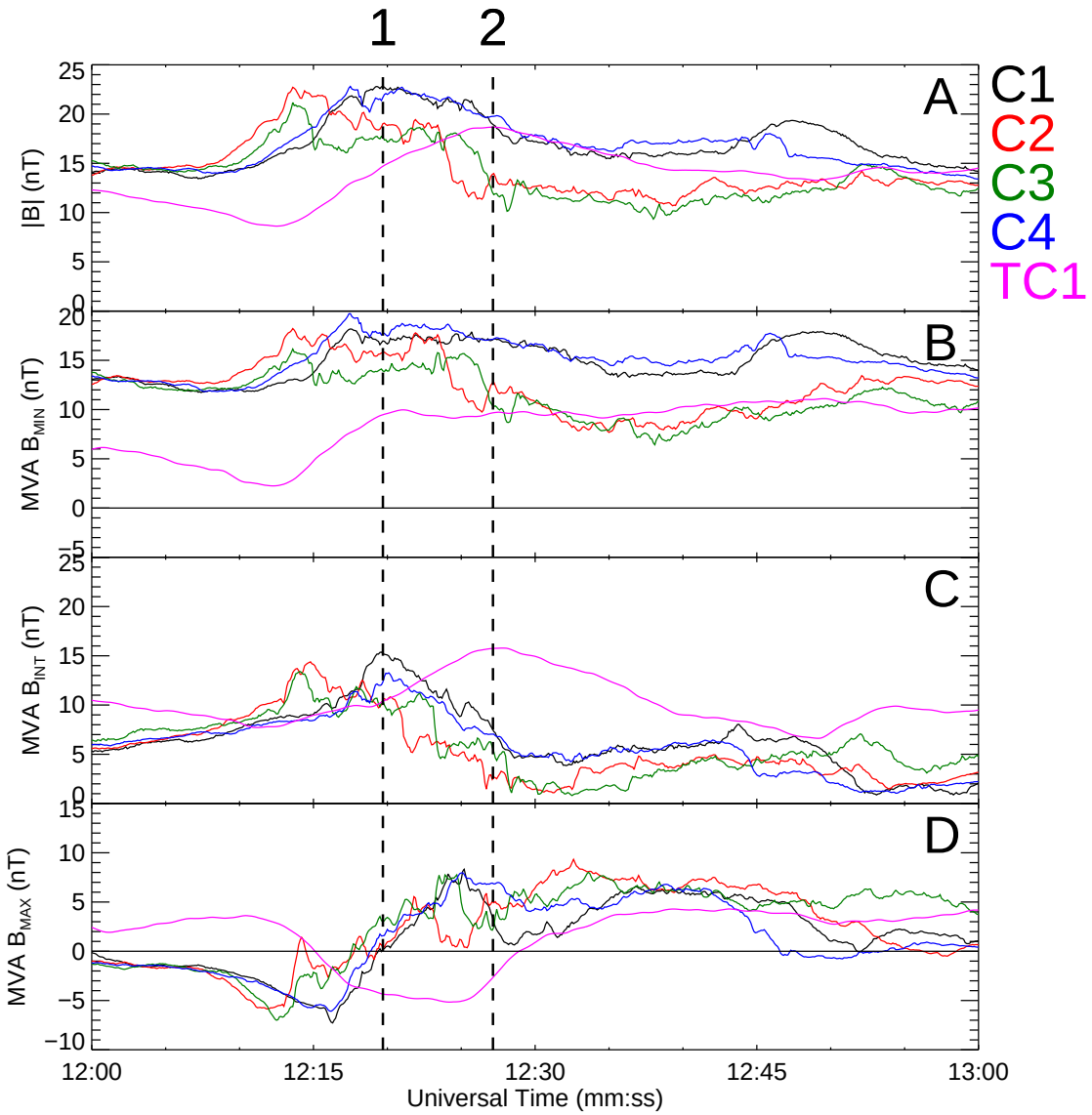

Figure 3.8: Flux rope Signatures 1 and 2 in a minimum variance coordinate frame. Panel A shows the magnitude of the magnetic field and Panels B-D show the minimum, intermediate and maximum variance components of magnetic field respectively. Cluster data are plotted in the minimum variance frame determined from C2's encounter with Signature 3, while the TC-1 data are plotted in the minimum variance frame determined from TC-1's encounter with Signature 2. Trace colours are the same as Figure 3.6, Panel A.

at 23:16:24 UT (Signature 3) was not the same over all four spacecraft. C2 and C3 saw a bipolar signature in GSM B_Z, and peaks in B_Y and $|\boldsymbol{B}|$, whereas C1 and C4 observed a bipolar signature in B_Z and peaks in B_X and $|\boldsymbol{B}|$. The observed signatures are consistent with the passage of an Earthward-moving flux rope for C2 and C3, and an Earthward-moving TCR (Slavin *et al.*, 2005) for C1 and C4.

Note that bipolar signatures observed in the GSM coordinate frame (Figure 3.7, Panel D) need not pass through $B_Z = 0$ to represent a flux rope. As described above, flux ropes are not necessarily perfectly aligned with a GSM axis. A coordinate frame closer to the natural frame of the flux rope will reveal a true bipolar signature in one of its components. Figure 3.8 shows flux rope signatures 1 and 2 and Figure 3.9 shows flux rope signature 3 in such a coordinate system, as determined by MVA (Sonnerup and Scheible, 2000). The minimum variance frame chosen for Signatures 1 and 3 is based on C2's encounter with Signature 3 while the minimum variance frame chosen for Signature 2 is based on TC-1's encounter with that structure. The eigenvalues and rotation matrix from GSM for the Cluster MVA frame are

$$\begin{array}{c} 0.0444 \\ 1.42 \\ 5.04 \end{array} \begin{pmatrix} 0.977 & -0.006 & -0.213 \\ -0.151 & -0.724 & -0.674 \\ -0.150 & 0.690 & -0.708 \end{pmatrix}$$

and the eigenvalues and rotation matrix from GSM for the TC-1 MVA frame are

$$\begin{array}{c} 0.0475 \\ 2.78 \\ 11.5 \end{array} \begin{pmatrix} 0.617 & -0.709 & 0.340 \\ 0.696 & -0.292 & -0.656 \\ -0.366 & 0.642 & -0.674 \end{pmatrix}$$

The separation of the minimum, intermediate and maximum eigenvalues is an indicator of how well defined each variance direction is. In both of these cases, that the ratio between the minimum and maximum variance eigenvalues is in excess of two orders of magnitude and that the maximum variance eigenvalue is a factor of $\sim$4 greater than the intermediate indicates that the variance directions are well defined and that the MVA is likely to be accurate.

In the ideal case, for a force-free flux rope, the bipolar signature is usually found in the maximum variance component (the bottom row of the matrices) and the core field in the intermediate component (the middle row of the matrices) (Xiao

et al., 2004). B_{MAX} is plotted in Figures 3.8 and 3.9, Panels D and, in the case of Signatures 1 and 2 (Figure 3.8) a bipolar signature is evident in B_{MAX} for all four Cluster spacecraft and TC-1 respectively. For Signature 3, in the minimum variance frame used here C2 and C3 data show a bipolar signature in B_{MAX} (Figure 3.9, Panel D) while C1 and C4 data do not include a bipolar signature per se, but rather a decrease then increase in B_{MAX} that does not cross B_{MAX}=0, further evidence that C1 and C4 did not sample the signature 3 flux rope whereas C2 and C3 did.

The flux rope signatures are all of short duration (between 9 and 20 seconds), therefore high-time resolution magnetic field data are required for accurate determination of the flux rope axis. Cluster FGM has more than sufficient time resolution, however because of contamination from the spacecraft magnetic field, only spin (4 second) resolution FGM data are normally available for TC-1. So that there were a high enough number of data points for effective MVA (i.e. so that aliasing in the magnetic field data did not introduce inaccuracies), a 4-second sliding window average was applied to the raw TC-1 magnetic field data, removing any high frequency components, including much of the contamination. A constant offset was then removed from the spin-axis component such that the new, higher resolution data matched the spin-resolution data (see Section 2.2.3 for an explanation of this "B_Z" problem).

3.2.4 Ion Beam Observations

Figure 3.10 shows the magnitude (Panel A) and three GSM components (Panels B-D) of magnetic field from all four Cluster spacecraft and ion pitch angle-time spectrograms from the CIS-HIA instruments onboard C1 and C3 (Panels E and F, respectively). Data covering the entire energy range of the HIA instrument are plotted in the spectrograms. Signatures 1 and 3 are marked here with dashed lines. Earthward-directed, field-aligned ion beams were observed just after the encounter with Signature 1, and before and after Signature 3. These ion beams were detected

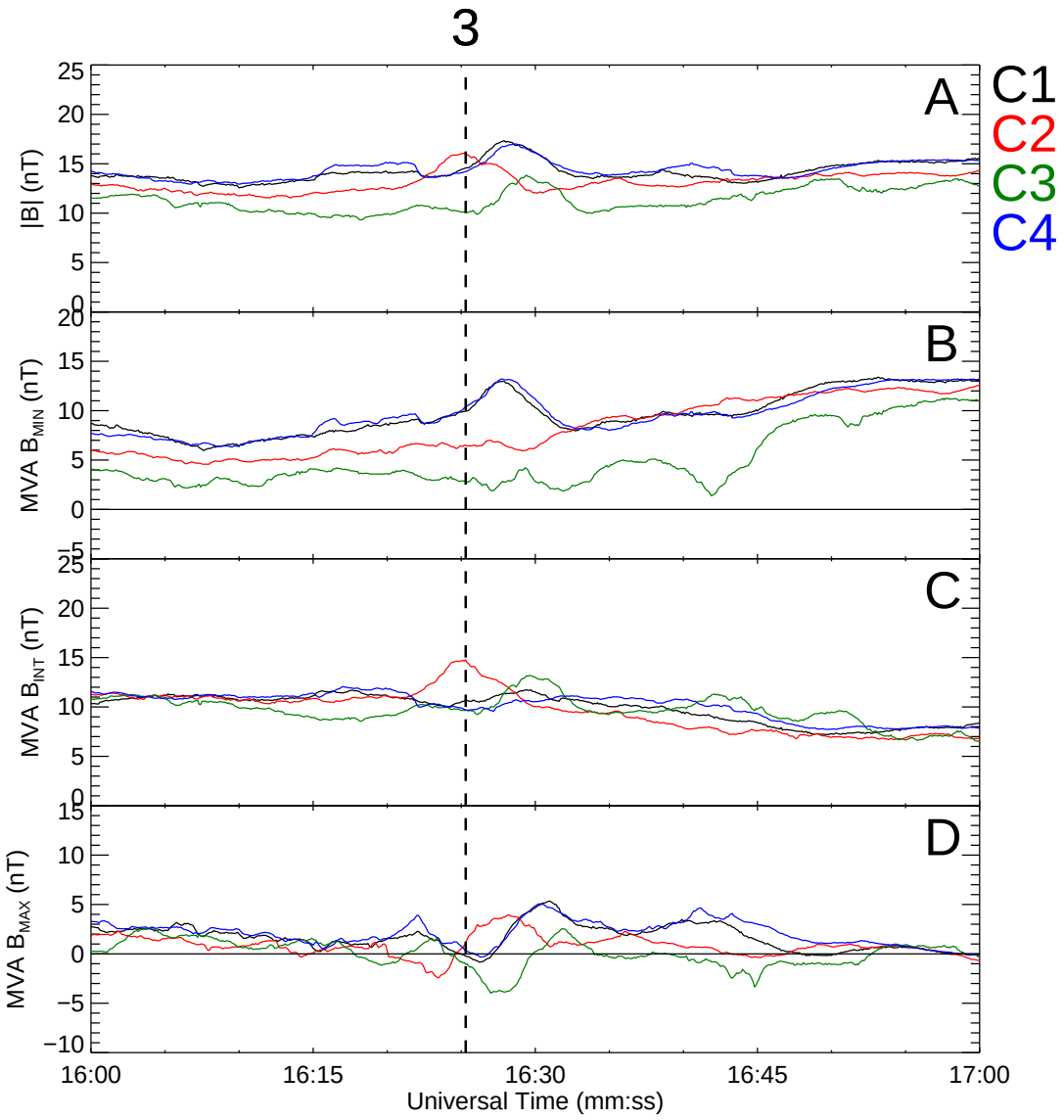

Figure 3.9: Flux rope signature 3 in a minimum variance coordinate frame. Panel A shows the magnitude of the magnetic field and Panels B-D show the minimum, intermediate and maximum variance components of magnetic field respectively. Data are plotted in the minimum variance frame determined from C2's encounter with Signature 3. Trace colours are the same as Figure 3.6, Panel A.

in energy bins above ∼4 k eV and are accompanied by a weakening of $|B_X|$ and a strengthening of $|B_Z|$. The beams are stronger and of longer duration at C3 than C1 and show no evidence of velocity dispersion. Similar ion features are seen at C3 at 23:19 and 23:20 UT, however there is no indication in the magnetic field data of any flux rope-like structures at these times. No such ion features are seen in the TC-1 data, around the time of Signature 2 or otherwise.

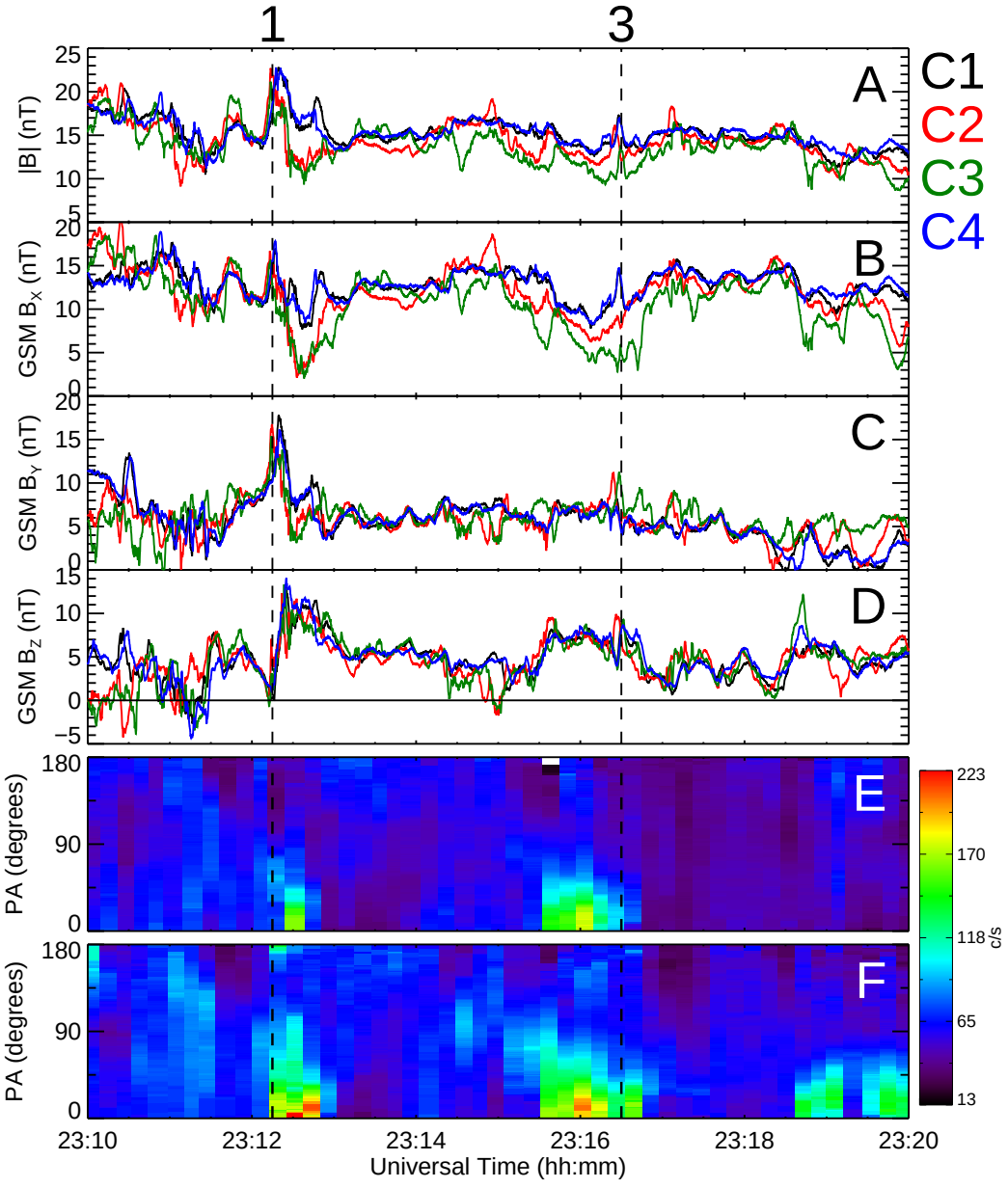

Figure 3.10: Panel A shows the magnitude of the magnetic field for all 4 Cluster spacecraft while panels B-D show GSM magnetic field components. Panels E and F show pitch angle-time spectrograms summed over energy for HIA onboard C1 and C3 respectively. Signatures 1 and 3 are marked by black dashed lines.

3.3 Data Analysis

The observations of Signatures 1 and 2 may either be interpreted as a single flux rope seen at Cluster then TC-1 in quick succession, or two individual flux ropes existing in the tail simultaneously. The expected delay time for the observation of one flux rope at two points depends on the speed of the rope and its orientation. In order to ascertain whether Signatures 1 and 2 represent a single flux rope or two flux ropes, it is therefore essential to confidently determine the axis orientation of each flux rope signature.

3.3.1 Flux Rope Modelling

While MVA has been used to successfully obtain an estimate of the orientation of a flux rope axis (e.g. Eastwood *et al.*, 2002), deviations from a force-free state may introduce ambiguity to the results of an MVA (Xiao *et al.*, 2004). Fitting magnetic field data to a specific flux rope model often provides a more definitive result (e.g. Mulligan *et al.*, 2001). Here we will use a simplified version of the cylindrically symmetric flux rope model described by Mulligan and Russell (2001) to determine the orientations of each flux rope signature. This model was chosen because it does not assume flux ropes to be in a force-free state and Henderson *et al.* (2006a) reported flux ropes seen in the Cluster dataset that were not force free. The Cartesian vector components of magnetic field are modelled as follows:

$$B_X = B_p \frac{Z}{R}\left[1 - e^{-\left(\frac{R}{\sigma_p l}\right)^n}\right] \tag{3.1}$$

$$B_Y = B_a e^{-\left(\frac{R}{\sigma_a l}\right)^m} \tag{3.2}$$

$$B_Z = -B_p \frac{X}{R}\left[1 - e^{-\left(\frac{R}{\sigma_p l}\right)^n}\right] \tag{3.3}$$

where B_a and B_p represent axial and poloidal magnetic fields, respectively; R is the distance to the flux rope axis; l is the radius of the flux rope and σ_a, σ_p, m and

n are dimensionless parameters relating to the shape of the exponential. X and Z represent the spacecraft position within the flux rope, and are generated from an impact parameter. In this coordinate system, the Y direction points along the flux rope axis, X along the spacecraft trajectory and Z completes the right handed set. Note that there is no boundary condition setting the axial field to 0 nT at the flux rope edge. Two rotation angles, θ and ρ, needed to transform the modeled flux rope into GSM coordinates, as well as B_a, B_p, σ_a, σ_p, m, n and the impact parameter must be optimised, then, in order to determine the orientation of a flux rope axis. This fit is obtained through minimisation, using a downhill-simplex algorithm (Nelder and Mead, 1965), of the response function

$$B_{res}^2 = (B_{X'data} - B_{X'model})^2 + (B_{Y'data} - B_{Y'model})^2 + (B_{Z'data} - B_{Z'model})^2 \quad (3.4)$$

where $(B_{X'model}, B_{Y'model}, B_{Z'model})$ represents the model field rotated into GSM coordinates using θ and ρ, $(B_{X'data}, B_{Y'data}, B_{Z'data})$ are the data from FGM and B_{res} are the residuals.

Figures 3.11, 3.12 and 3.13 show the model fits for Signatures 1, 2 and 3 respectively. Panels A-C in each figure show the three components of the magnetic field in the flux rope model frame, and Panel D the field magnitude. The solid lines represent the FGM data and the dashed lines the model fits. For the purposes of fitting the model, the edges of each flux rope signature in the data were defined as the points of inflection in the bipolar signature seen in GSM B_Z. In Figure 3.11 data from C1, C2, C3 and C4 are time shifted for clarity by -12, 3, 18 and 30 seconds respectively. In the cases of C1 and C4, the model fit underestimates the contribution of GSM B_X to the total field while overestimating the contribution made by GSM B_Y during the early part of the rope interval. If the data are rotated into the model frame, however, the majority of this discrepancy becomes confined to B_X component, i.e. along the spacecraft trajectory. Since the model assumes cylindrical symmetry, any discrepancies between the model flux ropes and magnetic field data might be explained by a lack of cylindrical symmetry, which could be

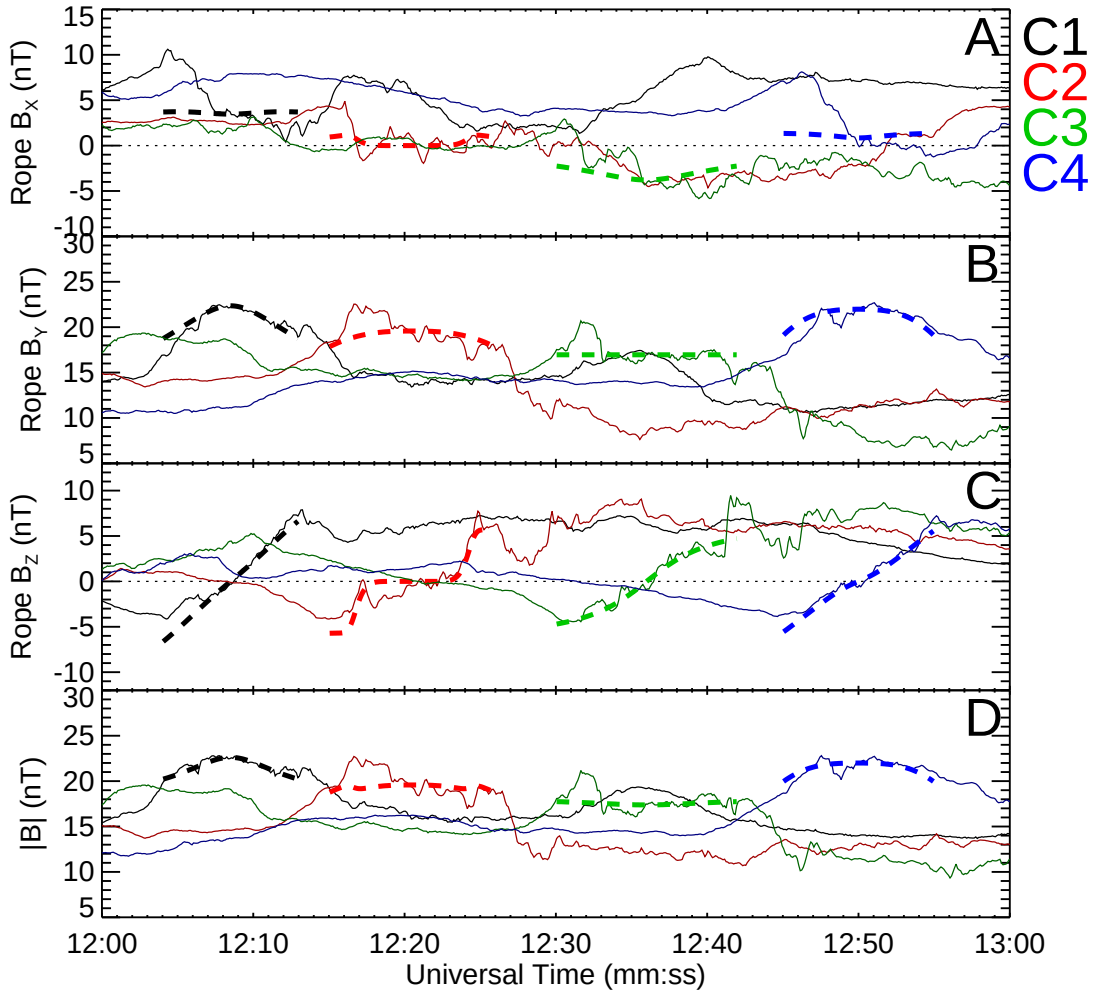

Figure 3.11: Model fits for Signature 1. The thick dashed lines represent the model flux ropes, the thinner solid lines the FGM data. Colours as before. Panels A-C show the three field components in the flux rope model frame and Panel D the total field. Data have been offset by -12, 3, 18 and 30 seconds for C1, C2, C3 and C4 respectively.

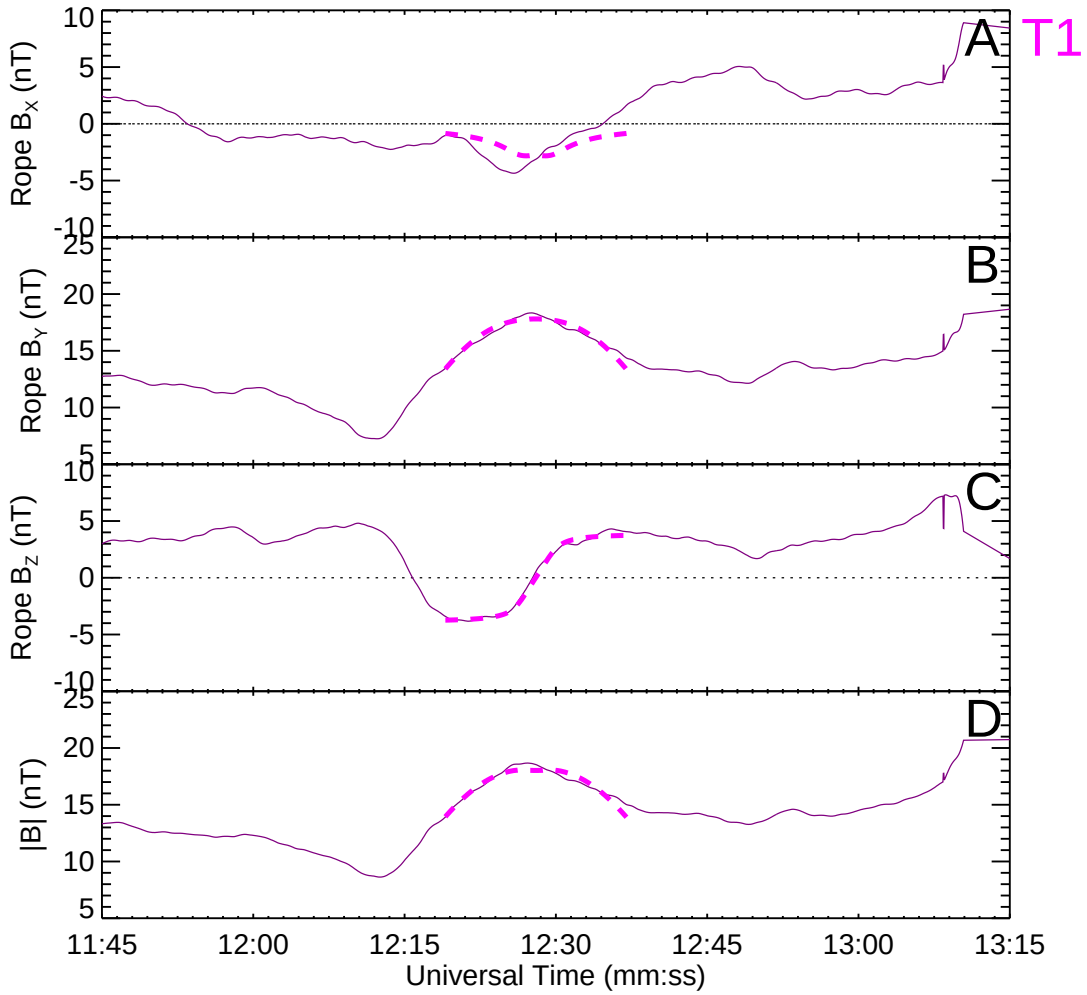

Figure 3.12: Model fit for Signature 2. The thick dashed line represents the model flux rope, the thinner solid line the FGM data from TC-1. Panels A-C show the three field components in the flux rope model frame and Panel D the total field.

caused by enhanced pressure between the moving flux ropes and the plasma and magnetic fields ahead of them distorting the flux ropes from an axially symmetric shape (Slavin *et al.*, 2003a,b). In Figure 3.12 it is again the GSM B_X component of the model field which fits the data least well. In Figure 3.13, the traces for C2 and C3 are offset by $\mp$10 seconds respectively.

Table 3.1 lists the axial and poloidal field strengths, rotation angles, impact parameters and radii returned from the model fits, as well as the estimated magnetic flux contained within the flux rope and the angle between the model axis and the

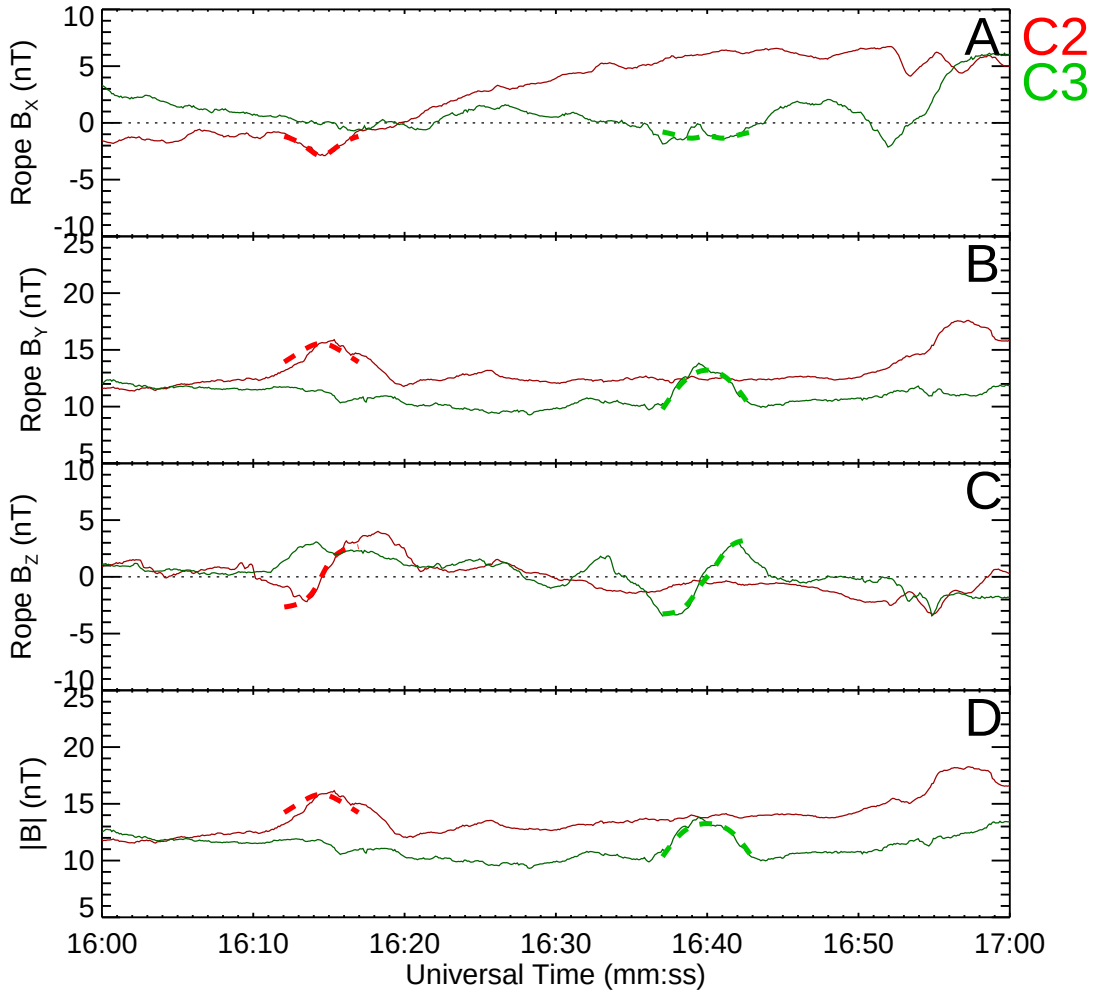

Figure 3.13: Model fits for Signature 3. The thick dashed lines represent the model flux ropes, the thinner solid lines the FGM data. Colours as before. Panels A-C show the three field components in the flux rope model frame and Panel D the total field. Data have been offset by -10 and 10 seconds for C2 and C3 respectively.

S/C	B_a (nT)	B_p (nT)	θ (°)	ρ (°)	z (km)	l (km)	Φ (kWb)	α (°)
Signature 1								
C1	30	13	21	-26	448	925	80	44
C2	20	6	24	-41	160	987	60	41
C3	17	6	21	-48	-506	1177	74	57
C4	22	12	28	-36	214	922	59	53
Signature 2								
TC1	18	8	45	5	-343	1156	77	43
Signature 3								
C2	17	3	37	-42	185	463	13	33
C3	13	3	38	-14	117	523	10	7

Table 3.1: Physical parameters returned from the flux rope model fits and the derived magnetic flux through each flux rope. B_a and B_p are the axial and poloidal fields, respectively; θ is the rotation angle about the model coordinate system X axis; ρ is the rotation angle about the model coordinate system Z axis; z is the impact parameter ; l the flux rope radius and Φ the magnetic flux through the rope. α is the angle between the flux rope axis returned from MVA and the axis returned from the model fit. Quantities are rounded to the nearest nT, °, km or kWb as appropriate. A positive (negative) impact parameter denotes that the spacecraft passed above (below) the flux rope axis.

MVA axis discussed above, for the spacecraft relevant to each signature. The impact parameters and radii were initially returned in time units, calculated from the spacecraft travel time through the flux rope signature (c.f. Khurana *et al.*, 1995), before being converted to kilometres by multiplying by the ion velocity ($\boldsymbol{v}_\perp$) as projected onto the plane perpendicular to the flux rope axis. This projection should eliminate any overestimation of radii and impact parameters from any component of the spacecraft trajectories which are not perpendicular to the rope axis. Motion along the rope axis is not considered in the model equations. Any changes in magnetic field behaviour along a flux rope axis are assumed to be negligible on the scale of these observations.

The model fits for Signature 1 return rotation angles for the four Cluster spacecraft that are mutually consistent to within 7° and 22° for θ and ρ respectively. This consistency increases confidence that the modelled rotation angles are correct, despite the differences in the magnetic field observed by each spacecraft. Furthermore, the impact parameters returned are largely consistent (i.e. to within 200 km) with the separation of the Cluster tetrahedron, as projected onto the plane perpendicular to the flux rope axis. This is illustrated in Figure 3.14, where the solid lines

represent the model derived impact parameters and the dashed lines the spacecraft positions, relative to that of C3 (hence there is no dashed line for C3), in the C1 model frame. In the case of Signature 3, the angles are also consistent (to within 30°) between the C2 and C3, however the difference in impact parameters between the two spacecraft is too small when compared with the separation of the Cluster tetrahedron, and therefore the flux rope radii and enclosed magnetic fluxes calculated for Signature 3 are likely to be underestimates. Signatures 1 and 2, on the other hand, have similar amounts of magnetic flux enclosed within them, which does not eliminate the possibility that Signatures 1 and 2 represent the same flux rope.

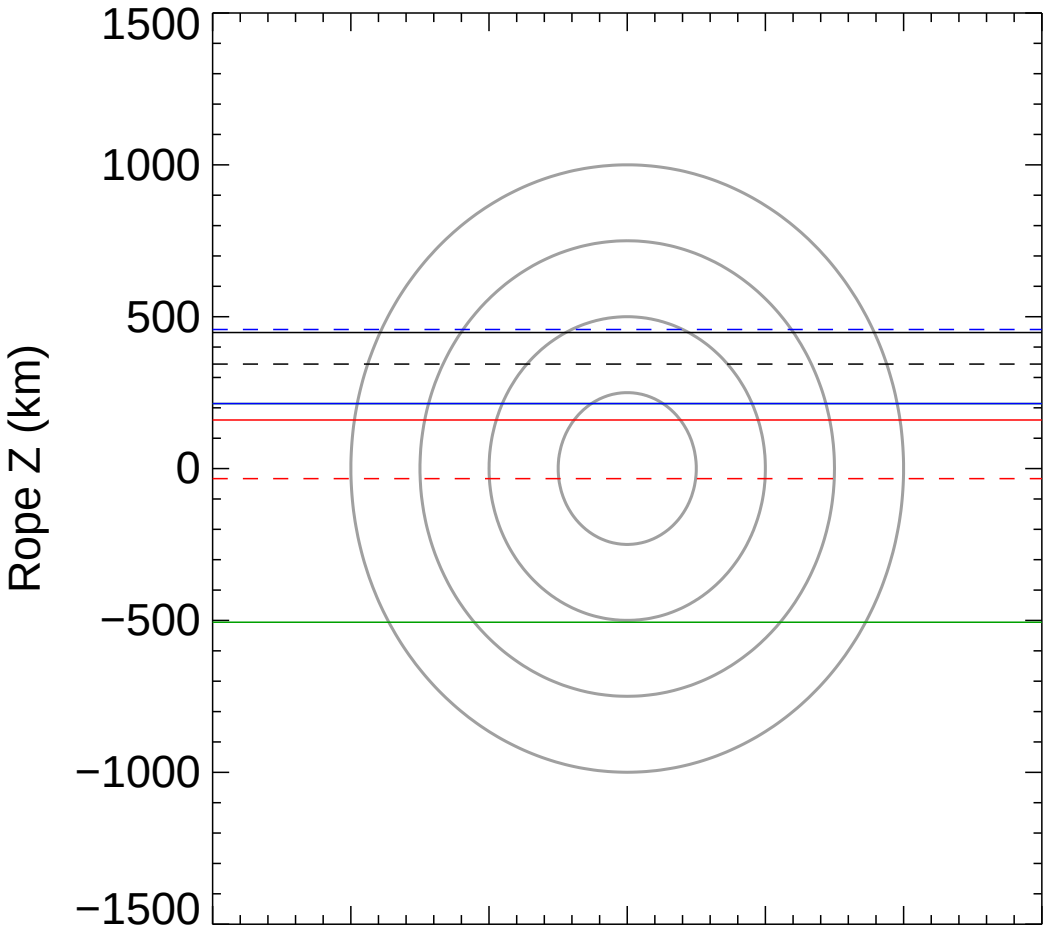

Figure 3.14: A comparison of spacecraft trajectories through Signature 1. Solid coloured lines represent the trajectories of the four Cluster spacecraft from the model-derived impact parameters while the dashed coloured lines are the positions of the Cluster spacecraft, relative to the position of C3 plotted in the C1 model frame for Signature 1.

The difference in enclosed flux between Signature 3 (∼10 kWb) and Signatures 1 and 2 (∼60-80 kWb) might, then, be a result of this underestimate, rather than Signature 3 representing a much smaller flux rope. Again, a departure from cylindrical symmetry could explain this underestimate. In comparison with the tens of kWb enclosed by the flux ropes, which are expected to either be connected at one or both ends to the Earth, or to the IMF in the magnetosheath, a typical substorm can close several tenths of GWb of open lobe flux (Milan *et al.*, 2004).

3.3.2 Flux Rope Axis Orientations

Assuming a flux rope axis orientation perpendicular to the line connecting the Cluster spacecraft and TC-1, for Signatures 1 and 2 to represent one flux rope, velocities of between ∼2,900 and ∼5,700 $\mathrm{km\,s^{-1}}$ would be required. This figure is inconsistent with the velocity of propagation from 4-spacecraft timing at Cluster (146 $\mathrm{km\,s^{-1}}$) and data from the ion instruments onboard the Cluster and TC-1 spacecraft; all of which give ion velocities of the order of 200 $\mathrm{km\,s^{-1}}$. Only if a notional flux rope axis were oriented along, or close to, the line connecting the Cluster and TC-1 could a slower propagation velocity be sufficient for one flux rope to be observed at both Cluster and TC-1 within a few seconds.

Figure 3.15 compares the axis orientations of each flux rope signature, as determined by the model fits on the magnetic field data from each individual spacecraft. Panel A of Figure 3.15 shows the XY plane and Panel B the YZ plane; the coloured squares represent the spacecraft positions at 23:12:30 UT, and the coloured lines the direction vector of the principal rope axis. The symbols representing Signature 3 have been offset by (-1,4,-1) $\mathrm{R_E}$ for clarity.

For context, the spacecraft positions are expressed in GSM coordinates, however the vectors representing the flux rope axes use a coordinate system based on the orientation of the neutral sheet local to Cluster or TC-1. This coordinate system is defined by a rotation of GSM about the X axis such that the new XZ plane contains

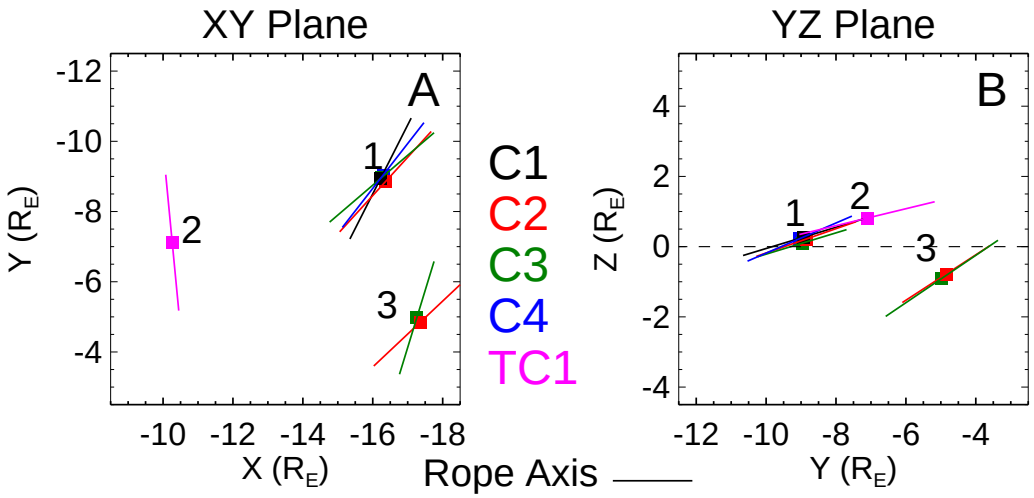

Figure 3.15: A comparison of the various spacecraft positions (coloured squares - colours as for Figures 3.6 and 3.7) and flux rope axis orientations (solid lines). Spacecraft positions are in GSM. The coordinate system used for flux rope axis directions is a rotation of GSM such that the XZ plane contains the normal to the tail current sheet, rather than the Earth's magnetic dipole axis. Signature 3 is offset by (-1,4,-1) R_E for clarity.

the normal to the tail neutral sheet, rather than the Earth's dipole axis. The normal to the neutral sheet was calculated once for the entire Cluster tetrahedron and separately for TC-1 by performing MVA on the closest possible neutral sheet crossing, by the correct spacecraft, to the flux rope encounter. For Signatures 1 and 3 this was a crossing by C3 as it left the thin current sheet region at 23:09:25 UT, 3 minutes before the encounter with Signature 1; for Signature 2 a TC-1 crossing at 23:11:50 UT, some 38 seconds before the flux rope encounter, was used. The neutral sheet normal was measured to be GSM$(0.043, -0.063, 0.997)$ at Cluster 3 and GSM$(0.181, -0.484, 0.856)$ at TC-1 while the eigenvalues for the two MVAs were $(0.0619, 0.611, 29.2)$ and $(0.028, 0.317, 3.46)$ respectively.

This rotated coordinate system was used because we believe that in a simple case any flux ropes present in the plasma sheet might lie in the plane of the neutral sheet. Both the tail plasma sheet and any flux ropes within it will be subject to magnetic pressure from the lobes which can apply a force to the plasma sheet and tilt it (Cowley, 1981). The same force would be exerted on flux ropes as well. The angles between the plane containing the neutral sheet normal and the flux rope axis orientation were calculated to be 72°, 70°, 72° and 66° for Cluster spacecraft 1-4 re-

spectively (Signature 1) and 74° for TC-1 (Signature 2), all within 25° of 90°, which is apparent in Panel B of Figure 3.15. Comparing the Signature 2 (TC-1) flux rope axis with the Cluster neutral sheet normal gives an angle of 49°. Simulations by Winglee (2004) have shown how shears in reconnection flows might skew flux rope axes from an East-West orientation; however because all of the flux rope signatures are at a consistent angle to the plane containing the neutral sheet normal, despite different local orientations of the neutral sheet at Cluster and TC-1, it can be inferred that flux rope orientation is linked to the tilt of the neutral sheet, at least in the north-south direction. These signatures do not lie exactly in the plane of the neutral sheet, which may be because they have a stronger magnetic field than their surroundings and thus would not be as affected by pressure from the lobes. There is no guarantee that the neutral sheet orientation remained the same between the crossing times and flux rope encounters, introducing an element of uncertainty to the calculated angles between rope axes and neutral sheet normals. As such the angles for Signature 3 were not calculated. Figure 3.15, however, shows Signature 3 has a orientation in YZ with respect to the neutral sheet normal comparable to that of the other flux ropes. The orientations of the flux rope axes are comparable to those observed by Slavin *et al.* (2003a) in their survey of flux ropes using the Geotail dataset, further increasing confidence in our axis orientations.

The Cluster and TC-1 rope axes lie approximately cross-tail (i.e. parallel to the YZ plane), the Cluster axes having a larger GSM X component, pointing slightly towards TC-1. This tilt towards TC-1 means that a lower velocity than those calculated assuming the rope axis is in Y GSM (i.e. 2,900-5,700 $\mathrm{km\,s^{-1}}$) is needed for Signatures 1 and 2 to represent the same flux rope. Table 3.2 lists these velocities ($\boldsymbol{u'}_{\perp}$) calculated individually for each Cluster spacecraft. The perpendicular displacement ($\boldsymbol{R}_{\perp}$) between each Signature 1 flux rope axis (assumed to be straight and long) and TC-1 were calculated and the plasma velocity as measured at Cluster projected onto this vector ($\boldsymbol{v'}_{\perp}$). From these quantities, the time required ($\delta \mathrm{t}_{\perp}$) for a flux rope to propagate from Cluster to TC-1 at $\boldsymbol{v'}_{\perp}$, the measured velocity, was calculated. For comparison, Table 3.2 also lists the actual elapsed times between

S/C	$\boldsymbol{R}_\perp$ (km)	$\boldsymbol{v'}_\perp$ ($\mathrm{km\,s^{-1}}$)	$\boldsymbol{u'}_\perp$ ($\mathrm{km\,s^{-1}}$)	δt (s)	$\delta t_\perp$ (s)
C1	29,496	180	3,687	8	164
C2	21,640	177	1,664	13	122
C3	17,125	171	1,223	14	100
C4	24,579	179	3,511	7	137

Table 3.2: $\boldsymbol{R}_\perp$ is the perpendicular displacement between the Signature 1 flux rope axis and TC-1; $\boldsymbol{v'}_\perp$ is the observed plasma velocity as projected on to the displacement vector; δt is the observed difference between the time of flux rope encounter at the Cluster spacecraft and TC-1; $\delta t_\perp$ is $\boldsymbol{R}_\perp/\boldsymbol{v'}_\perp$, the required time difference between observation of Signature 1 and Signature 2 for a rope to propagate at the observed speed; and $\boldsymbol{u'}_\perp$ is the required propagation speed for a flux rope to travel from Cluster to TC-1 in δt. The measured velocities are too low to carry the Signature 1 flux rope to TC-1 in the observed times.

Signature 1 and Signature 2 for each Cluster spacecraft (δt).

Despite the tilt towards TC-1, the required propagation velocities ($\boldsymbol{u'}_\perp$), $3{,}687\,\mathrm{km\,s^{-1}}$, $1{,}664\,\mathrm{km\,s^{-1}}$, $1{,}223\,\mathrm{km\,s^{-1}}$ and $3{,}511\,\mathrm{km\,s^{-1}}$ for C1, C2, C3 and C4 respectively, are still an order of magnitude greater than those measured at both Cluster and TC-1. Signatures 1 and 2, therefore cannot represent one straight flux rope. Because the axes of Signatures 1 and 2 are of different orientations, do not have opposing axial fields, and do not lie along the line separating Cluster and TC-1, for the observations to represent one flux rope, it would have to resemble a 'Z' shape. Magnetic tension forces would act to quickly straighten such a structure unless opposed by another force, however there is no evidence to suggest this sort of stressed flux rope is likely to exist. Another possibility is that the flux rope represented by Signature 1 is expanding rapidly such that it could encounter TC-1 at the correct time, even with its slow velocity. Plasmoids observed in the magnetotail have been known to expand at rates as high as $\sim$100 $\mathrm{kms^{-1}}$ as more reconnected magnetic flux and hot plasma is added to them (Slavin *et al.*, 1999). Earthward moving flux ropes, however are unlikely to expand so rapidly, or may even contract, because of increasing magnetic pressure closer to the Earth. Signatures 1 and 2, then, are unlikely to represent an expanding flux rope propagating over the spacecraft. This idea is also inconsistent with observed signature durations, plasma velocities and our model results, therefore we believe that the correct explanation is that Signatures 1 and 2, despite having similar flux content, represent two individual flux ropes existing in

the tail at the same time.

3.4 Discussion

The observation of these simultaneously existing flux ropes in the near-Earth magnetotail, while novel in itself, can also be used to learn about the structure and dynamics of the tail during this event, particularly in the context of MXR. Our suggested interpretation of the data is that the flux ropes formed as part of a spatially extended system of multiple competing X-lines, encompassing the orbits of Cluster and TC-1.

During the passage of the flux rope labelled Signature 1, B_X was seen to increase (Figure 3.7, Panel B). The spacecraft, therefore, sampled the upper portion of the flux rope. It is feasible then, and consistent with the short duration of the observed flows at the time of Signature 1 compared with those seen by TC-1 at Signature 2, that the tetrahedron was not ideally located to observe the flows associated with any reconnection, and it is only the passage of the flux rope creating a bulge in the plasma sheet that allowed the flowing plasma to be observed (c.f., Owen *et al.*, 2005). Signature 3 can be interpreted as a more extreme example of the same idea. Here, two of the spacecraft (C2 and C3) sample the very top of the flux rope (bipolar signature in B_Z and peak in B_Y), while C1 and C4 miss the flux rope and instead see a TCR-like feature (bipolar signature in B_Z and peak in B_X). The configuration of the Cluster tetrahedron, plotted in Signature 3 flux rope coordinates derived from the C2 model in Figure 3.16, is consistent with this interpretation. This provides further evidence that the passage of flux ropes in the plasma sheet is indeed the source of TCRs in the lobe (Owen *et al.*, 2005), rather than an alternative interpretation; where the passage of bulges created in the plasma sheet by time-varying, transient reconnection at a single X-Line (e.g. Semenov *et al.*, 2005; Ivanova *et al.*, 2007) is responsible for the presence of TCRs.

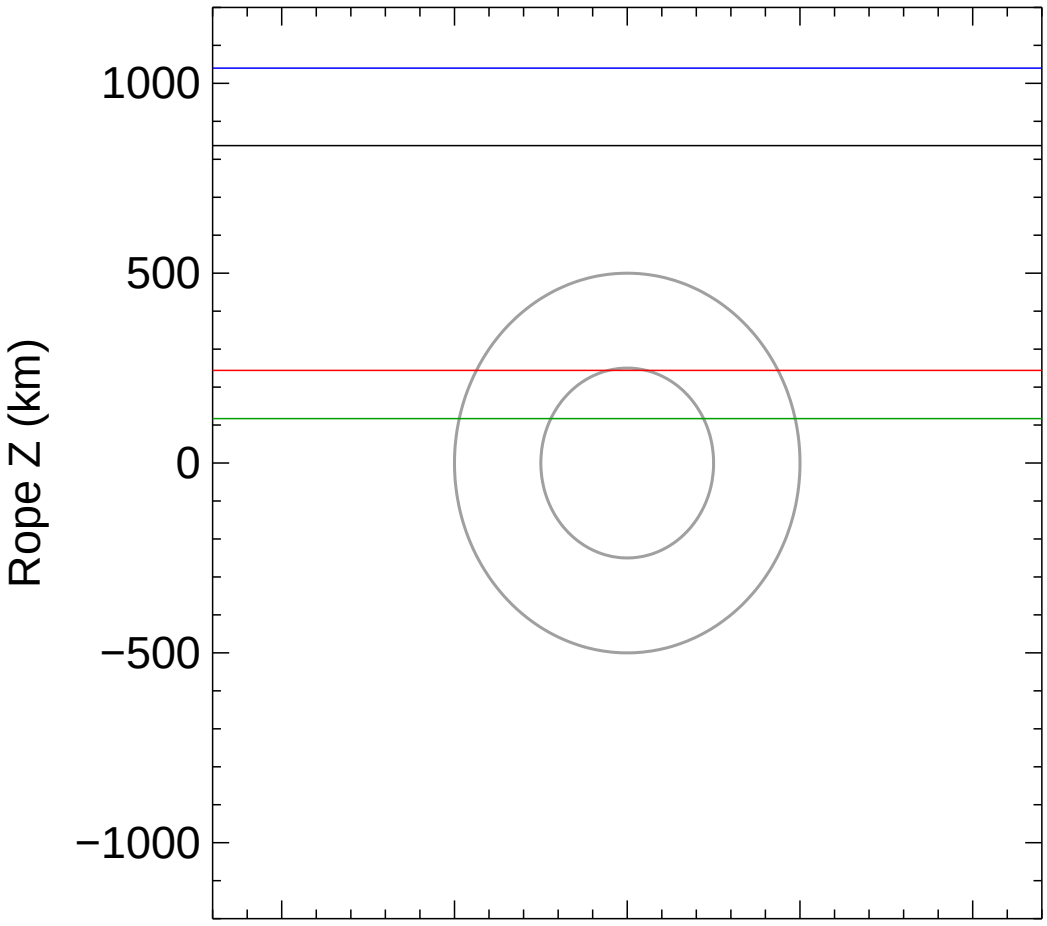

Figure 3.16: A comparison of spacecraft trajectories through Signature 3. Solid coloured lines represent the trajectories of the four Cluster spacecraft based on the positions of the Cluster spacecraft in the C3 model frame for Signature 3.

The observation of the Earthward-directed ion beams at Signatures 1 and 3 (Figure 3.10, Panels E and F) is consistent with this interpretation. Those field lines that were pushed into the path of the spacecraft by the flux ropes were apparently connected to the ion beams' source, perhaps an X-Line downtail from Cluster, which is operating at both 23:12 UT and 23:16 UT. Since the beams show no evidence of velocity dispersion and no bi-directionality is observed, it is likely that the source of the ions is close to the spacecraft, rather than a distant neutral line. The detection of the ions immediately after the flux rope at Signature 1, and then the switch-off of the ions at 23:12:40 UT (C1) and 23:12:48 UT (C3) may be explained by

the spacecraft moving from the flux rope, through the trailing edge of the bulge caused by the passage of the flux rope, and into the relatively undisturbed PSBL between flux ropes. C1 is further from the neutral sheet than C3, and it observes the switch-off first, which is consistent with the feature having a limited spatial extent as opposed to a short lifetime. The switch-on of ions at 23:15:35 UT (C1 and C3) then, indicate the spacecraft move onto the leading edge of the Signature 3 bulge. A reduction in ion flux is observed by C3 as it moves through the flux rope before entering the trailing edge of the bulge. C1 sees no reduction in ion flux, consistent with the spacecraft not entering the flux rope. Ion switch-off at 23:16:26 UT (C1) and 23:16:48 UT (C3) represent the spacecraft leaving the trailing edge of the bulge. No ion features associated with Signature 2 were observed by TC-1, consistent with our interpretation, since TC-1 was located much deeper in the central plasma sheet than Cluster ($\beta \sim 2$, $B_X \sim 0$).

In Figure 3.17 we suggest a sequence of events that can plausibly explain the presence of these flux ropes in the magnetotail. Panel A shows the situation at 23:07 UT, when Cluster lies within the thin current sheet region (a notional current sheet is represented by light blue shading on the figure). The tailward flows detected by CIS are consistent with the presence of a reconnection site located Earthward of the spacecraft. The Earthward flows detected by TC-1 HIA at this time imply a reconnection site was located tailward of that spacecraft. It is impossible to unambiguously determine from these data if there is more than one X-line present between Cluster and TC-1 at this time, however if a flux rope (later observed as Signature 2) was at that time extant, or being formed, between Cluster and TC-1 at least two reconnection sites would have to exist. By 23:09 UT, the time of substorm onset (Panel B), Cluster had moved away from the neutral sheet towards the PSBL (consistent with the observed decrease in β) and thus did not observe any plasma flows. TC-1 continued to observe moderate Earthward plasma flows, and we infer that the system of flux ropes was driven Earthward by the fastest reconnection site, that was involved in the substorm. At 23:12 UT (Panel C), Signature 1 had reached Cluster, and Signature 2 had reached TC-1. Upon leaving Signature 1, Cluster de-

tected the first Earthward ion beam then returned to the PSBL. At 23:16 UT (Panel D) Cluster detected the second Earthward ion beam then entered Signature 3, a flux rope which was being driven Earthward by the continuing substorm reconnection. On leaving Signature 3, the third ion beam was detected and Cluster returned to the PSBL. The tailward directed plasma flows detected by TC-1 from 23:14 UT - 23:21 UT are consistent with an active reconnection site having moved Earthward past the spacecraft, again driven by the substorm. At 23:30 UT (Panel E) Cluster returned to the central plasma sheet and crossed the neutral sheet, observing strong Earthward flows as it did so. This implies that the dominant X-line driving the entire system remained tailward of Cluster throughout the interval. For three flux ropes to exist in the tail, a minimum of four X-lines must exist. Figure 3.17 represents this minimum necessary configuration, where the tailmost X line responsible for substorm expansion is one of those that forms Signature 3. Because none of these reconnection sites are directly observed by Cluster, however, a different X-line not associated with the observed flux ropes could instead be responsible for the substorm expansion and driving the flux ropes Earthward. The significant difference between the amount of flux enclosed by each flux rope and the open flux closed in a substorm (Milan *et al.*, 2004) implies that the dominant reconnection site in our system has to reconnect much more flux than the quantity purely involved with the formation of the flux ropes to explain the substorm after 23:09 UT. Unfortunately the location of that reconnection site and a conclusive explanation of the cause of its higher reconnection rate cannot be determined in this case.

The rotation and later dipolarisation of the magnetic field at TC-1 is also consistent with the idea that there is an ongoing process working to restore the tail to a more relaxed configuration from its initial twisted state. This rotation and dipolarisation may be two different processes working in tandem - the rotation of the field due to IMF clock angle changes and a slow dipolarisation of the field due to steady (on the timescale of the event) reconnection further downtail. There is no evidence (e.g. sudden large dipolarisations) in the TC-1 magnetic field data for any bursty phenomena occurring further down tail.

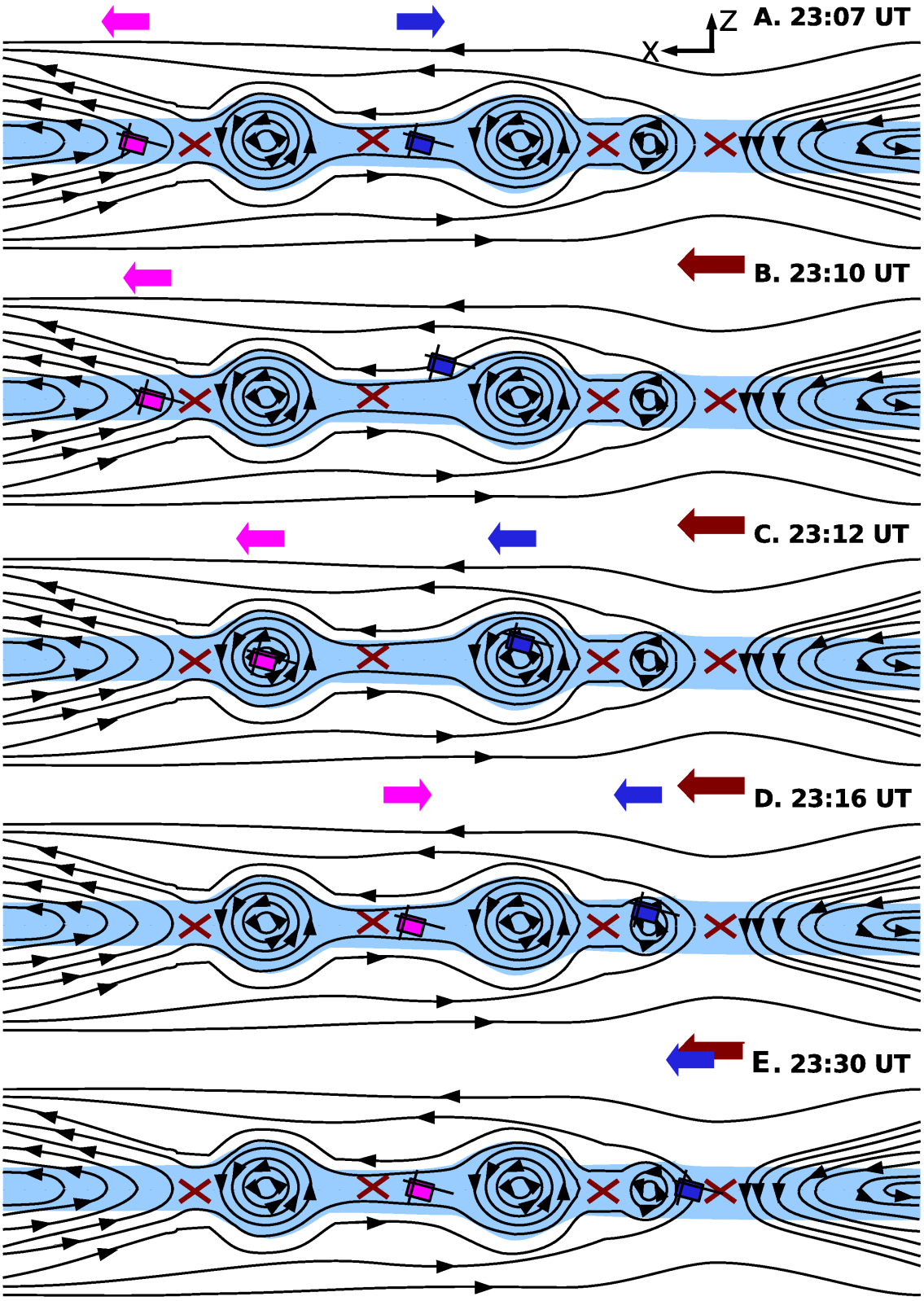

Figure 3.17: An illustration of a possible sequence of events explaining the data. The dark blue spacecraft represents Cluster, and the magenta represent TC-1. Flows detected by each spacecraft are depicted as arrows of the relevant colour, whereas the dark red arrows represent the reconnection outflow driving the system. Possible reconnection sites are marked as red Xs. A notional plasma sheet is depicted by the light blue shading. Panels A-E show the magnetotail configuration at 23:07 UT, 23:10 UT, 23:12 UT, 23:16 UT and 23:30 UT respectively. This figure represents the magnetotail configuration with the minimum number of reconnection sites necessary to explain the presence of three flux ropes. Further flux ropes, and therefore X-lines may have existed tailward of Cluster.

It is interesting to note that no evidence of the Cluster flux ropes (Signatures 1 and 3) was seen by TC-1 later in the interval, so the spacecraft was either in the wrong place to see them, or they did not reach the position of TC-1. The length of flux ropes in their axial direction is impossible to determine using point measurements, so it feasible that the structures were not long enough to cross both Cluster and TC-1. It is also feasible that the Cluster flux ropes' motion stalled, or that they were re-reconnected into the surrounding magnetic field before reaching TC-1. Signature 2 was observed unusually close to the Earth for a flux rope (Slavin *et al.*, 2003a), and the magnetic field measured at TC-1 became increasingly dipolar throughout the interval, increasing the likelihood of the Cluster flux ropes' re-reconnection with the surrounding field before they reached TC-1. This is consistent with the work of Takada *et al.* (2006), who determined that BBFs detected by Cluster close to apogee in the magnetotail did not always result in dipolarisations close to TC-1 apogee, particularly when the field measured by TC-1 was more dipolar.

The observations reported above add to a growing canon of observational and theoretical evidence that suggests the magnetotail can be significantly fragmented in three dimensions, and that simple 2D models will no longer be sufficient to further our understanding of tail dynamics. Unfortunately data from the fortuitous conjunctions of spacecraft that have been available until now, including that presented here, are not always ideally suited for probing large-scale 3D structures in the magnetotail. The recently launched THEMIS mission will greatly increase our capability in analysing larger scale magnetotail dynamics.

3.5 Conclusions

We have presented an unusual observation of three flux ropes existing in the near-Earth magnetotail, two of which were observed simultaneously some $6.3\,R_E$ apart. The third flux rope was seen at two of the four Cluster spacecraft, the others seeing

a feature resembling a TCR. These observations of multiple small flux ropes in the near-tail support the interpretation that TCRs in the near-tail are consequences of the presence of such flux ropes (Slavin *et al.*, 2005). All the flux ropes were observed to have similar orientations with respect to the local neutral sheet, despite differences in local neutral sheet orientation at different spacecraft, implying flux rope orientation is linked to neutral sheet tilt. Evidence suggests these flux ropes were formed through reconnection at a minimum of four competing X-points and were driven Earthward by the fastest reconnecting X point, located tailward of the Cluster tetrahedron.

Chapter 4

Cluster and Double Star Multipoint Observations of a Plasma Bubble

> You should call it entropy... no one really knows what entropy really is, so in a debate you will always have the advantage.
>
> *John Von Neumann*

4.1 Introduction

The exact mechanism by which magnetic flux and plasma are transported sunward through the Earth's magnetotail plasma sheet has been an active topic of research since the Dungey Cycle of magnetospheric convection (Dungey, 1961, see also section 1.4.1 of this thesis) was first proposed. In recent years much effort has been concentrated on explaining the localised transient fast flows, called Bursty Bulk Flows (BBFs) by Angelopoulos *et al.* (1992), that have been observed in the tail and that

Portions of this chapter have been published under the title "Cluster and Double Star Multipoint Observations of a Plasma Bubble" (Walsh *et al.*, 2009).

are thought to carry a significant proportion of mass and magnetic flux earthward during more geomagnetically active periods. The nature of the processes behind their creation and propagation, and their role in the development of substorms and other large-scale magnetotail phenomena, however, are still uncertain. One theoretical explanation that has been put forward for these BBFs is that they are depleted flux tubes, also called "plasma bubbles" (Chen and Wolf, 1993, 1999). Plasma bubbles were first suggested by Pontius and Wolf (1990) as a possible solution to the so-called "pressure balance inconsistency", whereby the adiabatic transport of magnetic flux and plasma earthward from the mid- to near-tail was shown to result in plasma pressures in the near-tail which are far too high to be confined by magnetic field intensities that are consistent with observed values (Erickson and Wolf, 1980).

4.1.1 Flux Tube Depletion and Plasma Bubbles

A plasma bubble is a flux tube that has a lower specific entropy, i.e. pV^{γ} (where γ is the ratio of specific heats; p is the plasma pressure within the flux tube and V the volume per unit magnetic flux of the flux tube integrated over the length the flux tube's length, given by $\int B^{-1}\,dS$. S is the length of the flux tube), than surrounding flux tubes, which convects earthward under the action of the interchange instability. This is expected to cause tailward-directed, return flows around the flanks of the plasma bubble as its earthward motion pushes other flux tubes out of the way. Because of its lower entropy content, the depleted flux tube cannot support as much gradient-curvature-drift current as neighbouring flux tubes and excess current is diverted into field-aligned current systems at the boundaries of the bubble, flowing into the ionosphere on the dawnward boundary and out of the ionosphere on the duskward boundary, similar to the substorm current wedge concept. Recent simulations by Sitnov *et al.* (2005, 2009) have illustrated that transient reconnection on closed field lines in the plasma sheet would eject a small plasmoid tailwards, and might also result in the formation of a plasma bubble.

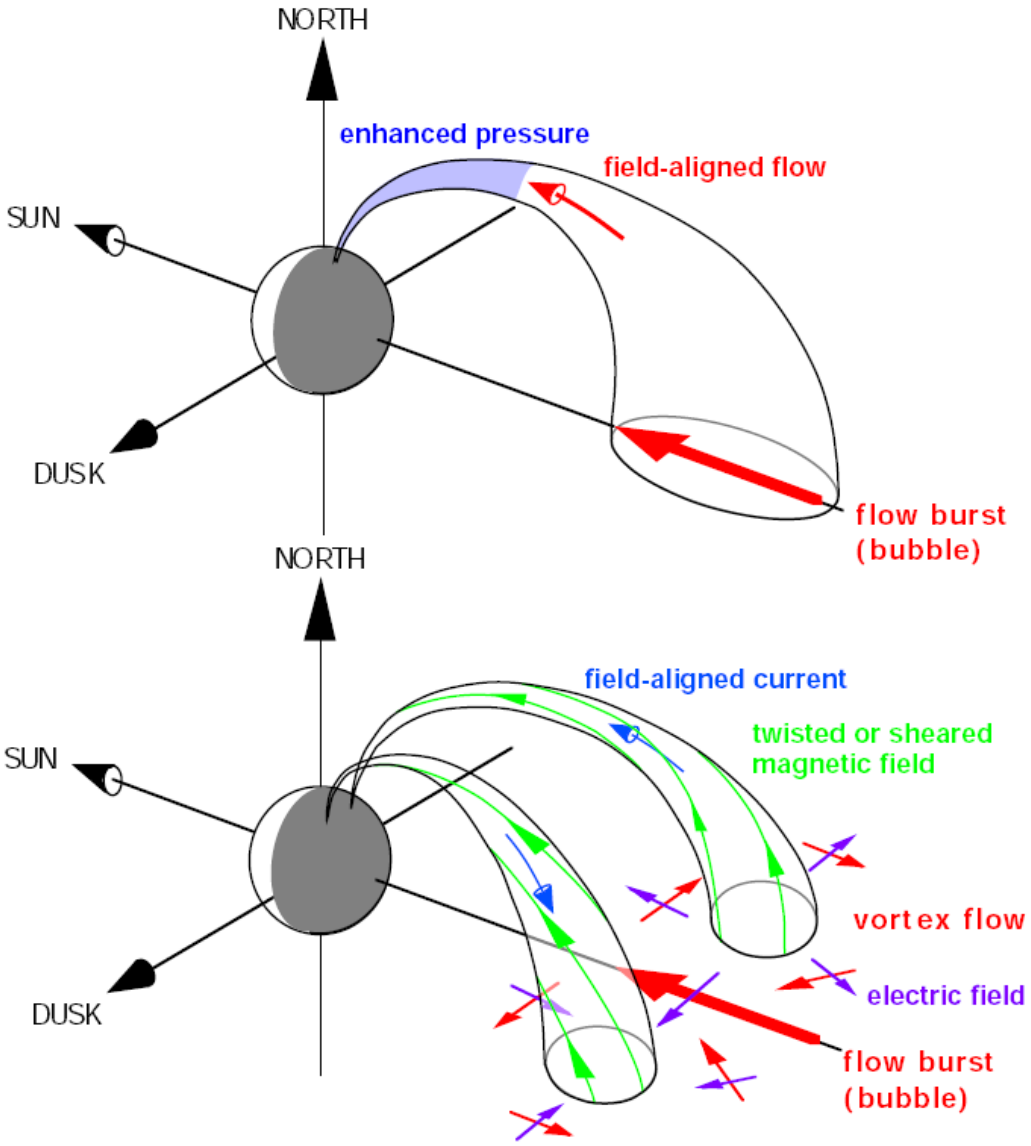

Figure 4.1: The expected features of a plasma bubble from theory and simulation. (Birn *et al.*, 2004, Figure 19).

Using 3D MHD simulations, Birn *et al.* (2004) determined that the pressure along a depleted flux tube need not be constant or steady. Their simulations showed that a newly formed plasma bubble would quickly reach a total pressure balance with surrounding flux tubes. According to the simulation, at the central plasma sheet this pressure balance would be achieved through the plasma pressure returning to its undisturbed value soon after its initial depletion; this is inconsistent with some observations (e.g. Sergeev *et al.*, 1996), however. Further away from the equatorial plane, in lower density regions, the plasma pressure would remain low and pressure balance would be attained through an increase in the magnetic pressure. This would

set up a plasma pressure gradient within the flux tube, resulting in field aligned flows from the equatorial plane to the poles. Over time these flows would cause a build-up of plasma in the near-Earth "horns" of the flux tube, evidenced as an increase in plasma pressure and commensurate decrease in magnetic pressure within the flux tube.

The expected features of a plasma bubble, from theory and simulations, are illustrated in Figure 4.1

4.1.2 Observations of Plasma Bubbles

Observations interpreted as plasma bubbles have been reported by Sergeev *et al.* (1996), for example, who, using ISEE 1 and 2 (then located at X_{GSM} $\sim$-20 R_E), identified several bubbles by looking for a decrease in plasma pressure and a concurrent sharp, transient dipolarisation in the magnetic field. Magnetic shear regions just outside the bubble boundary were also identified. From the sense of magnetic shear in these regions (i.e. the sign of $B_X \cdot \delta B_Y$), it was determined whether the spacecraft entered the bubble on its dawnward or duskward side (see Figure 4.2).

If $B_X \cdot \delta B_Y$ is positive the spacecraft entered the bubble on the dawnward edge and vice versa. The presence of field-aligned currents at the edges of plasma bubbles were inferred from these magnetic shear observations. Additionally, the bubble boundaries were found to be, in almost all cases, tangential discontinuities and the cross-tail extent of the bubbles was estimated to be between approximately 1 R_E and 3 R_E, consistent with later work on BBFs using the Cluster spacecraft by Nakamura *et al.* (2004). The expected field-aligned currents for the bubble model have also been detected at the boundaries of BBFs (e.g. Nakamura *et al.*, 2005a), and the currents within a BBF as a whole have been quantitatively compared with the brightness of an auroral streamer and found to be similar (Forsyth *et al.*, 2008), lending support to the idea that auroral streamers are the ionospheric manifestation of these tail phenomena (Amm and Kauristie, 2002, and references therein).

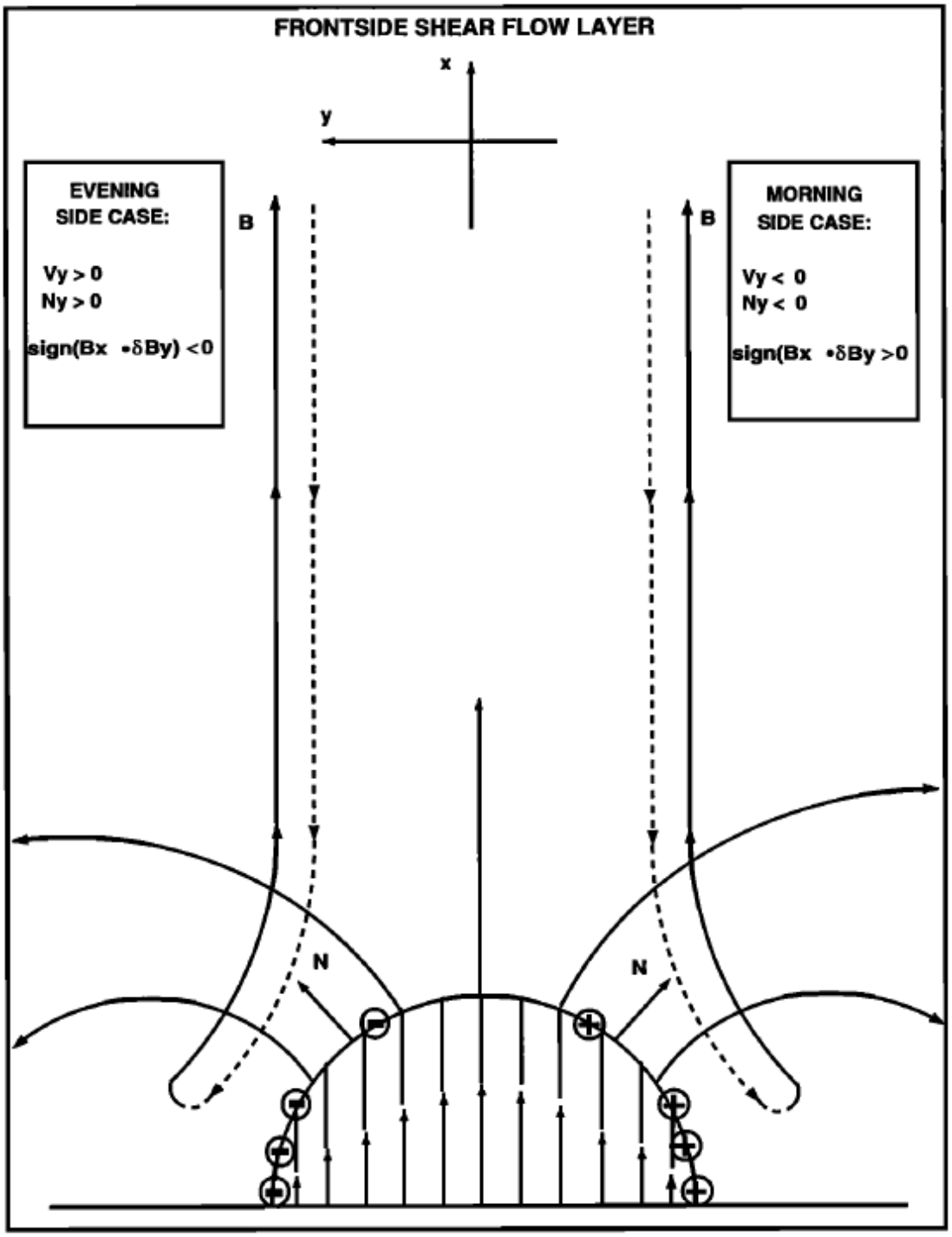

Figure 4.2: The magnetic shear found ahead of a plasma bubble can be used to determine which side of the bubble a spacecraft passes through. Adapted from Sergeev *et al.* (1996), Figure 2.

In this chapter we present observations from the four Cluster spacecraft and the Double Star TC-2 spacecraft of what we interpret to be a plasma bubble penetrating to within $8\,\mathrm{R}_E$ of the Earth, provide the first direct evidence of the existence of the expected return flows around the flanks of the plasma bubble, report other features of the plasma bubble that are not present in simulations, and discuss the possible

effects of a strong magnetotail B_Y on plasma bubbles.

4.2 Observations

4.2.1 Event Context and Overview

On 21 September 2005 between 13:45 UT and 14:15 UT the four Cluster spacecraft (hereafter referred to as C1, C2, C3 and C4) were operating in a high telemetry rate "burst" mode and located at GSM (-14.5, 2.6, 1.2) R_E near midnight MLT in the Earth's magnetotail, while Double Star TC-2 was located at GSM (-6.74, 1.42, -1.39) R_E (see Figure 4.3, Panels A-C). In the 2005 tail season, the Cluster spacecraft were in a so-called "multiscale" configuration, with C1, C2 and C3 making a triangle of side $\sim$10,000 km in the plane of a model neutral sheet while C4 was displaced $\sim$1,000 km in $\sim Z_{GSM}$ from C3, forming a flattened tetrahedron (see Figure 4.3, Panels D-F). This configuration allows for the study of current sheet thickness and motion with C3 and C4, while the large separation between C1, C2 and C3/C4 is designed to provide contextual information and study the cross-tail extent of larger features such as BBFs. The large flattened tetrahedron, however, precludes the use of certain multi-spacecraft analysis techniques, for example the curlometer (Dunlop *et al.*, 2002), when studying features of a similar scale to BBFs.

During the interval of interest the Interplanetary Magnetic Field (IMF), as measured by the MFI instrument (Smith *et al.*, 1998) on board the ACE spacecraft, was directed predominantly southward and duskward, with clock angles between 90°and 135°, and had been for some time (Figure 4.3, Panels G-K). The FUV-WIC imager (Mende *et al.*, 2000b) on board the IMAGE spacecraft detected a substorm onset at 14:05:55 UT (Frey and Mende, 2006). The cadence of WIC, however, means that the actual onset time could be up to 2 minutes earlier. Figure 4.4 shows FUV-WIC images around the time of substorm onset, with the magnetic footprints of TC-2 and C3, as calculated from the T96 magnetic field model (Tsyganenko and Stern,

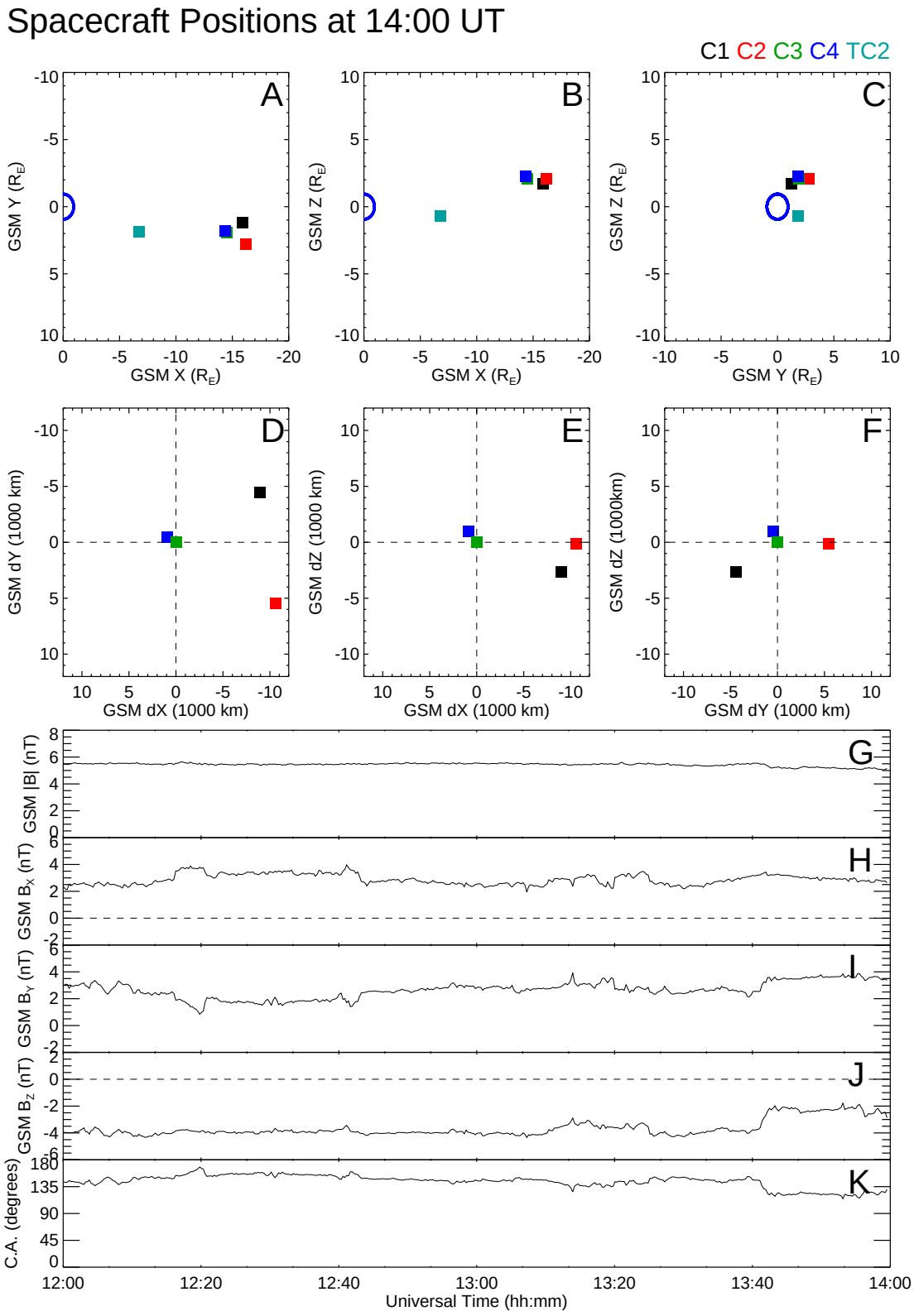

Figure 4.3: The positions of Cluster and Double Star TC-2 (Panels A-C) and the configuration of the Cluster tetrahedron (Panels D-F) at 14:00 UT on 21 September 2005 in the GSM coordinate system. The Cluster spacecraft are in a so-called "multiscale" configuration, where C1 (black), C2 (red) and C3 (green) form a triangle of side ∼10,000 km with C4 (blue) displaced in ∼Z by ∼1000 km. Panels G-J are the magnitude and GSM components of the Interplanetary Magnetic Field, and Panel K the IMF clock angle as measured by the MFI instrument on board the ACE spacecraft. These data have not been lagged to the magnetopause.

1996), with inputs from High Res OMNI solar wind data, marked as black diamond outlines just duskward of midnight MLT. The spacecraft footpoints were located within a few degrees MLAT and a few minutes of MLT of each other. Auroral activity is evident duskward of the spacecraft footpoints in the few minutes before substorm onset, however it appears to be dying down. A small, localised activation was observed close to midnight MLT, beginning at ∼13:57 UT and lasting until the westward travelling surge of the substorm encompassed its location after onset. The onset itself (Figure 4.4, lower middle image) was located significantly dawnward of the spacecraft footpoint, at ∼02:00 MLT.

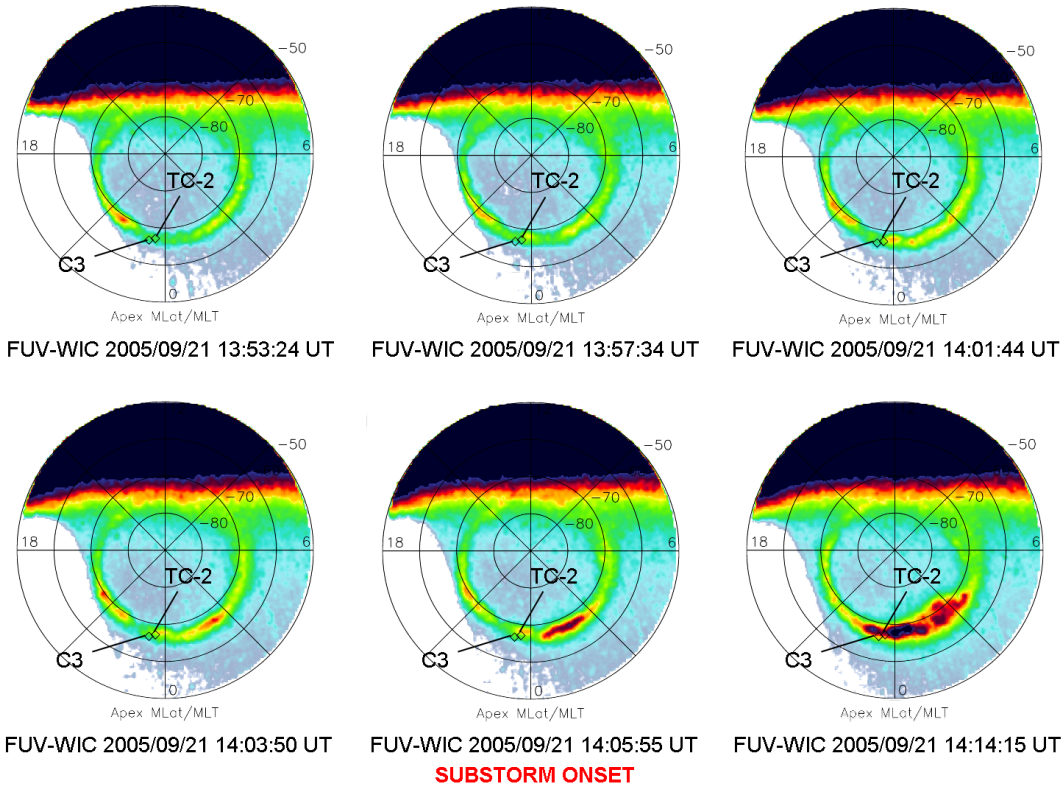

Figure 4.4: Auroral images of the South polar region, in AACGM Geomagnetic Latitude / Magnetic Local Time coordinates, taken by FUV-WIC on board the IMAGE spacecraft. The footprints of C3 and TC-2, as calculated from the T96 magnetic field model (Tsyganenko and Stern, 1996), are marked by black diamonds on each image.

Figure 4.5 shows the line of sight velocities from the two TIGER ionospheric radars, part of the southern hemisphere SuperDARN network (Greenwald *et al.*, 1995; Chisham *et al.*, 2007). The coloured squares show line of sight velocity, positive towards the appropriate radar, the contours are equipotentials derived from the map-potential technique and the T96 Cluster footpoint is marked by the black circle. The

ionospheric velocities detected by the TIGER radars are predominantly duskward so despite the lack of backscatter at the footpoint itself, it is reasonable to assume that the velocity in the ionosphere at this point will have a significant duskward component. It should be noted that the equipotential contours are derived from an IMF-driven statistical model constrained by available data, so the contours by themselves cannot be used to prove the presence of any flow as expected for a particular IMF direction.

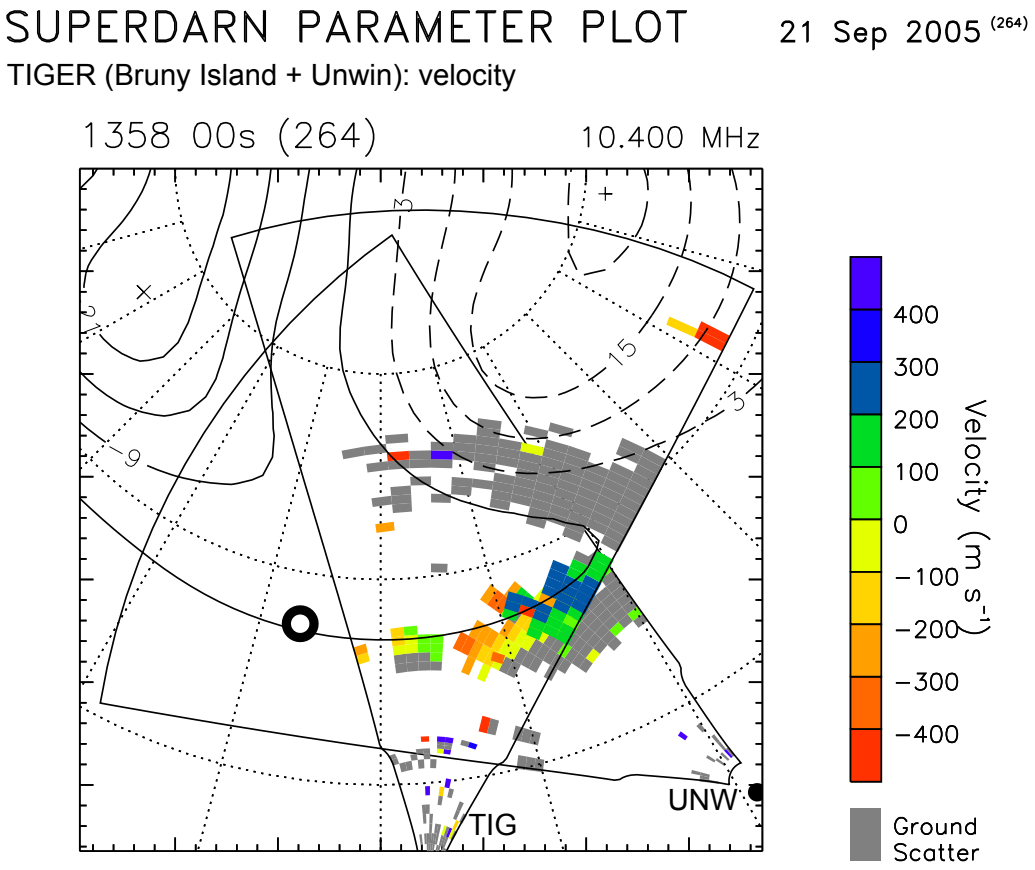

Figure 4.5: A line of sight velocity plot from the two TIGER southern hemisphere SuperDARN radars in AACGM Geomagnetic Latitude / Magnetic Local Time coordinates. The coloured squares represent plasma velocity, with positive velocity towards the radar and vice versa. Overlaid are equipotential contours showing the ionospheric convection pattern, as predicted by the map-potential technique. The T96 footpoint of the Cluster spacecraft is marked by the black circle.

In Figure 4.6 data from the four Cluster spacecraft, taken during the period of interest, are plotted. Panel A shows $|\boldsymbol{B}|$ and Panels B-D GSM B_X, B_Y and B_Z from the fluxgate magnetometer (FGM) experiment on board all four Cluster spacecraft (Balogh *et al.*, 2001). Panel E shows $v_{\perp X}$, the field-perpendicular velocity projected onto the GSM X axis (i.e. the X component of $\boldsymbol{v} - (\boldsymbol{v} \cdot \hat{\boldsymbol{b}})\hat{\boldsymbol{b}}$, where $\hat{\boldsymbol{b}}$ is the unit

vector of magnetic field) which is a measure of magnetic flux transport, for ions, as measured by CIS-HIA (Rème *et al.*, 2001, C1 and C3); for protons as measured by CIS-CODIF (Rème *et al.*, 2001, C4) and for electrons as measured by PEACE (Johnstone *et al.*, 1997, C2). There is no working ion instrument onboard C2. The electron velocities presented throughout this chapter were calculated on the ground from three-dimensional distributions that have been corrected for spacecraft potential and had photoelectron contamination removed. Panels F-I are energy-time spectrograms plotting omnidirectional differential energy flux for electrons from the PEACE instruments on board C1, C2, C3 and C4 respectively.

At 13:45 UT, the four Cluster spacecraft were located in the plasma sheet boundary layer north of the magnetotail neutral sheet (Figure 4.6, Panels B, F-I). Between 13:46 UT and 13:48 UT, C2, the southernmost spacecraft, measured a decrease in $|\mathbf{B}|$ from 19 nT to 9 nT and an increase in electron fluxes consistent with the spacecraft moving closer to the neutral sheet. C2 then crossed the neutral sheet at 13:51 UT. A minimum variance analysis (Sonnerup and Scheible, 2000) on this crossing determined the neutral sheet normal (i.e. the minimum variance direction) to be almost perfectly aligned with GSM Z:

$$\begin{array}{c} 0.212 \\ 2.05 \\ 81.1 \end{array} \left(\begin{array}{ccc} -0.058 & 0.048 & 0.997 \\ -0.074 & -0.996 & 0.043 \\ -0.996 & -0.071 & -0.062 \end{array} \right)$$

Here the well-separated eigenvalues (to the left of the rotation matrix) indicate a well-defined minimum variance direction. Consequently, to provide orientation with respect to the neutral sheet, GSM coordinates will be used throughout this chapter unless otherwise stated. C1, C3 and C4 also observed decreases in $|\boldsymbol{B}|$ of ~ 10 nT as they approached the neutral sheet. C1 and C3 observed this decrease between 13:50 UT and 13:53 UT, accompanied by increases in electron flux. C4 observed the $|\boldsymbol{B}|$ decrease over a much longer period (13:52 UT to 13:59 UT) but saw a similar increase in electron flux to the other spacecraft at 13:53 UT. Because C2 was the southernmost spacecraft and C4 the northernmost, the timing of these decreases in

$|\boldsymbol{B}|$ is consistent with the plasma sheet moving northward over the Cluster tetrahedron. While an expansion of a moving plasma sheet over the spacecraft cannot be ruled out, in this case it is unlikely that a static plasma sheet expanded over the spacecraft because relatively slow-moving spacecraft, such as Cluster near apogee, initially located as they were away from the neutral sheet, would not be expected to cross a static neutral sheet during such an expansion. Note that although there is a strong Y component of magnetic field, it remains approximately constant during the motion of the current sheet over the spacecraft, so we suggest that it can be considered to be related to the strong IMF B_Y rather than a result of any tilt of the neutral sheet (Cowley, 1981), consistent with the results of the MVA.

Between ∼13:58 UT and ∼14:01 UT C1, C3 and C4 each observe a dipolarisation in the magnetic field (Figure 4.6, Panel D) accompanied by an earthward flow of $\sim 300\,\mathrm{km\,s^{-1}}$. C2 observes no change in magnetic field direction but does see a tailward flow of $\sim 300\,\mathrm{km\,s^{-1}}$ between ∼13:59 UT and ∼14:03 UT. All the spacecraft detect a change in electron fluxes around the time of the flows.

After the auroral substorm onset, which according to the IMAGE data (Figure 4.4, middle bottom panel) occurred later, between 14:03:50 UT and 14:05:55 UT (The time of substorm onset is marked by dashed line 2 on Figure 4.6) at least two hours in MLT away from the spacecraft footpoints, the magnetic field as measured by all of the Cluster spacecraft becomes much more disturbed. C2 re-crosses the neutral sheet, subsequently remaining in the northern plasma sheet until 14:12 UT. No successful MVA could be carried out on this crossing. Further transient dipolarisation signatures and earthward flows were seen at ∼14:07 UT on all of the Cluster spacecraft and all spacecraft recorded a drop in electron fluxes. The magnetic field continued to evolve into a more dipolar configuration as the substorm progressed (not shown here).

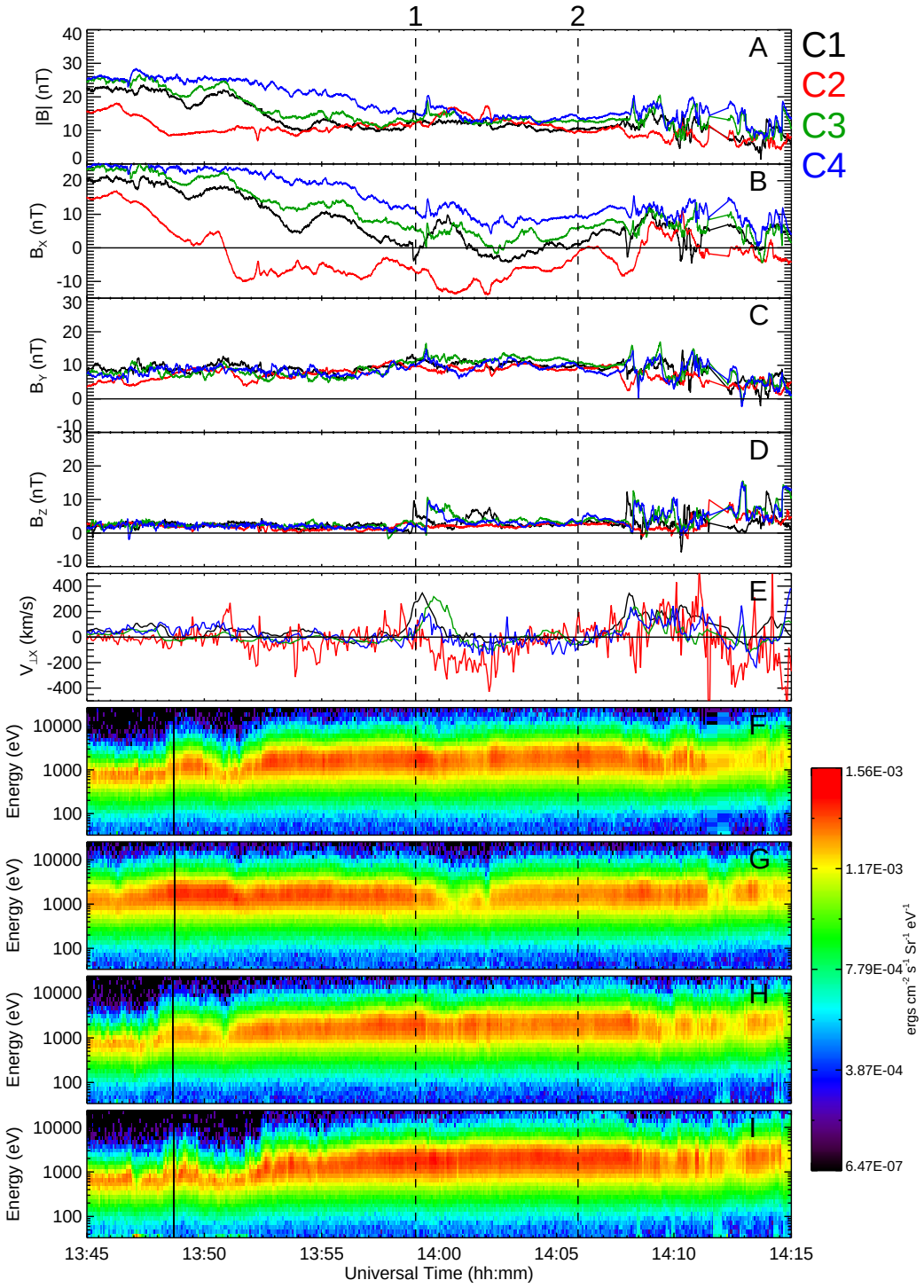

Figure 4.6: An overview of the interval of interest. Panel A shows the magnitude of the magnetic field as measured by FGM for C1, C2, C3 and C4 (black, red, green and blue traces, respectively); Panels B-D show the three vector components of magnetic field in the GSM coordinate system; Panel E shows the X component of the field-perpendicular velocity projected onto GSM axes for ions, as measured by CIS-HIA (C1 and C3); protons as measured by CIS-CODIF (C4) and electrons as measured by PEACE (C2). Panels F-I show energy-time spectrograms of omnidirectional differential energy flux for electrons from PEACE for C1, C2, C3 and C4 respectively. The dashed black lines labelled 1 marks the feature of interest, shown in more detail in Figures 4.7, 4.8, 4.9 and 4.10. The dashed black line marked 2 shows the latest possible time of substorm onset in the IMAGE FUV observations.

4.2.2 Detailed Cluster Observations

Figures 4.7, 4.8, 4.9 and 4.10 show more detail of the period of dipolarisation and flow (13:57:00 UT - 14:04:30 UT). Each figure shows data from one of the Cluster spacecraft, all following the same format. Panels A show GSM magnetic field components, Panels B $v_{//}$ and GSM components of $\boldsymbol{v}_{\perp}$, Panels C magnetic and (where available) ion contributions to total pressure; and Panels D-F electron spectrograms for pitch angles of 0, 90 and 180 degrees respectively. As before, velocities are taken from CIS-HIA on C1 and C3, CIS-CODIF on C4 and PEACE on C2. It should be noted here that a one-to-one comparison between plasma moments from different instruments is not always appropriate, although the PEACE and CIS instruments have been carefully cross-calibrated and $\boldsymbol{v}_{\perp}$ found to be comparable (Fazakerley *et al.*, 2009). Furthermore, in this case the direction of flow is more important than the magnitude so the difference in the top of the energy ranges of CIS-HIA and CIS-CODIF should not significantly alter our conclusions. The electron spectrograms are taken from PEACE-HEEA on all spacecraft apart from C3 where a non-functioning anode makes comparison of fluxes at different pitch angles difficult. The energy range of the LEEA sensor still covers the majority of the electron distribution and as such data from that sensor are used for C3.

C1, C3 and C4 all observed similar features during this period, consistent with the passage of a plasma bubble over those spacecraft. All three spacecraft observed a sharp increase in B_Z, marked by a vertical dashed line on each figure. C1 detected it first at $\sim$13:58:55 UT, C3 and C4 detected it $\sim$30 s later (Figures 4.7, 4.9 and 4.10, Panels A). A smaller sharp change in B_X was also detected at the time of dipolarisation; C1 and C3 observed a negative δB_X while C4 observed a positive δB_X. Contemporary with the dipolarisation the three spacecraft detected a sharp drop in perpendicular electron fluxes (Figures 4.7, 4.9 and 4.10, Panels E) and an increase in parallel and anti-parallel electron fluxes (Figures 4.7, 4.9 and 4.10, Panels D and F). C1 and C3 detected a decrease in ion pressure at the time of dipolarisation that lasted for $\sim$180 s at C1 and $\sim$90 s at C3. These decreases were accompanied by

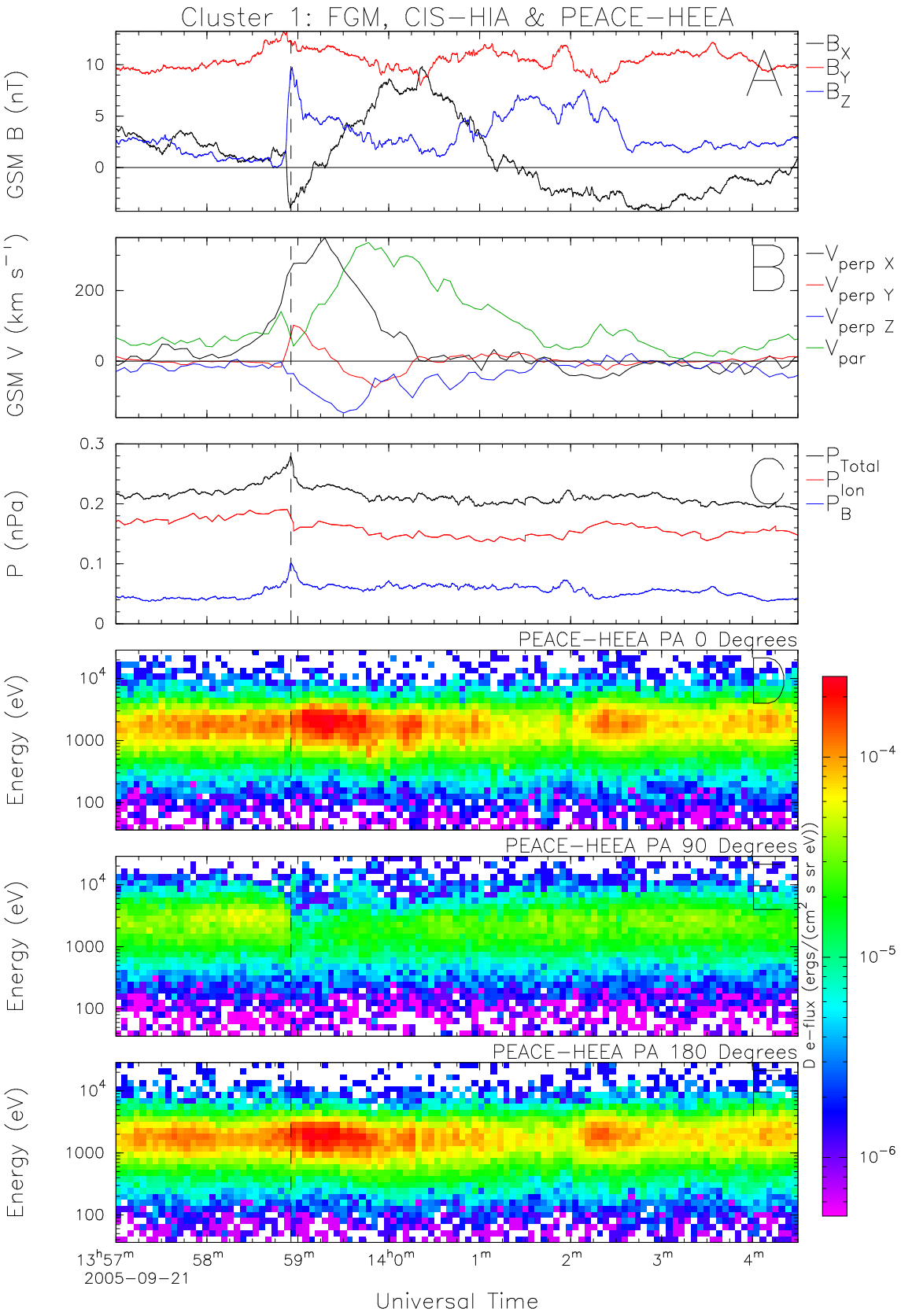

Figure 4.7: C1 observations of the field dipolarisation and associated plasma features. Panel A shows GSM B_X (black), B_Y (red) and B_Z (blue) from FGM; Panel B GSM $v_{\perp X}$ (black), $v_{\perp Y}$ (red), $v_{\perp Z}$ (blue) and $v_{//}$ (green) for ions from CIS-HIA; Panel C total (i.e. magnetic + ion) pressure (black), ion pressure (red) and magnetic pressure (blue) and Panels D-F energy time spectrograms from PEACE-HEEA for pitch angles of 0°, 90° and 180° respectively. The vertical dashed line marks the entry of the spacecraft into the region of interest.

increases in magnetic pressure which began just prior to dipolarisation and peaked at the time of the dipolarisation front arriving at each spacecraft. C4 observed a similar increase in magnetic pressure, although no decrease in proton pressure is evident in the somewhat noisy CODIF data (Figures 4.7, 4.9 and 4.10, Panels C).

The behaviour of velocity (Figures 4.7, 4.9 and 4.10, Panels B) is also similar on C1, C3 and C4. In all cases an earthward flow (i.e. $v_{\perp X} > 0$) was detected. The flow began just before the dipolarisation and, on C1 and C3, peaked $\sim 15\,\mathrm{s}$ after dipolarisation. The dipolarisation observed by C4 was contemporary with the approximate centre of the earthward flow period, which in this case peaked just prior to dipolarisation. The period of earthward flow continued for approximately one minute after dipolarisation in the case of both C1 and C3 while on C4 the earthward flow stopped $\sim 40\,\mathrm{s}$ after dipolarisation. The peak velocities recorded by the ion instruments were $\sim 350\,\mathrm{km\,s^{-1}}$, $\sim 320\,\mathrm{km\,s^{-1}}$ and $\sim 180\,\mathrm{km\,s^{-1}}$ for C1, C3 and C4 respectively. In all cases, the earthward flow was followed by a period of weaker (i.e. $|v_{\perp X}| < 100\,\mathrm{km\,s^{-1}}$) tailward flow, although while C3 and C4 observed this immediately after the earthward flow, C1 observed a short stagnation period of duration $\sim 90\,\mathrm{s}$ where no significant earthward or tailward flow was detected. Another enhancement in parallel and anti-parallel electron fluxes was detected by C1 at the same time as the tailward flow. In the case of C3 and C4, the earthward flow stopped at the end of the period of enhanced magnetic pressure/reduced ion pressure; while for C1, the enhanced magnetic pressure/reduced ion pressure continued until the short burst of tailward flow and (anti-)parallel electron flux enhancement some time after the end of the earthward flow. Slower (i.e. $|v_{\perp Y}| \lesssim 100\,\mathrm{km\,s^{-1}}$) dawnward and duskward flows were detected by C3 and C4 contemporary with the earthward and tailward flows (i.e. $v_{\perp Y}$ and $v_{\perp X}$ were in antiphase), again beginning just prior to dipolarisation. No significant $v_{\perp Y}$ was detected by C1 prior to dipolarisation, instead a short interval of duskward flow was detected just after dipolarisation while B_X was negative, turning dawnward when B_X became positive. In all cases, a negative $v_{\perp Z}$ was detected, beginning at the time of dipolarisation.

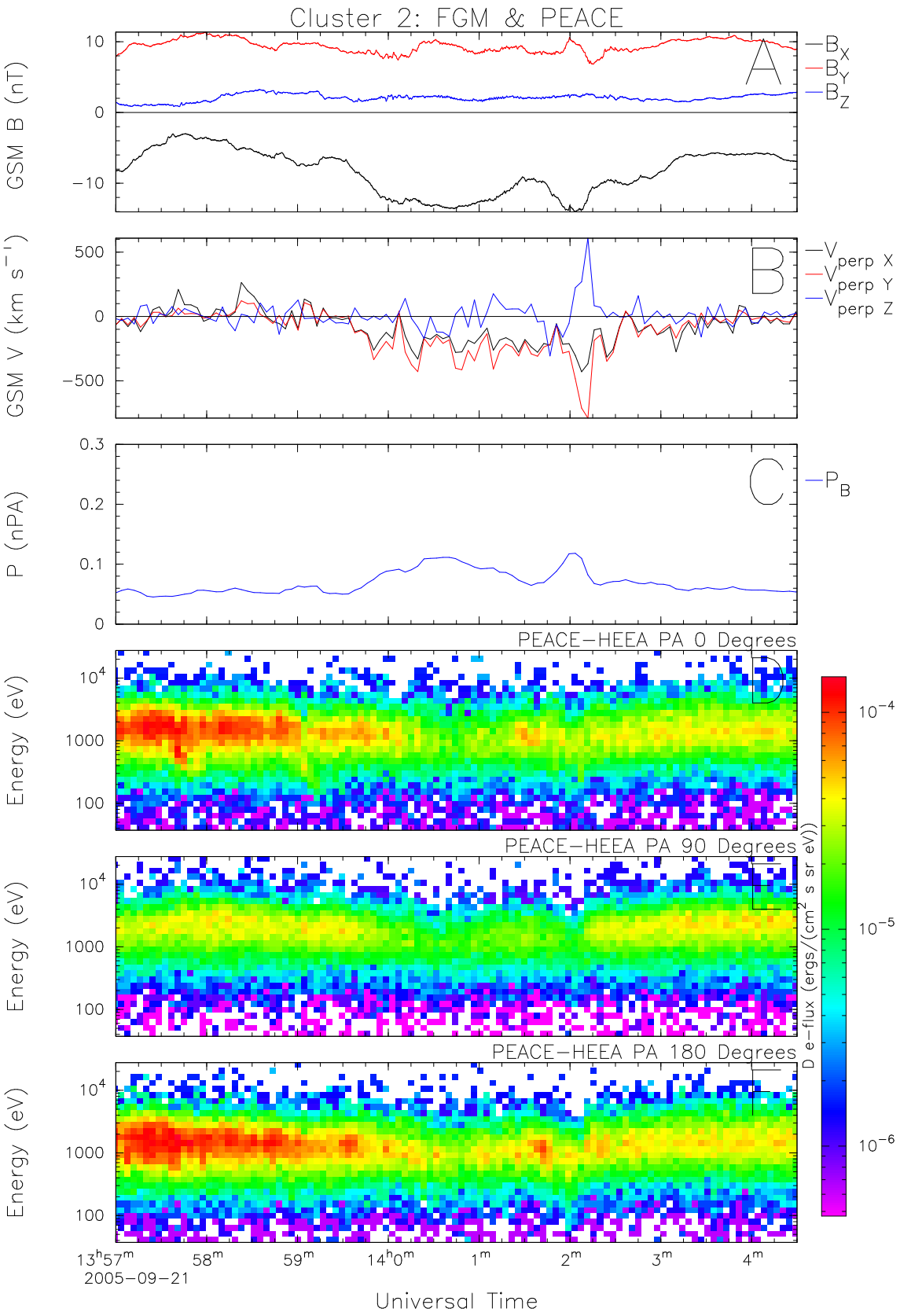

Figure 4.8: C2 observations of the field dipolarisation and associated plasma features. Panel A shows GSM B_X (black), B_Y (red) and B_Z (blue) from FGM, Panel B GSM $v_{\perp X}$ (black), $v_{\perp Y}$ (red), $v_{\perp Z}$ (blue) and $v_{//}$ (green) for electrons from PEACE, Panel C magnetic pressure (blue) and Panels D-F energy time spectrograms from PEACE-HEEA for pitch angles of 0°, 90° and 180° respectively.

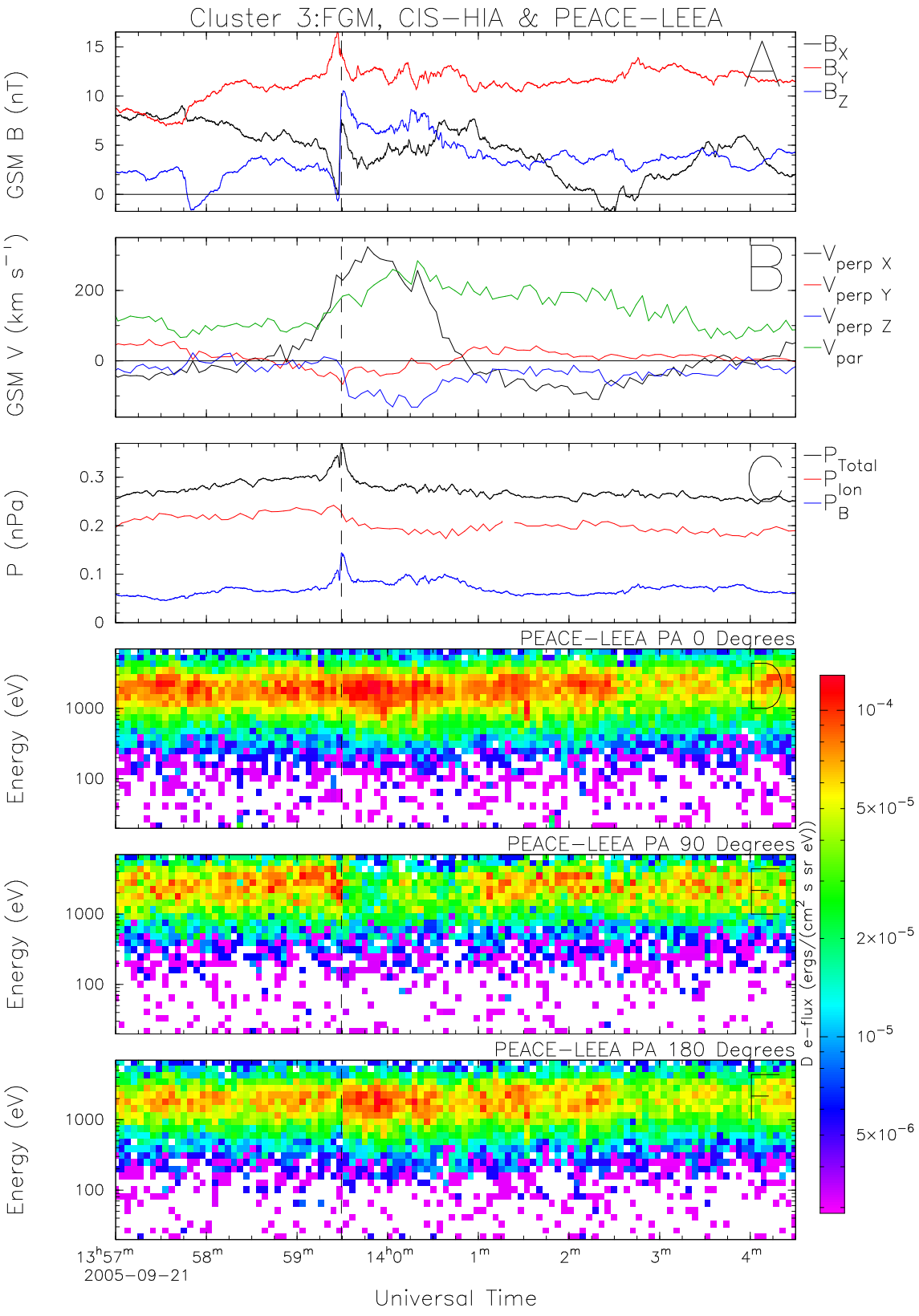

Figure 4.9: C3 observations of the field dipolarisation and associated plasma features. Panel A shows GSM B_X (black), B_Y (red) and B_Z (blue) from FGM, Panel B GSM $v_{\perp X}$ (black), $v_{\perp Y}$ (red), $v_{\perp Z}$ (blue) and $v_{//}$ (green) for ions from CIS-HIA, Panel C total (i.e. magnetic + ion) pressure (black), ion pressure (red) and magnetic pressure (blue) and Panels D-F energy time spectrograms from PEACE-LEEA for pitch angles of 0°, 90° and 180° respectively. Note that the energy range for these PEACE spectrograms is different from those in the The vertical dashed line marks the entry of the spacecraft into the region of interest.

C1, C3 and C4 all detected enhanced positive $v_{//}$ in the region of enhanced magnetic pressure (Figures 4.7, 4.9 and 4.10, Panels B). In the case of C1 the increase in $v_{//}$ began just after the dipolarisation, when B_X began to recover from its sharp decrease in magnitude. $v_{//}$ reached a peak value of $\sim 340\,\mathrm{km\,s^{-1}}$ at 13:59:45 UT, 30 seconds after the peak in $v_{\perp X}$ and then decreased gradually to its undisturbed value by 14:02 UT, when the spacecraft exited the region of enhanced magnetic pressure. C3 detected a slightly different signature in $v_{//}$: $v_{//}$ increased from a higher background level of $\sim 100\,\mathrm{km\,s^{-1}}$ to a peak $\sim 280\,\mathrm{km\,s^{-1}}$, again $\sim 30\,\mathrm{s}$ after the peak in $v_{\perp X}$. The increase began at the time of dipolarisation and $v_{//}$ returned to its undisturbed value at the end of the period of tailward flow, $\sim$14:03:30 UT. C4 recorded similar features in $v_{//}$ to C3.

During the same interval C2 observed quite different features. No dipolarisation was evident, nor was there any period of earthward flow. Instead a prolonged period of tailward and dawnward flow was measured in the electron moments at the same time as increases in magnetic pressure and $|B_X|$. In contrast to the other three spacecraft, no significant $v_{\perp Z}$ was detected, nor any increase in parallel or antiparallel electron fluxes. Indeed these electron fluxes actually decreased, as did the perpendicular electron flux.

4.2.3 Double Star TC-2 Observations

In Figure 4.11 data from the Double Star TC-2 spacecraft, taken between 14:00 UT and 14:05 UT are plotted. Panel A shows the three GSM components of magnetic field from the FGM instrument on board TC-2 (Carr *et al.*, 2005), Panel B shows the three components of magnetic field with the mean field removed, Panel C shows the magnitude of the field with the mean field removed and Panel D is feather plot of magnetic field vectors (see Volwerk *et al.*, 1996, for example) showing any rotations of the magnetic field in a mean-field-aligned coordinate system, whereby one of the axes is defined as the direction of the magnetic field when filtered to remove any

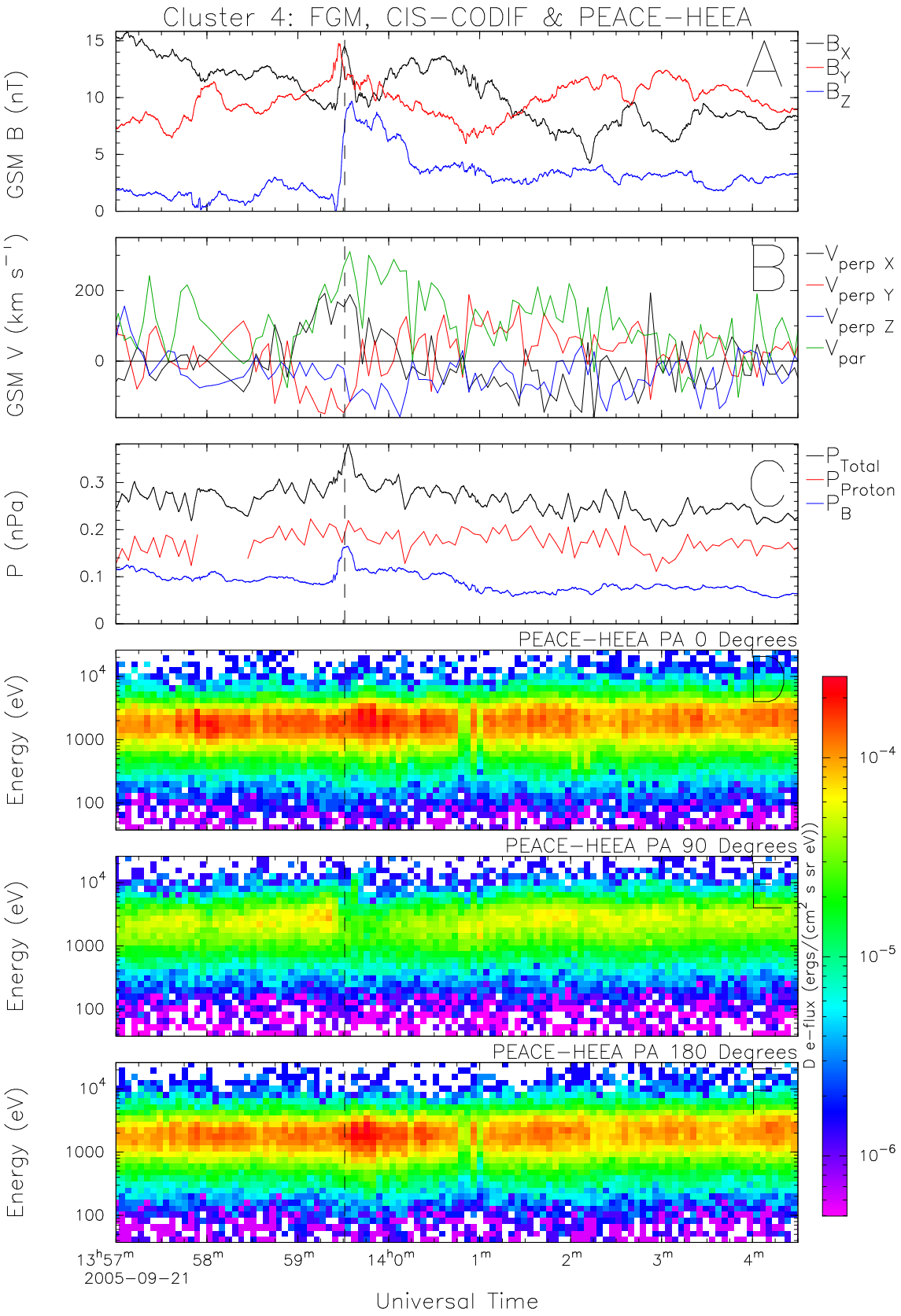

Figure 4.10: C4 observations of the field dipolarisation and associated plasma features. Panel A shows GSM B_X (black), B_Y (red) and B_Z (blue) from FGM, Panel B GSM $v_{\perp X}$ (black), $v_{\perp Y}$ (red), $v_{\perp Z}$ (blue) and $v_{//}$ (green) for ions from CIS-CODIF, Panel C total (i.e. magnetic + ion) pressure (black), ion pressure (red) and magnetic pressure (blue) and Panels D-F energy time spectrograms from PEACE-HEEA for pitch angles of 0°, 90° and 180° respectively. The vertical dashed line marks the entry of the spacecraft into the region of interest.

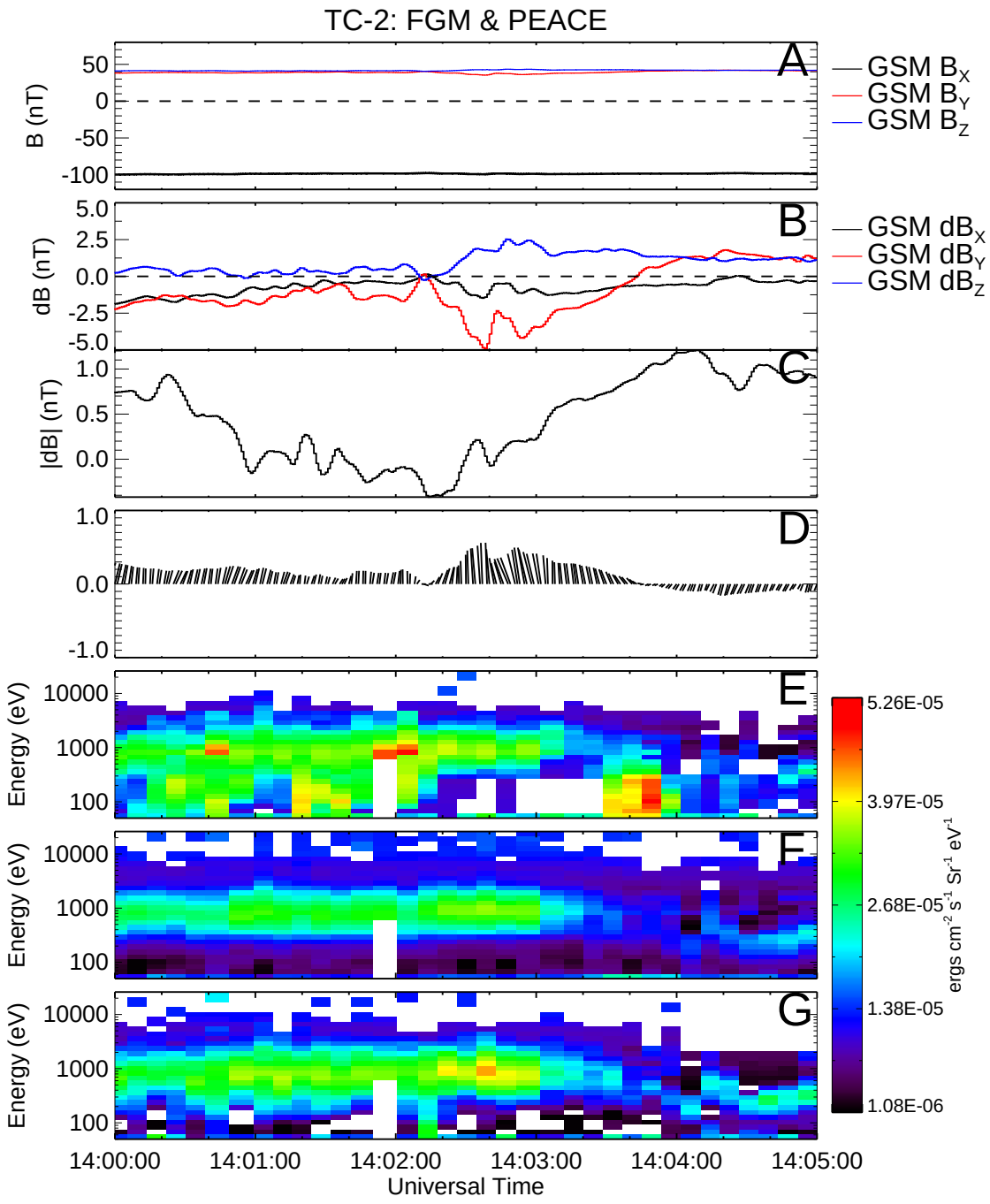

Figure 4.11: Data from the FGM and PEACE instruments on board Double Star TC-2. Panel A shows the 3 GSM components of magnetic field, Panel B the 3 GSM components of magnetic field with the mean field subtracted and Panel C $|d\boldsymbol{B}|$ (i.e. the magnitude of any deviations from the mean field). Panel D is a feather plot showing rotations in the magnetic field that indicate the presence of field-aligned currents near the spacecraft, and Panels E, F and G show electron energy time spectrograms for electrons with pitch angles of 0, 90 and 180 degrees respectively.

oscillations with periods shorter than ten minutes, a second axis is defined as the cross product of the first axis and the GSM position vector of the spacecraft and the third completes a right handed set. Here the mean field axis points out of the page, so an anticlockwise rotation of the field vectors with time on the plot represents the effect of a parallel current and vice versa. Panels E-G are energy-time spectrograms for electrons with pitch angles of 0°, 90° and 180°, respectively, as measured by the PEACE instrument on board TC-2 (Fazakerley *et al.*, 2005). It should be noted that because the Double Star PEACE instrument has one sensor, rather than the two that make up each Cluster instrument, a distribution covering the full energy range is accumulated every two spins (i.e. eight seconds) rather than every spin (see Section 2.3.1 for details).

At 14:00 UT, the TC-2 spacecraft was located south of the tail neutral sheet (Figure 4.11, Panel A) some $7\,R_E$ antisunward of Earth moving north towards the central plasma sheet. At ∼14:02 UT, the spacecraft detected a small clockwise rotation in the magnetic field, (Figure 4.11, Panel D) and an enhancement in the flux of parallel electrons (Figure 4.11, Panel E). At the same time a transient peak in B_Y is observed (Figure 4.11, Panel B). Immediately following these features, at 14:02:20 UT a transient dipolarisation of the field was detected, accompanied by a small increase in magnetic pressure (Figure 4.11, Panel C). An enhancement in antiparallel electron flux was detected, peaking at ∼14:02:40 UT (Figure 4.11, Panel G), accompanied by a minor anticlockwise rotation in the field and a short dip in the otherwise increasing magnetic pressure. After 14:03 UT the spacecraft entered a more lobe-like environment, as evidenced by a drop in electron fluxes and increase in magnetic pressure, before detecting a low energy (i.e. with a peak flux at ∼200 eV) field-aligned electron beam at ∼14:03:40 UT accompanied by a much larger anticlockwise rotation in magnetic field. All of this occurred before the substorm onset a few hours dawnward in Magnetic Local Time.

4.3 Discussion

4.3.1 Cluster Data

The magnetic field dipolarisations and associated plasma data observed by C1 (Figure 4.7) C3 (Figure 4.9) and C4 (Figure 4.10) are consistent with signatures predicted by theory, simulation and reported from previous near-equatorial observations of plasma bubbles; namely a transient dipolarisation and earthward flow, a reduction in plasma pressure and an increase in magnetic pressure (maintaining approximately constant total pressure). Sergeev *et al.* (1996) interpreted regions of earthward-flowing plasma with lower plasma pressure than their surroundings, accompanied by transient dipolarisations in the magnetic field as plasma bubbles; all of these features have been reported here. More recently Forsyth *et al.* (2008) reported enhancements in bi-directional electron fluxes inside a structure interpreted to be a plasma bubble, which were explained as a product of reconnection. A similar pitch angle distribution has been observed here by C1, C3 and C4.

The entry of the Cluster spacecraft into the depleted flux tube (plasma bubble) can be identified from several features in the data, most obviously the increases in B_Z and P_B (Figures 4.7, 4.9 and 4.10, Panels A and C) and decreases in P_{Ion} and perpendicular electron flux (Figures 4.7, 4.9 and 4.10, Panels C and E).

The direction of any field-aligned currents detected at the edge of a plasma bubble can help determine where a spacecraft entered the depleted flux tube, as can the magnetic shear just outside the boundary of the plasma bubble (Sergeev *et al.*, 1996). In general there are several possible ways of determining if any field-aligned currents are present. The curlometer technique (Dunlop *et al.*, 2002) has been used to study larger scale current systems within a bubble at a 300 km tetrahedron scale size (Forsyth *et al.*, 2008) but cannot be applied here because the scale size of the Cluster tetrahedron in our event is much larger, and is comparable to the scale size of previously observed BBFs and plasma bubbles . The curlometer is only accu-

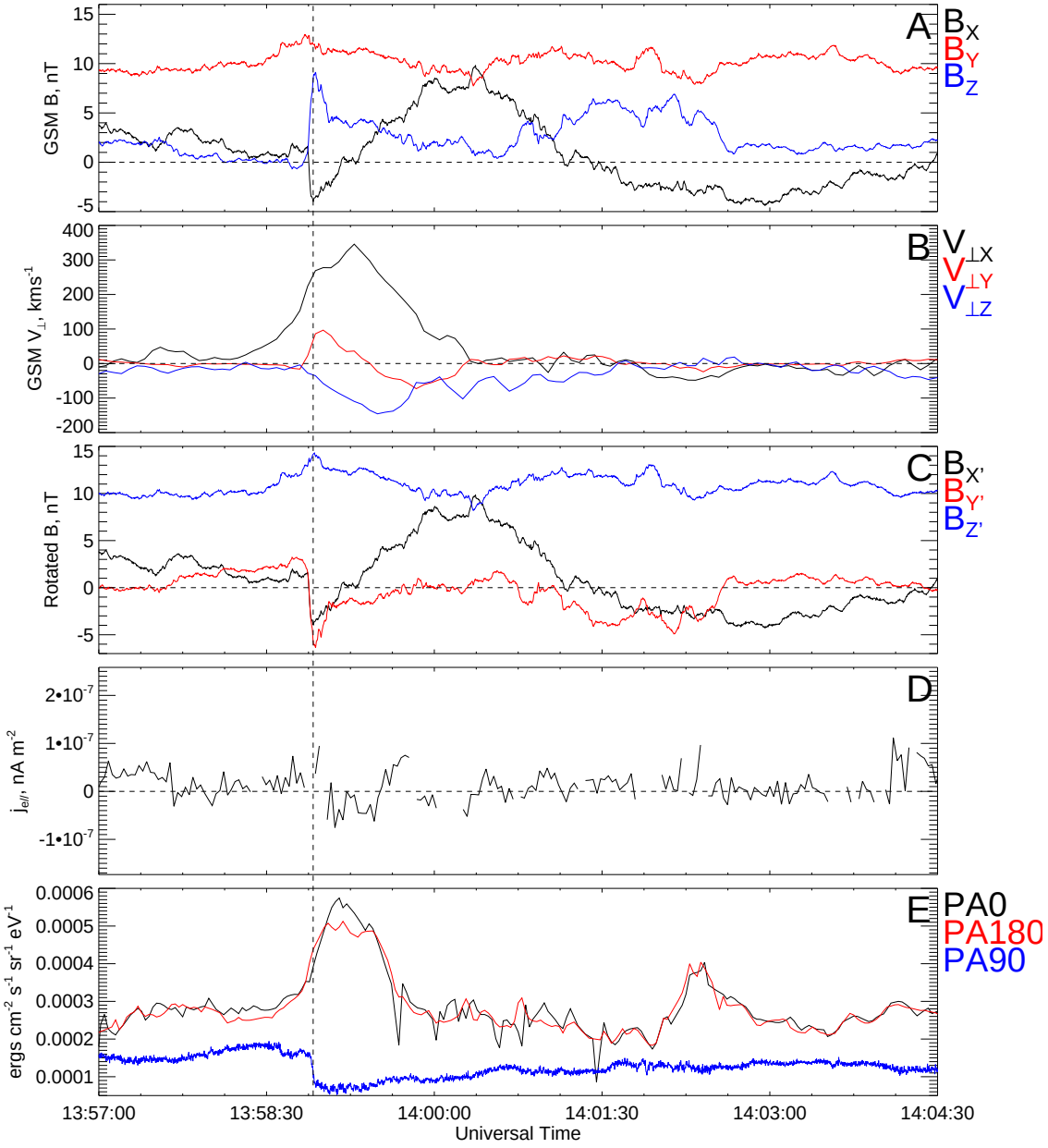

Figure 4.12: Data pertaining to the entry of C1 into the plasma bubble. Panel A shows GSM components and magnitude of magnetic field, Panel B the GSM components of $\boldsymbol{v}_\perp$, Panel C the magnetic field rotated about GSM X into a coordinate frame that eliminates any Y component in the undisturbed magnetic field, in order to identify any draping in the field around the plasma bubble. Panel D is the parallel electron current calculated from 2D pitch angle distributions in the energy range covered by both PEACE sensors. Panel E shows the electron differential energy fluxes separately for 0° PA (pitch angle), 180° PA and 90° PA, taken from 3D distributions returned by both the HEEA and LEEA sensors and summed over their common energy range. The vertical dashed line marks the entry of the spacecraft into the plasma bubble.

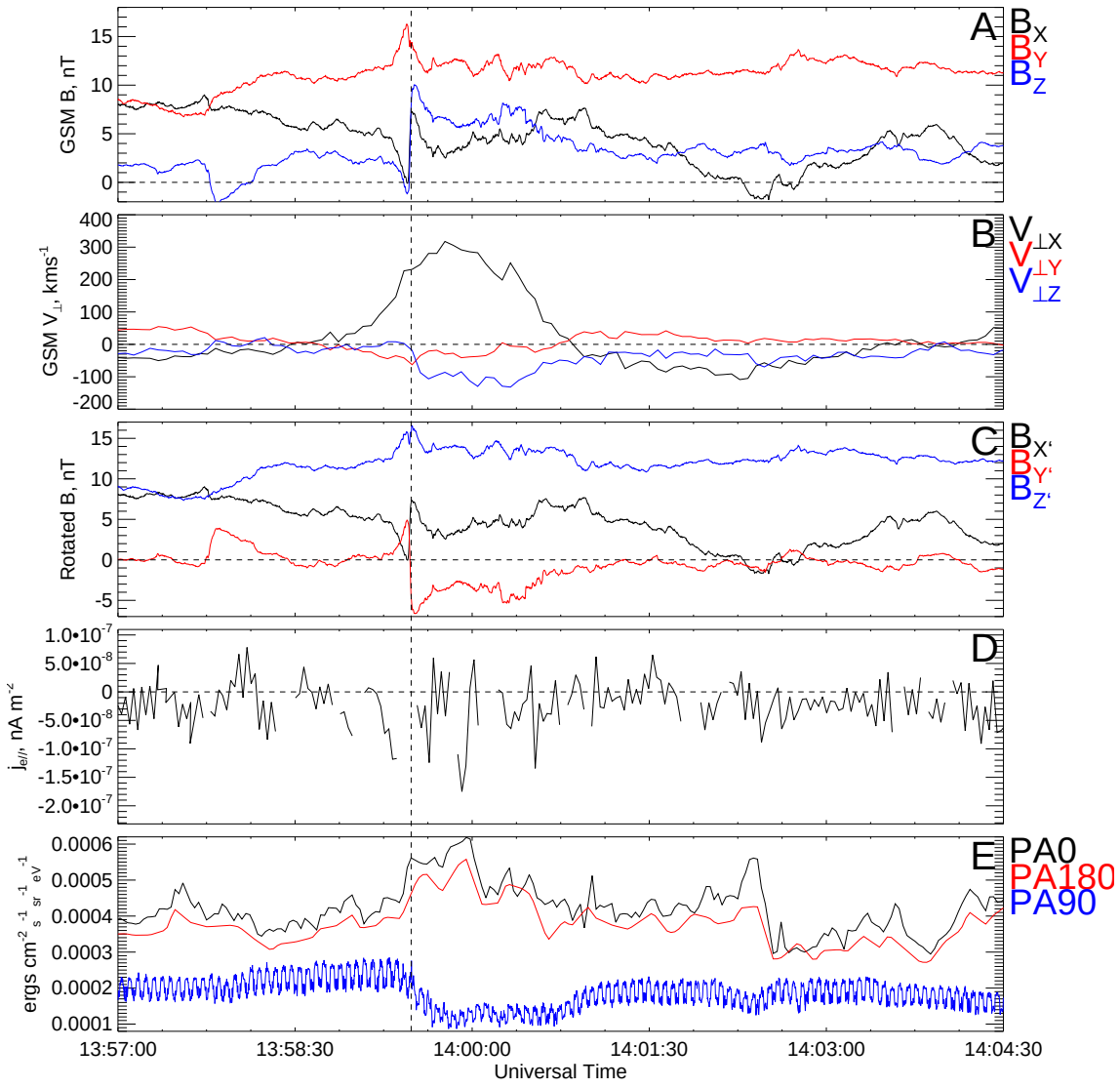

Figure 4.13: Data pertaining to the entry of C3 into the plasma bubble. Panel A shows GSM components and magnitude of the magnetic field, Panel B the GSM components of $\boldsymbol{v}_\perp$, Panel C the magnetic field rotated about GSM X into a coordinate frame that eliminates any Y component in the undisturbed magnetic field, in order to identify any draping in the field around the plasma bubble. Panel D is the parallel electron current calculated from 2D pitch angle distributions in the energy range covered by both PEACE sensors. Panel E shows the electron differential energy fluxes separately for 0° PA, 180° PA and 90° PA, taken from 3D distributions returned by both the HEEA and LEEA sensors and summed over their common energy range. The vertical dashed line marks the entry of the spacecraft into the plasma bubble.

rate when used to study currents much larger than the scale size of the Cluster tetrahedron. Furthermore, C2 is located south of the neutral sheet while the other spacecraft are located north of the neutral sheet; this would render multispacecraft techniques like the curlometer ineffective since bubble-related FACs in either hemisphere are expected to flow in different directions. Below we have attempted to identify any field aligned currents by looking for magnetic shear and also by seeking evidence in the electron data from the PEACE instruments.

Figures 4.12, 4.13 and 4.14 show data from which the presence and direction of any field-aligned currents around the plasma bubble can be determined. For context, Panels A show GSM magnetic field components and Panels B GSM components of $\boldsymbol{v}_\perp$. Panels C show the magnetic field components in a different coordinate system discussed in more detail below. Panels D show a partial parallel electron current density calculated from moments of the two-dimensional pitch angle distributions returned from the PEACE-LEEA and PEACE-HEEA sensors, restricted to energies covered by both sensors (i.e. $\sim$30 eV-6 keV), while Panels E show a scalar energy flux of electrons calculated from 3D distributions returned by both PEACE sensors that have been summed over the sensors' common energy range. Fluxes at 0° PA, 90° PA and 180° PA are plotted. Each of these methods can be used to detect the presence of FACs and they each have advantages and disadvantages as described below. On each plot the vertical dashed line marks the time of the spacecraft's entry into the depleted flux tube, based on the time of dipolarisation and decrease in 90° pitch angle electron flux.

2D pitch angle distributions are returned from each PEACE sensor every spin and have a pitch angle resolution of 15°. Pitch angle selection is carried out on-board using the inter-experiment link with the FGM instrument and is based on magnetic field data collected at the end of the previous spin. As such, should the magnetic field direction change over the course of one spin the instrument will not necessarily be looking along the field when the pitch angle distribution is returned, giving incorrect data. This data is corrected on the ground where a rebinning process assigns

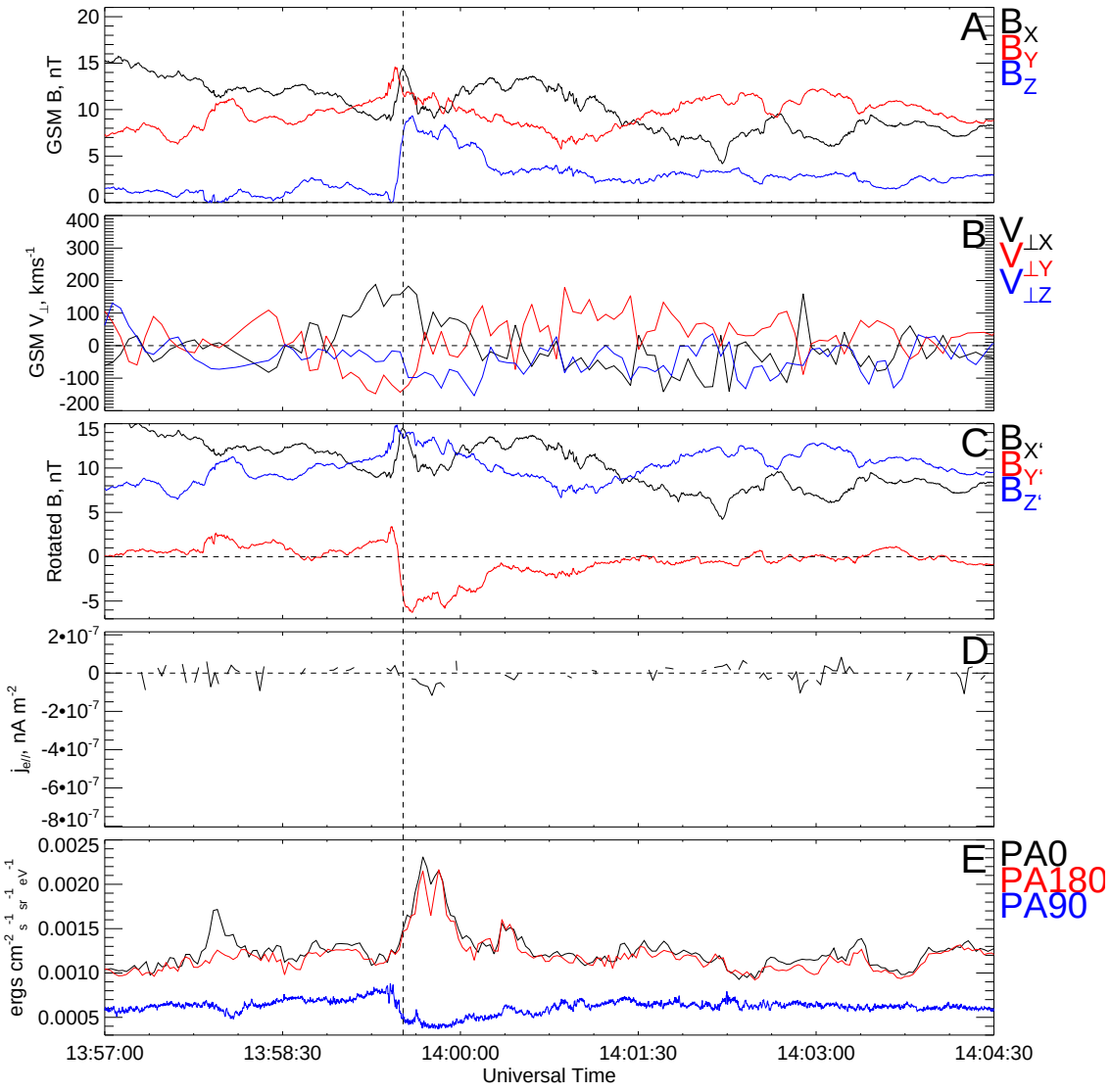

Figure 4.14: Data pertaining to the entry of C4 into the plasma bubble. Panel A shows GSM components and magnitude of the magnetic field, Panel B the GSM components of $\boldsymbol{v}_\perp$, Panel C the magnetic field rotated about GSM X into a coordinate frame that eliminates any Y component in the undisturbed magnetic field, in order to identify any draping in the field around the plasma bubble. Panel D is the parallel electron current calculated from 2D pitch angle distributions in the energy range covered by both PEACE sensors. Panel E shows the electron differential energy fluxes separately for 0° PA, 180° PA and 90° PA, taken from 3D distributions returned by both the HEEA and LEEA sensors and summed over their common energy range. The vertical dashed line marks the entry of the spacecraft into the plasma bubble.

accurate pitch angles each PEACE anode. When a full pitch angle distribution cannot be recovered this results in data gaps such as those seen in the Figures 4.12-4.14, Panels D. For more details of the acquisition of pitch angle distributions, see Section 2.2.2.3.2. In a burst mode telemetry interval in the magnetotail 3D distributions are returned from both sensors every spin by C2 and C4, while on C1 and C3 3D distributions are returned from HEEA every spin and from LEEA for most spins. Because of telemetry constraints, these 3D distributions, while providing more complete pitch angle coverage in all but the most rapidly varying magnetic fields, have reduced angular or energy resolution (depending on instrument mode) when compared to the 2D pitch angle distributions. In both the 2D and 3D cases, because of the position of the sensors on the spacecraft, when data from both sensors is combined a full pitch angle distribution (albeit a distribution restricted to the energy range covered by both of the sensors) can be collected every two seconds. When a 3D LEEA distribution was unavailable from C1 or C3 for a given spin, interpolation was used to create a consistent time series across all spacecraft. The majority of the electron distribution lay within the energy range of LEEA (see Figure 4.9, bottom 3 panels), so our assumption that most of the electron contribution to the current density is being measured using this method seems reasonable.

Any shear in the ambient plasma magnetic field caused by the passage of a moving flux tube should manifest itself in the field component perpendicular to both the direction of motion of the flux tube and the flux tube "axis". For a canonical magnetotail with no significant B_Y, the shear is in the Y direction (Sergeev *et al.*, 1996). In this case, because there is a strong B_Y in the tail, that effectively rotates the flux tube axis out of the XZ plane, any shear should be in the plane perpendicular to the axis. As such, the FGM data in Panels C have been rotated about the GSM X axis such that any B_Y in the undisturbed tail tends to zero, thus any shear in the magnetic field caused by the passage of the plasma bubble should only appear in the new Y component, Y'.

C1 detected an increase in $B_{Y'}$ beginning at 13:57:30 UT (Figure 4.12, Panel C)

which lasted until the entry into the plasma bubble. Because the spacecraft was located north of the neutral sheet, this field draping is consistent with C1 entering the bubble on its dawnward flank, i.e. $B_{X'} \cdot \delta B_{Y'} > 0$ (Sergeev *et al.*, 1996). There is evidence of an imbalance in the 0° PA and 180° PA electron fluxes (Figure 4.12, Panel E) at the time of dipolarisation, which could represent a parallel electron current, consistent with the magnetic field draping. This feature, however, occurs over a very short period of time and consists of only two data points. Because of the rapidly varying magnetic field direction at this time, the pitch angle selection on board the spacecraft was imperfect. This resulted in a data gap in the 2D distributions from which the partial current density (Figure 4.12, Panel D) was calculated, as described above. We cannot be sure, therefore, that the imbalance in electron flux was actually a real current. An attempt to calculate a "parallel current flux" from the 3D distributions (not shown) did not reveal any currents larger than the background noise level, presumably because of the coarser angular resolution of the 3D distributions. Just after the dipolarisation there was a period of several spins where PEACE detected a greater flux of 0° PA electrons than 180° PA electrons. We suggest this feature is too far from the bubble boundary to represent a FAC at its edge. The sharp (i.e. 1 data point) drops in the parallel electron fluxes at 13:59:40 UT, 14:00:46 UT and 14:01:25 UT are artefacts of the process used to combine data from the two PEACE sensors. The magnetic field data then, suggest that C1 entered the plasma bubble on its dawnward side and while the electron data do not contradict this interpretation, data gaps mean that they cannot confirm it either.

Although there is evidence of magnetic field draping on C3 before entering the plasma bubble (Figure 4.13, Panel C), its duration is much shorter than that of the draping observed by C1. This limited draping is still consistent with entry of the spacecraft into the dawnward side of the plasma bubble. Just prior to the time of dipolarisation there is evidence in the PEACE data of an antiparallel current (Figure 4.13, Panel D) above background levels. Although, like on C1, there is a data gap at the time of dipolarisation, in this case the magnitude of the current

density is above the background level for the 4 data points preceding the gap, making it more convincing evidence of a current. In this case the current is consistent with spacecraft entry through the duskward edge of the plasma bubble since $B_X > 0$. This contradictory electron and magnetic data may be a result of the spacecraft being located close to the centre line of the plasma bubble, although the imperfect electron pitch angle selection and resulting data gap at the time of dipolarisation make it is impossible to tell for sure. The systematic imbalance between 0° PA and 180° PA electron fluxes, seen on the bottom panel of Figure 4.13 but not reflected in the current moments, continues for the entire duration of the burst mode and is most probably a result of an imperfect instrument calibration on this particular day.

C4 seems to show a smaller degree of draping than C1 (Figure 4.14, Panel C) though the draping that is evident is consistent with an entry into the plasma bubble on the dawnward side. The PEACE moments, however, are inconclusive containing as they do numerous data gaps, again a result of imperfect pitch angle selection on board the spacecraft.

While C4 is the only spacecraft that detects a significant $v_{\perp Y}$ before entry into the flux tube (the flow shear layer predicted and observed by Sergeev *et al.*, 1996), C1, C3 and C4 observe earthward flow before the entry into the plasma bubble. We suggest that this flow represents plasma being swept up in front of the earthward moving bubble. This sweep-up can be seen as a gradual increase in the perpendicular electron flux (Figures 4.12, 4.13 and 4.14, Panels E) beginning $\sim$1 minute before entry into the depleted flux tube. An increase in magnetic pressure is also seen closer to the edge of the bubble as magnetic flux is also swept up in front of the depleted flux tube (Figures 4.7, 4.9 and 4.10, Panel C). Plasma sweep up has been previously observed by Slavin *et al.* (2003a) in front of earthward-moving, BBF type flux ropes.

The exit from the plasma bubble is much less clear in the data, in fact different features are observed by the different spacecraft. In the case of C1, the earthward flow ended just after 14:00 UT (Figure 4.7, Panel B), some two minutes before the

ion pressure returns to its undisturbed value (Figure 4.7, Panel C), at which time B_Z also decreases to its undisturbed value (Figure 4.7, Panel A). C3 on the other hand detected the end of the earthward flow (Figure 4.9, Panel B) at exactly the same time as the ion pressure (Figure 4.9, Panel C) returned to its undisturbed value and B_Z (Figure 4.9, Panel A) decreased, although not all the way to its undisturbed value. C4 also observed the end of the earthward flow (Figure 4.10, Panel B) and a decrease in B_Z (Figure 4.10, Panel A) at the same time. The examination of perpendicular electron fluxes on all four Cluster spacecraft (Figures 4.12-4.15, bottom panel, discussion below) will help to resolve this apparent inconsistency in the data.

Figure 4.15, following the same format as Figures 4.12-4.14, examines the PEACE data for C2 in more detail. Given that C2 did not observe the plasma bubble, but was instead located duskward of it, and in the southern hemisphere, it might be expected that during the tailward flow, depending on the spatial extent of the field-aligned current system associated with the bubble, weak parallel currents would be detected. No currents above the background level are seen in the PEACE data, however (Figure 4.15, Panel D). Unlike the other Cluster spacecraft, however, the 0° PA and 180° PA electron fluxes did not increase during the flow period, instead, on average, they decreased as did the 90° PA electron flux. The tailward flows detected by PEACE at this time are consistent with return flows that are expected to be found around the edges of a plasma bubble (e.g. Birn *et al.*, 2004) which have not been directly measured in the past. What is not predicted by theory or simulation, though, is the decrease in electron flux (i.e. plasma density) in the tailward flowing plasma around the edges of a BBF. This may be a situation analogous to plasma depletion layers at the magnetopause (Zwan and Wolf, 1976), whereby the flux tubes piled-up in front of the plasma bubble are compressed by its earthward motion, squeezing the plasma contained within them away from the equatorial plane, before the newly-emptied flux tube slips around the sides of the plasma bubble through interchange motion, finally forming a locally depleted wake behind it. Figure 4.16 illustrates this. The increases in $v_{//}$ observed by C1, C3 and C4 (Figures 4.7,4.9 and 4.10, Panels B) before entry into the plasma bubble then

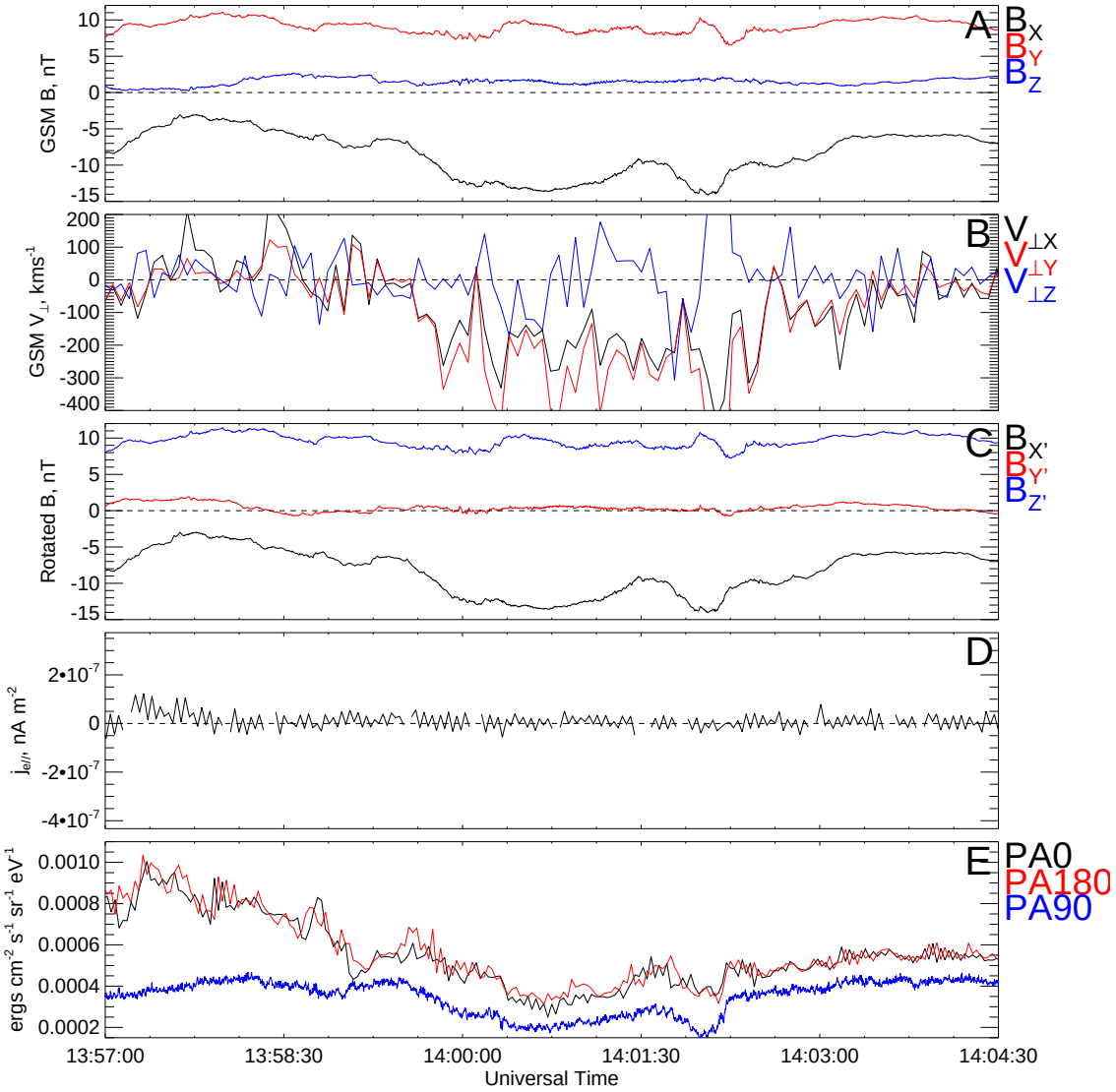

Figure 4.15: A more detailed examination of the PEACE data for C2. Panel A shows GSM components and magnitude of the magnetic field, Panel B the GSM components of $\boldsymbol{v}_\perp$, Panel C the magnetic field rotated about GSM X into a coordinate frame that eliminates any Y component in the undisturbed magnetic field, included here for completeness. Panel D is the parallel electron current calculated from 2D pitch angle distributions in the energy range covered by both PEACE sensors. Panel E shows the electron differential energy fluxes separately for 0° PA, 180° PA and 90° PA, taken from 3D distributions returned by both the HEEA and LEEA sensors and summed over their common energy range.

represent the plasma flowing along the field lines away from the equatorial plane, and the increase in P_B observed by C2 (Figure 4.8, Panel C) during the lower density tailward flows is the compressed flux tubes slipping around the sides of the bubble. Note that despite similar nomenclature, the "depleted wake" is not depleted in entropy, and does not have lower plasma content than the surroundings, instead the plasma is simply squeezed away from the equatorial plane.

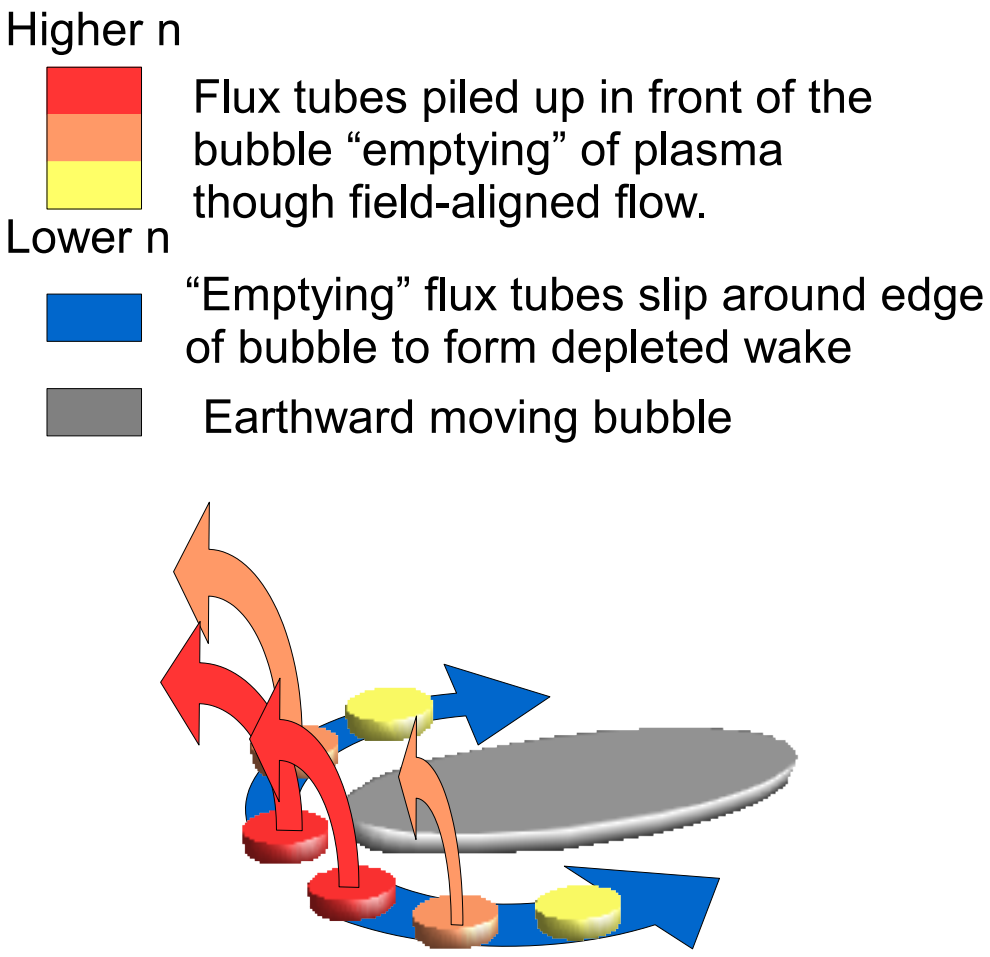

Figure 4.16: An illustration of the suggested formation mechanism of the depleted wake. The bubble is grey while the flux tubes that pile up in front of it are colour-coded red-orange-yellow with decreasing plasma content near the equatorial plane. Arrows of the corresponding colour represent the field-aligned plasma flow that "empties" the flux tube. Blue arrows mark the motion of the emptied flux tubes as they slip around the sides of the bubble forming the wake.

The idea of a depleted wake behind an earthward moving plasma bubble might also help explain the differences between the features that the other Cluster space-

craft observed at the end of the earthward flow. C1, C3 and C4 detected a sharp drop in perpendicular electron fluxes on entry into the plasma bubble, the fluxes then began to gradually increase (Figures 4.12, 4.13 and 4.14, Panels E). This gradual increase, however was not smooth. There is a change in the gradient of increase detected for each Cluster spacecraft (but most obviously on C3) at the time the earthward flow ends. After this change in gradient the electron fluxes were more stable but still below undisturbed levels, perhaps indicating the spacecraft had entered a wake. In the case of C3 and C4, the tailward flows detected during this period (Figures 4.9 and 4.10, Panel B) are consistent with the idea of infilling behind the bubble, while C1 detected a stagnant wake immediately after the passage of the bubble followed by a tailward flowing wake of much shorter duration. All of the spacecraft exit the wake at roughly the same time, between 14:02:30 UT and 14:03:30 UT, the time that C2 exited the region of tailward flow. In the case of C1 and C3 this exit was accompanied by another increase in bidirectional electron fluxes, while C4 detected a decrease. It is clear from these data that the exit from a BBF/plasma bubble is not as simple and clear cut as some models and simulations might suggest, and more detailed studies and simulations of the wakes of these features are necessary to fully understand their structure and motion.

The general morphology of this plasma bubble, as inferred from the Cluster data and described above, is illustrated in Figure 4.17, where velocities are marked in red, the bubble itself in grey, regions of FAC in green, the region of plasma and magnetic flux pile-up in yellow and the stagnant and tailward flowing wakes in different shades of blue.

The cross-tail extent of the plasma bubble can be estimated because C1, according to the sense of the field-aligned currents, entered the bubble dawnward of its centre while C2, which was duskward of C1, missed it entirely. This means that the entire duskward half of the bubble was bracketed between the two spacecraft, so an upper limit (i.e. the Y separation of C1 and C2, $\sim$10,000 km) can be placed on the cross-tail extent of the duskward half of the bubble. If approximate symmetry

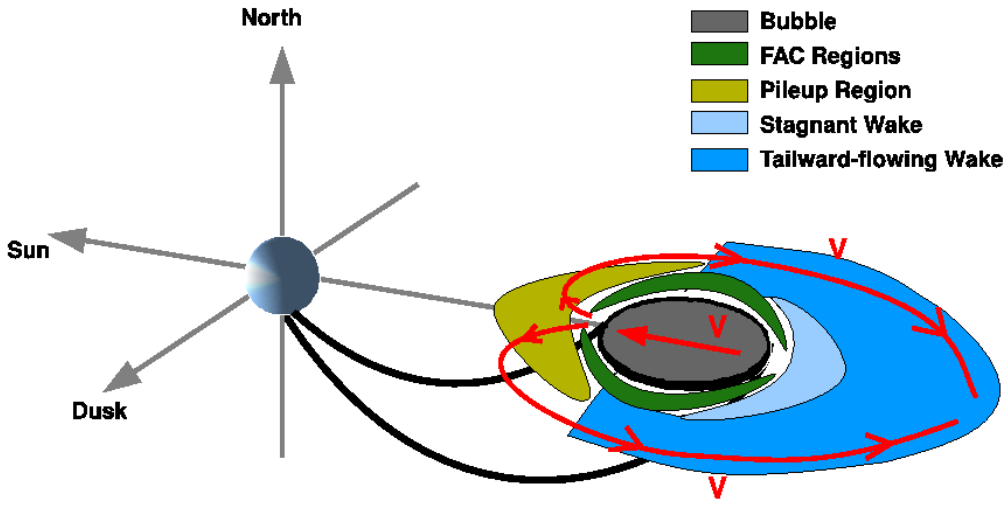

Figure 4.17: An illustrated equatorial cut of the morphology of the plasma bubble, as seen by Cluster. The region of flux and plasma pileup in front of the bubble is in yellow, the bubble itself is grey, the stagnant and tailward flowing wakes lighter and darker blues respectively and the field-aligned current regions green. Flow velocity is marked by the red arrows.

either side of the bubble's centre line is assumed, then this particular bubble cannot extend more than $\sim$20,000 km ($\sim 3\,R_E$) across the tail, consistent with previous observations of bubbles and BBFs (Sergeev *et al.*, 1996; Nakamura *et al.*, 2004). The estimated size of the bubble along its direction of motion, assuming the bubble itself ends with the earthward flow, is defined here as the peak value of $|\boldsymbol{v}_\perp|$, measured after the dipolarisation but before the end of the earthward flow, multiplied by the elapsed time between the dipolarisation and the end of the earthward flow. For C1 and C3 the size of the bubble along its direction of motion was $\sim 4\,R_E$, while for C4 the size was only $\sim 1\,R_E$.

4.3.2 TC-2 Data

Tracking the propagation of features through the magnetotail can be problematic (e.g. Walsh *et al.*, 2007, Chapter 3 of this thesis). In this case, however, there is evidence that the plasma and magnetic signatures seen by Cluster (Figure 4.6) and TC-2 (Figure 4.11) are manifestations of the same feature. Figure 4.18 shows the

elevation angle of the magnetic field for C1-C4 (Panels A-D) and the elevation angle of the magnetic field with the mean field subtracted for TC-2 (Panel E). The disturbances in elevation are qualitatively the same (although it should be noted that the scales on the Y-axes for Cluster and TC-2 on Figure 4.18 are different), and the time difference between them is consistent with the time taken for a feature to propagate from C1 to C3, C3 to TC-2 at the velocities measured by C1 and C3 to within 15 %. Specifically, the distance travelled by a flux tube moving Earthward at 350 km s^{-1}, the peak velocity measured by C1, in the 30 seconds that elapsed between the bubble's detection at C1 and C3 is 10,500 km. C3 was located approximately 9,000 km Earthward of C1. In the ∼3 minutes that elapsed between the bubble's detection at C3 and TC2, a flux tube moving Earthward at the peak velocity detected by C3 would have travelled 57,600 km. TC-2 was located ∼50,000 km Earthward of C3, so a reduction in average velocity of ∼15% to 270 kms^{-1} would result in the correct propagation time from C3 to TC-2. While a depleted flux tube has not been observed so close to the Earth before, a recent study by Takada *et al.* (2006) determined that BBFs observed by Cluster did not always result in a dipolarisation close to the Earth (at Double Star TC-1 in Takada *et al.*, 2006), but were more likely to do so when the magnetic field at TC-1 was more stretched. During the interval reported here, X is still the dominant component of magnetic field and has a greater magnitude than the X component of the T96 model field at the location of TC-2. It is consistent with Takada *et al.* (2006), then, that a BBF could penetrate to within 7 R_E of the Earth and cause a dipolarisation. Furthermore, the velocity vector (i.e. $\boldsymbol{v}_\perp$) measured by C3 points at TC-2, increasing confidence that the feature observed by Cluster is the same as that detected by TC-2.

Simulations have studied the features of a depleted flux tube that might be expected close to the Earth (Birn *et al.*, 2004), and the effect the presence of a depleted flux tube might have on the inner magnetosphere (Zhang *et al.*, 2008), although to date no plasma bubbles have been detected at $X_{GSM} >$ -8 R_E. Birn *et al.* (2004) predicted that, close to the Earth, after sufficient time had passed since the creation of a depleted flux tube, the plasma depletion and commensurate increase in

magnetic pressure that characterise a plasma bubble actually reverse - field-aligned flows from further downtail transport plasma to the higher latitude, near-Earth region, increasing the local plasma pressure. This causes the flux tube to expand, decreasing the magnetic pressure to maintain the pressure balance between the flux tube and its surroundings. Some of these features are evident in the TC-2 data, despite the latitude of its footpoint not being significantly higher than that of Cluster, though it should be noted here that the accuracy of T96 magnetic field mapping, particularly during more geomagnetically disturbed periods, is not sufficient to precisely determine spacecraft footpoints. The depleted flux tube can be identified as a small, transient, dipolarisation in the field at 14:02:20 UT (Figure 4.11, Panel B), accompanied by an increase in antiparallel (i.e. earthward), electron flux (Figure 4.11, Panel G). This electron flux could either represent a field-aligned current or a simple parallel flow, depending on the motion of the ions relative to that of the electrons. There is very little rotation in the magnetic field (Figure 4.11, Panel D) when compared with the lower energy electron beam detected at 14:03:40 UT so it can be assumed that the flux enhancement does not contribute significantly to any field-aligned current. There is also an enhancement of perpendicular electron flux (Figure 4.11, Panel F) during the transient dipolarisation, accompanied by a short dip in $|dB|$ (Figure 4.11, Panel C) - consistent with the increase in plasma pressure and decrease in magnetic pressure expected from the simulations. Unfortunately no velocity data, which could strengthen the association between the features seen by Cluster and TC-2, is available from TC-2 during this event.

4.3.3 The effect of $B_Y > 0$

The presence of a positive B_Y in the magnetotail will undoubtedly have an effect on the properties and motion of a plasma bubble, for example the change in the direction of the magnetic field draping around its edges. The presence of a strong B_Y in the magnetosphere, and the IMF, will also have an effect on the convection in the ionosphere (Cowley and Lockwood, 1992), and therefore the motion of the

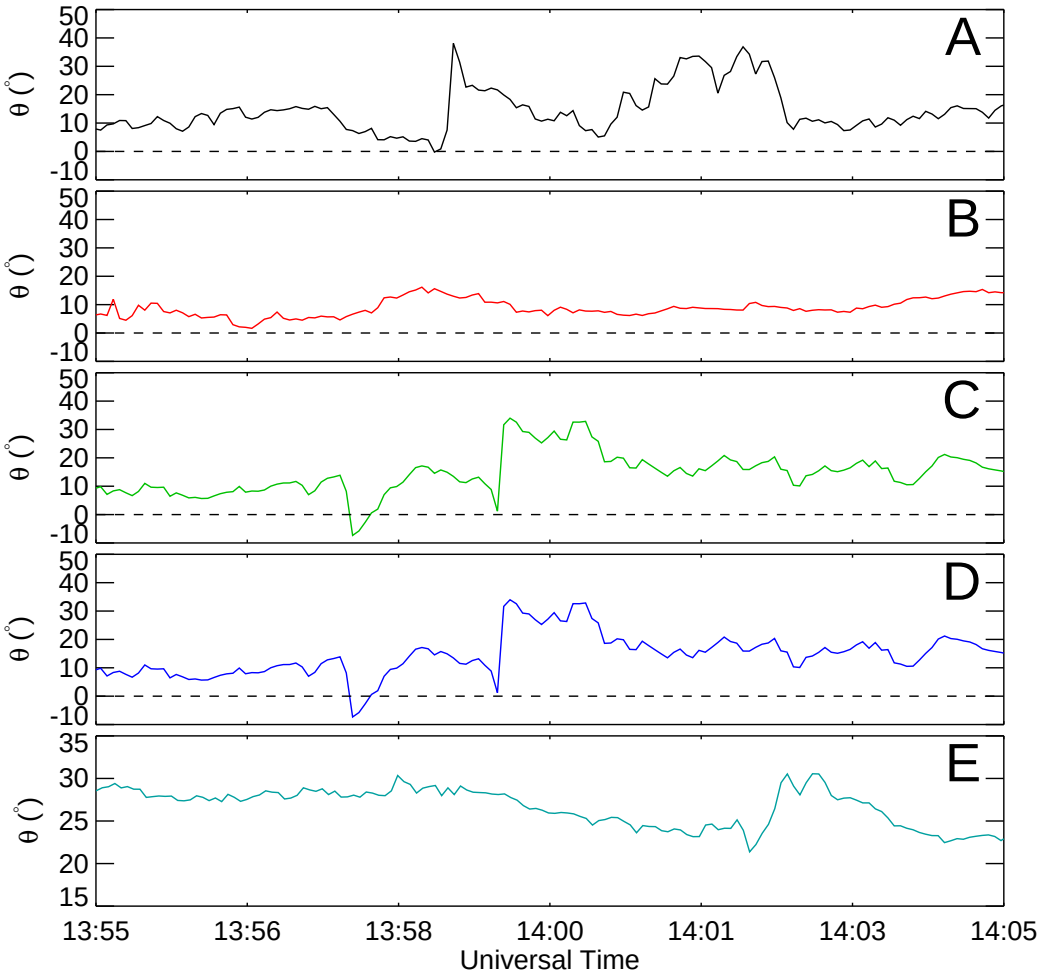

Figure 4.18: The GSM elevation angle of magnetic field for the four Cluster spacecraft (Panels A-D) and the latitude angle of ***dB*** for TC-2 (Panel E).

footpoint of the depleted flux tube. The SuperDARN data described in Figure 4.5 do indeed show a convection pattern consistent with those expected in a B_Y dominated magnetosphere (e.g. Grocott *et al.*, 2003). The footpoint of the depleted flux tube is expected to be moving equatorwards because of the earthwards motion of the plasma bubble in the tail and, because of the B_Y-dominated magnetosphere, is also expected to have a duskward component to its motion, consistent with the SuperDARN data (Figure 4.5). Figure 4.19 illustrates the expected current systems in the case of no B_Y and the case reported here.

In the case of B_Y=0 (Figure 4.19A), the cross-tail current is diverted into the ionosphere via field-aligned currents at the edges of the depleted flux tube. The flux tube is moving earthward in the tail, so its ionospheric footpoint is moving towards the equator. The direction of velocity is then consistent with the directions of the magnetic field, $\boldsymbol{B}$; current, $\boldsymbol{j}$ and electric field, $\boldsymbol{E}$ in both the ionosphere and magnetotail.

If there is a duskward component to the velocity of the foot point of the depleted flux tube in the ionosphere, assuming the electric field is a convection electric field, this will have the effect of rotating the electric field vector from a purely dawn-dusk direction. A rotation in the electric field vector might also cause a rotation in $\boldsymbol{j}$, since the ionosphere is dissipative (i.e. $\boldsymbol{j}\cdot\boldsymbol{E} > 0$) and therefore a current would follow the electric field direction. This would have the effect of shifting the distribution of field-aligned currents at the edges of the flux tube equatorward in the ionosphere (and therefore earthward in the magnetotail) on the dawnward edge of the flux tube and poleward (tailward) in the ionosphere (magnetotail) on the duskward edge of the flux tube, which in turn might cause a rotation in the current and electric field across the depleted flux tube, imparting a duskward component of motion to the bubble in the tail (Figure 4.19B). Equally, a duskward motion of the bubble in the tail could alter the bubble current systems and hence impart a duskward component to the motion of the flux tube's foot point in the ionosphere. The duskward direction of $v_{\perp Y}$ seen while C1 is located in the depleted flux tube and

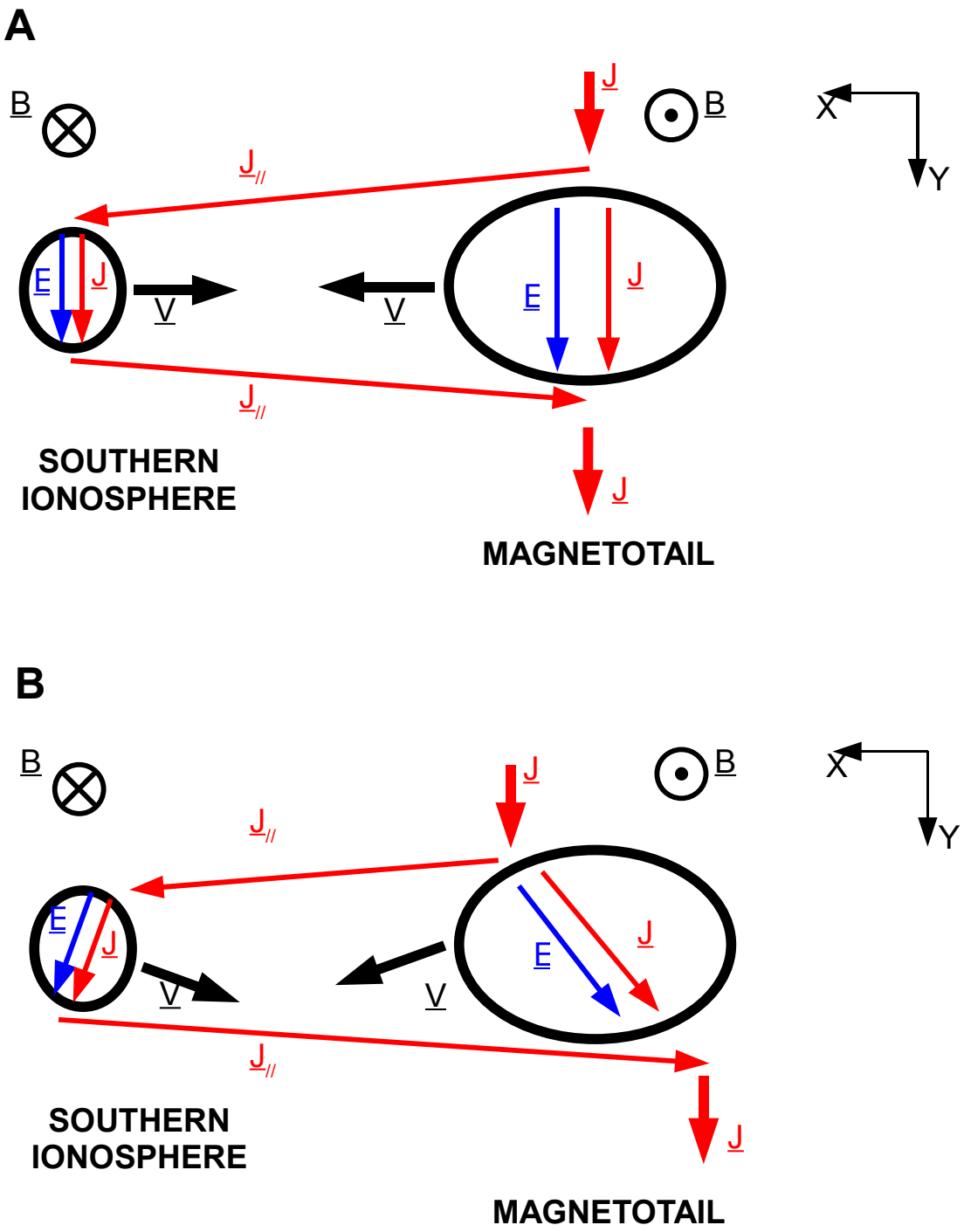

Figure 4.19: An illustration, looking down on the north pole, of the expected plasma bubble current systems during (A) the simplest (B_Y=0) case and (B) when there is a positive B_Y present. Currents are drawn in red, electric fields in blue and velocities in black. The black ellipses represent the boundaries of the depleted flux tube in the magnetotail just south of the neutral sheet (right) and the southern ionosphere (left).

$B_X < 0$ (Figure 4.7, Panels B and A) is consistent with this interpretation, as is the ionospheric velocity inferred from the radar data. Unfortunately without higher resolution current data, and a clear time of exit from the plasma bubble, it is difficult to determine whether the rotation in field-aligned current systems suggested here is, in fact, observed. Additionally, from the available data, it is difficult to determine whether the ionospheric or magnetospheric flows are driving the system. The apparent flow shear across the tail neutral sheet within the plasma bubble ($v_{\perp Y} > 0$ in the south, $v_{\perp Y} < 0$ in the north; Figure 4.7, Panels A and B), and enhanced duskward convection in the southern ionosphere (Figure 4.5) suggest a situation analogous to the so-called TRINNI events that have been observed in the SuperDARN and Cluster data (e.g. Grocott *et al.*, 2005, Grocott *et al.*, 2007). During these events, which have been observed in periods of B_Y-dominated, but northward IMF, reconnection in a twisted tail and the subsequent untwisting of the newly reconnected flux tubes result in flow shears across the tail neutral sheet, and between the northern and southern ionospheres. This event occurred during a period of southward IMF, but the auroral data (Figure 4.4) seem to indicate that the plasma bubble was unrelated to the substorm with onset at ∼02:00 MLT and ∼14:05 UT and instead associated with the more localised auroral activation in the midnight MLT sector a few minutes earlier. In this case there is no SuperDARN coverage at relevant MLTs in the northern hemisphere, so analysis of further events is necessary to determine whether or not the flow shear observed in tail here is TRINNI-like, or if the directions of $v_{\perp Y}$ observed by the different spacecraft are related to flow patterns within a depleted flux tube and internal to it.

4.4 Summary and Conclusions

Multipoint observations of a depleted flux tube have been made using the Cluster and Double Star TC-2 spacecraft that are broadly consistent with previous observations (Sergeev *et al.*, 1996; Forsyth *et al.*, 2008, and references therein) and MHD simulations (Birn *et al.*, 2004). In particular the first direct observations of the

expected return flows around the flanks of a plasma bubble, made simultaneously with the observations of the bubble itself, have been reported; as have the first observations of near-Earth (i.e. within $8\,R_E$) plasma bubble features predicted by simulations (Birn *et al.*, 2004), such as an increase in plasma pressure and decrease in magnetic pressure, accompanied by earthward, field-aligned, plasma flows detected by PEACE. Although no ion data are available from TC-2, ion flow in the same direction is expected here because of the lack of rotation in the magnetic field when the electrons were detected, implying that these electrons were not carrying significant current. This particular plasma bubble seemed to have associated with it a complex wake of lower plasma content than its surroundings, that was not predicted by simulations. The separation of the Cluster spacecraft allows us to estimate the cross-tail extent of the bubble to be $\leq 3\,R_E$, again consistent with previous observations (Sergeev *et al.*, 1996; Nakamura *et al.*, 2004), while along its direction of motion the bubble measured $\sim 4\,R_E$ based on the C1 and C3 data and $\sim 1\,R_E$ based the C4 data. A model of how the field aligned currents at the edge of the plasma bubble might be shifted around its boundary by the presence of a strong B_Y in the magnetotail has also been presented. The analysis of further events, however, particularly when higher resolution current data are available, is necessary to better understand how changes in the magnetotail and in ionospheric conditions affect the development and propagation of plasma bubbles.

Chapter 5

Constraining Substorm Onset with Space- and Ground-Based Observations

> The Aurora Borealis? At this time of year? At this time of day? In this part of the country? Localized entirely within your kitchen?
>
> *The Simpsons, 22 Short Films About Springfield, 1996.*

5.1 Introduction

After almost half a century of study many different observational characteristics of the substorm process have been identified. Even so, the exact sequence of events surrounding the onset of the substorm expansion phase has not been conclusively determined. High temporal resolution measurements of the aurora and geomagnetic field coupled with in-situ spacecraft measurements in the correct locations in the magnetotail are needed to resolve the two minute problem alluded to in Section 1.4.2. NASA's THEMIS mission (Sibeck and Angelopoulos, 2008) was designed with this in mind, however combinations of Cluster, Double Star, IMAGE and ground-based

observations can also play a part in solving the substorm problem.

5.1.1 Observational Characteristics of Substorms

No matter which substorm model (e.g. Baker *et al.*, 1996; Lui, 1996) is closer to the truth, certain observational features are known to be present during the substorm process. The equatormost auroral arc brightens and then the aurora expand westwards and polewards (Akasofu, 1964), this expansion of the aurora is thought to be a consequence the formation and expansion of the substorm current wedge (McPherron *et al.*, 1973), whereby the cross-tail current is diverted into field-aligned currents which close in the ionosphere. The disruption (i.e. reduction) of the cross-tail current is also seen as the dipolarisation of the near-Earth (i.e. $X_{GSM} > -8\,\mathrm{R_E}$) magnetotail, often detected by spacecraft at geosynchronous orbit (e.g. Lui *et al.*, 2008). The mechanism responsible for the disruption of the cross-tail current has not yet been conclusively identified. Proponents of the NENL (e.g. Baker *et al.*, 1996) model of substorms believe that the braking, in the transition region between tail-like and dipolar field lines (Shiokawa *et al.*, 1997), of fast flows (i.e. BBFs) generated by reconnection at a Near-Earth Neutral Line is responsible for the disruption of the cross-tail current and thus the aurora (Baumjohann, 2002). Proponents of the current disruption model (e.g. Lui, 1996) of substorms, on the other hand, believe that the disruption of the cross-tail current, caused by an as yet unidentified instability (e.g. Liu *et al.*, 2008; Yoon *et al.*, 2009), is itself the cause of expansion phase onset. This current disruption launches a rarefaction wave tailwards, causing a near-Earth Neutral line to subsequently develop from one of several other current disruption sites distributed along the magnetotail.

Ultra Low Frequency (ULF) waves are an integral part of the substorm process, and have been associated in the literature with auroral activity since the 1800s (Stewart, 1861). ULF waves are generally classified based on frequency (Jacobs *et al.*, 1964). So-called Pi2 pulsations, with periods between 40 and 200 seconds,

have long been associated with substorm onset and the formation of the SCW (Olson, 1999, and references therein). Pi2s can be compressional or shear-mode Alfvén waves and have been detected in association with flow channels in the magnetotail plasma sheet (Volwerk *et al.*, 2005). They are thought to be directly driven by BBFs (Kepko and Kivelson, 1999) or generated as a consequence of the process that produces BBFs (Murphy *et al.*, 2009a). Shorter period Pi1 pulsations (1-40 s), which can be further subcategorised into impulsive Pi1Bs and more continuous Pi1Cs (Heacock, 1967), have also been studied in the context of substorms (Arnoldy *et al.*, 1998; Lessard *et al.*, 2006) although unlike Pi2s, which respond globally to substorm onset (Olson, 1999), the Pi1B response in the ionosphere is confined to the locality of substorm onset (Bösinger and Yahnin, 1987). Thus Pi1B pulsations very useful in diagnosing substorm onset in both space and time (Milling *et al.*, 2008). In the magnetosphere, Pi1B pulsations are thought to be related to the dipolarisation of the magnetic field detected at geosynchronous orbit around substorm onset (Arnoldy *et al.*, 1998).

The substorm process is also responsible for the injection of energetic particles into the space near geosynchronous orbit. These injections are not necessarily always located at GEO itself, however they have been most often measured there, thanks to the large number of spacecraft operating at that location. These particle injections are confined to a fairly small space and after injection gradient-curvature drift around the Earth, clockwise (when looking down on the north pole) for ions and anticlockwise for electrons. When the particles are detected by a spacecraft at a different MLT to the injection site, the higher drift velocity of particles of higher energy (see Equation 1.13) results in an energy-dispersed particle injection as higher energy particles drift onto the spacecraft's longitude before lower energy particles (e.g. Reeves *et al.*, 1991). Spacecraft close to the injection site will therefore see a dispersionless particle injection where all particle energies are detected by the spacecraft at almost the same time. The energisation mechanism of the particles that make up the injections has been argued to be an increased cross-tail electric field from enhanced convection of particles earthward, coupled with the dipolarisation of the near-tail magnetic field (the convection surge model). This "convection surge" is

perhaps driven by reconnection at a near-Earth neutral line (Birn *et al.*, 1998), or as a direct consequence of the disruption of the cross-tail current local to the injection region (Lopez *et al.*, 1990). If the former is true, one would expect the earthward edge of the injection region (the injection boundary) to propagate earthward as the energetic particles convect towards the planet. Conversely, if the latter is true, one would expect the tailward edge of the injection boundary to propagate away from Earth as the current disruption region expands tailward (Reeves *et al.*, 1996; Lopez *et al.*, 1990).

In this Chapter observations pertaining to the coupling between the ionosphere and magnetosphere around the time of substorm onset, and in particular relating to the formation of the substorm current wedge (McPherron *et al.*, 1973) are presented, although a conclusive solution to the substorm onset problem cannot be gleaned from analysis of available data from the studied event.

5.2 Observations

5.2.1 Event Context and Overview

Between 03:00 UT and 06:00 UT on 1 October 2005, the Geotail spacecraft was located around GSM (13.93, 21.77, -12.62) R_E in the solar wind. The IMF, as measured by the Geotail magnetic field instrument (Kokubun *et al.*, 1994) is plotted in Figure 5.1. The IMF was predominantly directed northward and duskward throughout the interval, with the GSM Y component dominant during its first half. There were, however, some brief intervals of southward-directed IMF before 03:40 UT and after 05:20 UT. The Auroral Electrojet (AE) index (Figure 5.2) shows an increase, indicative of a substorm onset, at ∼04:23 UT.

At this time the IMAGE spacecraft was observing the southern auroral oval and the FUV-WIC instrument (Mende *et al.*, 2000a,b), data from which are plotted

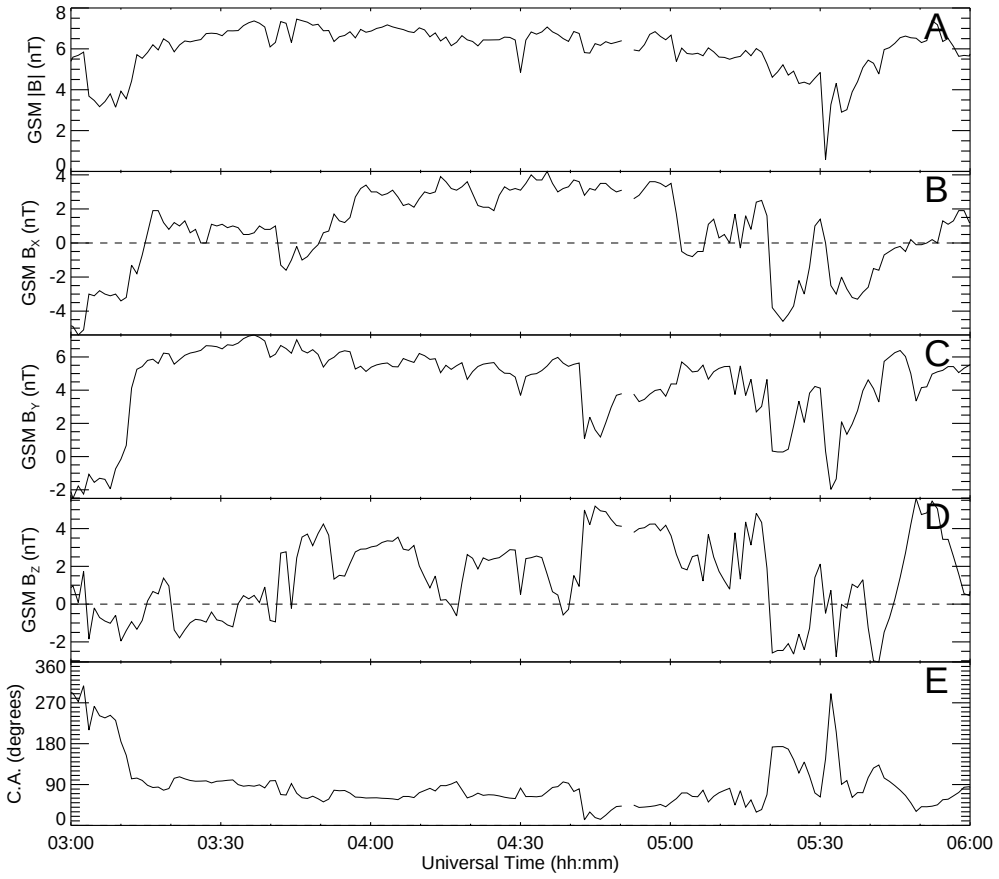

Figure 5.1: IMF magnitude, GSM components and clock angle as measured by Geotail. These data have not been time lagged as the solar wind travel time from Geotail to the Earth is very small.

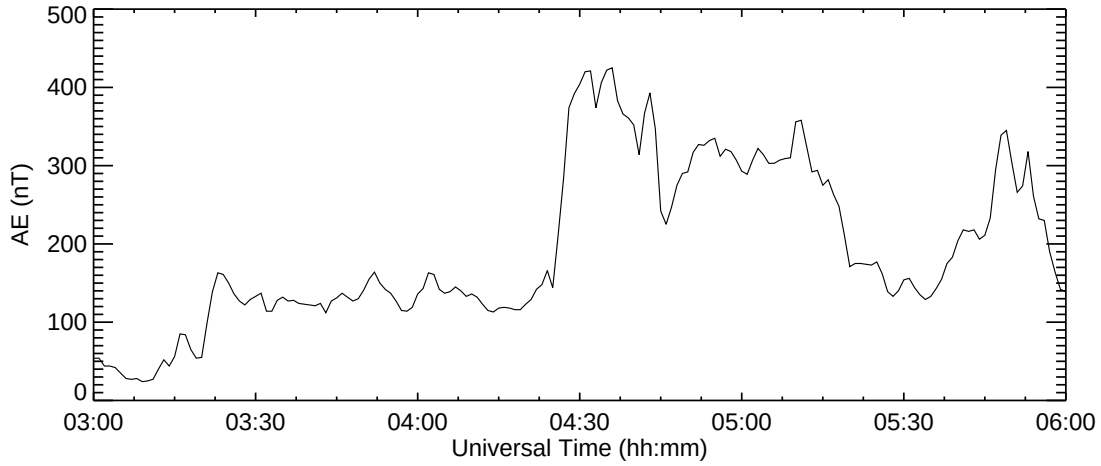

Figure 5.2: The AE index from the World Data Center, Kyoto.

in Figure 5.3, recorded a brightening of the aurora in the premidnight sector of the ionosphere at 04:21:20 UT (instrument cadence means this could have happened any time between 04:19:15 UT and 04:21:20 UT). Frey and Mende (2006) used an automated process to identify substorm onsets and listed this brightening (henceforth referred to as the Frey onset and labelled in red on Figure 5.3) as one such substorm onset. A substorm does indeed develop after this time, however we will argue that the onset occurs two minutes later, and approximately an hour in MLT closer to midnight.

The Frey onset occurred while the IMAGE spacecraft was observing the southern polar region and the onset was determined to be located at (-65.6°, 338.9°) in geomagnetic coordinates, over a section of the Antarctic with no ground-based magnetometer coverage. The conjugate location of this onset in the northern hemisphere is in the Canadian sector close to the Churchill Line of CARISMA magnetometers (see Mann *et al.*, 2008, and Figure 2.9). The Geodetic X (i.e. north-south) component from all the available CARISMA magnetometer stations is plotted in Figure 5.4.

The CARISMA data reveal a complicated period with fine structure in the magnetic field not resolved in the AE index. The first hint of geomagnetic activity was detected at ∼04:16 UT at the RABB and GILL magnetometer stations, both

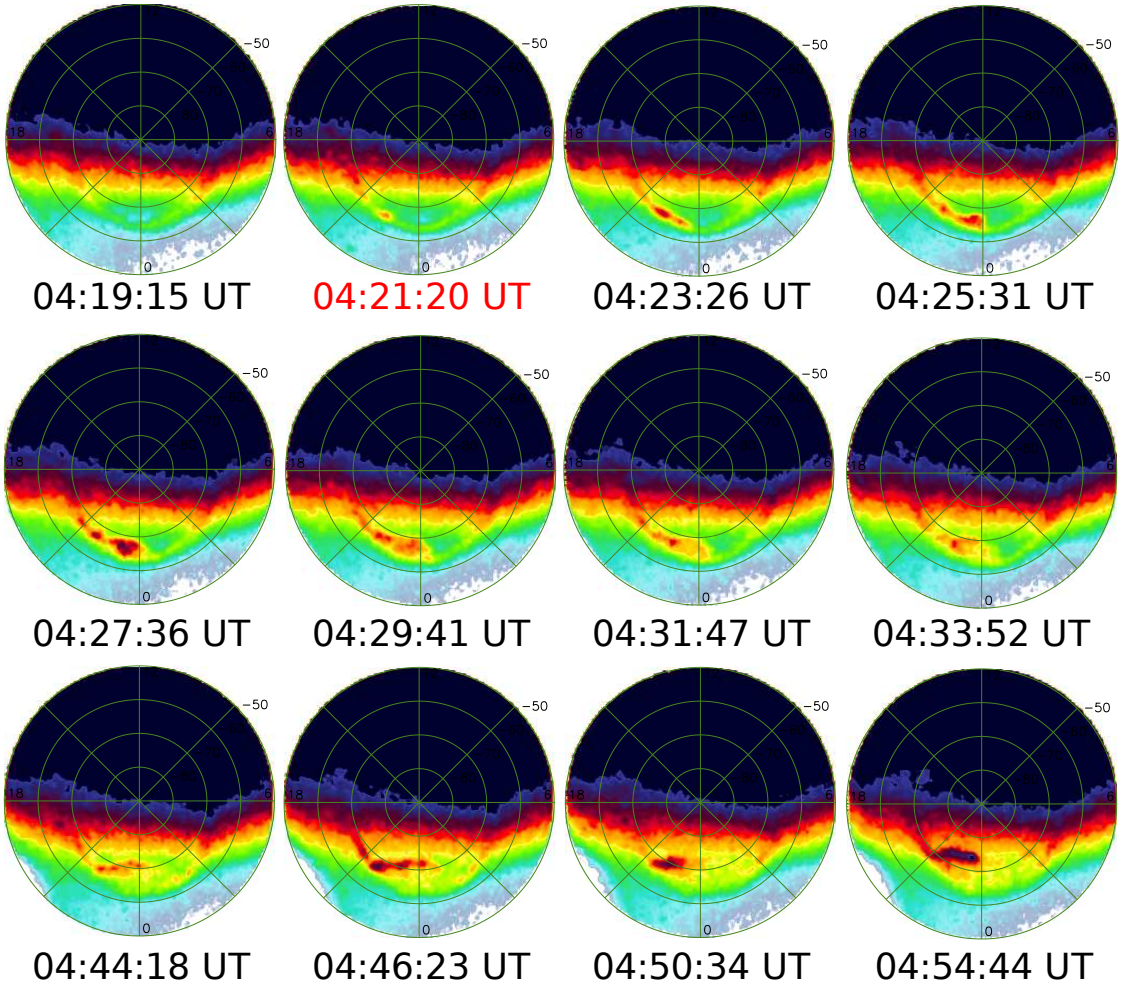

Figure 5.3: Selected auroral images taken by the IMAGE FUV-WIC camera around the time of Frey onset, which is marked with the red time label.

of which saw a slow decrease in B_X which lasted around 5 minutes before the rate of decrease became greater, with both magnetometer stations observing a feature closer to a classical substorm bay with a depth of approximately 150 nT. The FCHU magnetometer station, north of GILL, detected a steeper and deeper (i.e. ∼390 nT) substorm bay beginning at ∼04:22 UT. The largest disturbance in the magnetic field, however, was recorded by the RANK magnetometer, located further north than FCHU outside the nominal auroral oval, beginning at ∼04:45 UT. This bay, with a magnitude of close to 900 nT, is larger than any of the bays detected close to the time and location of the Frey onset by a factor of 2.

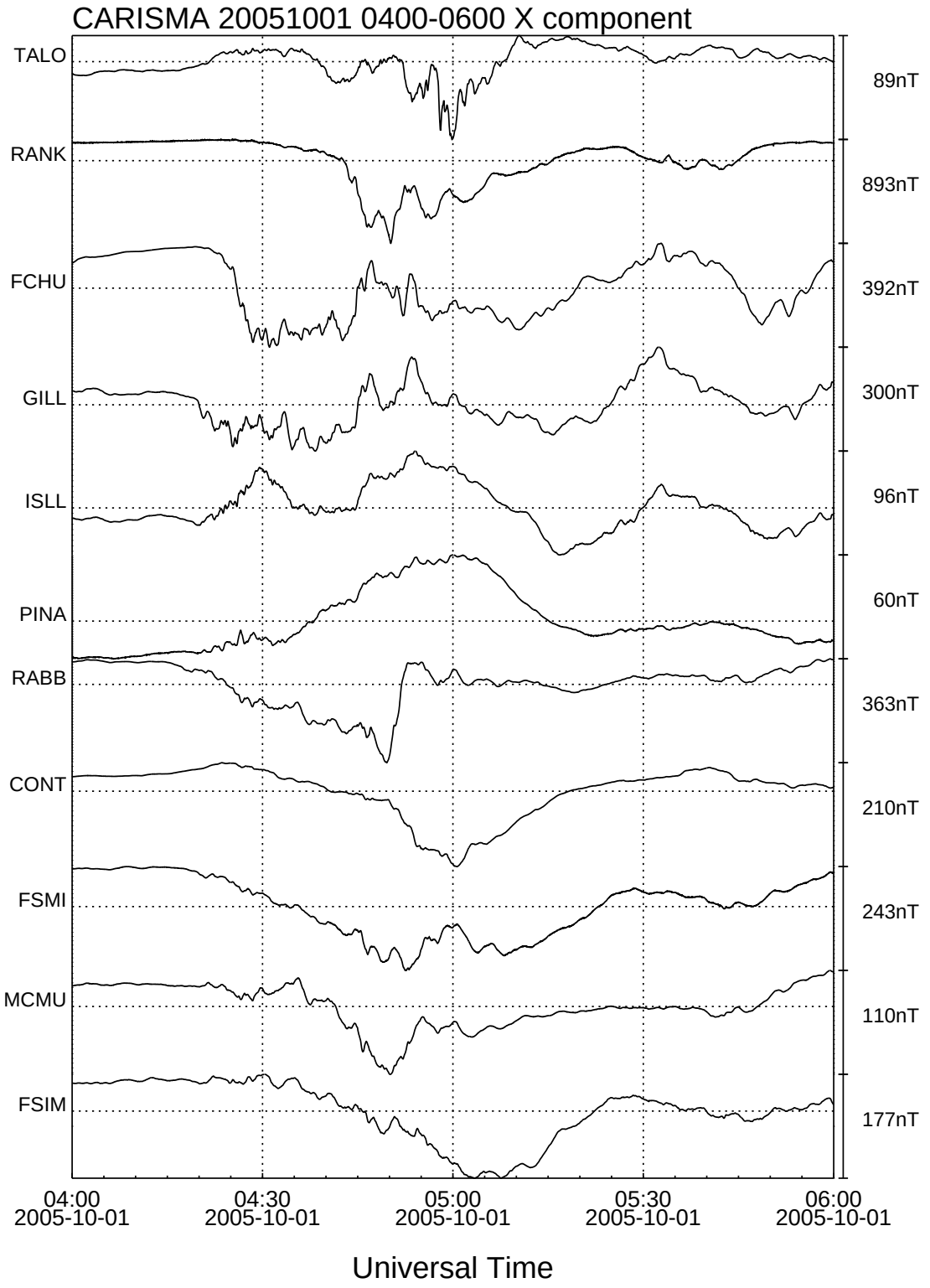

Figure 5.4: The Geodetic X component of the terrestrial magnetic field measured by various CARISMA magnetometer stations. The trace for each magnetometer station is scaled independently and the scale is marked with the bar on the right hand side of the plot. Horizontal dotted lines mark the average field strength at that particular station for the entire calendar day.

5.2.2 Auroral Data

Selected IMAGE WIC frames that document the development of the auroral substorm are plotted in Figure 5.3. The Frey onset occurs in the frame time-tagged 04:21:20 UT. Prior to the Frey onset the auroral oval is quiet with no localised features visible in the midnight sector. In the first image taken after the Frey onset (labelled 04:23:26 UT), the Frey onset aurora grow slightly and a brightening to the east of the Frey onset's location, closer to midnight MLT, can be seen. As time passes this eastern activation expands poleward and westward in the manner of a canonical auroral substorm, in contrast, the brightening associated with the Frey onset remains relatively steady eventually being subsumed by the substorm aurora (similarly to the auroral feature associated with the plasma bubble analysed in Chapter 4). The poleward edge of this expanded aurora brightens further at 04:46:23 UT, around the time of the magnetic disturbance detected by the RANK magnetometer. Another brightening of the poleward edge of the expanded aurora was observed from 04:50:34 UT, though this brightening is more localised than that observed at 04:46:23 UT.

In Figure 5.5, the Frey onset and three subsequent images are plotted in a larger format. The auroral brightening corresponding to the Frey onset is marked with a black circle in each case. From Figure 5.5, it can be seen that the auroral brightening that occurred to the east of the Frey onset at 04:23:26 UT is a distinct feature, and this feature had started to expand by 04:25:31 UT, while by this time the auroral brightening associated by the Frey onset had begun to dim. It would appear, then, that the Frey onset, which was identified through an automated process, was not in fact the onset of the auroral substorm. It was the eastern activation that expanded poleward and westward after the onset of the auroral substorm expansion phase, which therefore occurred between 04:21:20 UT and 04:23:26 UT. The Frey onset can be more properly characterised as a pseudobreakup, a brightening of the aurora that does not expand much beyond its initial location (Akasofu, 1964).

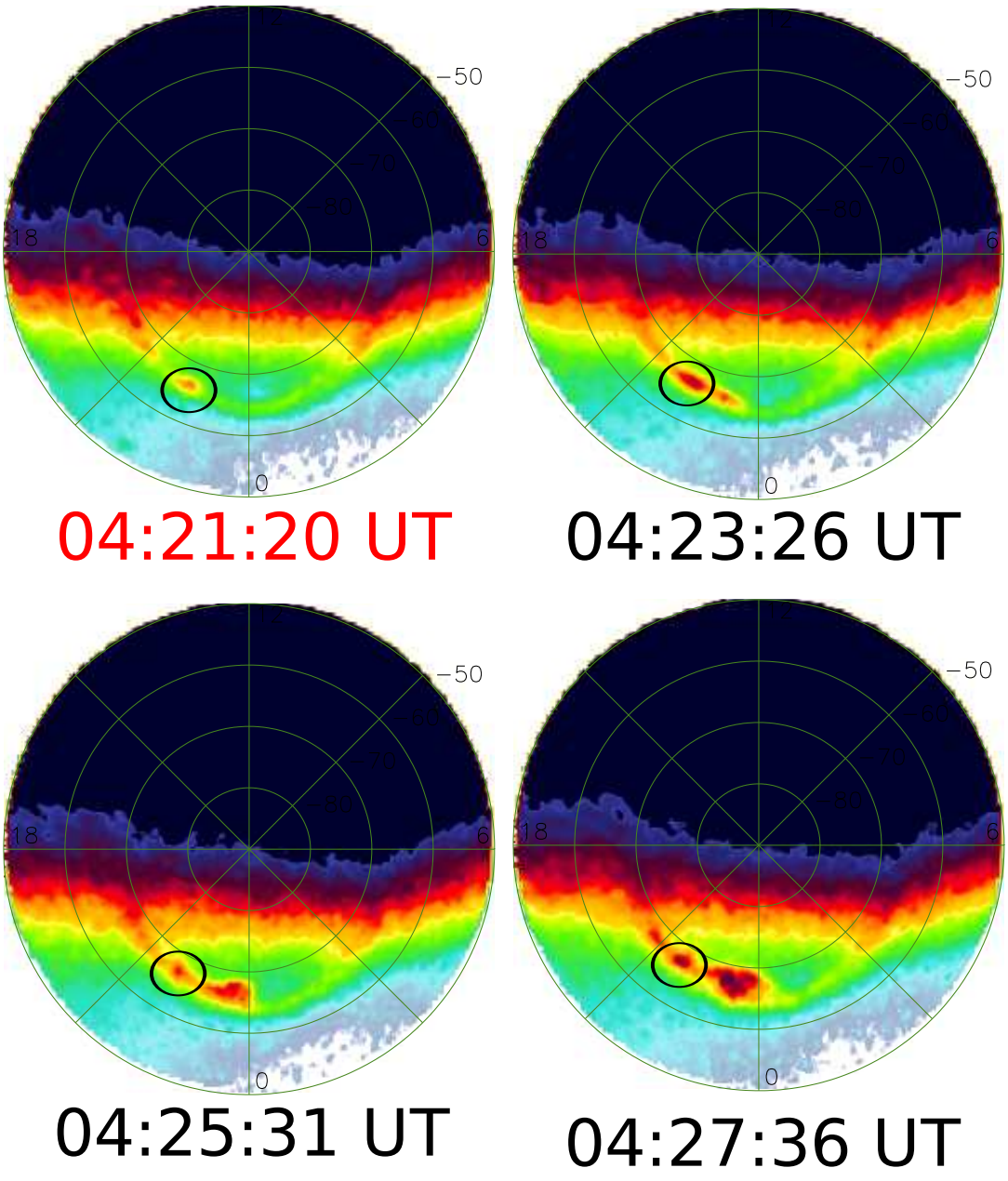

Figure 5.5: The Frey onset and the three subsequent WIC images. The auroral brightening identified as substorm onset by Frey and Mende (2006) is circled in black.

5.2.3 Magnetic Pulsations

CARISMA data that have been band-pass filtered with a low-period cut-off of 1 s and a high-period cut-off of 200 s (i.e. to highlight the Pi1/Pi2 band) are plotted in Figure 5.6. The traces from each magnetometer station are scaled independently. Pulsations in the Pi1 and Pi2 bands can be seen at at all of the magnetometer stations during the interval, however the highest amplitude pulsations are in the GILL, FCHU and RANK magnetometers. FCHU and GILL record significant pulsations beginning at ∼04:20 UT, presumably related to substorm onset, while RANK records the largest amplitude pulsations approximately 25 minutes later, beginning at 04:45 UT, the same time as the large geomagnetic bay. Determining the time and location of ULF wave onset by eye can be somewhat subjective, however so below we perform a wavelet timing analysis (Milling *et al.*, 2008, details below) to determine how these pulsations fit into the overall substorm picture.

5.2.4 Near-Earth Space-Based Data

The orbits of various Los Alamos Geosynchronous Satellites, GOES-12 and Double Star TC-2, projected into the GSE XY plane, are plotted in Figure 5.7. The Earth is represented by the light blue circle and the position of the Churchill line of magnetometers at 04:20 UT is indicated by the radial blue line. Coloured squares on the orbit tracks represent spacecraft positions at 04:20 UT. TC-2 and GOES-12 are located near the same local time as the Churchill line, the Frey onset and subsequent eastern activation, with TC-2 positioned just Earthward of geosynchronous orbit and northward of the equatorial plane at GSE (-6.03, 2.17, 0.99) R_E. Two of the Los Alamos Satellites, 1990-095 and 1994-084 were located dawnward (1994-084) and duskward (1990-095) of local times of interest.

Data from the GOES-12 magnetometer (Singer *et al.*, 1996) are plotted in Figure 5.8. Between 03:00 UT and 04:20 UT the magnetic field as measured by GOES-12 remained fairly steady. The smooth change in the B_Y component of the field

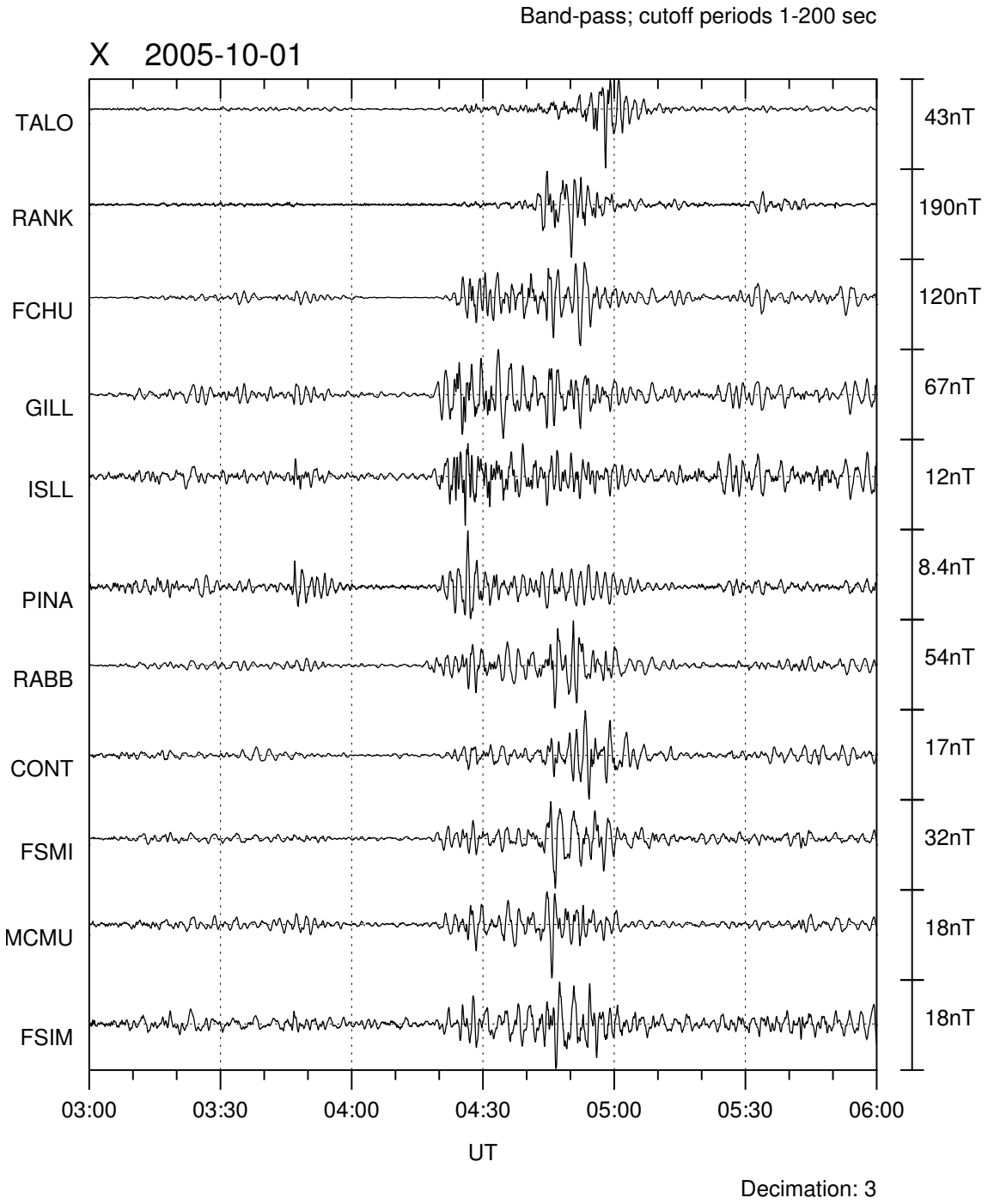

Figure 5.6: The geodetic X component of magnetic field from the CARISMA magnetometers, bandpass filtered with a low-period cut-off of 1 s and a high period cut-off of 200 s (to show only the Pi1 and Pi2 bands).

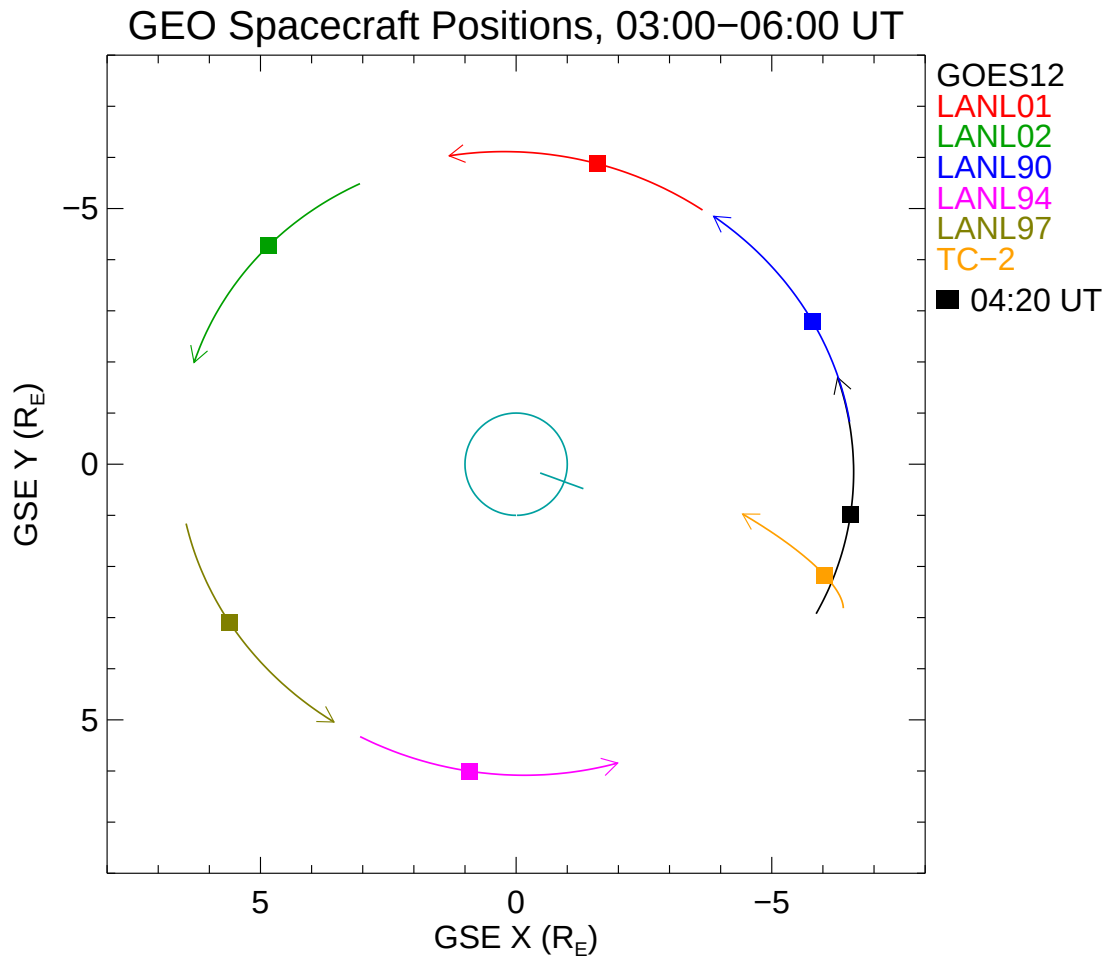

Figure 5.7: The orbits of several near-Earth spacecraft projected into the GSE XY plane. The Square on each orbit track marks the position of the spacecraft at 04:20 UTand the light blue radial line the position of the Churchill line of magnetometers, also at 04:20 UT.

(Figure 5.8, Panel C) is a result of the movement of the spacecraft along its orbit in a dawnward direction. At ∼04:26 UT the spacecraft observed a sharp decrease in B_X and increase in B_Z, resulting in a net increase in $|\boldsymbol{B}|$, a dipolarisation associated with the developing substorm. Unfortunately no particle measurements are available from GOES-12.

Data from Double Star TC-2 FGM (Carr *et al.*, 2005) and PEACE (Fazakerley *et al.*, 2005), taken between 03:00 UT and 06:00 UT, are plotted in Figure 5.9. The magnitude and GSM magnetic field components are plotted in Panel A, Panels B-D show GSM magnetic field components with a T96 model field (Tsyganenko and Stern, 1996) removed while $v_{\perp X}$, smoothed over 5 data points, is plotted in Panel

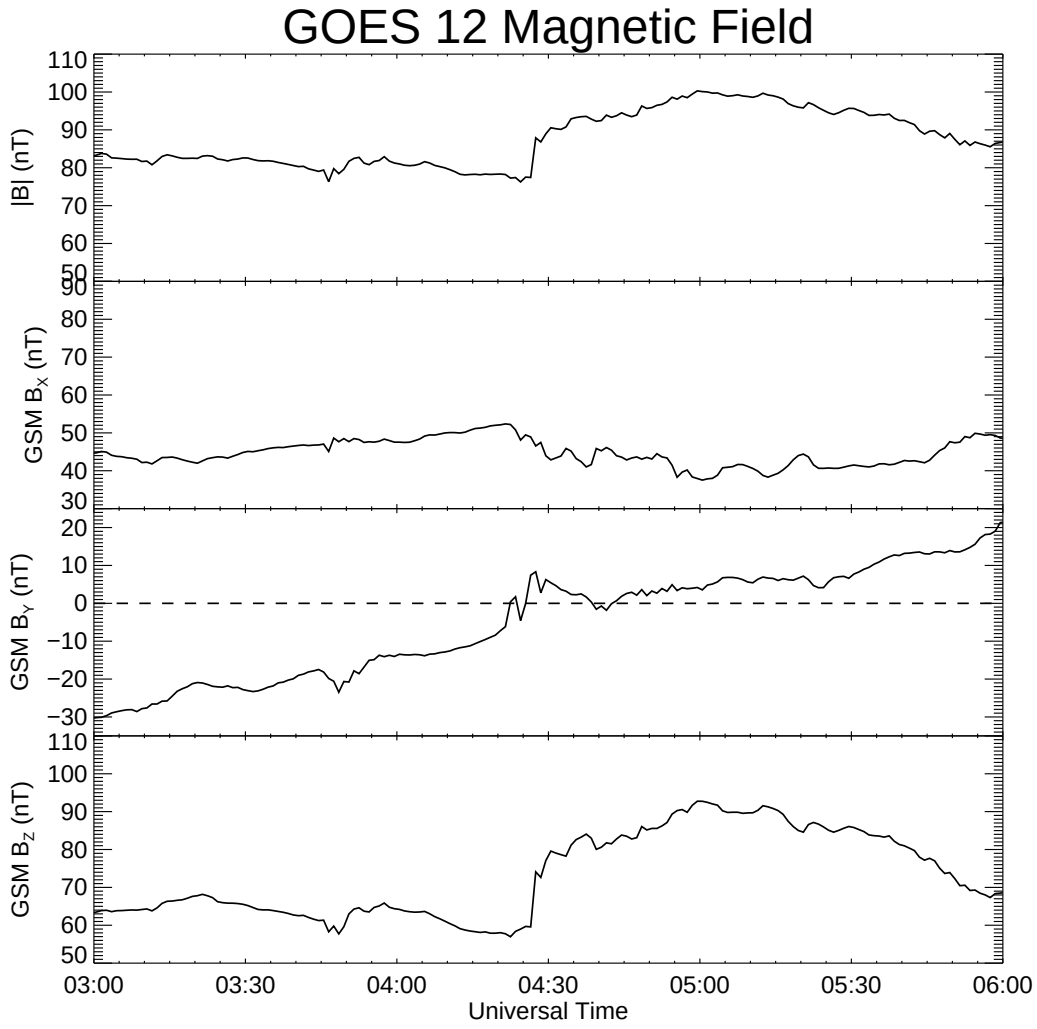

Figure 5.8: Magnetic field magnitude and GSM field components from the GOES 12 magnetometer at 1 minute resolution.

E and $T_{e///}/T_{e\perp}$ (unsmoothed) is plotted in Panel F. Panels G-I are energy-time spectrograms showing electron differential energy flux of particles with pitch angles of 0°, 90° and 180° respectively.

At 03:00 UT TC-2 was north of the magnetotail neutral sheet ($B_X > 0$, Figure 5.9, Panel A) inbound towards perigee. At ∼03:20 UT the spacecraft entered the magnetotail plasma sheet from the PSBL, experiencing an increase in electron flux at all pitch angles (Figure 5.9, Panels F-H) and a decrease in $T_{e///}/T_{e\perp}$ from ∼1.1 to ∼0.8 (Figure 5.9, Panels E). At 04:20 UT, when the spacecraft was located at GSM(-6.02, 2.38, 0.09) R_E, fluctuations in dB_Z were detected (Figure 5.9, Panel D)

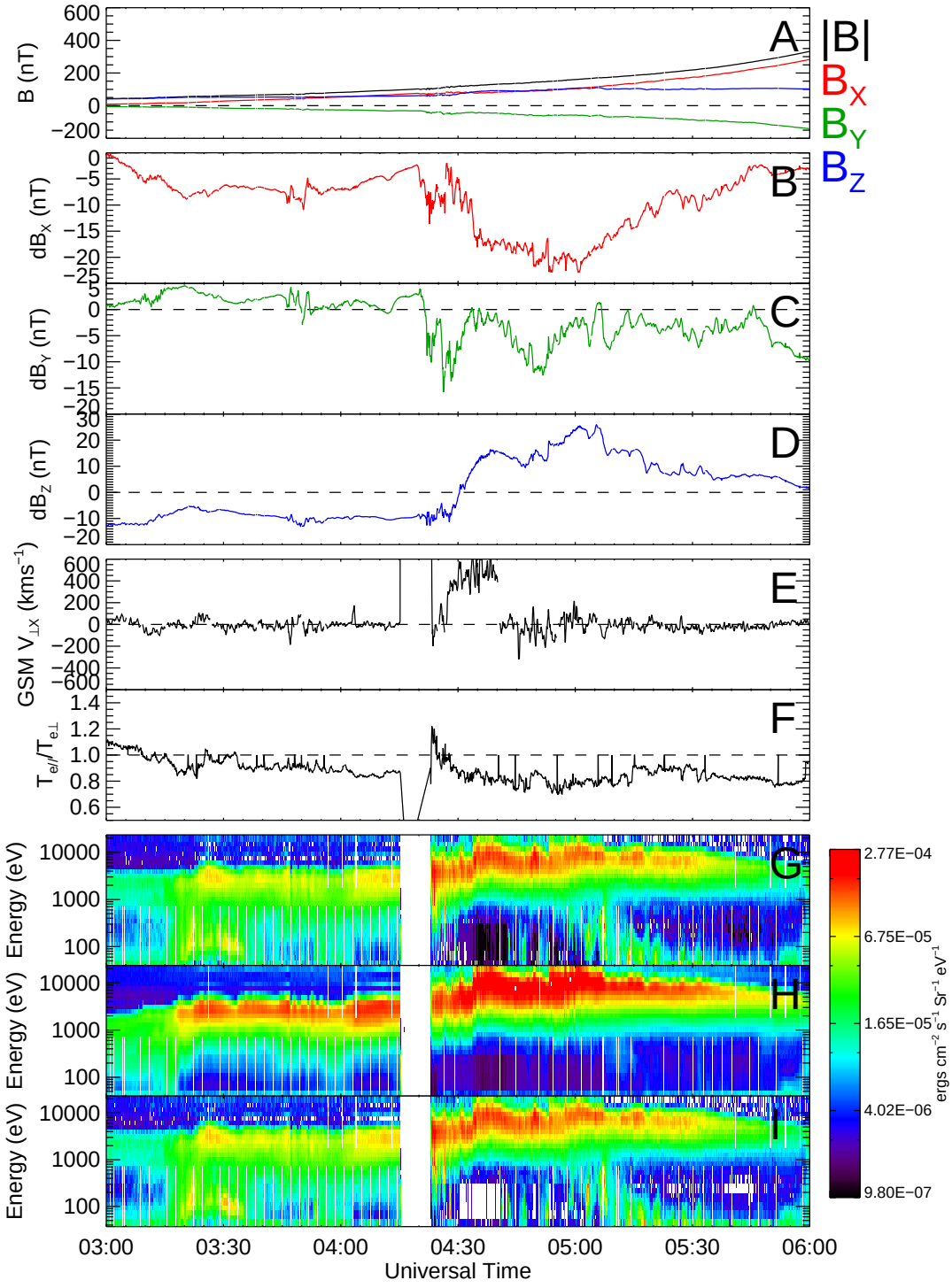

Figure 5.9: Data from the Double Star TC-2 spacecraft. The magnitude (black) and GSM components (X - red, Y - green, Z - blue) of magnetic field from the FGM instrument are plotted in Panel A, Panels B-D show the GSM components of magnetic field with a model magnetic field subtracted, Panel E is $v_{\perp X}$from PEACE , smoothed over 5 data points and Panel F is the ratio between the parallel and perpendicular electron temperatures (these have not been smoothed), also from PEACE. Panels G-I are electron energy time spectrograms of differential energy flux for particles with pitch angles of 0°, 90° and 180° respectively.

and both dB_X (Figure 5.9, Panel B) and dB_Y (Figure 5.9, Panel C) became more strongly negative. The magnetic field fluctuations in dB_Z stopped at ∼04:28 UT, just prior to a dipolarisation in the magnetic field similar to that seen by GOES-12. There is an unfortunate gap in the PEACE data caused by a commanded instrument reset between 04:16 and 04:22. After the data gap PEACE measured enhanced $T_{e//}/T_{e\perp}$, which lasted only as long as the pulsations, and a generally hotter electron distribution. During the dipolarisation, which was accompanied by Earthward flows of ∼400 km s^{-1} (Figure 5.9) PEACE recorded a further increase in electron energy. This was followed by two more energy increases at ∼04:50 UT and ∼04:55 UT, each coincident with a further sharp increase in B_Z.

Energetic electron and proton data from the SOPA instruments (e.g. Belian *et al.*, 1992) onboard the LANL Geosynchronous satellites are plotted in Figures 5.10 and 5.11 respectively. Between 04:26 UT and 04:35 UT the 1990-095 spacecraft, located ∼2.5 hours of local time dawnward of the Frey onset, observed an increase in fluxes of energetic electrons which had a small degree of dispersion. The particle injections were subsequently detected at LANL-01A then LANL-02A with increased dispersion, as expected for drifting elections. A smaller, dispersed, increase in energetic proton fluxes beginning at ∼04:30 UT was observed by the 1994-084 spacecraft, which was located ∼ 5 hours of local time duskward of the Frey onset. No significant proton injections were detected by the other Los Alamos satellites, however.

5.2.5 Riometer data

Data from some of the NORSTAR riometers are plotted in Figure 5.12. The first increase in ionospheric absorption of cosmic radio waves, a proxy for the precipitation of energetic electrons into the ionosphere (e.g. Spanswick *et al.*, 2007), during the interval of interest was detected by the GILL riometer at ∼04:20 UT. The FCHU riometer detected a larger increase at ∼04:25 UT followed by a smaller increase at ∼04:52 UT and the RANK riometer detected increases in absorption at ∼04:45 UT

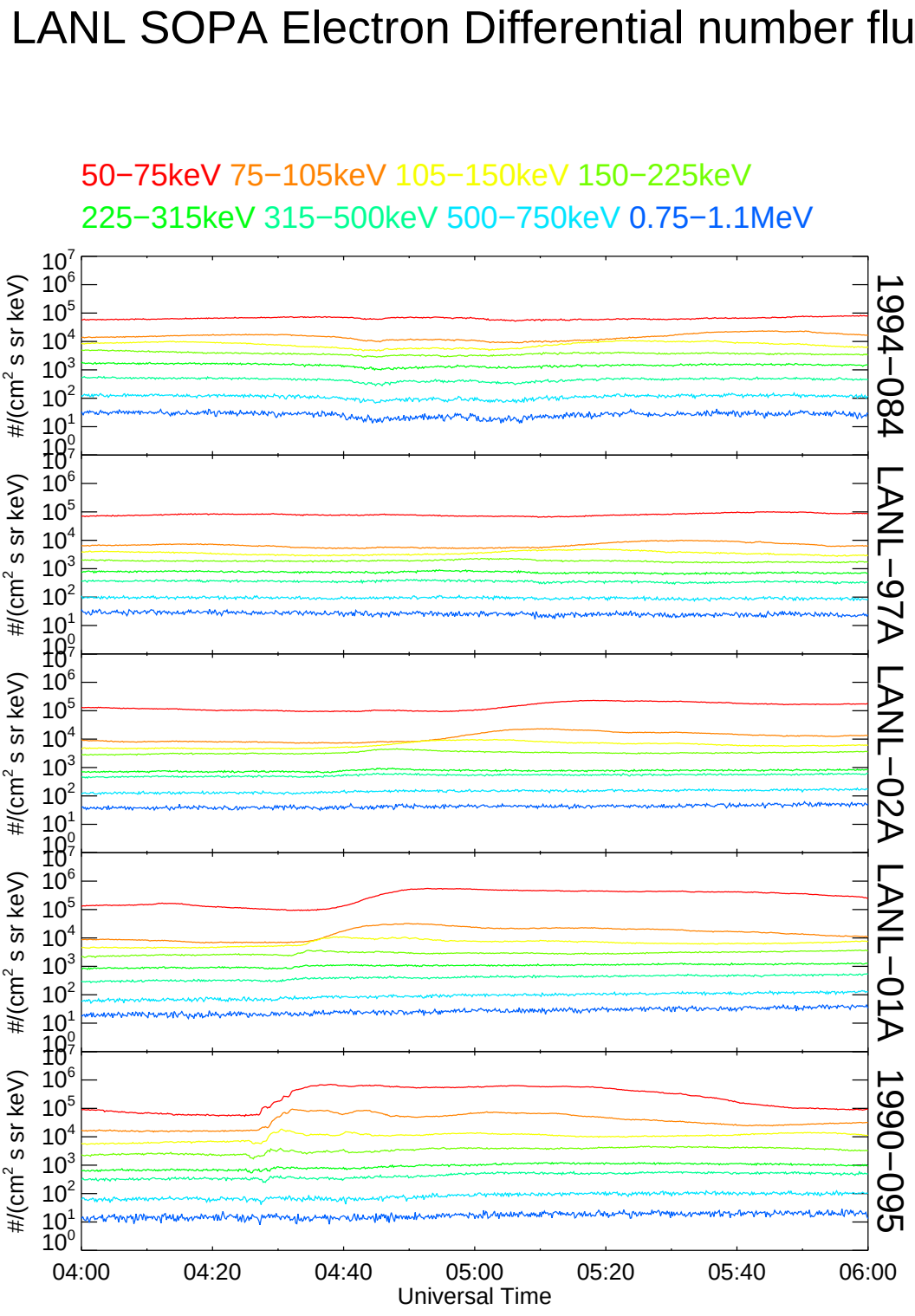

Figure 5.10: Energetic electrons from the SOPA instrument on the LANL geosynchronous satellites. Each panel has the differential number flux of electrons from a different spacecraft. Different coloured traces represent different energy channels of the instrument.

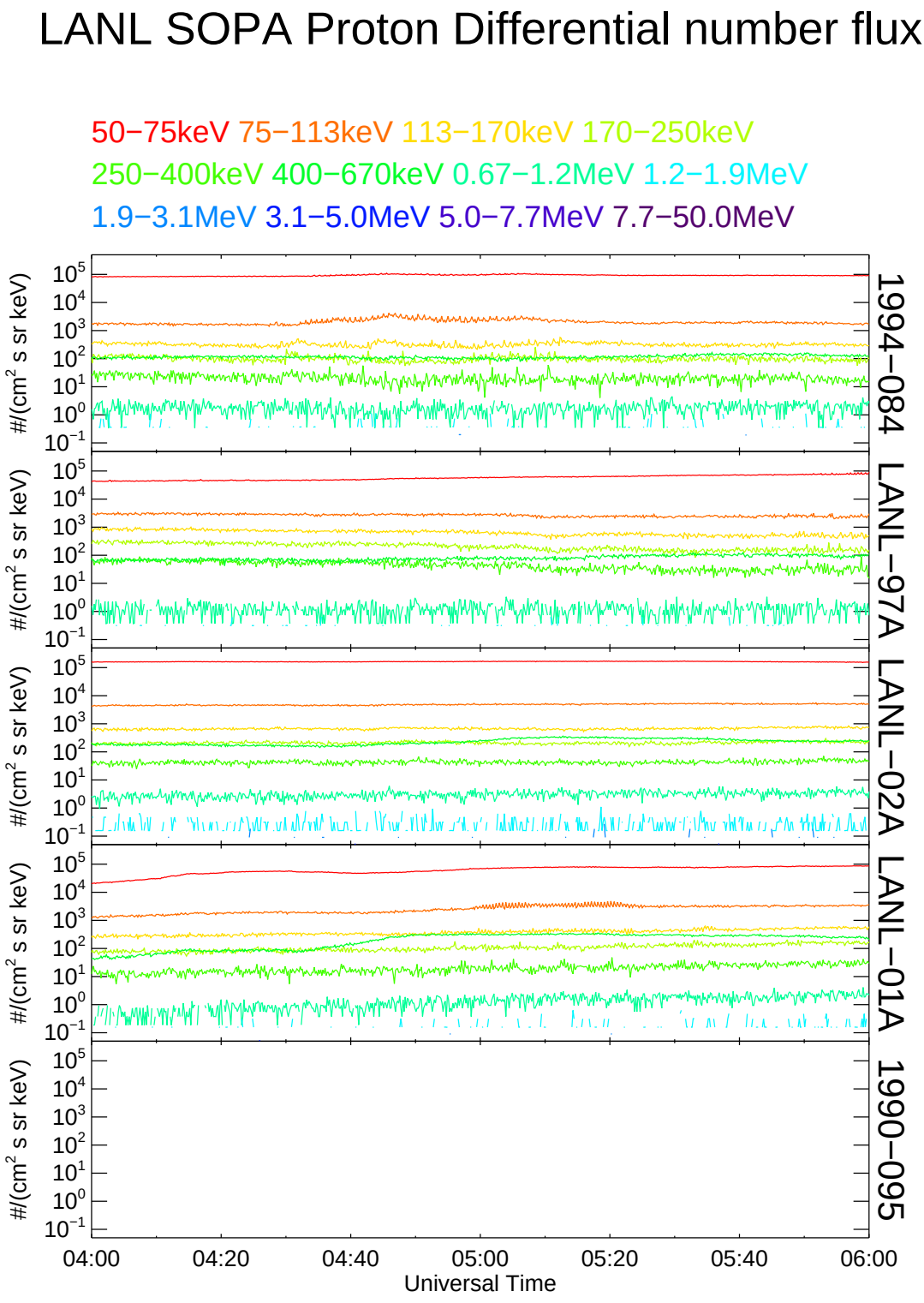

Figure 5.11: Energetic protons from the SOPA instrument on the LANL geosynchronous satellites. Each panel has the differential number flux of protons from a different spacecraft. Different coloured traces represent different energy channels of the instrument. There are no proton measurements from the 1995-095 satellite.

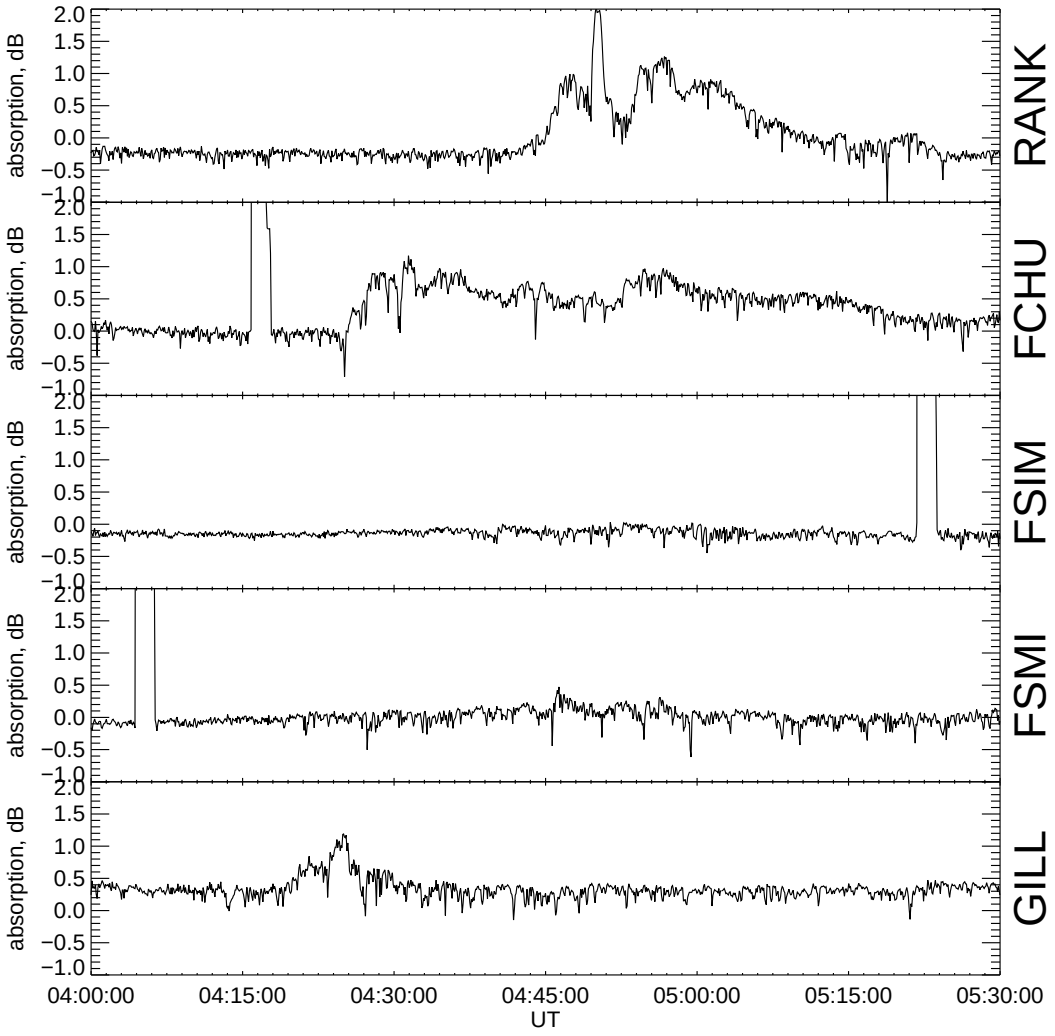

Figure 5.12: Ionospheric radio absorption data from several of the NORSTAR Riometers

and 04:52 UT. The peaks in absorption that are larger than the Y-axis scale in the FCHU, FSIM and FSMI plots are instrumental artefacts.

5.2.6 Cluster Data

Between 03:00 UT and 06:00 UT, the four Cluster spacecraft were close to apogee in the magnetotail, at a similar local time to Double Star TC-2 (Figure 5.13, Panels A-C). At 04:20 UT, the reference spacecraft (C3) was located at GSM(-14.97, 4.99, -1.02) R_E. During this interval the Cluster tetrahedron was in a "multi-scale" configuration: C1, C2 and C3 made a 10,000 km triangle while C4 was offset from C3

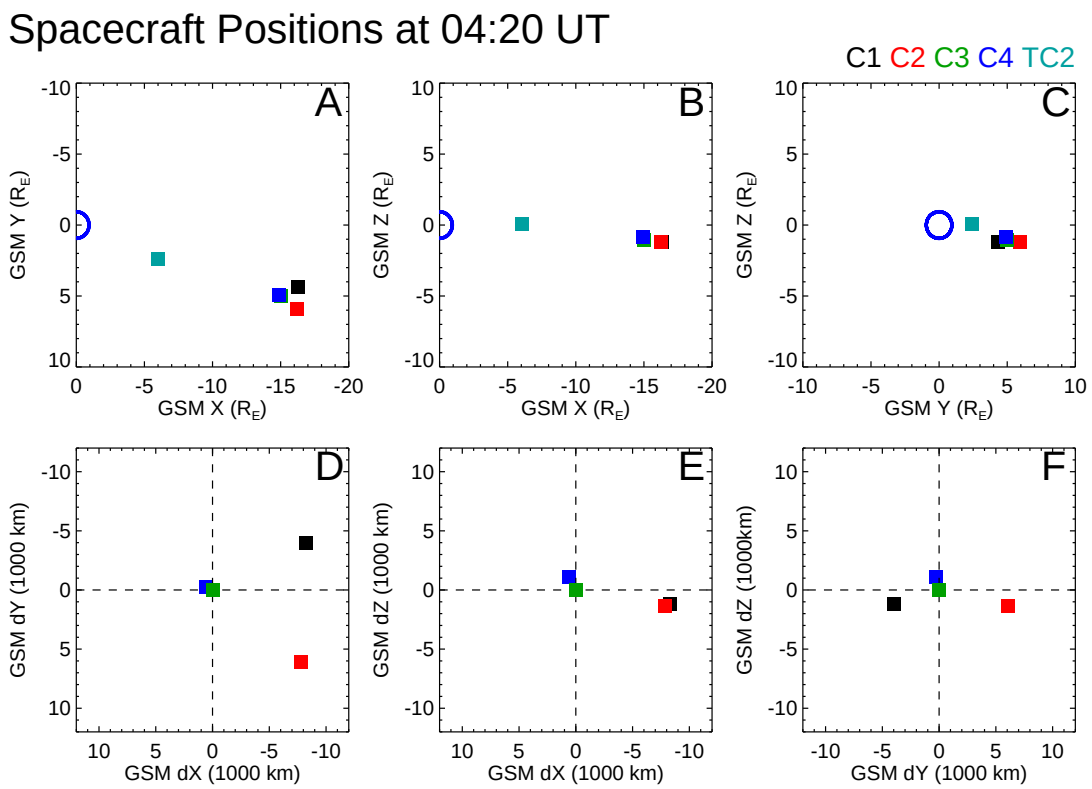

Figure 5.13: The GSM position of the Cluster tetrahedron and Double Star TC-2 at 04:20 UT (Panels A-C) and the configuration of the Cluster tetrahedron (Panels D-F).

by 1,000 km (Figure 5.13, Panels D-F).

An overview of the Cluster data is presented in Figure 5.14. The magnitude and GSM components of magnetic field from FGM (Balogh *et al.*, 2001) on all four Cluster spacecraft are plotted in Panels A-D, $v_{\perp X}$ from C2, C3 and C4 is plotted in Panel E and PEACE (Johnstone *et al.*, 1997) electron energy time spectrograms for each of the Cluster spacecraft are plotted in Panels F-I. Velocity data are from PEACE on C2, HIA (Rème *et al.*, 2001) on C3 and CODIF (Rème *et al.*, 2001) on C4. During this interval there were no ion data from C1 and, as the spacecraft were in normal telemetry mode, no high time-resolution 3D moments from PEACE are available. Traces in black, red, green and blue are from C1, C2, C3 and C4 respectively. At the start of the interval the Cluster spacecraft were located in the northern plasma sheet boundary layer of the magnetotail moving southwards towards the central plasma sheet, as evidenced by decreases in $|\boldsymbol{B}|$ and B_X (Figure 5.14, Panels A and B) and an increase in electron fluxes and energies (Figure 5.14,

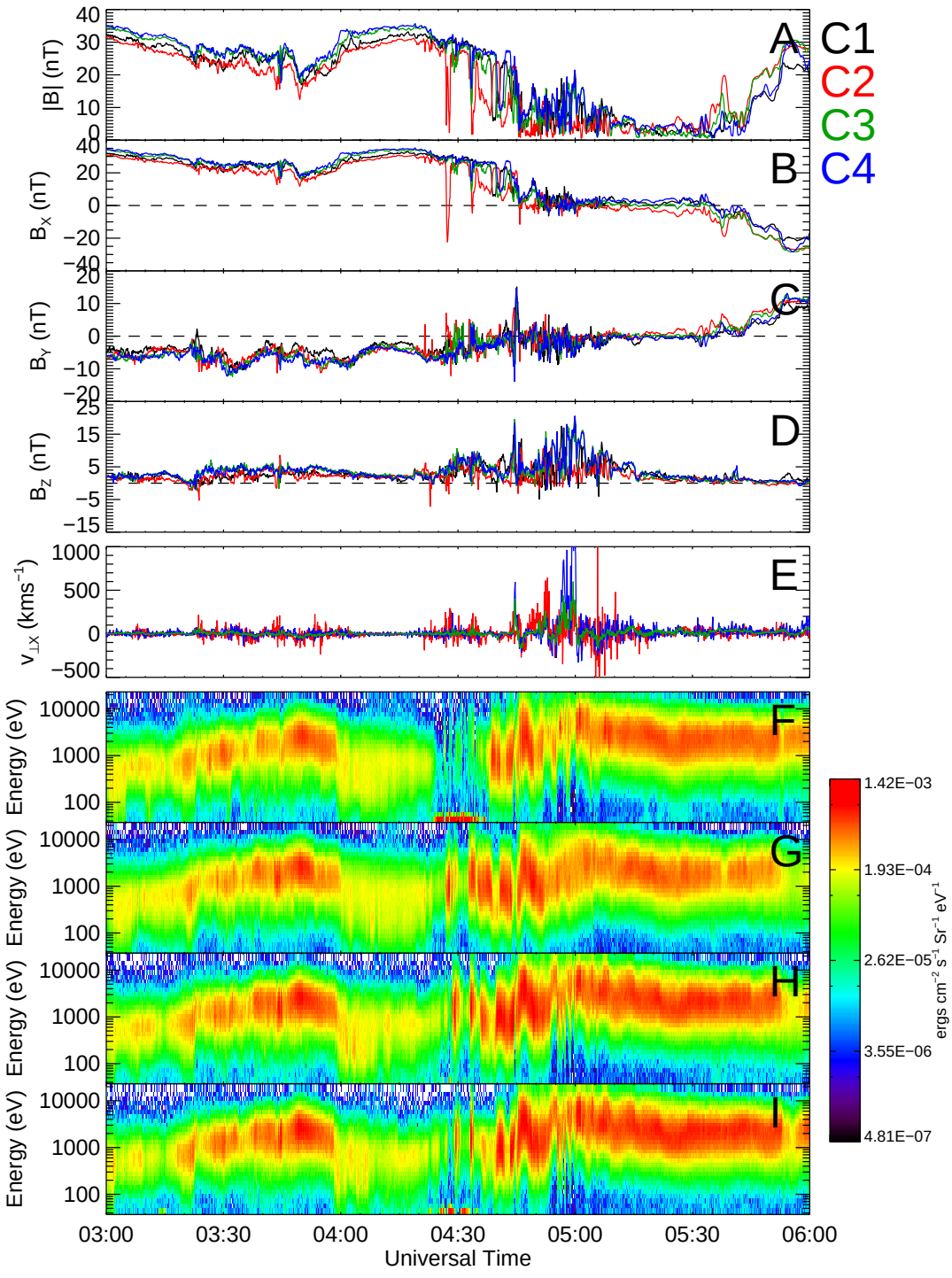

Figure 5.14: The magnitude (Panel A) and GSM components (Panels B-D) ad magnetic field from FGM, $v_{\perp X}$ from CIS-HIA (Panel E) and PEACE electron energy time spectrograms for each of the Cluster spacecraft (Panels F-I). Traces in black, red, green and blue are from C1, C2, C3 and C4 respectively.

Panels E-I). At ∼03:50 UT B_X and $|\boldsymbol{B}|$ began to increase. By 04:00 UT the Cluster spacecraft had dropped out of the central plasma sheet and returned to the PSBL, where the magnetic field continued to increase until ∼04:25 UT. The spacecraft then had several transient encounters with the central plasma sheet, with C2, the southernmost Cluster spacecraft, briefly crossing the neutral sheet and entering the southern hemisphere. During this crossing the PEACE instrument recorded an earthward flow of $\sim 200\,\mathrm{km\,s^{-1}}$ (Figure 5.14, Panel E). At ∼04:40 UT, the Cluster tetrahedron re-entered the central plasma sheet (as evidenced by the low $|\boldsymbol{B}|$) and remained there until the end of the interval of interest. Between 04:44 UT and 05:00 UT Cluster observed three Earthward-directed (i.e. $v_{\perp X} > 0$) fast flows, each followed by a slower, tailward flow. We will discuss these data in more detail below.

5.3 Discussion

5.3.1 Identifying Onset and Substorm Development

5.3.1.1 Growth Phase Signatures

The first signature of the growth phase of the substorm were detected by Cluster at 03:50 UT: an increase in $|\boldsymbol{B}|$ while the spacecraft was located in the central plasma sheet (Figure 5.14). This was followed at 03:58 UT by spacecraft moving from the central plasma sheet into the plasma sheet boundary layer. Both of these signatures are a result of magnetic flux being added to the tail lobes, increasing the tail field strength and magnetic pressure on the plasma sheet, causing it to thin. Interestingly, prior to this addition of flux, the IMF was predominantly directed northwards so the addition of flux to the tail lobes was somewhat unusual. A short period of southward IMF was detected between 03:20 UT and 03:40 UT, however, which was likely responsible for the growth and subsequent onset of the substorm.

5.3.1.2 Auroral and Ground-Based Magnetic Data

The IMAGE FUV auroral data plotted in Figures 5.3 and 5.5 seem to indicate a localised auroral activation (the Frey onset) approximately two minutes (i.e. one WIC frame) before the actual onset of the substorm expansion phase, which, according to the FUV data, occurred a few degrees in longitude eastward of the Frey onset, closer to midnight MLT. Because IMAGE was observing the southern hemisphere it is difficult to directly link the two sites of auroral activity with any disturbances in the northern hemisphere ground-based magnetometer data. During intervals of strong IMF B_Y such as this, auroral features in the northern and southern hemispheres can be displaced by as much as 1.5 hours in local time (Østgaard *et al.*, 2004) and field line tracing from magnetic field models (e.g. Tsyganenko and Stern, 1996) can significantly underestimate the amount of local time shift for a given IMF B_Y (Østgaard *et al.*, 2005). Østgaard *et al.* (2004) devised an empirical formula to estimate the amount of local time shift between conjugate auroral features, based on IMF clock angle, however their formula is only valid for periods of prolonged southward IMF, and so it is not applicable in this case. Thus without any northern hemisphere auroral data, only circumstantial links can be made between the auroral and magnetic substorm signatures during this interval.

Milling *et al.* (2008) recently presented a method (Automated Wavelet Estimation of Substorm Onset and Magnetic Events - AWESOME) whereby wavelet analysis of Pi1B (i.e. 0.025 Hz - 1 Hz) pulsations in ground based magnetometer data can be used to localise, in space and in time, the initial onset of Pi1B pulsations in the ionosphere by fitting contours to the arrival times of wave power above a certain background at the different magnetometer stations using minimum curvature analysis. Murphy *et al.* (2009b) compared the results of this method to IMAGE FUV auroral data and found that the Pi1B onset precedes auroral onset, as detected by FUV, by a few minutes. The location of Pi1B onset was usually found to be within a few degrees of latitude and longitude of the auroral onset location. Rae *et al.* (2009b,a), however, also using the AWESOME technique, found that Pi1B onset

was co-located and contemporaneous with undulations on the equatormost auroral arc which are likely too small and fast to be resolved with a global auroral imager.

AWESOME results for the interval of interest are presented in Figures 5.15 and 5.16. A ULF onset and subsequent intensification have been identified during this event. The onset (Figure 5.15) was localised near GILL and occurred at 04:16:00 UT ±16 s, while the intensification was first detected at ISLL at 04:22:24 UT ±16 s and localised south east of that station according to the contour fit. The intensification is less well constrained in space than the initial onset because of the relative lack of active magnetometer sites south east of GILL/ISLL.

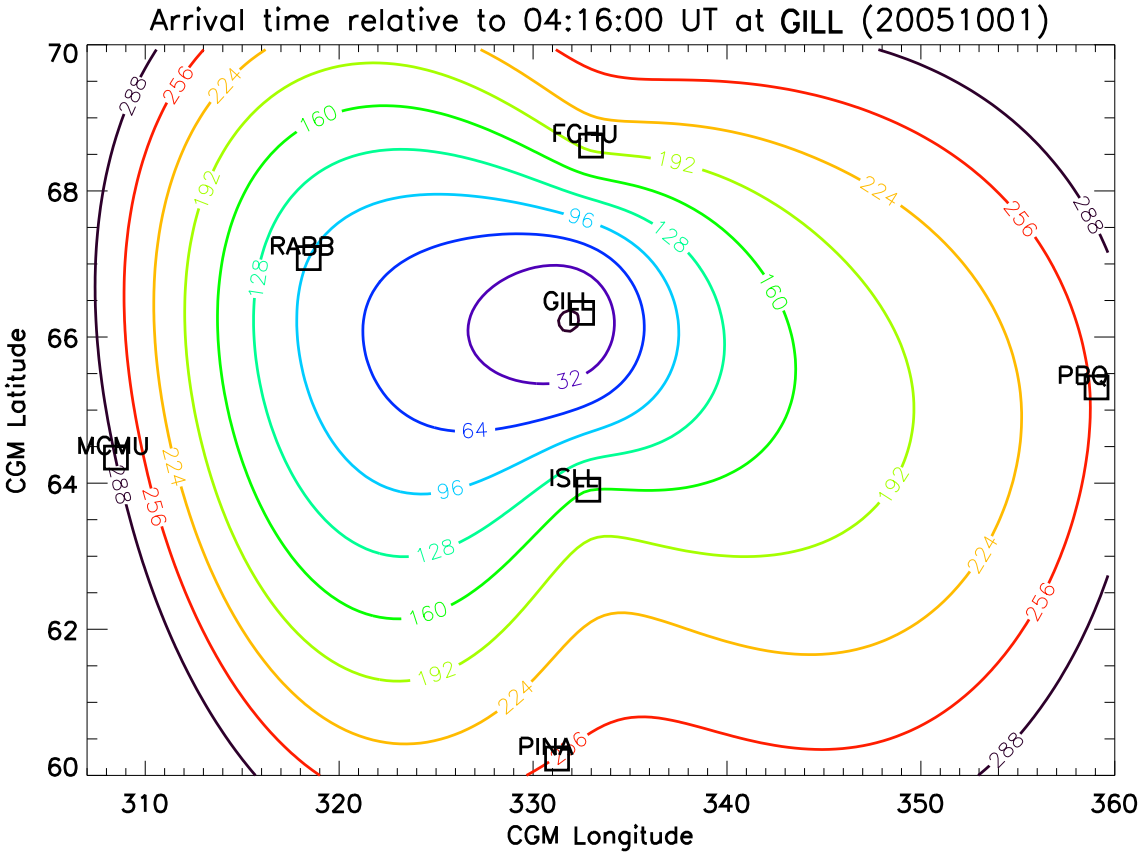

Figure 5.15: Results of wavelet timing analysis. The coloured contours show the arrival propagation pattern of Pi1B pulsations from their onset location, constrained by pulsation arrival time at the various magnetometer stations relative to the initial detection of Pi1B pulsations at GILL (Figure courtesy I. J. Rae).

The timing of the GILL onset relative to the auroral brightening of the Frey onset (i.e. preceding it by ∼3-5 minutes) is consistent with the ULF waves being associated with those aurora (Murphy *et al.*, 2009b). Furthermore, the location

of the subsequent ULF intensification detected at ISLL at 04:22 UT, east of the GILL onset, is consistent with the appearance of the aurora, i.e. the actual auroral substorm onset, east of the Frey onset, between 04:21:20 UT and 04:23:25 UT. It has been reported (Rae *et al.*, 2009b; Murphy *et al.*, 2009b) that in events where there is more than one auroral activation, more than one localised ULF signature may be recorded, as is the case here. The detection of the ISLL ULF intensification, however, may be affected by the earlier ULF onset in that identifying a suitable wave power threshold to distinguish between waves associated with the onset and those associated with the subsequent intensification is not easy. Thus if the threshold is set too high, the very beginning of the intensification may not be detected by the AWESOME algorithm. Even so, two separate ULF events were detected during the interval, the latter event located east of the former, which is consistent with the FUV data. This further validates the AWESOME algorithm and provides the northern hemisphere location of the substorm onset.

5.3.1.3 Energetic Particle Data

The Los Alamos 1990-095 satellite which was positioned eastward of the North American sector (and thus both the Frey onset and subsequent substorm onset) detected a slightly dispersed injection of energetic electrons (Figure 5.10), consistent with the electrons being injected duskward of the 1990-095 spacecraft, closer to the substorm onset location (e.g. Reeves *et al.*, 1991). That the most obvious feature in the proton data was detected by LANL 1994-084, the spacecraft immediately west of the onset locations is also consistent with particle injections over the North American sector. Attempts to localise the injection region and time by studying the difference in the energy-dispersion of the electrons between the different spacecraft did not produce a useful result. Reeves *et al.* (1991) suggest that this method would work better for protons than electrons because relativistic effects become important for higher energy electrons, however the lack of significant proton injections renders the method unsuitable for this event.

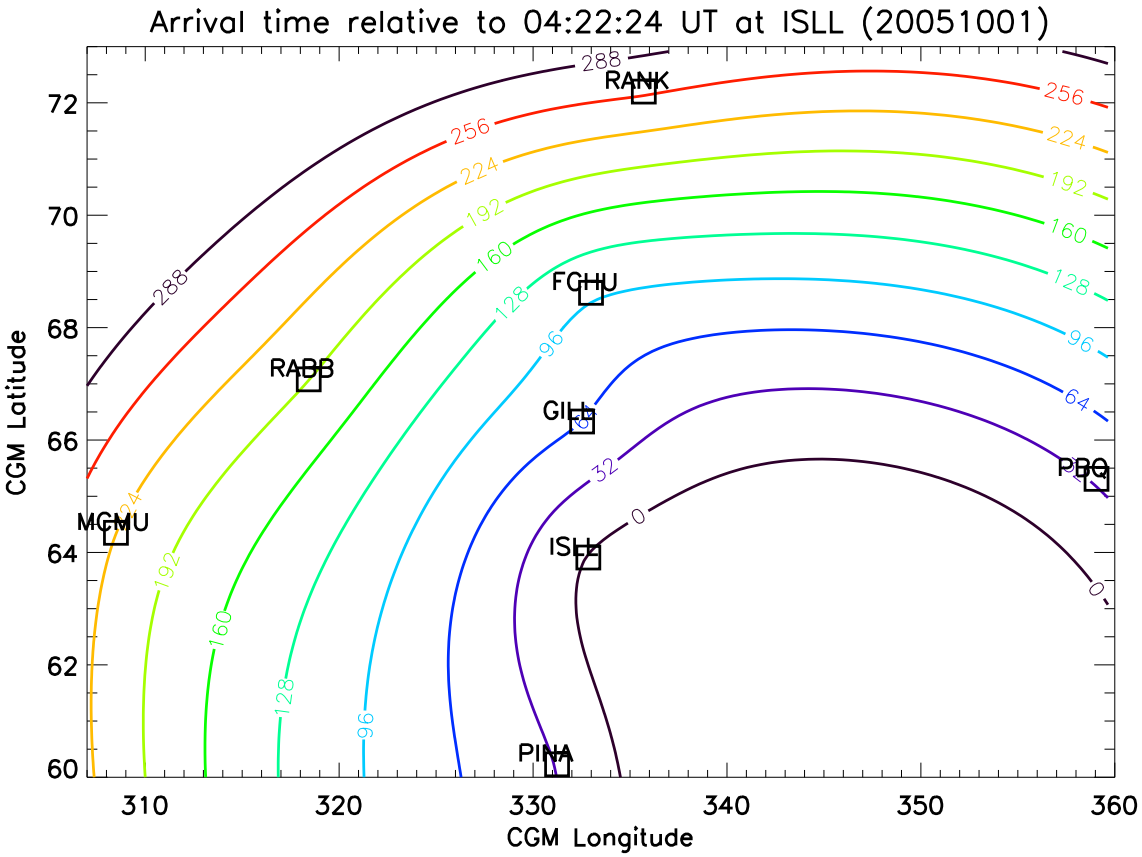

Figure 5.16: Results of wavelet timing analysis. The coloured contours show the arrival propagation pattern of Pi1B pulsations from their onset location, constrained by pulsation arrival time at the various magnetometer stations relative to the initial detection of Pi1B pulsations at ISLL (Figure courtesy I. J. Rae).

Riometers can perform a similar role to energetic particle detectors placed in geosynchronous orbit. The precipitation of electrons of energies above ~30 keV into the ionosphere causes an increase in the local ionospheric opacity to cosmic radio waves. Spanswick *et al.* (2007) used this to detect particle injections, and their degree of dispersion, using the NORSTAR (formerly CANOPUS) network of riometers (Rostoker *et al.*, 1995) located across Canada. Assuming some of the injected particles are in the loss-cone, a particle injection manifests as a temporary increase in the radio absorption of the ionosphere local to that injection (ionospheric opacity is in part governed by the electron density), the rise time of that temporary increase in opacity can be used as a proxy for the degree of energy dispersion in the electron injection. In a dispersionless injection, all of the energetic electrons would enter the ionosphere at once resulting in a short rise time of the absorption increase as measured by the riometer. Spanswick *et al.* (2007) calculated the characteristic

rise time for a dispersionless particle injection to be 3 minutes or less.

The riometer data plotted in Figure 5.12 can be used to further localise the particle injection. The first increase in absorption during the interval of interest was detected by the GILL riometer at ∼04:20 UT. The FCHU riometer detected a larger increase at ∼04:25 UT followed by a smaller increase at ∼04:52 UT and the RANK riometer detected increases in absorption at ∼04:45 UT and 04:52 UT. No increases in absorption were detected by the FSMI and FSIM riometers, located ∼17° and ∼27° of longitude west of the Churchill line respectively. Since electrons drift from dusk to dawn on the nightside, the lack of any absorption signatures at FSMI and FSIM place the initial injection point east of FSMI, consistent with both of the FUV onset locations and both of the ULF onset locations. The RABB observation site is located between GILL and FSMI but unfortunately no riometer data from that site is available for this interval. Without further riometer coverage, it is difficult to say whether or not the two responses seen in the GILL and FCHU represent two separate injections, perhaps associated with the two auroral forms, or the expansion of one injection site poleward from GILL to FCHU. The later RANK absorption signature will be discussed below in terms of the RANK geomagnetic bay and Cluster data.

5.3.1.4 TC-2 and GOES-12 Data

The IMAGE FUV data suggest that there were two instances of auroral activity around 04:20 UT on 1 October 2005 separated by only ∼1.5 hours of MLT, the latter of which develops into a fully-fledged substorm. CARISMA magnetometer data are also consistent with this idea. Uncertainties in magnetic field mapping means that distinguishing between spaceborne features associated with these two different auroral activations is difficult. The dipolarisations observed by GOES-12 (Figure 5.8) and TC-2 (Figure 5.9), however, are more likely to have been associated with the substorm than with the Frey onset: the magnetospheric counterpart of a localised auroral form similar to the Frey onset, reported in Chapter 4 of this thesis

and by Walsh *et al.* (2009), which was also observed by TC-2, did not have a large scale dipolarisation associated with it.

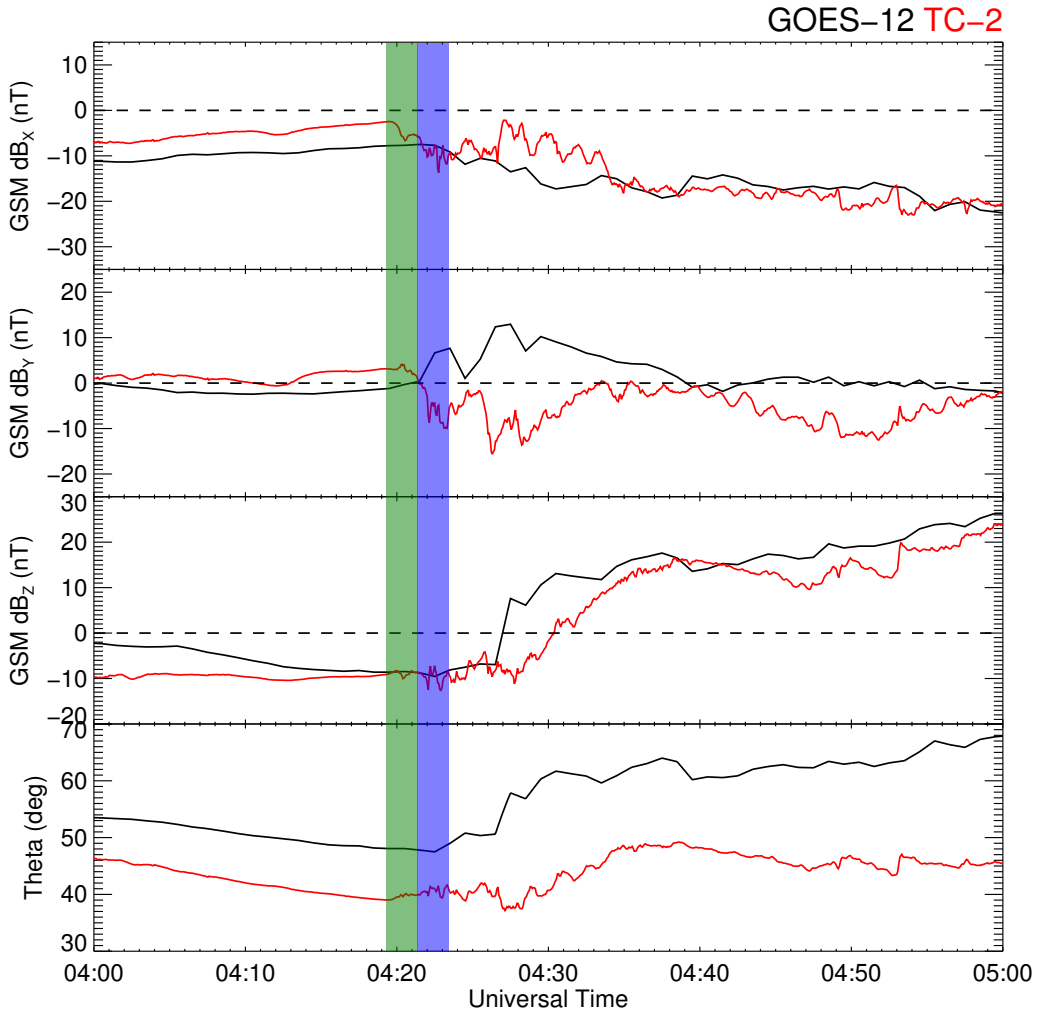

Figure 5.17: The top 3 panels are GSM magnetic field components from GOES-12 (Black) and TC-2 (Red). The data have had a model magnetic field (Tsyganenko and Stern, 1996) removed. The bottom panel is the GSM latitude angle of the magnetic field from the two spacecraft. Note this has not had any model field removed. The blue shaded region represents the time range covered by the 04:23 UT IMAGE-FUV frame containing the auroral substorm onset, while the green rectangle represents the time covered by the IMAGE frame corresponding to the Frey onset (pseudobreakup).

One hour of GOES-12 (black) and TC-2 (red) magnetic field data with a Tsyganenko 96 magnetic field model (Tsyganenko and Stern, 1996) subtracted, along with the latitude angle of the magnetic field with no model field subtracted is plotted in Figure 5.17. The blue shaded region represents the time range covered by the

IMAGE-FUV frame of substorm onset (04:21:20 UT - 04:23:26 UT). The dipolarisation was first observed by GOES-12, beginning between 04:26 UT and 04:27 UT (Unfortunately only 1 minute resolution magnetic field data are so far available from the GOES spacecraft from this event). TC-2 first observed the dipolarisation at 04:28 UT, which would be consistent with the spacecraft's Earthward position relative to GOES-12 (Figure 5.7) if the dipolarisation front were to propagate Earthwards.

TC-2 and GOES-12 also observed anti-correlated fluctuations in dB_Y (Figure 5.17, middle panel) beginning just prior to substorm onset and continuing until ∼04:40 UT, when the dipolarisation at TC-2 stopped. It is likely, then, that the changes in dB_Y at the two spacecraft are the result of a changing current flowing between them. The sense of the changes in dB_Y, given that both spacecraft were in the northern hemisphere and TC-2 was located earthwards and westwards of GOES-12, is consistent with a current flowing out of the northern ionosphere, i.e. the westward part of the substorm current wedge (McPherron *et al.*, 1973). This is illustrated, albeit in a simplified manner in Figure 5.18. A more realistic scenario than that pictured in Figure 5.18 is that the westward part of the substorm current wedge had a non-zero azimuthal extent, encompassing the spacecraft. This would explain the lack of any dB_X fluctuations in the magnetometer data, which would be expected from the current system illustrated in the figure.

At the same time that the B_Y signatures of the SCW were first detected at TC-2, pulsations in the magnetic field were also detected, most obviously in dB_X and dB_Z. A similar wavelet timing analysis to that performed on the ground-based magnetometer data placed the onset time of these TC-2 pulsations at 04:20:00 UT±20 s. The available GOES magnetometer data are not of sufficient resolution to determine whether similar pulsations were observed at that spacecraft, however Rae *et al.* (2009a) did observe similar pulsations at the GOES spacecraft during another event. The timing of the TC-2 pulsations (i.e. their appearance at the same time as the SCW) suggest a link to the formation of the SCW - i.e. the disruption of the cross-

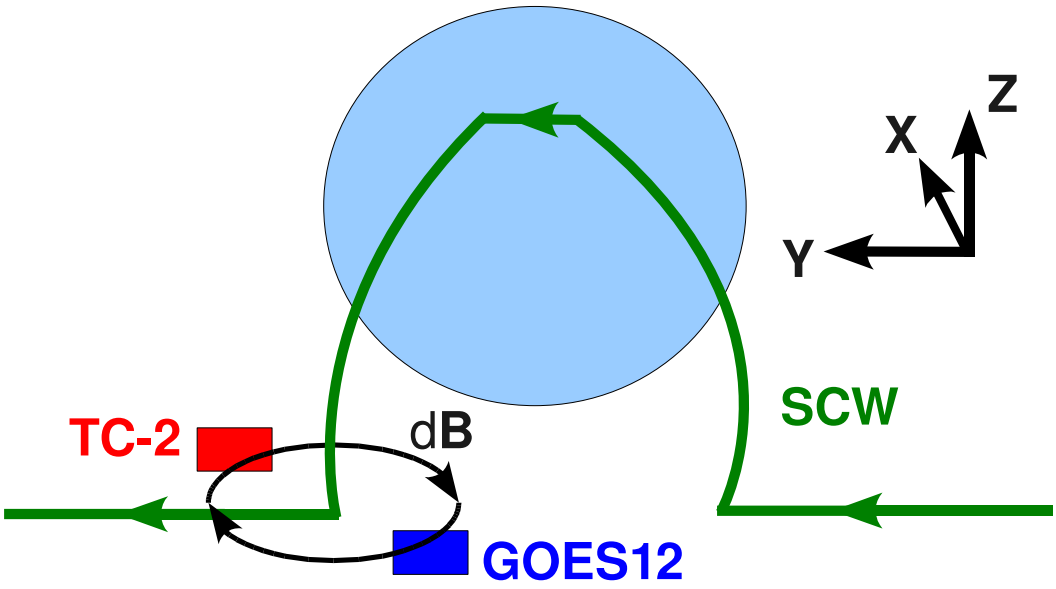

Figure 5.18: Possible Substorm Current Wedge geometry relative to the positions of GOES-12 and TC-2. Currents are drawn in green and the associated $\boldsymbol{B}$ field in black. The blue rectangle represents GOES-12 and the red TC-2.

tail current and, under the Current Disruption paradigm, potentially the substorm onset mechanism. The frequency range of the pulsations is similar to those reported by Yoon *et al.* (2009) who determined that, during a substorm observed by the THEMIS spacecraft, waves caused by the Alfvén drift instability might be responsible for disrupting the cross-tail current. The frequency of the TC-2 pulsations is also close to the gyrofrequency of singly charged oxygen, so oxygen ion-cyclotron waves may also be important. The Dst index shows no major magnetic storms in the preceding weeks, however, so the background level of oxygen in the plasma sheet is likely to be relatively low (e.g. Kistler *et al.*, 2006). Indeed Cluster CODIF observations taken further downtail than TC-2 do not show enhanced oxygen levels, so if the presence of oxygen is important in generating these pulsations it is likely to be fairly localised in the near-Earth region, perhaps drawn out of the ionosphere by auroral current systems. The spacecraft's position at the westward edge of the SCW is consistent with this - an upward current would draw positive ions out of the ionosphere. The TC-2 PEACE data gap, occurring as it did at the onset of the TC-2 pulsations, is unfortunate. The PEACE data that are available during

the pulsations (enhanced $T_{e//}/T_{e\perp}$, an additional low-energy field-aligned electron population that disappear when the pulsations stop) point to these electrons being associated with the pulsations. In the absence of electron data at the moment of ULF onset it is difficult to determine exactly how the electrons are linked to the pulsations, however. Additionally, without further data (electric field and ion composition for example), identification of the pulsations observed by TC-2 during this interval and the exact role they play in disrupting the cross-tail current is difficult.

That the SCW-related changes in B_Y and the TC-2 ULF pulsations appear several minutes before the dipolarisation of the magnetic field may be a function of TC-2's and GOES-12's positions relative to the current disruption region. Geosynchronous orbit (and indeed just inside it, where TC-2 was located) is at the inner edge of the region where the cross tail current is expected to be typically disrupted (Lui, 1996), however the difference in sense of the B_Y fluctuations between TC-2 and GOES-12 is consistent with a field aligned current flowing in the space between the spacecraft, so a more likely explanation is that the spacecraft are separated azimuthally from the current disruption site and are seeing the establishment of the very edge of the Substorm Current Wedge, which then expands azimuthally with the westward travelling surge of the auroral substorm, such that the region of dipolarised field expands first over GOES-12 and then over TC-2 (cf. Lui *et al.*, 2008, for example). That TC-2 does not see any significant plasma flow before the dipolarisation, even during the the establishment of the substorm current wedge is also consistent with this.

5.3.2 Cluster Data

In order to fully understand the development of this particular substorm and determine which of the various substorm models most closely describe its features, evidence of reconnection downtail of the geosynchronous region, either before or after auroral onset, is necessary (e.g. Angelopoulos *et al.*, 2008; Lui *et al.*, 2008; Draper

et al., 2004). Unfortunately, in the minutes surrounding auroral onset the Cluster spacecraft were located in the plasma sheet boundary layer (Figure 5.14) and as such were not ideally placed to measure signatures of reconnection in the plasma sheet, for example BBFs (Angelopoulos *et al.*, 1992). Other signatures of reconnection can be observed by spacecraft located in the PSBL however. Low energy electrons have been observed streaming into a reconnection site along the separatrix between open and closed field lines and higher energy electrons have been observed flowing along the separatrix out of a reconnection site (Nagai *et al.*, 2001; Alexeev *et al.*, 2006). It is these electrons that support the Hall currents associated with quadrupolar Hall magnetic field seen near reconnection X-lines (Hoshino *et al.*, 2001; Runov *et al.*, 2003).

A population of low energy, anti-field-aligned (i.e. tailward streaming) electrons was detected by C2 PEACE and is plotted in Figure 5.19. The magnetic field magnitude and GSM components are plotted in Panel A, The differential energy flux of pitch angle 0° electrons minus the differential energy flux of pitch angle 180° electrons is plotted in Panel B while Panels C-E are differential energy fluxes of PA0°, PA90° and PA180° electrons respectively. A population of antiparallel (i.e. tailward streaming) electrons of energy ∼100eV is evident in Panels B and E between 04:20 UT and 04:24 UT. However unlike in the intervals reported by Nagai *et al.* (2001) and Alexeev *et al.* (2006), no higher energy earthward electron beams were detected by any of the Cluster spacecraft around 04:20 UT. Furthermore, recent work by Åsnes *et al.* (2009[1]) has revealed the existence of a population of low energy field-aligned electrons that are present in the plasma sheet a significant proportion of the time, often streaming tailward. Without any Hall magnetic field signatures, then, it is difficult to say whether or not these electrons are flowing along the separatrix towards a reconnection region (and whether or not this reconnection region is a near-Earth or distant neutral line) or are unrelated to the substorm.

The first clear evidence of reconnection in the Cluster data was the 200 $\mathrm{km\,s^{-1}}$

[1]Manuscript in preparation

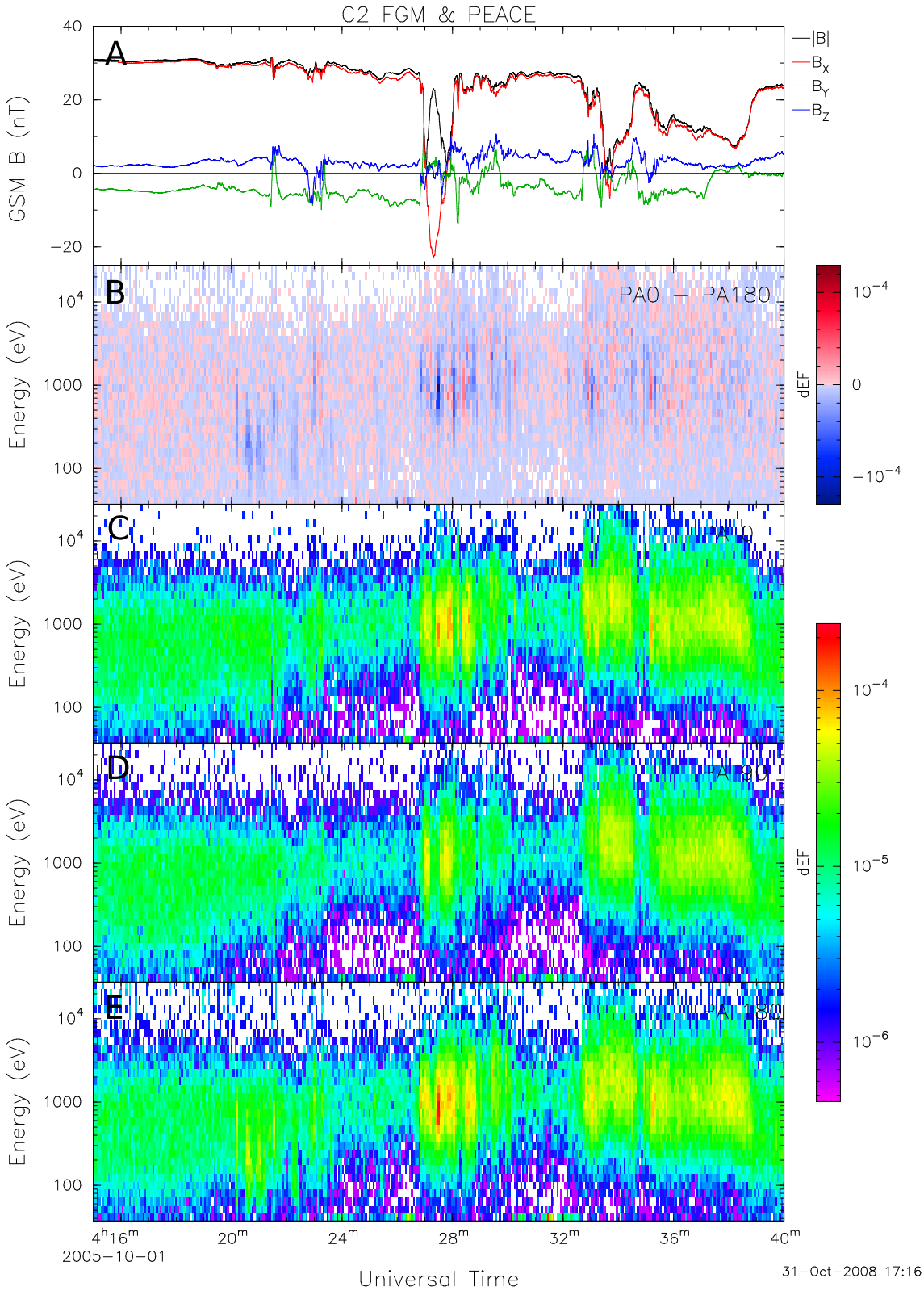

Figure 5.19: C2 FGM and PEACE data. Panel A shows the magnitude and GSM components of magnetic field, Panel B is an energy-time spectrogram plotting the differential energy flux of pitch angle 180° electrons subtracted from the differential energy flux of pitch angle 0 electrons, while Panels C-E are the differential energy flux of pitch angle 0°, 90° and 180° electrons respectively.

flow observed by C2 PEACE at ∼04:27 UT. Cluster observed the flow during a transient encounter with the plasma sheet and as such it is impossible to say when it started, and thus whether or not it could be the same flow observed by TC-2 at the same time as dipolarisation. C3 and C4 also recorded increased electron fluxes around this time (Figure 5.14, Panels G-I), although did not enter into the plasma sheet as far as C2 and thus did not see significant flow in the ion moments. It is consistent with the time-ordering of this plasma sheet encounter between the spacecraft (C2→C3→C4) that these data represent an earthward-moving bulge in the plasma sheet, possibly caused by time-varying reconnection downtail of Cluster (e.g. Semenov *et al.*, 2005), however further investigation is required to confirm this. Even so, the data do suggest that reconnection of some sort has started downtail of Cluster before 04:27 UT.

5.3.3 High Latitude Activity

At ∼04:45 UT, when the magnetotail plasma sheet had expanded over the Cluster spacecraft (Figure 5.14, Panels F-I), further convincing evidence for reconnection was found in the form of fast Earthward flows detected by the HIA instrument onboard C3. More detail of these flows is plotted in Figure 5.20 where Panel A is the geodetic X component of magnetic field as measured by the RANK CARISMA magnetometer (which recorded the strongest geomagnetic disturbance of the entire interval at this time), Panel B the magnitude and GSM components of magnetic field as measured by FGM onboard C3, Panel C the GSM components of $\boldsymbol{v}_\perp$ as measured by HIA onboard C3 and Panel D an energy time spectrogram plotting omnidirectional electron differential energy flux from PEACE-HEEA, again onboard C3.

The expansion of the magnetotail plasma sheet during substorms is thought to be a result of the reconnection of open, lobe magnetic flux that removes flux from the lobes and thus reduces magnetic pressure on the plasma sheet (Baumjohann

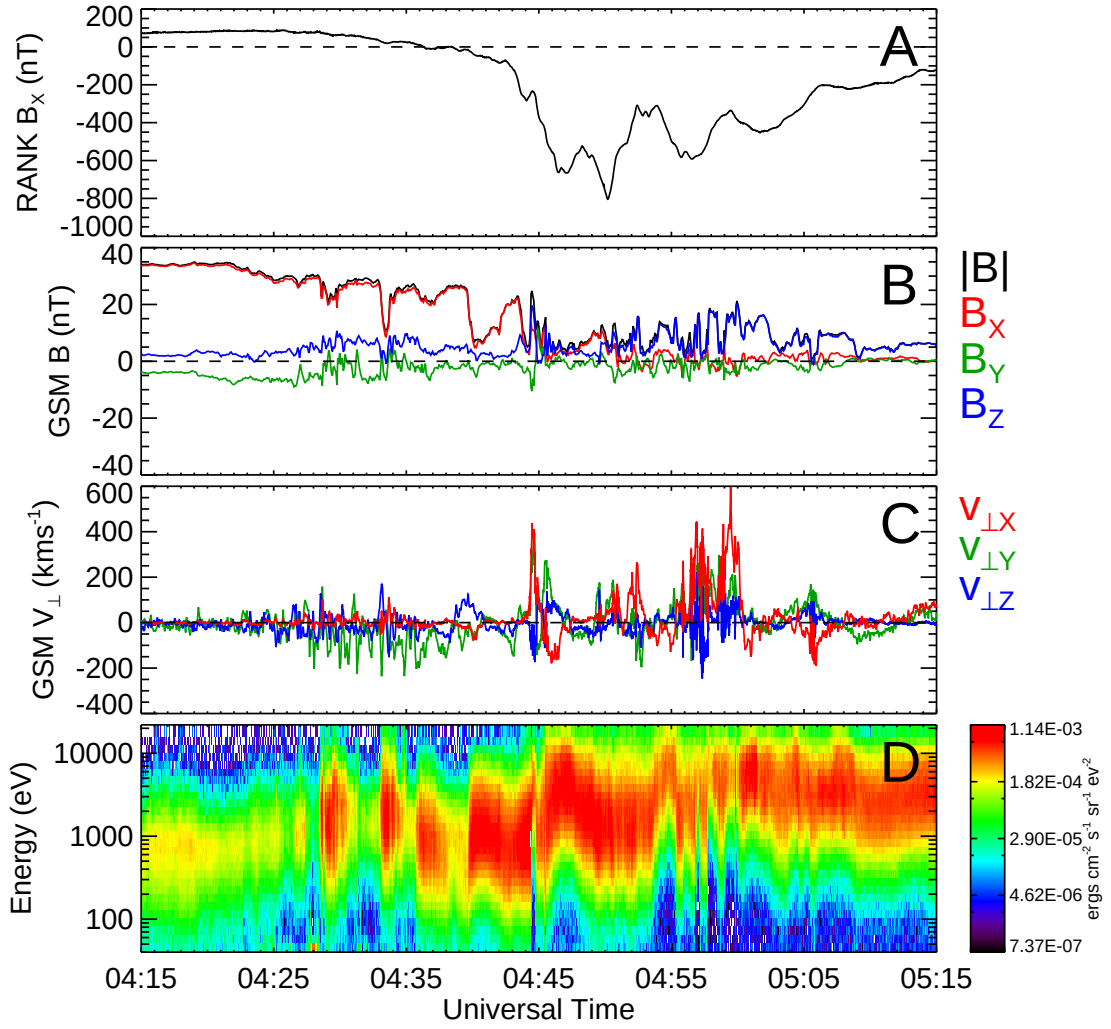

Figure 5.20: The geodetic X component of magnetic field from the RANK magnetometer (Panel A), $|\boldsymbol{B}|$ and the GSM components of magnetic field from C3 FGM (Panel B), GSM components of $\boldsymbol{v}_\perp$ from C3 HIA (Panel B) and a PEACE energy-time spectrogram, also from C3 (Panel D)

et al., 1992; Dewhurst *et al.*, 2004) it can therefore be argued that the reconnection of lobe magnetic flux began before the tail plasma sheet expanded over the Cluster spacecraft. The detection of high speed flows soon after the plasma sheet expansion at 04:45 UT (Figure 5.20, Panel C) is also consistent with reconnection occurring tailward of the spacecraft. At the same time as the flows were first detected, the polar edge of the auroral oval, which had by then expanded considerably from its quiescent latitude, brightened (Figure 5.3). Furthermore the CARISMA magnetometer at RANK, registered a large magnetic bay in the B_X component at the same time as the brightening of the aurora (Figure 5.20, Panel A) and the fast flow is detected

by Cluster 3 (Figure 5.20, Panel C). The RANK riometer (Figure 5.12) also detects an increase in absorption at this time, consistent with an increase in ionospheric particle precipitation. Further fast flows detected by Cluster until ∼05:00 UT also coincide with a bright poleward edge of the aurora (Figure 5.3) and further decreases in B_X at RANK.

The increase in ionospheric radio absorption at RANK, at ∼04:45 UT is too long delayed from the injection at GILL/FCHU to be a result of the radial expansion of the initial injection region tailwards (A. J. Kavanagh, private communication, 2009). Furthermore, no energetic particle injection associated with the riometer signature was observed by any of the LANL spacecraft, placing the injection region of those particles outside of geosynchronous orbit. Whether the particles responsible for the increase in ionospheric opacity above RANK entered the ionosphere direct from a reconnection site or via a further convection surge which stopped outside geosynchronous orbit is unknown. Also unknown is whether or not the reconnection signatures were a result of an increased reconnection rate at the existing NENL, which by then might have begun to retreat downtail, or the development of an entirely new reconnection site perhaps unrelated to the earlier substorm onset. In any case, the link between an increase in the reconnection rate and/or reconnection of lobe field lines, as evidenced by the plasma sheet expansion and fast flows seen by Cluster, the high latitude bay and increased particle precipitation at RANK, and the brightening of the poleward edge of the aurora seems solid.

5.4 Summary and Conclusions

Bringing all of the above together, a sequence of events describing this interval can be written:

03:20−03:40 UT	Southward turning of the IMF
03:50 UT	Cluster observed increasing $\|\boldsymbol{B}\|$ (first evidence of growth phase)
03:58 UT	Plasma Sheet thins and Cluster drops into the PSBL
04:16 UT±16 s	Initial ULF onset at GILL
04:19 UT	Signature of particle injection at GILL riometer
04:19:15−04:21:20 UT	Frey Onset (pseudobreakup)
04:20 UT±20 s	ULF Onset at TC-2 B_Y fluctuations seen at TC-2 and GOES-12 (Evidence of SCW formation)
04:21:20−04:23:26 UT	Auroral Onset
04:22:24 UT±16 s	ULF intensification at ISLL
04:25 UT	Injection signature at FCHU riometer
04:26 UT	Dipolarisation at GOES-12 Particle injection seen at LANL 1990-095
04:27 UT	Transient crossing of the plasma sheet by C2, flows seen
04:28 UT	Dipolarisation and flows at TC-2
∼04:45 UT	High Latitude bay and pulsations seen at RANK Injection signature at RANK riometer Brightening of poleward edge of the aurora Plasma sheet expansion and fast flows seen by Cluster

The first sign of any activity in the magnetosphere during this interval was the growth phase of the substorm, which was measured by Cluster as an increase in the magnitude of the magnetic field in the plasma sheet and inferred from the passage of the spacecraft from the central plasma sheet into the PSBL (Figure 5.14). A pseudobreakup was subsequently detected, first as a ULF wave onset (Figure 5.15) and

then in global auroral images (the Frey onset, Figure 5.3) and perhaps as a small particle injection signature in the GILL riometer (Figure 5.12). The first evidence of substorm expansion phase onset was the ULF onset at 04:20 UT detected by TC-2, which was accompanied by B_Y fluctuations in the magnetic field, a signature of FACs consistent with the formation of the westward edge of the substorm current wedge between TC-2 and GOES-12 (Figures 5.17 & 5.18). This was followed by the detection of a further source of ULF waves south east of ISLL (Figure 5.16) and the auroral onset (Figure 5.5) between 04:21:20 UT and 04:23:25 UT. Dipolarisation was subsequently detected, first by GOES-12 (04:26 UT) and then TC-2 (04:28 UT, Figure 5.17), where it was accompanied by Earthward flow. This has been interpreted as a region of dipolarisation expanding westwards from its initial location east of the spacecraft (consistent with their position relative to the SCW). The detection of the particle injection signature at FCHU at ∼04:25 UT and LANL 1990-095 at 04:26 UT is consistent with this since particle injections are thought to be associated with dipolarisation (e.g. Birn *et al.*, 1998).

For this event, it is impossible to say whether or not any reconnection was occurring prior to the auroral substorm onset because Cluster was located outside of the central plasma sheet and thus was not ideally located to observe any fast flows associated with the reconnection (Baumjohann *et al.*, 1990), nor did it observe any of the expected electron (Nagai *et al.*, 2001; Alexeev *et al.*, 2006; Angelopoulos *et al.*, 2008) or magnetic (Runov *et al.*, 2003; Borg *et al.*, 2005) signatures of the Hall reconnection geometry in the PSBL. The Hall magnetic signatures are only observed close to the reconnection site, however, so if there were an active Near-Earth Neutral Line in the magnetotail before auroral onset it must be located away from Cluster. The first evidence of reconnection came when C2 briefly crossed the plasma sheet at 04:27 UT and detected an earthward flow of $\sim$200 km s^{-1}. This slow flow is more likely a product of the reconnection of closed plasma sheet field lines rather than open lobe flux. The expansion of the plasma sheet, fast flows and high latitude bays seen around 04:45 UT are much more convincing evidence of the reconnection of lobe field lines, especially in light of the brightening of the poleward edge of the

aurora at this time and the fact that the bay at RANK is more than twice as large as any of the bays associated with the onset of the substorm. Whether or not this later reconnection is simply an increase in reconnection rate at the existing NENL, which by then had retreated downtail, or the development of a further reconnection site is unknown.

In conclusion, while this event does not provide conclusive proof for either the Near-Earth Neutral Line or Current Disruption substorm models, it does provide insights into the substorm process, namely that higher latitude geomagnetic activity can be somewhat decoupled from the lower latitude activity and this high latitude activity could be a result of direct particles from an X-Line reconnecting lobe flux, rather than through a substorm current wedge type current system. Study of further events is needed to determine how common this high latitude activity is during substorms and to more concretely identify the link between it and reconnection. This event also provides further validation for the AWESOME technique of identifying and localising substorm onset through Pi1B pulsations. We have also provided more evidence that the onset of ULF pulsations, not only Pi2s but also Pi1Bs in space, is linked with the formation of the substorm current wedge and this can precede auroral onset and ULF onset on the ground by a few minutes. Further work where more comprehensive data are available is needed however to fully quantify and study these pulsations and determine what role, if any they play in the formation of the substorm current wedge and the substorm process in general. The evolution of Cluster's orbit so that it now passes through the current disruption region in the magnetotail will provide an ideal opportunity to do this.

Chapter 6

Conclusions and Future Work

> ...as we know, there are known knowns; there are things we know we know. We also know there are known unknowns; that is to say we know there are some things we do not know. But there are also unknown unknowns – the ones we don't know we don't know.
>
> *Donald Rumsfeld, Feb. 2002*

6.1 Conclusions

In this thesis, several different phenomena and processes that occur in the magnetotail have been investigated using combined Cluster and Double Star measurements, with supporting data from many other ground- and space-based sources.

In Chapter 3 magnetic flux ropes, which were interpreted as a product of Multiple X-Point Reconnection, were investigated and the first observations of the simultaneous existence of more than one flux rope, one at Cluster and one at TC-1 (which were 6.3 R_E apart) presented. A third flux rope was also observed by two of the four Cluster spacecraft, the others seeing a feature resembling a TCR, providing further evidence for the flux rope-TCR link (Owen *et al.*, 2005). All the flux ropes were observed to have similar orientations with respect to the local neutral sheet,

despite differences in local neutral sheet orientation at different spacecraft, providing the first conclusive evidence that flux rope orientation is linked to neutral sheet tilt. Evidence suggests these three flux ropes were formed through reconnection at a minimum of four competing X-points and were driven Earthward by the fastest reconnecting X-point, located tailward of the Cluster tetrahedron.

In Chapter 4 a detailed analysis of a depleted flux tube (plasma bubble), based on data from the Cluster and TC-2 spacecraft, was presented. In particular the first simultaneous measurements of a plasma bubble and the expected return flows around its flanks were reported. Additionally a partially stagnant, partially tailward-flowing wake behind the depleted flux tube was discovered. This wake itself had a lower plasma density than the undisturbed plasma sheet and this was explained in terms of a process similar to that which forms plasma depletion layers at the dayside magnetopause. The positions of the different Cluster spacecraft with respect to the bubble centre line, as determined from identification of the FACs at the bubble flanks allowed for the estimation of the cross-tail extent of the structure, which was calculated to be not larger then $3\,\mathrm{R_E}$, consistent with previous observations of BBFs (Nakamura *et al.*, 2004). The first observations of certain near-Earth plasma bubble features, as predicted by simulations (Birn *et al.*, 2004), namely an increase in plasma pressure, decrease in magnetic pressure and field-aligned plasma flows within the flux tube were reported. A simple model of how the field-aligned current systems associated with the plasma bubble might map to the ionosphere, and how the presence of a strong B_Y in the magnetotail might rotate this current system, consistent with observed ionospheric conditions during this event, was put forward, however the available data were not sufficient to confirm the model.

Finally, in Chapter 5, a substorm onset was studied with a comprehensive array of near-Earth spacecraft and ground based instrumentation. It was possible to distinguish between the onset of the substorm and a prior pseudobreakup, as observed by IMAGE-FUV using ground based magnetometer measurements and the AWESOME technique (Milling *et al.*, 2008; Murphy *et al.*, 2009b). The establishment of

the substorm current wedge was observed by TC-2 and GOES-12, prior to dipolarisation and prior to any large scale auroral activity. The spacecraft were inferred to be located on the westward edge of the developing SCW and it is this separation in azimuth that was responsible for the delay between seeing the formation of the SCW and seeing the associated dipolarisation. No flows were seen at TC-2 prior to dipolarisation either, which may also be an effect of spacecraft location. Unfortunately the Cluster spacecraft, located in the PSBL around the time of onset, were not ideally positioned to detect signatures of the onset of reconnection prior to the activation of the aurora. However, after onset the plasma sheet expanded over the Cluster spacecraft, which subsequently detected fast earthward flows, both taken to be consistent with the reconnection of lobe field lines, at the same time as the CARISMA magnetometers recorded a disturbance in the geomagnetic field poleward of typical substorm activity (a high latitude bay) that was at least a factor of 2 larger than those disturbances at more typical onset latitudes during this event. Riometer data suggest that this higher latitude activity was somewhat decoupled from the development of the substorm in the near-Earth tail and at lower latitudes, however analysis of further events is necessary to be certain.

Each of the investigations summarised above has revealed that the magnetotail is a much more complex system than the simple two-dimensional sketches so often used as frameworks around which data are interpreted. The magnetotail not only has radial and elevational structure, but also azimuthal structure which must be considered in order to reach a full understanding of the magnetosphere-ionosphere system. Reconnection sites have been proved to be operating at several locations in the near-earth magnetotail; multiple auroral features, and their associated magnetospheric signatures, have been shown to exist simultaneously; and we conclude that only a synoptic approach combining space-and ground-based measurements of both the magnetosphere and ionosphere is capable of unravelling their complexities.

6.2 Future Work

Each of the studies presented in this thesis regard only a single event, and their conclusions can be strengthened by considering many events in a statistical manner. The ever-increasing archive of Cluster and Double Star data, some of which taken in previously unstudied (by those spacecraft) regions of the magnetosphere can be combined with data from increasingly common and advanced ground-based instrumentation to try and answer long-unresolved questions in magnetospheric and space plasma physics.

In terms of magnetic flux ropes, radial constellations of spacecraft (e.g. THEMIS) can be used to track the propagation of flux ropes through the magnetosphere and determine, for example, what controls how close a flux rope can penetrate to the Earth, how many flux ropes are created during MXR events and how flux ropes develop as they propagate Earthward or tailward - are they formed force free and do they relax to a force-free state before they are subsequently deformed by interaction with stronger magnetic fields close to the Earth? Is the concept of a force-free flux rope even valid in the magnetotail? Large-separation Cluster measurements can also aid in our understanding of the link between flux ropes and TCRs. The 2006 tail season, when Cluster was configured in a 10,000 km tetrahedron, provides an increased chance that some of the spacecraft would sample the flux rope in the plasma sheet while others would remain the the lobe or PSBL and instead observe a TCR, as happened with Signature 3 analysed in Chapter 3 (see also Beyene *et al.,* 2009[1]). Flux ropes are known to have ionospheric counterparts (Amm *et al.*, 2006; Juusola *et al.*, 2008) however these have also not been investigated in a statistical way, nor have the properties of the edges of flux ropes. The ever-expanding array of ground based magnetometers and increasing archives of space-based data may now make this feasible.

A statistical study of the properties of plasma bubbles would also provide in-

[1]Manuscript in Preparation

sights into the dynamics of the magnetotail, while surveys of BBFs have previously been carried out these are mostly based on single spacecraft data. The increasing availability of data from large-scale Cluster separation tail seasons (i.e. 10,000 km in the GSM $\sim XY$ plane, 2005+) allows for a survey of events where both earthward and tailward flows are seen simultaneously by the Cluster spacecraft. This would make possible a study of the link between the earthward flow speed of a bubble and tailward flow speed of plasma around it's edges for example, potentially shedding light on the propagation mechanism (is it interchange motion, reconnection-driven, or both?) and also the formation mechanism of plasma bubbles as well as a more general investigation of the geometry and properties (and indeed occurrence frequency) of the wake structure discussed in Chapter 4. Further investigation of the link between IMF B_Y and the plasma bubble current system would also be made possible by studying events with more comprehensive SuperDARN coverage, for example, or where the ionospheric footpoint of a bubble was located over areas with magnetometer coverage.

In the field of substorm science there are many unanswered questions additional to those highlighted in Chapter 5. The evolution of the Cluster orbit is now enabling the spacecraft to make the first detailed multi-point measurements of the current disruption region (e.g. Nakamura *et al.*, 2009), which could contribute significantly to studies of the current disruption mechanism. These Cluster data, coupled with advanced ground-based data analysis techniques like AWESOME, will help shed light on the link between the ULF pulsations reported in Chapter 5 and the disruption of the cross-tail current. Furthermore the link between high-latitude geomagnetic activity and BBFs in the magnetotail needs to be studied statistically to determine if it is indeed the reconnection of open lobe flux that is responsible for both of these phenomena. A combination of Cluster, Double Star, CARISMA, THEMIS (both ground- and space-based) and other ground-based magnetometer data should provide a very rich dataset suitable for solving this problem.

Looking further ahead, ESA's proposed Cross-Scale mission, designed to probe

the fundamental plasma physics that governs the magnetosphere and other space plasmas throughout the universe, will at the very least provide many more data in regions of interest for magnetospheric physics. Furthermore, through its investigations of processes such as magnetic reconnection, it will provide insights that can then be applied to the magnetosphere increasing our understanding of near-Earth space and beyond.

Selected Acronyms & Abbreviations

ACE	Advanced Composition Explorer
ASPOC	Active Spacecraft Potential Control
AWESOME	Automated Wavelet Estimation of Substorm Onset and Magnetic Events
BBF	Bursty Bulk Flow
CARISMA	Canadian Array for Realtime InvestigationS of Magnetic Activity
CIS	Cluster Ion Spectrometry experiment
CODIF	Composition and Distribution Function analyser
DPU	Data Processing Unit
FAC	Field-Aligned Current
FGM	Fluxgate Magnetometer
GSE	Geocentric Solar Ecliptic
GSM	Geocentric Solar Magnetic/Magnetospheric
HAR	High Angular Resolution
HEEA	High Energy Electron Analyser
HIA	Hot Ion Analyser
IMAGE	Imager for Magnetopause to Aurora Global Exploration
IMF	Interplanetary Magnetic Field
LAR	Low Angular Resolution
LEEA	Low Energy Electron Analyser
MAR	Medium Angular Resolution
MCP	Micro Channel Plate
MHD	Magnetohydrodynamic(s)
MVA	Minimum Variance Analysis
MXR	Multiple X-Point Reconnection
NENL	Near-Earth Neutral Line
PA	Pitch Angle
PEACE	Plasma Electron and Current Experiment
PSBL	Plasma Sheet Boundary Layer
TCR	Travelling Compression Region
TRINNI	Tail Reconnection during IMF-Northward Non-substorm Intervals

Bibliography

Akasofu, S.-I.: The development of the auroral substorm, *Planet. Space. Sci.*, **12**, 273–+, 1964.

Alexeev, I. V., Sergeev, V., Owen, C. J., Fazakerley, A., Lucek, E., and Réme, H.: Remote sensing of a magnetotail reconnection X-line using polar rain electrons, *Geophys. Res. Lett.*, **33**, 19 105–+, doi:10.1029/2006GL027243, 2006.

Alfvén, H.: Existence of electromagnetic-hydrodynamic waves, *Nature*, **150**, 405–+, doi:10.1038/150405d0, 1942.

Amm, O. and Kauristie, K.: Ionospheric Signatures Of Bursty Bulk Flows, *Surveys in Geophysics*, **23**, 1–32, 2002.

Amm, O., Nakamura, R., Frey, H. U., Ogawa, Y., Kubyshkina, M., Balogh, A., and Rème, H.: Substorm topology in the ionosphere and magnetosphere during a flux rope event in the magnetotail, *Ann. Geophys.*, **24**, 735–750, 2006.

Angelopoulos, V., Baumjohann, W., Kennel, C. F., Coronti, F. V., Kivelson, M. G., Pellat, R., Walker, R. J., Luehr, H., and Paschmann, G.: Bursty bulk flows in the inner central plasma sheet, *J. Geophys. Res.*, **97**, 4027–4039, 1992.

Angelopoulos, V., McFadden, J. P., Larson, D., Carlson, C. W., Mende, S. B., Frey, H., Phan, T., Sibeck, D. G., Glassmeier, K.-H., Auster, U., Donovan, E., Mann, I. R., Rae, I. J., Russell, C. T., Runov, A., Zhou, X.-Z., and Kepko, L.: Tail Reconnection Triggering Substorm Onset, *Science*, **321**, 931–, doi:10.1126/science.1160495, 2008.

Arnoldy, R. L., Posch, J. L., Engebretson, M. J., Fukunishi, H., and Singer, H. J.: Pi1 magnetic pulsations in space and at high latitudes on the ground, *J. Geophys. Res.*, **103**, 23 581–23 592, doi:10.1029/98JA01917, 1998.

Baker, D. N., Pulkkinen, T. I., Angelopoulos, V., Baumjohann, W., and McPherron, R. L.: Neutral line model of substorms: Past results and present view, *J. Geophys. Res.*, **101**, 12 975–13 010, doi:10.1029/95JA03753, 1996.

Balogh, A., Carr, C. M., Acuna, M. H., Dunlop, M. W., Beek, T. J., Brown, P., Fornaçon, K.-H., Georgescu, E., Glassmeier, K.-H., Harris, J., Musmann, G., Oddy, T., and Schwingenschuh, K.: The Cluster Magnetic Field Investigation: overview of in-flight performance and initial results, *Ann. Geophys.*, **19**, 1207–1217, 2001.

Baumjohann, W.: Modes of convection in the magnetotail, *Physics of Plasmas*, **9**, 3665–3667, doi:10.1063/1.1499116, 2002.

Baumjohann, W. and Treumann, R. A.: Basic Space Plasma Physics, Imperial College Press, 1997.

Baumjohann, W., Paschmann, G., and Luehr, H.: Characteristics of high-speed ion flows in the plasma sheet, *J. Geophys. Res.*, **95**, 3801–3809, doi:10.1029/JA095iA04p03801, 1990.

Baumjohann, W., Paschmann, G., and Nagai, T.: Thinning and expansion of the substorm plasma sheet, *J. Geophys. Res.*, **97**, 17 173–+, doi:10.1029/92JA01519, 1992.

Belian, R. D., Gisler, G. R., Cayton, T., and Christensen, R.: High-Z energetic particles at geosynchronous orbit during the great solar proton event series of October 1989, *J. Geophys. Res.*, **97**, 16 897–+, doi:10.1029/92JA01139, 1992.

Biermann, L.: Kometenschweife und Solare Korpuskularstrahlung, *Zeitschrift Für Astrophysik*, **29**, 274–286, 1951.

Birn, J., Thomsen, M. F., Borovsky, J. E., Reeves, G. D., McComas, D. J., Belian, R. D., and Hesse, M.: Substorm electron injections: Geosynchronous observations and test particle simulations, *J. Geophys. Res.*, **103**, 9235–9248, doi:10.1029/97JA02635, 1998.

Birn, J., Raeder, J., Wang, Y., Wolf, R., and Hesse, M.: On the propagation of bubbles in the geomagnetic tail, *Ann. Geophys.*, **22**, 1773–1786, 2004.

Boakes, P. D., Milan, S. E., Abel, G. A., Freeman, M. P., Chisham, G., and Hubert, B.: A statistical study of the open magnetic flux content of the magnetosphere at the time of substorm onset, *Geophys. Res. Lett.*, **36**, 4105–+, doi:10.1029/2008GL037059, 2009.

Borg, A. L., Øieroset, M., Phan, T. D., Mozer, F. S., Pedersen, A., Mouikis, C., McFadden, J. P., Twitty, C., Balogh, A., and Rème, H.: Cluster encounter of a magnetic reconnection diffusion region in the near-Earth magnetotail on September 19, 2003, *GRL*, **32**, L19 105, doi:10.1029/2005GL023794, 2005.

Bösinger, T. and Yahnin, A. G.: Pi1B type magnetic pulsation as a high time resolution monitor of substorm development, *Ann. Geophys.*, **5**, 231–237, 1987.

Bothmer, V. and Schwenn, R.: Eruptive prominences as sources of magnetic clouds in the solar wind, *Space Sci. Rev.*, **70**, 215–220, doi:10.1007/BF00777872, 1994.

Bryant, D., Krimigis, S., and Haerendel, G.: Outline of the active magnetospheric particle tracer explorers (ampte) mission, *Geoscience and Remote Sensing, IEEE Transactions on*, **GE-23**, 177–181, doi:10.1109/TGRS.1985.289511, 1985.

Carlson, C. W., Curtis, D. W., Paschmann, G., and Michel, W.: An instrument for rapidly measuring plasma distribution functions with high resolution, *Advances in Space Research*, **2**, 67–70, doi:10.1016/0273-1177(82)90151-X, 1982.

Carr, C., Brown, P., Zhang, T. L., Gloag, J., Horbury, T., Lucek, E., Magnes, W., O'Brien, H., Oddy, T., Auster, U., Austin, P., Aydogar, O., Balogh, A., Baumjohann, W., Beek, T., Eichelberger, H., Fornacon, K.-H., Georgescu, E.,

Glassmeier, K.-H., Ludlam, M., Nakamura, R., and Richter, I.: The Double Star magnetic field investigation: instrument design, performance and highlights of the first year's observations, *Ann. Geophys.*, **23**, 2713–2732, 2005.

Chapman, S. and Ferraro, V. C. A.: A new theory of magnetic storms, Part 1, The initial phase, *Terrest. Magnetism and Atmospheric Elec.*, **36**, 171–186, 1931.

Chapman, S. and Zirin, H.: Notes on the Solar Corona and the Terrestrial Ionosphere, *Smithsonian Contributions to Astrophysics*, **2**, 1–+, 1957.

Chen, C. X. and Wolf, R. A.: Interpretation of high-speed flows in the plasma sheet, *J. Geophys. Res.*, **98**, 21 409–+, 1993.

Chen, C. X. and Wolf, R. A.: Theory of thin-filament motion in Earth's magnetotail and its application to bursty bulk flows, *J. Geophys. Res.*, **104**, 14 613–14 626, doi:10.1029/1999JA900005, 1999.

Chisham, G., Lester, M., Milan, S. E., Freeman, M. P., Bristow, W. A., Grocott, A., McWilliams, K. A., Ruohoniemi, J. M., Yeoman, T. K., Dyson, P. L., Greenwald, R. A., Kikuchi, T., Pinnock, M., Rash, J. P. S., Sato, N., Sofko, G. J., Villain, J.-P., and Walker, A. D. M.: A decade of the Super Dual Auroral Radar Network (SuperDARN): scientific achievements, new techniques and future directions, *Surveys in Geophysics*, **28**, 33–109, doi:10.1007/s10712-007-9017-8, 2007.

Cowley, S. W. H.: Magnetospheric asymmetries associated with the y-component of the IMF, *Planet. Space. Sci.*, **29**, 79–96, doi:10.1016/0032-0633(81)90141-0, 1981.

Cowley, S. W. H.: The Distant Geomagnetic Tail in Theory and Observation, in Magnetic Reconnection in Space and Laboratory Plasmas, edited by E. W. Hones, pp. 228–239, American Geophysical Union, 1984.

Cowley, S. W. H. and Lockwood, M.: Excitation and decay of solar wind-driven flows in the magnetosphere-ionosphere system, *Ann. Geophys.*, **10**, 103–115, 1992.

Davis, T. N. and Sugiura, M.: Auroral Electrojet Activity Index AE and Its Universal Time Variations, *J. Geophys. Res.*, **71**, 785–801, 1966.

Dewhurst, J., Owen, C., Fazakerley, A., and Balogh, A.: Thinning and expansion of the substorm plasma sheet: Cluster PEACE timing analysis, *Ann. Geophys.*, **22**, 4165–4184, 2004.

Draper, N., Lester, M., Wild, J., Milan, S., Provan, G., Grocott, A., Cowley, S., Bogdanova, Y., Dewhurst, J., Fazakerley, A., Davies, J., and Bosqued, J.: A joint Cluster and ground-based instruments study of two magnetospheric substorm events on 1 September 2002, *Ann. Geophys.*, **22**, 4217–4228, 2004.

Dungey, J. W.: Interplanetary magnetic field and the auroral zones, *Phys. Rev. Let.*, **6**, 47–48, 1961.

Dunlop, M. W. and Woodward, T. I.: Multi-Spacecraft Discontinuity Analysis: Orientation and Motion, in Analysis Methods for Multi-Spacecraft Data, edited by G. Paschmann and P. W. Daly, pp. 271–305, ISSI, 1.1 edn., 2000.

Dunlop, M. W., Balogh, A., Glassmeier, K.-H., and Robert, P.: Four-point cluster application of magnetic field analysis tools: The Curlometer, *J. Geophys. Res.*, **107**, 1384–1397, 2002.

Eastwood, J. P., Balogh, A., Dunlop, M. W., and Smith, C. W.: Cluster observations of the heliospheric current sheet and an associated magnetic flux rope and comparisons with ACE, *J. Geophys. Res.*, **107**, 1365–1373, 2002.

Eastwood, J. P., Sibeck, D. G., Slavin, J. A., Goldstein, M. L., Lavraud, B., Sitnov, M., Imber, S., Balogh, A., Lucek, E. A., and Dandouras, I.: Observations of multiple X-line structure in the Earth's magnetotail current sheet: A Cluster case study, *Geophys. Res. Lett.*, **32**, 11 105, doi:10.1029/2005GL022509, 2005.

Erickson, G. M. and Wolf, R. A.: Is steady convection possible in the earth's magnetotail, *Geophys. Res. Lett.*, **7**, 897–900, 1980.

Escoubet, C. P., Fehringer, M., and Goldstein, M.: The Cluster mission, *Ann. Geophys.*, **19**, 1197–1200, 2001.

Farris, M. H. and Russell, C. T.: Determining the standoff distance of the bow shock: Mach number dependence and use of models, *J. Geophys. Res.*, **99**, 17 681–17 689, doi:10.1029/94JA01020, 1994.

Fazakerley, A. N., Carter, P. J., Watson, G., Spencer, A., Sun, Y. Q., Coker, J., Coker, P., Kataria, D. O., Fontaine, D., Liu, Z. X., Gilbert, L., He, L., Lahiff, A. D., Mihaljcic, B., Szita, S., Taylor, M. G. G. T., Wilson, R. J., Dedieu, M., and Schwartz, S. J.: The Double Star Plasma Electron and Current Experiment, *Ann. Geophys.*, **23**, 2733–2756, 2005.

Fazakerley, A. N., Lahiff, A. D., Rozum, I., D., K., Bacai, H., Anekallu, C., West, M., and Åsnes, A.: Cluster PEACE In-Flight Calibration Status, in Proceedings of the 15th Cluster Workshop and CAA School, edited by H. Laakso and C. P. Escoubet, ESA, Springer, in press, 2009.

Fear, R. C.: Cluster Multi-Spacecraft Observations of Flux Transfer Events, Ph.D. thesis, University of London, 2006.

Forsyth, C., Lester, M., Cowley, S. W. H., Dandouras, I., Fazakerley, A. N., Fear, R. C., Frey, H. U., Grocott, A., Kadokura, A., Lucek, E., Rème, H., Milan, S. E., and Watermann, J.: Observed tail current systems associated with bursty bulk flows and auroral streamers during a period of multiple substorms, *Ann. Geophys.*, **26**, 167–184, 2008.

Frey, H. U. and Mende, S. B.: Substorm onsets as observed by IMAGE-FUV, *Proc. 8th Int. Conf. Substorms*, pp. 71–75, 2006.

Galeev, A. A., Galperin, Y. I., and Zelenyi, L. M.: The INTERBALL Project to study solar-terrestrial physics, *Cosmic Res.*, **34**, 339–363, 1996.

Gibson, W. C., Burch, J. L., Scherrer, J. R., Tapley, M. B., Killough, R. L., Volpe, F. A., Davis, W. D., Vaccarello, D. C., Grismore, G., Sakkas, D., and Housten, S. J.: The IMAGE Observatory, *Space Sci. Rev.*, **91**, 15–50, 2000.

Greenwald, R. A., Baker, K. B., Dudeney, J. R., Pinnock, M., Jones, T. B., Thomas, E. C., Villain, J.-P., Cerisier, J.-C., Senior, C., Hanuise, C., Hunsucker, R. D.,

Sofko, G., Koehler, J., Nielsen, E., Pellinen, R., Walker, A. D. M., Sato, N., and Yamagishi, H.: Darn/Superdarn: A Global View of the Dynamics of High-Lattitude Convection, *Space Sci. Rev.*, **71**, 761–796, doi:10.1007/BF00751350, 1995.

Grocott, A., Cowley, S. W. H., and Sigwarth, J. B.: Ionospheric flow during extended intervals of northward but B_y -dominated IMF, *Ann. Geophys.*, **21**, 509–538, 2003.

Grocott, A., Yeoman, T. K., Milan, S. E., and Cowley, S. W. H.: Interhemispheric observations of the ionospheric signature of tail reconnection during IMF-northward non-substorm intervals, *Ann. Geophys.*, **23**, 1763–1770, 2005.

Grocott, A., Yeoman, T. K., Milan, S. E., Amm, O., Frey, H. U., Juusola, L., Nakamura, R., Owen, C. J., Rème, H., and Takada, T.: Multi-scale observations of magnetotail flux transport during IMF-northward non-substorm intervals, *Ann. Geophys.*, **25**, 1709–1720, 2007.

Gustafsson, G., André, M., Carozzi, T., Eriksson, A. I., Fälthammar, C.-G., Grard, R., Holmgren, G., Holtet, J. A., Ivchenko, N., Karlsson, T., Khotyaintsev, Y., Klimov, S., Laakso, H., Lindqvist, P.-A., Lybekk, B., Marklund, G., Mozer, F., Mursula, K., Pedersen, A., Popielawska, B., Savin, S., Stasiewicz, K., Tanskanen, P., Vaivads, A., and Wahlund, J.-E.: First results of electric field and density observations by Cluster EFW based on initial months of operation, *Ann. Geophys.*, **19**, 1219–1240, 2001.

Heacock, R. R.: Two subtypes of type pi micropulsations, *J. Geophys. Res.*, **72**, 3905–3917, 1967.

Henderson, P. D., Owen, C. J., Alexeev, I. V., Slavin, J., Fazakerley, A. N., Lucek, E., and Rème, H.: Cluster observations of flux rope structures in the near-tail, *Ann. Geophys.*, **24**, 651–666, 2006a.

Henderson, P. D., Owen, C. J., Lahiff, A. D., Alexeev, I. V., Fazakerley, A. N., Lucek, E., and Rème, H.: Cluster PEACE observations of electron pres-

sure tensor divergence in the magnetotail, *Geophys. Res. Lett.*, **33**, 22 106–+, doi:10.1029/2006GL027868, 2006b.

Henderson, P. D., Owen, C. J., Lahiff, A. D., Alexeev, I. V., Fazakerley, A. N., Yin, L., Walsh, A. P., Lucek, E., and Réme, H.: The relationship between $\boldsymbol{j} \times \boldsymbol{B}$ and $\nabla \cdot P_e$ in the magnetotail plasma sheet: Cluster observations, *J. Geophys. Res.*, **113**, 7–+, doi:10.1029/2007JA012697, 2008.

Holzworth, R. H. and Meng, C.-I.: Mathematical representation of the auroral oval, *Geophys. Res. Lett.*, **2**, 377–380, doi:10.1029/GL002i009p00377, 1975.

Hoshino, M., Mukai, T., Terasawa, T., and Shinohara, I.: Suprathermal electron acceleration in magnetic reconnection, *J. Geophys. Res.*, **106**, 25 979–25 998, doi:10.1029/2001JA900052, 2001.

Hughes, W. J.: Magnetospheric Configuration, in Introduction to Space Physics, edited by M. G. Kivelson and C. T. Russell, pp. 227–287, Cambridge Unversity Press, 1st edn., 1995.

Hughes, W. J. and Sibeck, D. G.: On the 3-dimensional structure of plasmoids, *Geophys. Res. Lett.*, **14**, 636–639, 1987.

Imber, S. M., Milan, S. E., and Hubert, B.: The auroral and ionospheric flow signatures of dual lobe reconnection, *Ann. Geophys.*, **24**, 3115–3129, 2006.

Ivanova, V. V., Semenov, V. S., Penz, T., Ivanov, I. B., Sergeev, V. A., Heyn, M. F., Farrugia, C. J., Biernat, H. K., Nakamura, R., and Baumjohann, W.: Reconstruction of the reconnection rate from Cluster measurements: Method improvements, *J. Geophys. Res.*, **112**, 10 226–+, doi:10.1029/2006JA012183, 2007.

Jacobs, J. A., Kato, Y., Matsushita, S., and Troitskaya, V. A.: Classification of Geomagnetic Micropulsations, *J. Geophys. Res.*, **69**, 180–+, doi:10.1029/JZ069i001p00180, 1964.

Johnstone, A. D., Alsop, C., Burge, S., Carter, P. J., Coates, A. J., Coker, A. J., Fazakerley, A. N., Grande, M., Gowen, R. A., Gurgiolo, C., Hancock, B. K.,

Narheim, B., Preece, A., Sheather, P. H., Winningham, J. D., and Woodliffe, R. D.: Peace: a plasma electron and current experiment, *Space Sci. Rev.*, **79**, 351–398, 1997.

Juusola, L., Amm, O., Frey, H. U., Kauristie, K., Nakamura, R., Owen, C. J., Sergeev, V., Slavin, J. A., and Walsh, A.: Ionospheric signatures during a magnetospheric flux rope event, *Ann. Geophys.*, **26**, 3967–3977, 2008.

Kepko, L. and Kivelson, M.: Generation of Pi2 pulsations by bursty bulk flows, *J. Geophys. Res.*, **104**, 25 021–25 034, doi:10.1029/1999JA900361, 1999.

Khurana, K. K., Kivelson, M. G., Frank, L. A., and Paterson, W. R.: Observations of magnetic flux ropes and associated currents in Earth's magnetotail with the Galileo spacecraft, *Geophys. Res. Lett.*, **22**, 2087–2090, doi:10.1029/95GL01518, 1995.

Kistler, L. M., Mouikis, C. G., Cao, X., Frey, H., Klecker, B., Dandouras, I., Korth, A., Marcucci, M. F., Lundin, R., McCarthy, M., Friedel, R., and Lucek, E.: Ion composition and pressure changes in storm time and nonstorm substorms in the vicinity of the near-Earth neutral line, *J. Geophys. Res.*, **111**, doi:10.1029/2006JA011939, 2006.

Klein, L. W. and Burlaga, L. F.: Interplanetary magnetic clouds at 1 AU, *J. Geophys. Res.*, **87**, 613–624, doi:10.1029/JA087iA02p00613, 1982.

Kokubun, S., Yamamoto, T., Acuna, M. H., Hayashi, K., Shiokawa, K., and Kawano, H.: The Geotail Magnetic-Field Experiment, *Journal Of Geomagnetism And Geoelectricity*, **46**, 7–21, 1994.

Lepping, R. P., Jones, J. A., and Burlaga, L. F.: Magnetic Field Structure of Interplanetary Magnetic Clouds at 1 AU, *J. Geophys. Res.*, **95**, 11 957–11 965, 1990.

Lessard, M. R., Lund, E. J., Jones, S. L., Arnoldy, R. L., Posch, J. L., Engebretson, M. J., and Hayashi, K.: Nature of Pi1B pulsations as inferred from ground and satellite observations, *Geophys. Res. Lett.*, **33**, 14 108–+, doi:10.1029/2006GL026411, 2006.

Lester, M., Milan, S. E., Provan, G., and Wild, J. A.: Review of Ionospheric Effects of Solar Wind Magnetosphere Coupling in the Context of the Expanding Contracting Polar Cap Boundary Model, *Space Sci. Rev.*, **124**, 117–130, doi:10.1007/s11214-006-9132-8, 2006.

Liu, W. W., Liang, J., and Donovan, E. F.: Interaction between kinetic ballooning perturbation and thin current sheet: Quasi-electrostatic field, local onset, and global characteristics, *Geophys. Res. Lett.*, **35**, 20 107–+, doi:10.1029/2008GL035757, 2008.

Liu, Z. X., Escoubet, C. P., Pu, Z., Laakso, H., Shi, J. K., Shen, C., and Hapgood, M.: The Double Star mission, *Ann. Geophys.*, **23**, 2707–2712, 2005.

Lopez, R. E., Sibeck, D. G., McEntire, R. W., and Krimigis, S. M.: The energetic ion substorm injection boundary, *J. Geophys. Res.*, **95**, 109–117, doi:10.1029/JA095iA01p00109, 1990.

Lui, A. T. Y.: Road map to magnetotail domains., in Magnetotail Physics, pp. 3–9, Johns Hopkins Unversity Press, 1987.

Lui, A. T. Y.: Current disruption in the earth's magnetosphere: Observations and models, *J. Geophys. Res.*, **101**, 13 067–13 088, doi:10.1029/96JA00079, 1996.

Lui, A. T. Y., Volwerk, M., Dunlop, M. W., Alexeev, I. V., Fazakerley, A. N., Walsh, A. P., Lester, M., Grocott, A., Mouikis, C., Henderson, M. G., Kistler, L. M., Shen, C., Shi, J. K., Zhang, T. L., and Rème, H.: Near-Earth substorm features from multiple satellite observations, *J. Geophys. Res.*, **113**, 7–+, doi:10.1029/2007JA012738, 2008.

Mann, I. R., Milling, D. K., Rae, I. J., Ozeke, L. G., Kale, A., Kale, Z. C., Murphy, K. R., Parent, A., Usanova, M., Pahud, D. M., Lee, E.-A., Amalraj, V., Wallis, D. D., Angelopoulos, V., Glassmeier, K.-H., Russell, C. T., Auster, H.-U., and Singer, H. J.: The Upgraded CARISMA Magnetometer Array in the THEMIS Era, *Space Sci. Rev.*, **141**, 413–451, doi:10.1007/s11214-008-9457-6, 2008.

McFadden, J. P., Carlson, C. W., Larson, D., Ludlam, M., Abiad, R., Elliott, B., Turin, P., Marckwordt, M., and Angelopoulos, V.: The THEMIS ESA Plasma Instrument and In-flight Calibration, *Space Sci. Rev.*, **141**, 277–302, doi:10.1007/s11214-008-9440-2, 2008.

McPherron, R. L.: Growth phase of magnetospheric substorms, *J. Geophys. Res.*, **75**, 5592–5599, 1970.

McPherron, R. L., Russell, C. T., and Aubry, M. P.: Satellite studies of magnetospheric substorms on August 15, 1968. 9. Phenomenological model for substorms., *J. Geophys. Res.*, **78**, 3131–3149, doi:10.1029/JA078i016p03131, 1973.

Mende, S. B., Heetderks, H., Frey, H. U., Lampton, M., Geller, S. P., Abiad, R., Siegmund, O. H. W., Tremsin, A. S., Spann, J., Dougani, H., Fuselier, S. A., Magoncelli, A. L., Bumala, M. B., Murphree, S., and Trondsen, T.: Far ultraviolet imaging from the IMAGE spacecraft. 2. Wideband FUV imaging, *Space Sci. Rev.*, **91**, 271–285, 2000a.

Mende, S. B., Heetderks, H., Frey, H. U., Lampton, M., Geller, S. P., Habraken, S., Renotte, E., Jamar, C., Rochus, P., Spann, J., Fuselier, S. A., Gerard, J.-C., Gladstone, R., Murphree, S., and Cogger, L.: Far ultraviolet imaging from the IMAGE spacecraft. 1. System design, *Space Sci. Rev.*, **91**, 243–270, 2000b.

Milan, S. E., Cowley, S. W. H., Lester, M., Wright, D. M., Slavin, J. A., Fillingim, M., Carlson, C. W., and Singer, H. J.: Response of the magnetotail to changes in the open flux content of the magnetosphere, *Journal of Geophysical Research (Space Physics)*, **109**, 4220–+, doi:10.1029/2003JA010350, 2004.

Milan, S. E., Wild, J. A., Grocott, A., and Draper, N. C.: Space- and ground-based investigations of solar wind magnetosphere ionosphere coupling, *Advances in Space Research*, **38**, 1671–1677, doi:10.1016/j.asr.2005.08.009, 2006.

Milling, D. K., Rae, I. J., Mann, I. R., Murphy, K. R., Kale, A., Russell, C. T., Angelopoulos, V., and Mende, S.: Ionospheric localisation and expansion of

long-period Pi1 pulsations at substorm onset, *Geophys. Res. Lett.*, **35**, 17–+, doi:10.1029/2008GL033672, 2008.

Möbius, E., Hovestadt, D., Klecker, B., Scholer, M., Arbinger, H., Hoefner, H., Kuenneth, E., Laeverenz, P., Gloeckler, G., and Ipavich, F. M.: The time-of-flight spectrometer SULEICA for ions of the energy range 5-270 keV/charge on AMPTE IRM, *IEEE Transactions on Geoscience and Remote Sensing*, **23**, 274–279, doi:10.1109/TGRS.1985.289527, 1985.

Morley, S. K. and Freeman, M. P.: On the association between northward turnings of the interplanetary magnetic field and substorm onsets, *Geophys. Res. Lett.*, **34**, doi:10.1029/2006GL028891, 2007.

Mulligan, T. and Russell, C. T.: Multispacecraft modeling of the flux rope structure of interplanetary coronal mass ejections: Cylindrically symmetric versus nonsymmetric topologies, *J. Geophys. Res.*, **106**, 10 581–10 596, doi:10.1029/2000JA900170, 2001.

Mulligan, T., Russell, C. T., Anderson, B. J., and Acuna, M. H.: Multiple spacecraft flux rope modeling of the Bastille Day magnetic cloud, *Geophys. Res. Lett.*, **28**, 4417–4420, doi:10.1029/2001GL013293, 2001.

Murphy, K. R., Rae, I. J., Mann, I. R., Kale, A., and Walsh, A. P.: The dependence of pi2 waveforms on periodic velocity enhancements within bursty bulk flows, *J. Geophys. Res.*, submitted, 2009a.

Murphy, K. R., Rae, I. J., Mann, I. R., Milling, D. K., Watt, C. E. J., Ozeke, L., Frey, H. U., Angelopoulos, V., and Russell, C. T.: Wavelet-based ULF wave diagnosis of substorm expansion phase onset, *J. Geophys. Res.*, **114**, 0–+, doi:10.1029/2008JA013548, 2009b.

Nagai, T., Nakamura, R., Mukai, T., Yamamoto, T., Nishida, A., and Kokubun, S.: Substorms, tail flows and plasmoids, *Advances in Space Research*, **20**, 961–971, doi:10.1016/S0273-1177(97)00504-8, 1997.

Nagai, T., Shinohara, I., Fujimoto, M., Hoshino, M., Saito, Y., Machida, S., and Mukai, T.: Geotail observations of the Hall current system: Evidence of magnetic reconnection in the magnetotail, *J. Geophys. Res.*, **106**, 25 929–25 950, 2001.

Nakamura, R., Baumjohann, W., Mouikis, C., Kistler, L. M., Runov, A., Volwerk, M., Asano, Y., Vörös, Z., Zhang, T. L., Klecker, B., Rème, H., and Balogh, A.: Spatial scale of high-speed flows in the plasma sheet observed by Cluster, *Geophys. Res. Lett.*, **31**, 9804–+, doi:10.1029/2004GL019558, 2004.

Nakamura, R., Amm, O., Laakso, H., Draper, N. C., Lester, M., Grocott, A., Klecker, B., McCrea, I. W., Balogh, A., Rème, H., and André, M.: Localized fast flow disturbance observed in the plasma sheet and in the ionosphere, *Annales Geophysicae*, **23**, 553–566, 2005a.

Nakamura, R., Baumjohann, W., Zhang, T. L., Carr, C. M., Balogh, A., Fornacon, K.-H., Georgescu, E., Rème, H., Dandouras, I., Takada, T., Volwerk, M., Asano, Y., Runov, A., Eichelberger, H., Klecker, B., Mouikis, C., Kistler, L. M., and Amm, O.: Cluster and Double Star observations of dipolarization, *Ann. Geophys.*, **23**, 2915–2920, 2005b.

Nakamura, R., Retinò, A., Baumjohann, W., Volwerk, M., Erkaev, N., Klecker, B., Lucek, E. A., Dandouras, I., Andr, M., and Khotyaintsev, Y.: Evolution of dipolarization in the near-earth current sheet induced by earthward rapid flux transport, *Ann. Geophys.*, **27**, 1743–1754, 2009.

Nelder, J. A. and Mead, R.: A Simplex Method for Function Minimization, *The Computer Journal*, **7**, 308–313, doi:10.1093/comjnl/7.4.308, 1965.

Ogilvie, K. W., Rosenvinge, T. V., and Durney, A. C.: International Sun-Earth Explorer - 3-Spacecraft Program, *Science*, **198**, 131–138, 1977.

Ogino, T., Walker, R. J., and Ashour-Abdalla, M.: Magnetic flux ropes in 3-dimensional MHD simulations, *Washington DC American Geophysical Union Geophysical Monograph Series*, pp. 669–678, 1990.

Ohtani, S.-I.: Flow Bursts in the Plasma Sheet and Auroral Substorm Onset: Observational Constraints on Connection Between Midtail and Near-earth Substorm Processes, *Space Sci. Rev.*, **113**, 77–96, doi:10.1023/B:SPAC.0000042940.59358.2f, 2004.

Øieroset, M., Sandholt, P. E., Denig, W. F., and Cowley, S. W. H.: Northward interplanetary magnetic field cusp aurora and high-latitude magnetopause reconnection, *J. Geophys. Res.*, **102**, 11 349–11 362, doi:10.1029/97JA00559, 1997.

Olson, J. V.: Pi2 pulsations and substorm onsets: A review, *J. Geophys. Res.*, **104**, 17 499–17 520, doi:10.1029/1999JA900086, 1999.

Østgaard, N., Mende, S. B., Frey, H. U., Immel, T. J., Frank, L. A., Sigwarth, J. B., and Stubbs, T. J.: Interplanetary magnetic field control of the location of substorm onset and auroral features in the conjugate hemispheres, *J. Geophys. Res.*, **109**, 7204–+, doi:10.1029/2003JA010370, 2004.

Østgaard, N., Tsyganenko, N. A., Mende, S. B., Frey, H. U., Immel, T. J., Fillingim, M., Frank, L. A., and Sigwarth, J. B.: Observations and model predictions of substorm auroral asymmetries in the conjugate hemispheres, *Geophys. Res. Lett.*, **32**, 5111–+, doi:10.1029/2004GL022166, 2005.

Owen, C. J. and Slavin, J. A.: Energetic Ion Events Associated with Travelling Compression Regions, in Proceedings of the International Conference on Substorms (ICS-1), pp. 365–370, ESA SP-335, 1992.

Owen, C. J., Slavin, J. A., Fazakerley, A. N., Dunlop, M. W., and Balogh, A.: Cluster electron observations of the separatrix layer during traveling compression regions, *Geophys. Res. Lett.*, **32**, L03 104, 2005.

Parker, E.: Extension of the Solar Corona into Interplanetary Space, *J. Geophys. Res.*, **64**, 1675, doi:10.1029/JZ064i011p01675, 1959.

Parker, E. N.: Sweet's Mechanism for Merging Magnetic Fields in Conducting Fluids, *J. Geophys. Res.*, **62**, 509–520, doi:10.1029/JZ062i004p00509, 1957.

Parker, E. N.: Dynamics of the Interplanetary Gas and Magnetic Fields., *Astrophysical Journal*, **128**, 664, doi:10.1086/146579, 1958.

Parks, G. K.: Physics of Space Plasmas, Westview Press, 2nd edn., 2004.

Paschmann, G., Fazakerley, A. N., and Schwartz, S. J.: Moments of Plasma Velocity Distributions, in Analysis Methods for Multi-Spacecraft Data, edited by G. Paschmann and P. W. Daly, pp. 125–158, ISSI, 1.1 edn., 2000.

Petschek, H. W.: Magnetic Field Annihilation, in Physics of Solar Flares, NASA, 1964.

Pontius, Jr., D. H. and Wolf, R. A.: Transient flux tubes in the terrestrial magnetosphere, *Geophys. Res. Lett.*, **17**, 49–52, 1990.

Priest, E. R.: The Sun and its Magnetohydrodynamics, in Introduction to Space Physics, edited by M. G. Kivelson and C. T. Russell, pp. 58–90, Cambridge Unversity Press, 1st edn., 1995.

Primdahl, F.: The fluxgate magnetometer, *J. Phys. E: Sci. Instrum.*, **12**, 241–253, doi:10.1088/0022-3735/12/4/001, 1979.

Rae, I. J., Mann, I. R., Angelopoulos, V., Murphy, K. R., Milling, D. K., Frey, H. U., Kale, A., G., R., Russell, C. T., Watt, C. E. J., Engebretson, M. J., Moldwin, M. B., Mende, S. B., Singer, H. J., and Donovan, E. F.: Near-Earth Initiation of a Terrestrial Substorm, *J. Geophys. Res.*, in press, 2009a.

Rae, I. J., Mann, I. R., Murphy, K. R., Milling, D. K., Parent, A., Angelopoulos, V., Frey, H. U., Kale, A., Watt, C. E. J., Mende, S. B., and Russell, C. T.: Timing and localization of ionospheric signatures associated with substorm expansion phase onset, *J. Geophys. Res.*, **114**, 0–+, doi:10.1029/2008JA013559, 2009b.

Reeves, G. D., Belian, R. D., and Fritz, T. A.: Numerical tracing of energetic particle drifts in a model magnetosphere, *J. Geophys. Res.*, **96**, 13 997–+, doi:10.1029/91JA01161, 1991.

Reeves, G. D., Henderson, M. G., McLachlan, P. S., Belian, R. D., Friedel, R. H. W., and Korth, A.: Radial propagation of substorm injections, in International Conference on Substorms, edited by E. J. Rolfe and B. Kaldeich, vol. 389 of *ESA Special Publication*, pp. 579–584, 1996.

Rème, H., Aoustin, C., Bosqued, J. M., Dandouras, I., Lavraud, B., Sauvaud, J. A., Barthe, A., Bouyssou, J., Camus, T., Coeur-Joly, O., Cros, A., Cuvilo, J., Ducay, F., Garbarowitz, Y., Medale, J. L., Penou, E., Perrier, H., Romefort, D., Rouzaud, J., Vallat, C., Alcayd, D., Jacquey, C., Mazelle, C., d'Uston, C., Mobius, E., Kistler, L. M., Crocker, K., Granoff, M., Mouikis, C., Popecki, M., Vosbury, M., Klecker, B., Hovestadt, D., Kucharek, H., Kuenneth, E., Paschmann, G., Scholer, M., Sckopke, N., Seidenschwang, E., Carlson, C. W., Curtis, D. W., Ingraham, C., Lin, R. P., McFadden, J. P., Parks, G. K., Phan, T., Formisano, V., Amata, E., Bavassano-Cattaneo, M. B., Baldetti, P., Bruno, R., Chionchio, G., Lellis, A. D., Marcucci, M. F., Pallocchia, G., Korth, A., Daly, P. W., Graeve, B., Rosenbauer, H., Vasyliunas, V., McCarthy, M., Wilber, M., Eliasson, L., Lundin, R., Olsen, S., Shelley, E. G., Fuselier, S., Ghielmetti, A. G., Lennartsson, W., Escoubet, C. P., Balsiger, H., Friedel, R., Cao, J.-B., Kovrazhkin, R. A., Papamastorakis, I., Pellat, R., Scudder, J., and Sonnerup, B.: First multispacecraft ion measurements in and near the Earth's magnetosphere with the identical Cluster ion spectrometry (CIS) experiment, *Ann. Geophys.*, **19**, 1303–1354, 2001.

Rème, H., Dandouras, I., Aoustin, C., Bosqued, J. M., Sauvaud, J. A., Vallat, C., Escoubet, P., Cao, J. B., Shi, J., Bavassano-Cattaneo, M. B., Parks, G. K., Carlson, C. W., Pu, Z., Klecker, B., Moebius, E., Kistler, L., Korth, A., Lundin, R., and The Hia Team: The HIA instrument on board the Tan Ce 1 Double Star near-equatorial spacecraft and its first results, *Ann. Geophys.*, **23**, 2757–2774, 2005.

Rostoker, G., Samson, J. C., Creutzberg, F., Hughes, T. J., McDiarmid, D. R., McNamara, A. G., Jones, A. V., Wallis, D. D., and Cogger, L. L.: Canopus - A ground-based instrument array for remote sensing the high latitude

ionosphere during the ISTP/GGS program, *Space Sci. Rev.*, **71**, 743–760, doi:10.1007/BF00751349, 1995.

Runov, A., Nakamura, R., Baumjohann, W., Treumann, R. A., Zhang, T. L., Volwerk, M., Voros, Z., Balogh, A., Glasmeier, K.-H., Klecker, B., Reme, H., and Kistler, L.: Current sheet structure near magnetic X-line observed by Cluster, *Geophys. Res. Lett.*, **30**, 1579–1582, 2003.

Russell, C. T.: How northward turnings of the IMF can lead to substorm expansion onsets, *Geophys. Res. Lett.*, **27**, 3257–3260, doi:10.1029/2000GL011910, 2000.

Russell, C. T. and Elphic, R.: Observation of Magnetic-Flux Ropes In The Venus Ionosphere, *Nature*, **279**, 616–618, 1979.

Schindler, K.: A Theory of the Substorm Mechanism, *J. Geophys. Res.*, **79**, 2803–2810, 1974.

Semenov, V. S., Penz, T., Ivanova, V. V., Sergeev, V. A., Biernat, H. K., Nakamura, R., Heyn, M. F., Kubyshkin, I. V., and Ivanov, I. B.: Reconstruction of the reconnection rate from Cluster measurements: First results, *J. Geophys. Res.*, **110**, 11 217–+, doi:10.1029/2005JA011181, 2005.

Sergeev, V., Kubyshkina, M., Alexeev, I., Fazakerley, A., Owen, C., Baumjohann, W., Nakamura, R., Runov, A., Vörös, Z., Zhang, T. L., Angelopoulos, V., Sauvaud, J.-A., Daly, P., Cao, J. B., and Lucek, E.: Study of near-Earth reconnection events with Cluster and Double Star, *J. Geophys. Res.*, **113**, doi:10.1029/2007JA012902, 2008.

Sergeev, V. A., Angelopoulos, V., Gosling, J. T., Cattell, C. A., and Russell, C. T.: Detection of localized, plasma-depleted flux tubes or bubbles in the midtail plasma sheet, *J. Geophys. Res.*, **101**, 10 817–10 826, doi:10.1029/96JA00460, 1996.

Shiokawa, K., Baumjohann, W., and Haerendel, G.: Braking of high-speed flows in the near-Earth tail, *Geophys. Res. Lett.*, **24**, 1179–1182, doi:10.1029/97GL01062, 1997.

Shirataka, N., Fujimoto, M., Hasegawa, H., and TanDokoro, R.: Reproducing the bipolar magnetic signature at the jet leading edge by three-dimensional reconnection with nonzero guide field, *J. Geophys. Res.*, **111**, 7201–+, doi:10.1029/2005JA011521, 2006.

Shue, J.-H., Chao, J. K., Fu, H. C., Russell, C. T., Song, P., Khurana, K. K., and Singer, H. J.: A new functional form to study the solar wind control of the magnetopause size and shape, *J. Geophys. Res.*, **102**, 9497–9512, doi:10.1029/97JA00196, 1997.

Sibeck, D. G. and Angelopoulos, V.: THEMIS Science Objectives and Mission Phases, *Space Sci. Rev.*, **141**, 35–59, doi:10.1007/s11214-008-9393-5, 2008.

Singer, H., Matheson, L., Grubb, R., Newman, A., and Bouwer, D.: Monitoring space weather with the GOES magnetometers, in Society of Photo-Optical Instrumentation Engineers (SPIE) Conference Series, edited by E. R. Washwell, vol. 2812 of *Society of Photo-Optical Instrumentation Engineers (SPIE) Conference Series*, pp. 299–308, 1996.

Sitnov, M. I., Guzdar, P. N., and Swisdak, M.: On the formation of a plasma bubble, *Geophys. Res. Lett.*, **32**, 16 103–+, doi:10.1029/2005GL023585, 2005.

Sitnov, M. I., Swisdak, M., and Divin, A. V.: Dipolarization fronts as a signature of transient reconnection in the magnetotail, *J. Geophys. Res.*, **114**, 4202–+, doi:10.1029/2008JA013980, 2009.

Slavin, J. A., Smith, E. J., Tsurutani, B. T., Sibeck, D. G., Singer, H. J., Baker, D. N., Gosling, J. T., Hones, E. W., and Scarf, F. L.: Substorm associated traveling compression regions in the distant tail - ISEE-3 geotail observations, *GRL*, **11**, 657–660, doi:10.1029/GL011i007p00657, 1984.

Slavin, J. A., Hesse, M., Owen, C. J., Taguchi, S., Fairfield, D. H., Lepping, R. P., Kokubun, S., Mukai, T., Lui, A. T. Y., Anderson, R. R., Matsumoto, H., and Sutcliffe, P. R.: Dual spacecraft observations of lobe magnetic field perturbations

before, during and after plasmoid release, *Geophys. Res. Lett.*, **26**, 2897–2900, doi:10.1029/1999GL003606, 1999.

Slavin, J. A., Lepping, R. P., Gjerloev, J., Fairfield, D. H., Hesse, M., Owen, C. J., Moldwin, M. B., Nagai, T., Ieda, A., and Mukai, T.: Geotail observations of magnetic flux ropes in the plasma sheet, *J. Geophys. Res.*, **108**, 1015–1032, 2003a.

Slavin, J. A., Lepping, R. P., Gjerloev, J., Goldstein, M. L., Fairfield, D. H., Acuna, M. H., Balogh, A., Dunlop, M., Kivelson, M. G., Khurana, K., Fazakerley, A., Owen, C. J., Reme, H., and Bosqued, J. M.: Cluster electric current density measurements within a magnetic flux rope in the plasma sheet, *Geophys. Res. Lett.*, **30**, 1362–1365, 2003b.

Slavin, J. A., Transkanen, E. I., Hesse, M., Owen, C. J., Dunlop, M. W., Imber, S., Lucek, E. A., Balogh, A., and Glassmier, K.-H.: Cluster observations of traveling compression regions in the near-tail, *J. Geophys. Res.*, **110**, A06 207, 2005.

Smith, C. W., L'Heureux, J., Ness, N. F., Acuña, M. H., Burlaga, L. F., and Scheifele, J.: The ACE Magnetic Fields Experiment, *Space Sci. Rev.*, **86**, 613–632, doi:10.1023/A:1005092216668, 1998.

Sonnerup, B. U. O. and Cahill, L. J.: Magnetopause structure and attitude from Explorer 12 observations, *J. Geophys. Res.*, **72**, 171–183, 1967.

Sonnerup, B. U. O. and Scheible, M.: Minimum and Maximum Variance Analysis, in Analysis Methods for Multi-Spacecraft Data, edited by G. Paschmann and P. W. Daly, pp. 185–220, ISSI, 1.1 edn., 2000.

Spanswick, E., Donovan, E., Friedel, R., and Korth, A.: Ground based identification of dispersionless electron injections, *Geophys. Res. Lett.*, **34**, 3101–+, doi:10.1029/2006GL028329, 2007.

Steed, K., Owen, C. J., Harra, L. K., Green, L. M., Dasso, S., Walsh, A. P., Démoulin, P., and van Driel-Gesztelyi, L.: Locating the solar source of 13 April 2006 magnetic cloud, *Ann. Geophys.*, **26**, 3159–3168, 2008.

Stewart, B.: On the great magnetic disturbance which extended from august 28 to september 7, 1859, as recorded by photography at the kew observatory, *Philosophical Transactions of the Royal Society of London*, **151**, 423–430, 1861.

Stone, E. C., Frandsen, A. M., Mewaldt, R. A., Christian, E. R., Margolies, D., Ormes, J. F., and Snow, F.: The Advanced Composition Explorer, *Space Sci. Rev.*, **86**, 1–22, doi:10.1023/A:1005082526237, 1998.

Takada, T., Nakamura, R., Baumjohann, W., Asano, Y., Volwerk, M., Zhang, T. L., Klecker, B., Rème, H., Lucek, E. A., and Carr, C.: Do BBFs contribute to inner magnetosphere dipolarizations: Concurrent Cluster and Double Star observations, *Geophys. Res. Lett.*, **33**, 21 109–+, doi:10.1029/2006GL027440, 2006.

Torkar, K., Riedler, W., Escoubet, C. P., Fehringer, M., Schmidt, R., Grard, R. J. L., Arends, H., Rüdenauer, F., Steiger, W., Narheim, B. T., Svenes, K., Torbert, R., André, M., Fazakerley, A., Goldstein, R., Olsen, R. C., Pedersen, A., Whipple, E., and Zhao, H.: Active spacecraft potential control for Cluster - implementation and first results, *Ann. Geophys.*, **19**, 1289–1302, 2001.

Tsyganenko, N. A. and Stern, D. P.: Modeling the global magnetic field of the large-scale Birkeland current systems, *J. Geophys. Res.*, **101**, 27 187–27 198, doi:10.1029/96JA02735, 1996.

Volwerk, M., Louarn, P., Chust, T., Roux, A., de Feraudy, H., and Holback, B.: Solitary kinetic Alfvén waves: A study of the Poynting flux, *J. Geophys. Res.*, **101**, 13 335–13 344, doi:10.1029/96JA00166, 1996.

Volwerk, M., Zhang, T. L., Nakamura, R., Runov, A., Baumjohann, W., Glassmeier, K.-H., Takada, T., Eichelberger, H. U., Carr, C. M., Balogh, A., Klecker, B., and Rme, H.: Plasma flow channels with ulf waves observed by cluster and double star, *Ann. Geophys.*, **23**, 2929–2935, 2005.

Walsh, A. P., Fazakerley, A. N., Wilson, R. J., Alexeev, I. V., Henderson, P. D., Owen, C. J., Lucek, E., Carr, C., and Dandouras, I.: Near-simultaneous magne-

totail flux rope observations with Cluster and Double Star, *Ann. Geophys.*, **25**, 1887–1897, 2007.

Walsh, A. P., Fazakerley, A. N., Lahiff, A. D., Volwerk, M., Grocott, A., Dunlop, M., Lui, T., Kistler, L., Lester, M., Mouikis, C., Pu, Z., Shen, C., Shi, J., Taylor, M. G., Lucek, E., Zhang, T. L., and Dandouras, I.: Cluster and Double Star Multipoint Observations of a Plasma Bubble, *Ann. Geophys.*, **27**, 725–743, 2009.

Winglee, R. M.: Ion cyclotron and heavy ion effects on reconnection in a global magnetotail, *J. Geophys. Res.*, **109**, 9206–+, doi:10.1029/2004JA010385, 2004.

Wolf, R. A.: Magnetospheric Configuration, in Introduction to Space Physics, edited by M. G. Kivelson and C. T. Russell, pp. 288–329, Cambridge Unversity Press, 1st edn., 1995.

Xiao, C. J., Pu, Z. Y., Ma, Z. W., Fu, S. Y., Huang, Z. Y., and Zong, Q. G.: Inferring of flux rope orientation with the minimum variance analysis technique, *J. Geophys. Res.*, **109**, A11 218, 2004.

Yoon, P. H., Lui, A. T. Y., and Bonnell, J. W.: Identification of plasma instability from wavelet spectra in a current disruption event, *J. Geophys. Res.*, **114**, 4207–+, doi:10.1029/2008JA013816, 2009.

Zhang, J.-C., Wolf, R. A., Sazykin, S., and Toffoletto, F. R.: Injection of a bubble into the inner magnetosphere, *Geophys. Res. Lett.*, **35**, L02 110, doi:10.1029/2007GL032048, 2008.

Zhang, Y. C., Liu, Z. X., Shen, C., Fazakerley, A., Dunlop, M., Réme, H., Lucek, E., Walsh, A. P., and Yao, L.: The magnetic structure of an earthward-moving flux rope observed by Cluster in the near-tail, *Ann. Geophys.*, **25**, 1471–1476, 2007.

Zhou, X.-Z., Zong, Q.-G., Wang, J., Pu, Z. Y., Zhang, X. G., Shi, Q. Q., and Cao, J. B.: Multiple triangulation analysis: application to determine the velocity of 2-D structures, *Ann. Geophys.*, **24**, 3173–3177, 2006.

Zwan, B. J. and Wolf, R. A.: Depletion of solar wind plasma near a planetary boundary, *J. Geophys. Res.*, **81**, 1636–1648, 1976.

Zwingmann, W.: Self-consistent magnetotail theory - Equilibrium structures including arbitrary variation along the tail axis, *J. Geophys. Res.*, **88**, 9101–9108, 1983.